Modeling, simulation and experimental investigation of the thermal and electrochemical behavior of a LiFePO₄-based lithium-ion battery

**Von der Fakultät Chemie der Universität Stuttgart
zur Erlangung der Würde eines Doktors der
Naturwissenschaften (Dr. rer. -nat.) genehmigte Abhandlung**

Vorgelegt von

Dipl.-Chem. Christian Achim Hellwig

aus Köln

Hauptberichter: Prof. Dr. Wolfgang G. Bessler
Mitberichter: Prof. Dr. Emil Roduner

Tag der mündlichen Prüfung: 26.09.2013

Institut für Physikalische Chemie der Universität Stuttgart

2013

Der Berg als Sperre	*The hill as edge*
Der Horizont als Hoffnung	*The horizon as hope*
Der Ausblick Ansporn	*The prospect cheering*
Lange wächst der Baum,	*The tree grows along,*
Bis dass er stark und kräftig;	*Until he's robust and strong;*
Die Zeit lässt reifen.	*The time lets ripen.*
Das Große zeigt sich	*The large shows in*
Im Kleinen, aber Kleines	*The minor, but the minor*
Hat große Wirkung.	*Has a big impact.*
Alles, was du machst	*All, what you do is*
Ist richtig, denn es fördert	*Right, because it supports*
Deine Entwicklung.	*Your evolution.*
Große Schritte sind	*Big steps are good*
Gut für das Selbstbewusstsein.	*For your self-confidence.*
Kleine für'n Erfolg.	*Small steps for success.*
In Allem Denken	*The power is in*
Steckt die Kraft es bewegen	*All your thoughts to move and*
Und tun zu können.	*Act successfully*
Übe Arbeit und	*Cultivate work*
Geduld – so wirst Du reiche	*And patience – you will reap*
Ernte einfahren.	*Wealthy harvesting.*

All dicta are written by Christian Hellwig in 2004 and translated into English in 2013. As style the Japanese poetic form haiku was chosen which consists of 17 syllables in total composed in the traditional "5-7-5" form.

Table of content

List of abbreviations

EC	Ethylene carbonate
EMC	Ethylene methylene carbonate
ES	Energetically excited state
DMC	Dimethyl carbonate
DOD	Depth of discharge
FP	Iron phosphate, $FePO_4$
HFR	High-frequency range
LFP	Lithium iron phosphate, $LiFePO_4$
LFR	low-frequency range
Li	Lithium, Lithium atom
Li^+	Lithium ion
Li_xFePO_4	L_xFP, with $0 \leq x \leq 1$
L_xFP	Li_xFePO_4, with $0 \leq x \leq 1$
MFR	Medium-frequency range
OCV	Open circuit voltage
OCP	Open circuit potential
PC	Propylene carbonate
PD	Particle distribution
SEI	Solid electrolyte interphase
SOC	State of charge
SOH	State of health

List of symbols

Symbol	Unit	Description
a_{ji}	–	Activity coefficient of species i
A	–	Pre-exponential factor (Warburg impedance)
A_{dl}^{V}	m²/m³	Electric capacity area per volume due to double-layer
$A_{LFP,FP}^{V}$	m²/m³	Active interface between LFP and FP
A_{0}^{V}	m²/m³	Initial active interface
b	–	Source term due to diffusion and chemical reactions of charged species
c_0	kg/m³	Reference or initial concentration
c_i	kg/m³	Concentration of species i
c_p^{eff}	J/kg/K	Effective heat capacity
C_i^{chem}	J/mol	Chemical potential of species i
C_{dl}	F/m²	Electric capacity per area due to double-layer
$\tilde{D}_i$	m/s²	Chemical diffusivity of species i
D_i	m/s²	Diffusion coefficient of species i
e	C	Elementary charge ($1.6 \cdot 10^{-19}$ C)
E	V	Cell potential
E_{eq}	V	Cell potential at equilibrium
E_{ref}^{eq}	V	Reference half-cell potential at equilibrium
E_{act}	J/mol	Activation energy
f_{rel}	–	Relative sensitivity factor
$f(c_i)$	–	Activity coefficient dependent on concentration of species i
F	mol/C	Faraday's constant
f	–	Function depending on other parameters
ΔG	J/mol	Free Gibb's reaction enthalpy
ΔH	J/mol	Reaction enthalpy
i	A/m²	Current density

List of symbols

i_0	A/m²	Exchange current density
i_F^V	A/m³	Volumetric faradaic current density
i_{dl}^V	A/m³	Volumetric current density due to double-layer
J_i	A/m²	Current density of species i
k_b	J/K	Stefan Boltzmann constant
L	m	Length
l	m	Hopping length
M_i	g/mol	Molar mass of species i
n	−	Crystallinity
P_i	−	Model parameter, value
P_i^0	−	Model parameter, reference value
P_i^+	−	Model parameter, value variation
q_i	C	Electrical charge of species i
$\dot{q}_{sour}^V$	W/m³	Heat source per volume
r	m	Radius of particle
R	J/mol/K	Ideal gas constant
R_{SEI}	Ω	Resistance due to SEI
S	m²	Contact area between electrolyte and sample
ΔS	J/K/mol	Entropy
$\Delta_R S$	J/K/mol	Reaction entropy
s_i	J/K/mol	Molar entropy of species i
$\dot{s}_i^V$	mol/m³/s	Volumetric source term of species i
t	s	Time
t_+	−	Transference number of cations
T	K	Temperature
T_g	K	Glas temperature
T_{cell}	K	Temperature of cell
T_{env}	K	Temperature of environment
u	−	Displacement vector
V_m	m³/mol	Molar volume
x	m	Location, direction
x_{Li^1}	−	Stoichiometry of intercalated lithium in bulk

List of symbols

X_k	−	Molar fraction of species k
y	m	Location, direction
z	−	Number of transferred electrons
z_i	−	Number of electrons of species i

Greek letters

Symbol	Unit	Description
α	W/m²/K	Heat transfer coefficient
α_a	−	Anodic symmetry factor
α_c	−	Cathodic symmetry factor
ε	−	Porosity
ε_0	−	Vacuum permittivity
ε_r	−	Relative permittivity
η	V	Overpotential
γ_i	−	Thermodynamic factor
$\gamma_\pm$	−	Activation coefficient of positive or negative charged species
γ_{Li^V}	−	Activity coefficient of Lithium vacancies in bulk
κ	1/Ω/m	Electric conductivity
λ^{eff}	W/m/K	Effective heat conductivity
$\tilde{\mu}_i$	J/mol	Electrochemical potential of species i
μ_i	J/mol	Chemical potential of species i
μ_i^0	J/mol	Standard chemical potential of species i
v	Hz	Hopping frequeny
v_i	−	Stoichiometry factor of reaction correlated to species i
ϕ	V	Electric potential
$\Delta\phi$	V	Potential difference
ρ_i	kg/m³	Density of species i
σ_i	S/m²	Conductivity of species i

List of symbols

Summary

In this thesis the modeling and simulation of a LiFePO$_4$-based lithium-ion battery was presented. For a better understanding of the behavior of the cell, a model was developed which allows a detailed insight into occurring processes during operation.

Modeling framework. A multi-scale approach was used to describe physico-chemical processes occurring on different time and length scales. It includes transport processes within active materials and in a liquid electrolyte. Furthermore, a phase transition in the active material of the cathode, LiFePO$_4$, was included. Electron-transfer processes on particle surfaces were considered which were coupled with incorporation of lithium ions into the active materials. Structural information of a repeat unit was resolved. This enables the prediction of temperature variation within the whole battery across the windings during operation. Besides kinetic effects, the model includes thermodynamic information about the active materials of both electrodes. It was separated into an enthalpy and entropy contribution as a function of lithium concentration within the active material. Furthermore, a complex intercalation mechanism was proposed for the cathode material. It describes the phase transition between LiFePO$_4$ and the de-lithiated form FePO$_4$. The results were separated into two parts: the macro-model is based on global kinetics and describes the electrochemical and the thermal behavior of a complete battery. The micro-model focuses on the influence of the phase transition on the electrochemical performance.

Experimental work. For model parameterization and validation, experiments were performed using a LiFePO$_4$-based lithium-ion battery of the company A123 systems with a nominal capacity of 2.3 Ah. The focus of investigation was the electrochemical performance (charge curves, discharge curves, electrochemical impedance spectra) and the heat production and temperature variation under various conditions (current and ambient temperatures).

Macro-model. The macro-model showed a very good agreement with the experiments. Discharge and charge simulations for different C-rates reproduce the experimental electrochemical behavior of the battery. This means that the thermodynamic properties of both electrodes were correctly chosen from literature. Thermal simulations showed good agreement with experimental temperature behavior at various ambient temperatures and C-rates. The model allows the predictions of the internal temperature. Depending on applied current and

ambient temperature, simulations predict that the temperature at the center of the battery is up to 3 °C higher than at the surface. The internal temperature and the temperature distribution during operation depend on the boundary conditions of the experimental setup. Heat production and temperature variation correlate depending on applied current and ambient temperature. A general trend could be concluded: At high ambient temperatures, thermodynamic effects dominate the heat production. At low ambient temperatures, mainly kinetic effects affect the heating. Additionally, an increasing current leads to an increase of heat production due to a stronger kinetic contribution. While kinetic effects always lead to a positive heat production, heating due to thermodynamic properties depend on the current direction. As the electrode reaction entropies exhibit sign changes, complex heating and cooling effects were observed. The variation of temperature during cycling was successfully predicted. Regarding impedance spectra, the macro-model predicts different behavior compared to the experimental results. Although results are in a correct order of magnitude, the macro-model fails in reproducing time-resolved processes correctly.

Micro-model. Motivated by the need for a better agreement with the experimental impedance spectra, a more detailed model on the electrode scale was developed. It includes adsorption reactions on particle surfaces, intercalation reactions and bulk diffusion of lithium ions. Additionally on the cathode side, a phase transition was included to describe the characteristic behavior of $LiFePO_4$. Using this model, an improved agreement was obtained with experimental impedance spectra and discharge and charge curves up to 1 C. To achieve agreement for higher C-rates, the $LiFePO_4-FePO_4$ interfacial area had to be modeled as current and state-of-charge dependent. This shows that the interfacial processes are complex and govern the cell behavior. We conclude that the interface functions as a buffer for lithium ions depending on current and state of charge.

Conclusion. The main focus of this work was to describe and understand the electrochemical performance and the temperature behavior of a $LiFePO_4$-based lithium-ion battery under different ambient temperatures and applied currents. The developed macro-model was shown to be sufficient for reproducing discharge and charge curves and thermal behavior of the battery, while impedance spectra could not be fully reproduced. The developed micro-model contains additional detailed information on the elementary kinetic level regarding intercalation reactions and phase transition. Based on this model, it could be shown that the interface of the $LiFePO_4-FePO_4$ system acts as buffer for lithium ions.

Compared to previous publications, for the first time this work shows the contributions of thermodynamics and kinetics at different ambient temperatures and current requirements. For the first time discharge / charge curves and impedance spectra of a full $LiFePO_4$-battery are shown comparatively and interpreted on the base of thermodynamic and kinetic effects of the elementary kinetic micro-model and of the global kinetic macro-model.

Outlook.   This work is a base for further investigations. A coupling of both models over all scales is strongly recommended. This would enable the prediction of temperature distribution and electrochemical performance based on elementary kinetics. The assumed elementary reactions on the cathode side could be further improved by assuming an energetically excited state as interface. This could allow a more correct correlation between phase transition and current requirement. Furthermore, the idea of an energetically excited state may be transferred to the anode, too. This would open up the possibility to reproduce the behavior at different states of charge and volume changes. Additionally, the current model with its elementary reactions forms a base for including further side reactions, such as SEI formation or lithium plating. This will lead to a better understanding of aging and degradation behavior of a battery cell.

Zusammenfassung

In dieser Arbeit wurde die Modellierung und Simulation einer $LiFePO_4$-basierten Lithium-Ionen Batterie vorgestellt. Für ein besseres Verständnis des Zellverhaltens wurde ein Modell entwickelt, welches einen detaillierten Einblick in die während des Betriebes ablaufenden Prozesse ermöglicht.

Modellierung.   Es wurde ein Multi-Skalen-Ansatz verwendet, um die physikochemischen Prozesse, welche auf unterschiedlichen Zeit- und Längenskalen ablaufen, beschreiben zu können. Er berücksichtigt Transportprozesse in Aktivmaterialien und im flüssigen Elektrolyten. Desweiteren wurde der Phasenübergang des kathodischen Aktivmaterials eingearbeitet. Ebenso wurden Elektronenübertragungsprozesse berücksichtigt, welche mit der Einlagerung der Lithium-Ionen in das Aktivmaterial gekoppelt wurden. Auch die strukturellen Informationen einer Wiederholungseinheit wurden aufgelöst. Das Modell ermöglicht die Vorhersage von Temperaturvariationen innerhalb der gesamten Zelle, welche während des Betriebes auftreten. Neben kinetischen Einflüssen berücksichtigt das Modell thermodynamische Informationen über die Aktivmaterialien beider Elektroden. Diese wurden in einen Enthalpie- und einen Entropieanteil als Funktion der Lithiumkonzentration in den Aktivmaterialien separiert. Desweiteren wurde ein komplexer Einlagerungsmechanismus für das Kathodenmaterial vorgeschlagen. Es beschreibt den Phasenübergang zwischen $LiFePO_4$ und der delithiierten Form $FePO_4$. Die Ergebnisse wurden in zwei Abschnitte unterteilt: Das „Makro-Modell" basiert auf einem globalkinetischen Ansatz und beschreibt das elektrochemische und thermische Verhalten der gesamten Batterie. Das „Mikro-Modell" setzt den Schwerpunkt auf den Phasenübergang und dessen Einfluss auf die elektrochemische Arbeitsleistung.

Experimente.   Zur Parametrierung und Validierung des Modells wurden Experimente an einer $LiFePO_4$-basierten Lithium-Ionen-Batterie der Firma A123 systems mit einer Nennkapazität von 2.3 Ah durchgeführt. Der Fokus der Untersuchung bestand in der elektrochemischen Leistung (Ladekennlinien, Entladekennlinien, elektrochemische Impedanzspektren) und in der Wärmeproduktion und Temperaturvariation unter verschiedenen Bedingungen (Strom und Umgebungstemperaturen).

Makro-Modell.   Das Makro-Modell zeigt sehr gute Übereinstimmungen mit den Experimenten. Simulationen von Lade- und Entladevorgängen bei verschiedenen C-Raten reprodu-

zieren das experimentelle elektrochemische Verhalten der Batterie. Das bedeutet, dass die thermodynamischen Eigenschaften korrekt aus der Literatur ausgesucht wurden. Thermische Simulationen zeigen eine gute Übereinstimmung mit dem experimentellen thermischen Verhalten bei verschiedenen Umgebungstemperaturen und C-Raten. Das Modell erlaubt die Vorhersage der Temperatur im Inneren der Batterie. Abhängig vom angelegten Strom und der Umgebungstemperatur sagt das Modell vorher, dass die Temperatur im Zellinneren bis zu 3 °C höher als an der Oberfläche sein kann. Die Vorhersage der inneren Temperatur und der Temperaturverteilung während des Betriebes hängt von den Randbedingungen des experimentellen Aufbaus ab. Wärmeproduktion und Temperaturvariation korrelieren miteinander, was vom angelegten Strom und der Umgebungstemperatur beeinflusst wird. Eine generelle Tendenz kann gefolgert werden: Bei hohen Umgebungstemperaturen dominieren thermodynamische Effekte die Wärmeproduktion. Bei niedrigen Umgebungstemperaturen beeinflussen hauptsächlich kinetische Effekte die Erwärmung. Zusätzlich führt ein erhöhter Stromfluss wegen eines stärkeren Beitrags der Kinetik zu einer Steigerung der Wärmeproduktion. Während kinetische Prozesse immer zu einer positiven Wärmeproduktion führen, wird die Erwärmung, bedingt von den thermodynamischen Eigenschaften, von der Stromrichtung mitbeeinflusst. Weil die Entropien der Elektrodenreaktionen einen Vorzeichenwechsel durchlaufen, wurden komplexe Erwärmung- und Kühlungseffekte beobachtet. Die Temperaturvariation während des Zyklisierens wurde erfolgreich wiedergegeben. Betrachtet man die Impedanzspektren, gibt das Makro-Modell ein anderes Verhalten wieder als die experimentellen Ergebnisse. Obwohl die Ergebnisse in der korrekten Größenordnung liegen, ist das Makro-Modell nicht in der Lage, zeitaufgelöste Prozesse korrekt zu reproduzieren.

Mikro-Modell. Motiviert von dem Ziel, eine bessere Übereinstimmung mit den experimentellen Impedanzspektren zu erhalten, wurde ein detaillierteres Model auf der Elektrodenskala entwickelt. Es beinhaltet die Adsorptionsreaktionen auf Partikeloberflächen, Interkalationsreaktionen und Festkörperdiffusion von Lithium-Ionen. Zusätzlich wurde auf Kathodenseite ein Phasenwechsel miteingebunden, um das charakteristische Verhalten von $LiFePO_4$ wiederzugeben. Die Anwendung dieses Modells führte zu einer verbesserten Übereinstimmung mit Experimenten in Bezug auf Impedanzspektren und Entlade- und Ladekennlinien bis zu 1 C. Um Übereinstimmung mit höheren C-Raten zu erhalten, wurde die Grenzflächenschicht strom- und ladungszustandsabhängig modelliert. Das zeigt, dass die Grenzflächenprozesse komplex sind und das Zellverhalten beeinflussen. Daraus kann gefolgert werden, dass die Grenzfläche als Puffer für Lithium-Ionen fungiert, welche vom Strom und Ladungszu-

stand abhängig ist.

Ergebnis.   Der Hauptfokus dieser Arbeit war es, das elektrochemische Verhalten und das Temperaturverhalten einer LiFePO$_4$-basierten Lithium-Ionen-Batterie bei verschiedenen Temperaturen und angelegten Strömen zu beschreiben und zu verstehen. Es wurde gezeigt, dass das entwickelte Makro-Modell ausreicht, um Entlade- und Ladekennlinien oder thermisches Verhalten der Batterie wiederzugeben, während Impedanzspektren nicht reproduziert werden konnten. Das entwickelte Mikro-Modell beinhaltet zusätzlich detaillierte Informationen auf der elementarkinetischen Skala, bezüglich Interkalationsreaktionen und Phasenübergang. Mit diesem Modell konnte gezeigt werden, dass die Grenzfläche des LiFePO$_4$−FePO$_4$−Systems als Puffer für Lithium-Ionen agiert.

Im Vergleich zu früheren Arbeiten zeigt diese Arbeit erstmals die Beiträge von Thermodynamik und Kinetik bei verschiedenen Umgebungstemperaturen und Stromanforderungen. Erstmals werden Kennlinien und Impedanzen einer ganzen LiFePO$_4$-Batterie gleichzeitig auf Basis von thermodynamischen und kinetischen Effekten des elementar-kinetischen Micro- und des global-kinetischen Macro-Modells vergleichend dargestellt und interpretiert.

Ausblick.   Diese Arbeit stellt die Grundlage für weiterführende Untersuchungen dar. Das Verknüpfen beider Modelle über alle Skalen hinweg wird stark empfohlen. Das würde die Vorhersage von Temperaturverteilung und elektrochemischer Leistung auf Basis von Elementarkinetik ermöglichen. Die angenommenen Elementarreaktionen auf Kathodenseite können durch die Annahme eines energetisch angeregten Zustands an der Grenzfläche weiter verbessert werden. Der Zusammenhang zwischen Phasenübergang und Stromanforderungen können damit besser dargestellt werden. Desweiteren kann die Idee eines energetisch angeregten Zustandes auch auf die Anode übertragen werden. Das würde die Möglichkeit eröffnen, das Verhalten bei verschiedenen Ladungszuständen und Volumenänderungen zu reproduzieren. Zusätzlich bildet das derzeitige Modell mit seinen elementarkinetischen Reaktionen eine Grundlage für die Erweiterung um weitere Nebenreaktionen, wie SEI-Bildung oder Lithiumablagerung. Das wird zu einem besseren Verständnis vom Verhalten bei Alterungs- und Schädigungsvorgängen der Batterie führen.

1 Introduction

In the recent years, lithium-ion batteries became more and more important. They are used in laptops, mobile phones and, lately, in cars or even in airplanes. They offer electrical energy storage with high efficiency. In spite of the daily use, the behavior of a lithium-ion battery is not entirely understood today. Besides capacity losses and cycling degradation with operating time, accidents were also reported wherein batteries caught fire caused by side reactions. These thermal run-away events initiated detailed research investigations in science and industry in order to tackle safety issues. Also, an ongoing task is the estimation of the state of charge which depends on charge-discharge history and the battery age expressed as state of health. Further understanding of processes occurring within the battery is necessary to improve battery lifetime and cycling performance.

Batteries have been known and used for over two hundred years. Volta discovered the principle of the electrochemical cell already in 1799 [1]. Around twenty years ago the importance of batteries increased immensely. For portable electronic applications batteries were needed with more power, higher capacity and less weight. To satisfy the rising energy demand, many investigations were dedicated to different battery types. Already 100 years ago the lead-acid battery was in use. Despite several advantages, like low material and production cost, it offers only a low energy density. Figure 1 shows the different battery types and the development towards higher volumetric and gravimetric energy density, which means an improvement towards smaller sizes and lighter weights [2]. To increase the energy density, different battery types were developed, including Ni-Cd- and Ni-metal-hydride-batteries. Today the highest energy density is offered by lithium-ion batteries. Lithium is the lightest metal with a molar weight of 6.94 g/mol and the most electropositive element with a voltage of −3.04 V versus a standard hydrogen electrode. It has a density of only 0.53 g/cm³ which makes it favorable for high-energy-density batteries. The existing challenges concern further improvements of lifetime, safety, reliability and cost. Current batteries loose capacity and power during their lifetime caused by aging mechanisms, e.g., formation of a solid electrolyte interface or lithium plating. These aging mechanisms may affect other side reactions which can lead to dangerous reactions like thermal runaway, internal short circuit, etc. These mechanisms are strongly temperature dependent and not well understood. To avoid safety risks, not only applied current and temperature, but also the state of a battery plays an important role.
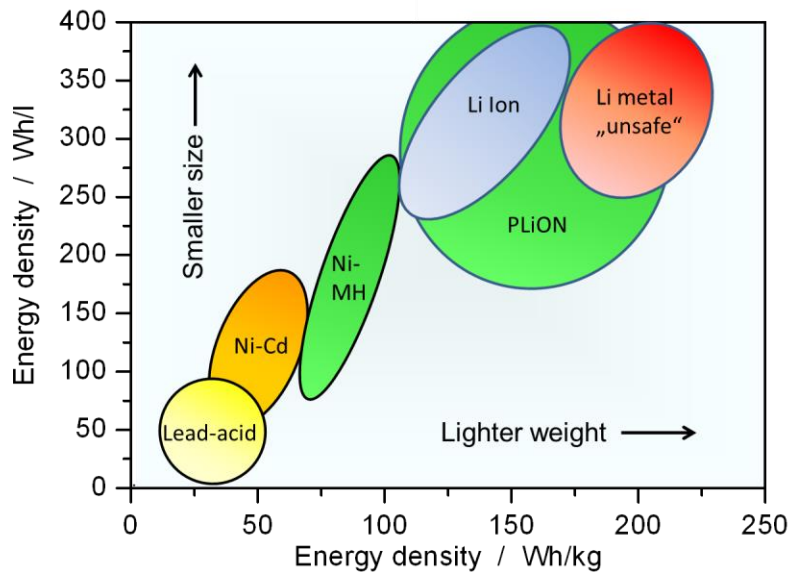
Figure 1: Comparison of different types of batteries with their volumetric and gravimetric energy densities, based on Tarascon et al. [2]. In contrast to the other battery types, a plastic lithium-ion battery (PLiON) does not contain free electrolyte.

Modeling and simulation of batteries offer more detailed insight into processes which are difficult to measure experimentally. Detailed information can be obtained regarding occurring processes or side reactions taking place. Furthermore, prediction of battery behavior under extreme conditions, such as thermal run-away, is possible.

This work contributes to these topics by focusing on the electrochemical and thermal performance of a LiFePO$_4$-based lithium-ion battery. The aim is to reproduce charge / discharge curves, impedance spectra and thermal behavior using the developed models to obtain a better understanding. In chapter 2 a general overview of batteries, their construction and materials, and their electric and thermal behavior is given. This chapter ends with an overview of the recent research investigations in literature concerning modeling and simulations of batteries. For validation experimental work has been performed which is presented in chapter 3. In chapter 4 the development of two models is presented. The first model, called macro-model, is used and discussed in chapter 5. The second model, called micro-model, is an extended model of the macro-model. Results are presented in chapter 6. The thesis is closed by a summary.

2 Background

2.1 Overview

In this work a commercially available 26650-size $LiFePO_4$-based lithium-ion battery produced by A123 with a nominal capacity of 2.3 Ah is studied. In the present chapter a general introduction about lithium-ion batteries is given. It treats the function, construction and typical behavior of batteries. This is followed by a special focus on graphite and $LiFePO_4$, where a general explanation of the materials and their typical behavior is given. Additionally, aging mechanisms, like solid electrolyte interface growth or lithium plating, are mentioned, which may occur during usage. Closing this chapter a general overview on the literature is given concerning modeling and simulation of batteries and their compounds.

2.2 Lithium iron phosphate based lithium-ion battery

2.2.1 Motivation

The motivation for using lithium iron phosphate based lithium-ion batteries is due to the cathode material lithium iron phosphate ($LiFePO_4$, LFP). This material offers lower production costs due to the use of iron instead of other metals like Co, Ni, Mn, etc. An important aspect is also the intrinsic safety of the host material, which is $FePO_4$ (FP). FP is an intercalation compound which stores lithium ions and has a stable configuration independent on the lithium-ion concentration. The stability of other materials depends on the lithium-ion concentration, e.g., lithium cobalt oxide ($LiCoO_2$) is stable at room temperature but not in its pure form of CoO_2. Only 50 % of the lithium-ion concentration can be extracted from the host material yielding $Li_{0.5}CoO_2$. Further extraction, as would happen upon overcharge, will lead to heavy exothermic reactions and, therefore, to a destruction of the battery. This already happened to some batteries applied, e.g. in laptops and cars, which caught fire within minutes. LFP does not show such behavior and, therefore, it offers more safety in battery technology.

2.2.2 General design and functionality

Lithium-ion batteries have different setups depending on their application. The pouch cell, also called coffee bag cell, is flat and offers a good possibility for stacking, e.g. in cars. The most popular and well known batteries are the cylindrical and prismatic cells used in mobile
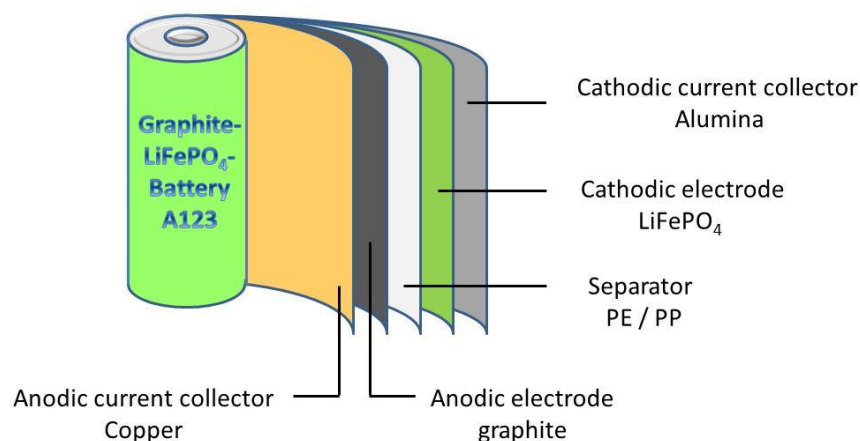
Figure 2: Construction of a cylindrical cell with the order of sheets of a repeat unit.
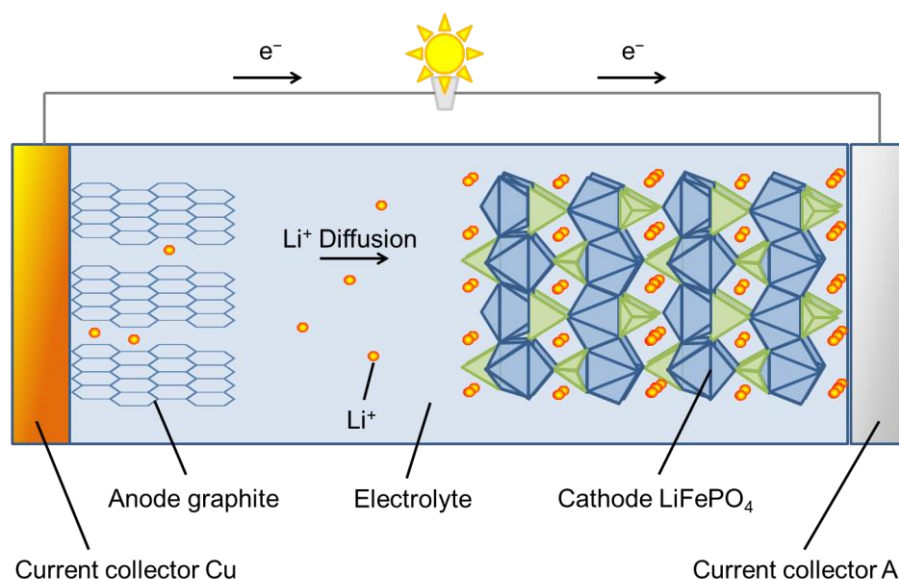

Figure 3: Repeat unit of a battery.

phones or cameras. All have in common that the construction consists of different sheets stacked together. These sheets build a repeat unit which are winded, or stacked, and packed in a container. The construction of a cylindrical cell and the order of sheets of one repeat unit are shown in Figure 2. In Figure 3 the construction of a repeat unit is shown in more detail. A repeat unit consists of an anodic current collector connected to the anodic electrode, a separator, the cathodic electrode and a cathodic current collector (Figure 3). All sheets are wetted with liquid electrolyte containing a conducting salt. Due to this stacking compact constructions are possible.

In the battery investigated in this work, the negative current collector consists of copper. It is connected to graphite which is the active material of the anode and is represented in Figure 3,

by showing few graphene layers to illustrate the coordination of lithium ions. The positive current collector consists of aluminum, and the active material $LiFePO_4$ forms the cathode. Here, the crystal structure of $LiFePO_4$ is used to illustrate the coordination of lithium ions. Between anode and cathode a separator is implemented to avoid direct contact of both electrodes (cf. Figure 2). The whole repeat unit is filled with liquid electrolyte containing salt to ensure the ionic conductivity. Here, often $LiPF_6$ is used. The function of a battery is quite simple and is shown in Figure 3, too. During the discharge process the electric current flows from the current collector of the anode to the current collector of the cathode through an appliance, e.g. a light bulb. Keeping the charge balance, lithium-ions have to move from anode to cathode crossing the separator. The transport can be described in the following way. Lithium ions are intercalated within the matrix of the graphite structure at which Lithium is stored as ion between the graphene layers and the electron is delocalized in the conjugated π-system of the graphene layers. Applying an electric current, the lithium ions move to the particle surface where they are solvated by molecules of the liquid electrolyte. Then they diffuse and migrate through the separator to the cathode. On the surface of a cathode particle the intercalation of lithium takes place while losing of the solvation shell. To be more specific, the electron is transferred to the iron ion changing the oxidation state. This leads to a structural rearrangement due to the change of electron density around the iron ion. Then the insertion of lithium ions occurs. The latter can be also used as description for the lithium-ion transport in $LiFePO_4$. While charging the battery, the process converts into the opposite direction.
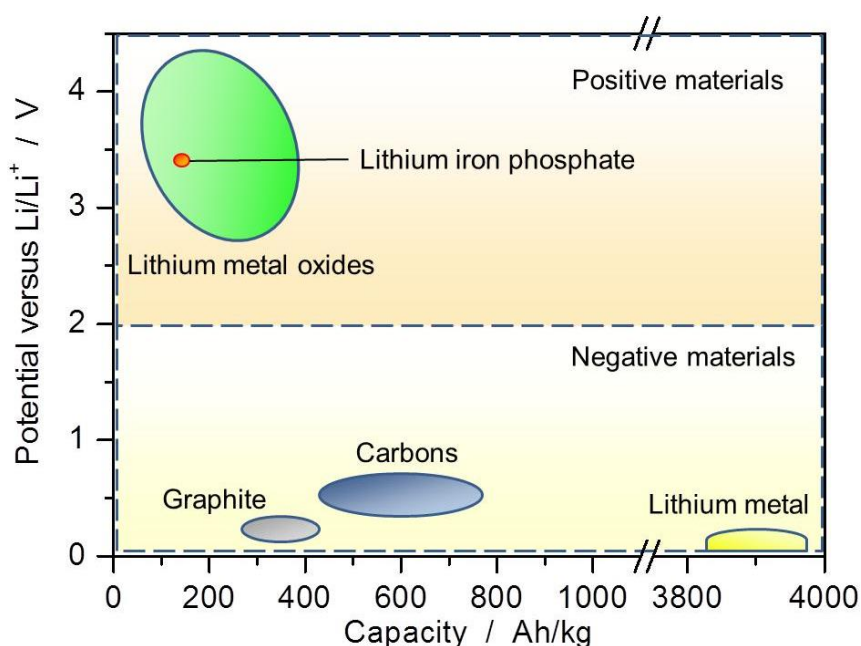

Figure 4: Generalized half-cell potentials of different materials depending on their capacity, based on Tarascon et al. [2].

22

This procedure and construction, described above, is nearly the same for each type of lithium-ion battery. They mainly differ in a use of various active materials. Each active material has a different half-cell potential and, therefore, an influence on the cell potential. The cell potential is the difference of the half-cell potentials of each electrode. Due to this fact the cell voltage depends on the active material. In Figure 4, a generalized overview of active materials is given [2]. It shows that pure lithium metal provides the best capacity (ca. 4000 Ah/kg) and half-cell potential (0 V per definition) of anodic active materials. Unfortunately pure lithium metal is not easy to handle while producing cells. Here, use of graphite or other carbon compounds provide advantage over lithium in terms of handling and lower costs. They have less capacity compared to pure lithium metal and slightly higher half-cell potentials. The active materials of the cathode show high half-cell potentials which are around $3 - 5$ V. Usually, lithium-metal-oxides are used with elements like Fe, Co, Mn, Ni, etc, or mixtures of these compounds. The capacity of around 200 Ah/kg is small. Due to this fact the cathode is the limiting compound in the battery concerning capacity. Therefore, the current focus of the investigations in the battery research community is on the cathode in order to compensate the small capacity while increasing the half-cell potential and the energy density.

2.2.3 Anode materials and properties

On the anode side three types of active materials are used: pure lithium metal, lithium alloys, and graphite. Lithium metal is the lightest element and the most electropositive vs. a standard hydrogen electrode. It has the highest capacity of ca. 4000 Ah/kg [2]. This makes it favored as anode active material. In the battery community, pure lithium metal is also used as standard reference electrode. Therefore the half-cell potential is set to 0 V per definition. The handling of pure lithium during battery manufacturing is difficult due to strong reactions with oxygen and water. This increases the cost of production. Further safety aspects forbid the use of pure lithium metal, like dendrites growth, which is explained in more detail in chapter 2.4.

Therefore, nearly every commercial battery consists of graphite, which is less expensive and easier to handle. Other materials are lithium metal alloys consisting of Sn and other main group elements. Compared to graphite they show higher capacities. However, these alloys tend to volume change during insertion of lithium ions. Due to this effect lithium alloys are rarely used usually.
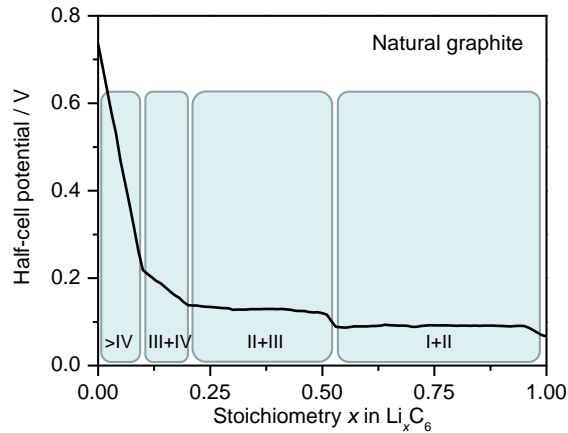
Figure 5: Half-cell potential of natural graphite with correlating stage transitions [3,8].
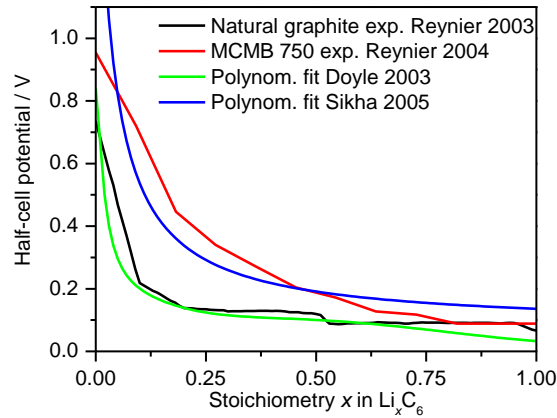

Figure 6: Half-cell potentials of different anode-types used in literature [3–6].

The most common material is graphite, as mentioned above. It offers a low half-cell potential, is cheap and easy to handle in production. Unfortunately the capacity of around 400 to 600 Ah/kg is low [2]. Generally, there are two different types of graphite: natural graphite and synthetic graphite. They show characteristic half-cell potentials which are explained in detail in the following. In Figure 5, the half-cell potential of natural graphite is shown with its characteristic shape [3]. It can be noticed that the half-cell potential changes with stoichiometry. Stoichiometry is the amount of intercalated lithium over the maximal amount of lithium which can be stored and has a value between 0 and unity, corresponding to x in Li_xC_6. At a stoichiometry towards 0 the half-cell potential is quite high with around 0.7 V. With increasing stoichiometry the potential decreases to nearly 0.1 V. The progressive form shows significant potential changes depending on stoichiometry x. This can be explained by a lithium-concentration change in the graphene layers [7]. The intercalation proceeds over several regions of continuously declining potential (Figure 5) [3,8]. The sharp discontinuities indicate phase transitions, e.g. $LiC_{12} - LiC_6$. The first stage transition is around $x = 0.08$ which corre-

sponds to high-order stage transfer. The succeeding transitions are around $x = 0.26$ and $x = 0.55$ which correspond to lower-order stage transition from stage III to stage II and stage II to stage I, respectively. Depending on the production process, the stage transitions are more or less intense [9]. Especially synthetic graphite shows a smoother distribution of the half-cell potential [4]. Such comparison is given in Figure 6. It shows the half-cell potential of natural graphite and synthetic graphite (MCMB 750) measured by Reynier et al. [3,4]. Additionally, two polynomial expressions are shown which are used in models by Doyle et al. and Sikha et al. [5,6]. It is worth noting that these expressions neglect the typical phase transitions. Especially the work of Doyle shows that the expression was fitted to experimental data of natural graphite.

A practical electrode consists not only of active material, but also of additional components such as carbon black and binder. The latter is necessary to fix the particles and to keep the structure. Carbon black is added to ensure a good electric conductivity. It can be assumed that also carbon black contributes to lithium storage due to adsorption on carbon black surfaces and, therefore, it influences the half-cell potential, too. In this work it is assumed, that the total contribution is due to the active material, which is graphite, and not due to added carbon black. Unfortunately for most commercial cells, including the one investigated in the present work, it is unknown which type of graphite is used. Therefore comparisons of different graphite types were performed using half-cell potentials and scanning electron microscopy pictures of Wissler et al. [9]. In this work, it is assumed that natural graphite is used. Further information is given in chapter 3.

2.2.4 Cathode materials and properties

Many different cathode materials, including $LiCoO_2$ and $LiFePO_4$, are being used in lithium-ion batteries [2]. For these materials the half-cell potential is high and around $3-5$ V vs. Li/Li^+ (Figure 4). There are two kinds of electrodes: intercalation and conversion electrodes. The intercalation electrodes are materials which function as a host material where lithium ions can intercalate. A typical example is $LiCoO_2$. This compound and its derivatives, which include other metals like Ni, Co, Al (NCA) or Ni, Mn, Co (NMC), are the most used cathode materials. They offer a high half-cell potential and a higher energy density compared to $LiFePO_4$. Usually, these intercalation materials show a characteristic half-cell potential which is dependent on the concentration of intercalated lithium. With increasing discharging the half-cell potentials of intercalation materials have a negative slope. This is shown in Figure 7 a) for $LiCoO_2$ [10]. Due to this the determination of SOC is easy and exact. However,
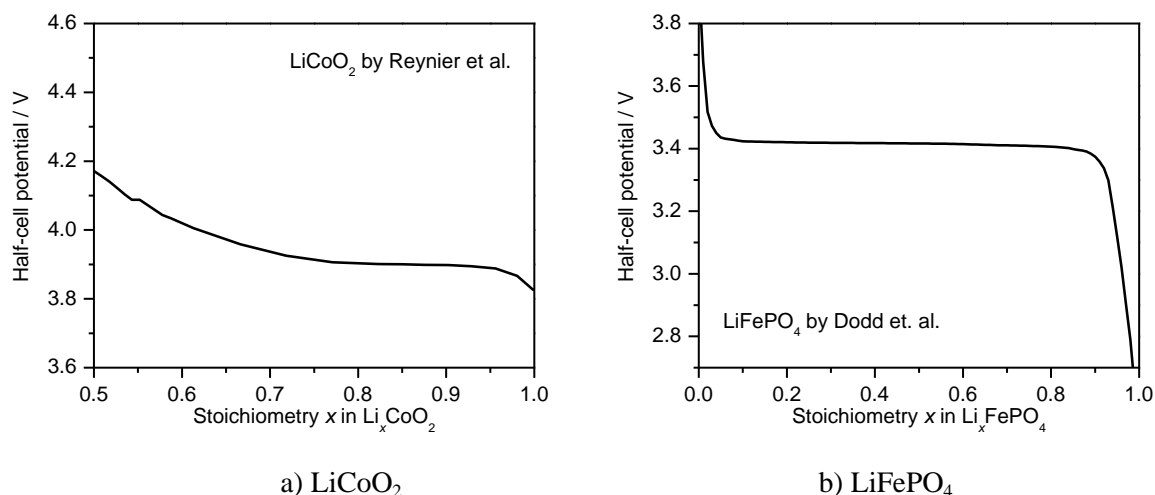
a) LiCoO$_2$ b) LiFePO$_4$

Figure 7: Characteristic half-cell potentials of a) LiCoO$_2$ and b) LiFePO$_4$ versus stoichiometry [10,11].

this can be a detriment requiring constant voltage. A change in crystal structure accompanied by a volume change can be observed due to insertion or extraction of lithium [9,10]. Additionally, the crystal becomes unstable due to structural changes. This means that not the whole amount of lithium can be used. In case of LiCoO$_2$ only 50 % of lithium can be extracted forming Li$_{0.5}$CoO$_2$ (cf. Figure 7 a).

Conversion electrodes do not show such a behavior. During the process of charging or discharging two different phases are coexistent. This results in a half-cell potential which is nearly constant over a wide range of SOC. LiFePO$_4$ has a half-cell potential of around 3.4 V vs. Li/Li$^+$ and is given as an example in Figure 7 b) [11]. Although, FePO$_4$ is a host material for lithium intercalation forming LiFePO$_4$ and, due to this, it can be counted to the intercalation electrode materials, it shows a half-cell potential behavior of a conversion electrode (Figure 7 b). This relatively flat discharge curve can be explained due to this fact that two phases, LiFePO$_4$ and FePO$_4$, are coexisting [14]. Both phases are stable therefore the total range of stoichiometry can be used. It means that the complete amount of lithium is available for charge-transfer processes within the battery.

In this work the active cathode material of the battery consists of lithium iron phosphate (LFP, LiFePO$_4$). LFP has a capacity of 170 Ah/kg and a half-cell potential around 3.4 V vs. lithium metal. In Figure 8 the crystal structure of LFP is shown [15]. The blue shaded sites are octahedra, occupied by Fe ions, and the green shaded tetrahedral, occupied by P atoms. Lithium ions occupy octahedral sites and are shown in yellow-red circles. Black lines represent the elementary unit cell. Along the c-axis the 1D-diffusion path of lithium ions can be seen. As mentioned above, LFP and the de-lithiated form FePO$_4$ (FP) are both stable. Both phases have
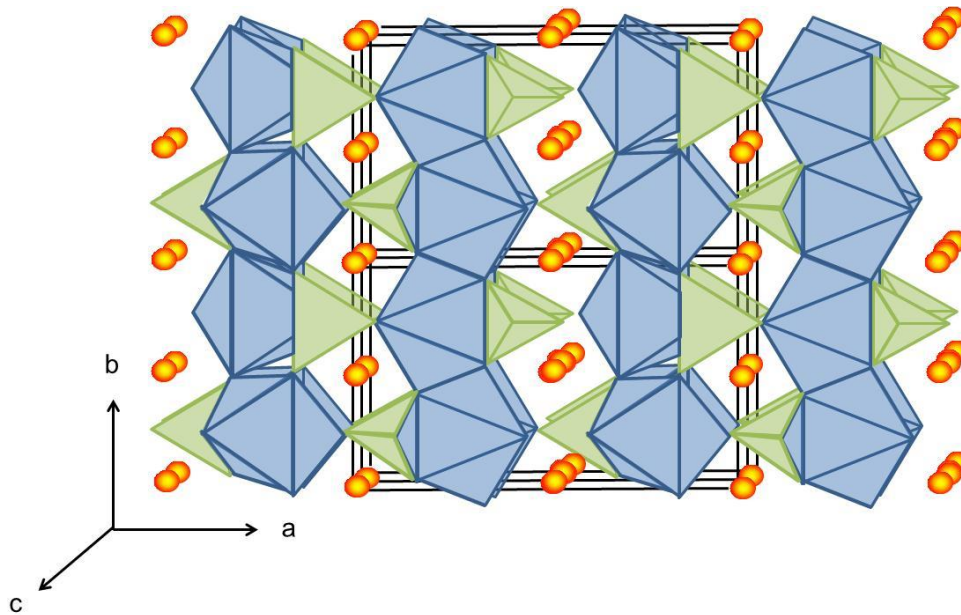
Figure 8: Crystal structure of LiFePO$_4$ along the c-axis [15].

olivine-type orthorhombic structures. LFP has the triphylite phase and FP the heterosite phase [16]. During charging and discharging both phases coexist within one particle [14]. However, there is no agreement about the interface between these phases in literature. Also, the occurrence of an interfacial zone is controversially discussed [17]. Dodd et al. made further investigations in different LFP phase compositions [17]. They observed a disordered phase which consists of Li$_x$FePO$_4$ with x between zero and one. Additionally, they showed the temperature dependence of the phase formation during manufacturing. This disordered solid solution of Li$_x$FePO$_4$ occurs above around 200°C. Between 200 and 300°C a mixture of the disordered solid solution and either a heterosite or triphylite is present. Above 300°C only the phase of disordered Li$_x$FePO$_4$ exists [18]. This shows that the manufacturing of LFP particles (size, temperature, solvent, etc.) can have an immense effect on the behavior measured later on. Also, the transport of lithium within the interfacial zone is not clarified. Delmas et al. concluded that LFP is a 1D-lithium-conductor along the c-axis of the elementary cell, and lithium transport takes place in the interfacial zone, where the lattice parameters changes depending on lithium chains [14]. But Li et al. reported that lithium diffusion along the b-axis is possible, too [19]. The distances of hopping places are nearly the same. This means that it is not clear if LFP is a 1D or a 2D conductor.

The phase-front propagation during cycling is not really understood. Delmas et al. proposed that the propagation is perpendicular to the lithium diffusion [14]. On the other hand Srinivasan et al. developed a model which describes the propagation in parallel to the lithium diffusion [20]. This model is known as shrinking core model. Here, it is assumed that the particles

are spherical and the complete surface is active for intercalation reactions. During discharging the phase-front propagates coming from the surface creating a shell of a lithium-rich phase which surrounds a lithium-poor core. In the reverse process, i.e. charging, a shell of lithium-poor material surrounds the lithium-rich core. It can be visualized like a tree-ring structure. This proposal is in strong contrast to the presentation that LFP is a 1D-lihtium conductor. Concerning the stability of these coexisting phases Dreyer et al. proposed that two phases within a particle are less stable than a single phase [21]. Due to this it is assumed that one particle after another is filled instead of all particles in parallel. In case that some particles are not completely filled, for reaching equilibrium it is proposed that a rearrangement occurs leading to particles consisting of either a lithium-poor or a lithium-rich phase.

Additionally LFP shows an asymmetry in charge and discharge behavior. The half-cell potential while charging is higher than while discharging. This effect can also be seen at very small currents. Morgan et al. explained it due to different diffusion velocities and calculated hopping energies of 270 meV for LFP and 200 meV for FP [22]. This confirms the multi-particle model of Dreyer et al. Another challenge when using LFP is the low intrinsic electrical conductivity [18]. To improve the electrical performance, Li et al. propose to minimize the particle size, to add carbon coating and to dope this material with supervalent cations [23]. Also Dominko et al. concluded that carbon coating has an immense influence on the performance of the battery. They showed that the thicker the coating is, the worse the recovered capacity will be [24]. In this work we assume that the particles are carbon coated because no graphite particles were visible in scanning electron microscopy pictures explicitly. The particle conglomerates are fixed with polymer. Further information is given in chapter 3.

2.2.5 Separator, electrolyte, current collector, container and pole caps

The separator has the important role within the battery of excluding a direct contact between anode and cathode. Besides, many other conditions are required [24,25]. To ensure a good lithium-ion transport, which results in a low ohmic resistance, the thickness of the separator should be very small while keeping mechanical stability. Additionally, necessary for a good transport is a well-defined pore size with a large porosity and high permeability. Also, the separator should wet easily in the electrolyte and retain the electrolyte permanently for increasing cycling life. Safety issues are present permanently. It has to be ensured that the material is chemically stable against electrolyte and electrode materials and under strongly reductive and oxidative reactions. Also thermal stability is necessary to avoid shrinkage or melting of the separator which can result in a direct contact of the electrodes. This temperature de-

pendence can be used otherwise to improve safety in form of a shutdown mechanism. This means that the transport of lithium ions is blocked due to melting of the polymer reaching its melting temperature. For example, polyethylene-polypropylene (PE-PP) bilayer separators, which are used currently in batteries, have ~130 °C shutdown temperature (melting point of PE) and ~165 °C melting temperature (melting point of PP). This combination provides a shutdown mechanism without losing mechanical integrity. In theoretical studies it is assumed that the separator has no influence on diffusion and no interaction with charge transport. However, it could be shown that the conductivity of electrolyte also in the separator region can be improved by adding ceramic crystallites like sand (soggy sand). It is assumed that the surface of these particles improve the rate of transport of lithium ions due to movements at grain boundaries [24,25]. In this work the separator was extracted from the battery and was a white sheet of a polymer. No coating with ceramics was observed. For further information see chapter 3.

The electrolyte has a very important role to fulfill. It has to conduct the ions for charge transfer from electrode to electrode, has to be stable over a wide range of potentials, and has to solvate the ions in such a way that the ion pair is separated, but not too strongly to ensure a good intercalation reaction at the electrode surface by opening the solvation shell [26]. The most popular electrolyte materials in literature are ethylene carbonate (EC), dimethyl carbonate (DMC) and diethyl carbonate (DEC) and their mixtures [27]. In commercial batteries additives are added to the electrolyte solvent. These additives have several functions [28]. One is that additives are more unstable against strong potential differences. This means that these additives react first in side reactions instead of electrolyte molecules ensuring the integrity of the electrolyte. In this case the additives react to gaseous CO or CO_2 which can be let out with pulps. In every electrolyte a leading salt is dissolved. In literature $LiPF_6$ is used usually. $LiBF_4$ or others are well known, too. It is important that the negative charge of the anion is widely distributed within the molecule or sterically shielded that ion aggregation does not occur and the whole amount of lithium ions contributes to conductivity. In the present work all sheets are wetted with liquid electrolyte with a composition of 4:6 EC:EMC. The conducting salt is $LiPF_6$ with a concentration of 1.2 mol/l [29].

The current collector on the anode side is copper leading to the negative pole where a safety-vent is implemented. The current collector on the cathode side consists of aluminum and is directly connected with the positive pole cap. Further information is given in chapter 3.

2.3 Thermal behavior of a battery

In the recent years lithium-ion batteries are largely used in mobile or portable applications, such as laptops, mobile phones or even in electric-driven cars. The increasing demand on this battery type leads to research in materials gaining improved capacity and cycle life and maximizing power and energy density [30]. Also, thermo-management is an important topic for car and plane industries. Due to higher power and energy densities, property hazard and safety issues have to be considered. Especially thermal run-away is a major problem which must be solved. Thermal run-away means strong self-accelerating heating, which is caused by an exo-thermal reaction that involves the electro-active material, binder and organic solvent [31]. This may happen when the ambient temperature rises or the heat conduction out of the cell is not efficient enough. Unfortunately, the reason for thermal run-away is not fully understood. Many investigations were performed in order to understand and to predict the temperature behavior of a cell during operation [30,32,33]. For example Hatchard et al. performed oven-exposure tests to simulate high environmental temperatures [34]. Not only inner temperature leads to fatal effects. At high ambient temperature the occurrence of side reactions, like solid electrolyte interface formation, is increased. They lead to an enhanced aging of the battery, which results in capacity losses and lower cycle life [26,35]. For cooling batteries to avoid these effects, several techniques are applied, like cooling the outer shell or the terminals of a battery [36]. Also, low ambient temperatures have an effect on the performance of a battery. Due to higher internal resistances, a loss of capacity can be observed during operation [35]. By rising the ambient temperature, the capacity can be reproduced reversibly. But due to slower kinetic reactions, other side reactions may occur, like lithium plating which result in aging of the battery, too. Being aware of the temperature dependence of a battery, companies give a temperature range for usage where side reaction may not have big influences on performance and aging. Therefore the temperature control of batteries is an important task.

2.4 Aging mechanisms

2.4.1 Overview

During operation batteries undergo many processes leading to capacity loss and higher internal resistances. These phenomena are summarized as aging. Many aging mechanisms are known but they are not well understood yet. Most of them appear during operation and become more dominating with time. There is solid electrolyte interface (SEI) formation occurring at the very first cycles mainly. Lithium plating can be named occurring at lower tempera-

tures. These two aging mechanisms are important; therefore, more information is given in the next subchapters. Other side reactions may occur, too, like forming gas due to electrolyte decomposition or separator shrinking which can lead to direct contact of both electrodes causing an internal short circuit. Also known is the fact that the particles crack due to inner lattice forces. The result is a worse connection to electronic conducting materials like carbon black and, therefore, a loss of available host material for intercalation, which means a loss of capacity. Further mechanisms can be found in literature [26,35].

2.4.2 SEI formation

SEI formation is a side reaction occurring especially at the beginning of the first charge process. SEI is the abbreviation for solid electrolyte interface. It describes that a thin film precipitates on the electrode surface (Figure 9) [26]. Usually, this is observed on the anodic electrode. The reaction mechanisms and the structure and composition of the SEI are not completely understood. It is known that the half-cell potential is not within the potential range in which the electrolyte keeps stable. This leads to a decomposition of the electrolyte and then to a production of a particle-covering surface film. It is assumed that this interphase production is due to a radical mechanism [28,37,38]. Wang et al. proposed that the lithium ion is solvated by a shell of electrolyte molecules [39]. This shell has to be opened when the ion adsorbs on the electrode surface. During intercalation of the ion into the graphene layers, in case of graphite as anode material, the distance of the layers increases. Then, it is possible that some electrolyte molecules may enter and react forming radicals and creating the SEI. This formation occurs in the first cycle and grows in every cycle reducing the capacity slowly. It can be noticed that this results in a capacity loss due to consumption of lithium ions and to an increase of the resistance due to a worse transport towards the anode and blocked adsorption sites.
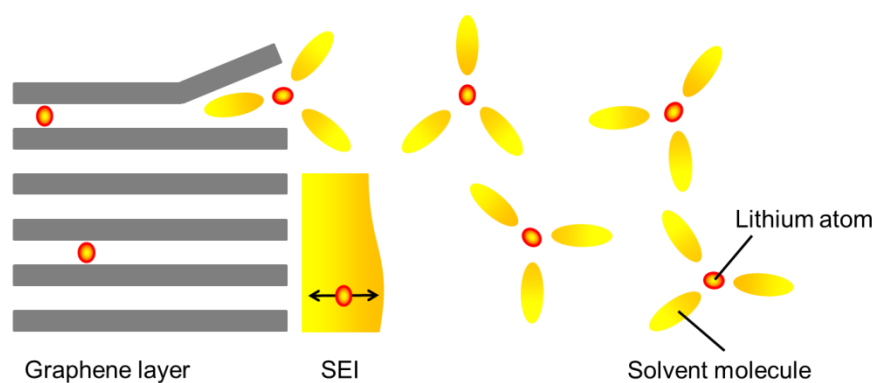

Figure 9 : SEI formation due to solvent decomposition at anode surface, based on Vetter et al. [26].

31

2.4.3 Lithium plating

Lithium plating is a side reaction on the anode side which may occur at temperatures below 0°C. It means that pure lithium metal precipitates on the surface of the particles (Figure 10). This precipitation leads to dendrite growth which is a dangerous side reaction. These dendrites may grow through the separator and may contact the cathode material. The result is an internal short circuit which can destroy the battery immediately. This is a reason for a thermal runaway.

The mechanism and the occurrence of lithium plating are not fully understood. It can be assumed that at lower temperatures the intercalation reaction is the rate-limiting step. Depending on the applied current, and mostly at higher C-rates, the electron demand has to be fulfilled and the electron transfer reaction becomes more evident than the intercalation reaction. In this case surface-adsorbed lithium-ions are reduced immediately instead of intercalating into the host material. When the first lithium metal occurs on the surface the intercalation sites are blocked and the lithium plating becomes dominant. In parallel to this metal production, the SEI formation increases, too, because the metal creates new reactive surface sites to decompose electrolyte molecules.

Until now no efficient mechanism is found to avoid or minimize this effect. To circumvent plating the batteries should not be charged at low temperatures under high current conditions. To reduce the dendrite growth polymer electrolytes can be used. Due to the polymer with its diffusion pathways the dendrites have to grow along these channels, which make it more difficult to reach the cathode material.
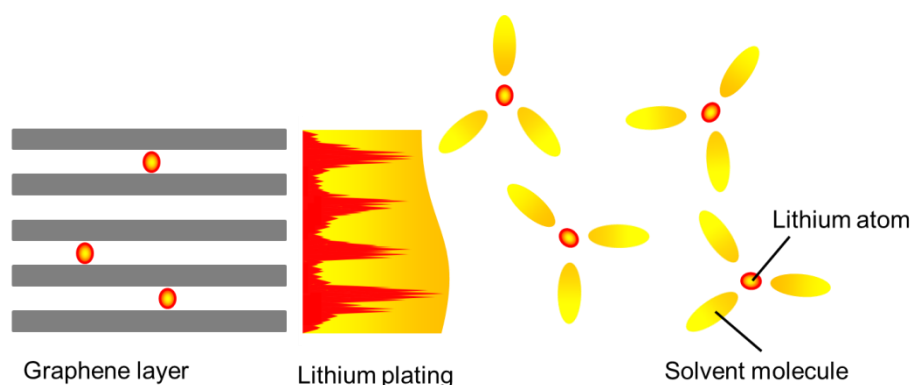

Figure 10: Lithium plating due to metal deposition accompanied by SEI formation, based on Vetter et al. [26].

2.5 Modeling and simulation

2.5.1 History of battery modeling

Although batteries are known for more than hundred years (Volta invented the first battery in 1799), many processes are not really understood. With increasing importance of mobile and portable electric applications, the need of batteries is still growing. Many investigations were carried out to understand the battery behavior over different time and size scales. However experimental research is difficult to carry out in-situ and is limited in resolution, depending on the experimental setup. To understand the battery in a theoretical way, based on equations describing physical and chemical behavior, models were presented already in the 1970s.

In 1973 Newman reviewed the current developments of porous electrodes surrounded by liquid electrolyte with regard to simulate primary and secondary batteries, adsorption of ions, double-layer charging and flow-through electrochemical reactions [40]. Based on their work, many groups published further investigations regarding reactions and transport in electrolyte and electrodes. Still up to now Newman's investigations are the base for current battery simulations. Newman investigated a model based on porous electrode theory which is a macro-homogenous approach. The material balance is described using concentrated solution theory within the liquid phase and assuming Fickian diffusion in spherical coordinates in the solid phase [41].

Doyle et al. used Newman's approach to simulate galvanostatic discharge of lithium-ion cells based on an isothermal electrochemical model [42–44].

Later Newman's model has been extended by Pals and Newman, Song and Evans and Wang et al. to include an energy balance for thermal calculations predicting cell temperature [45,46]. Pals and Newman used an averaged heat generation method while Song and Evans modeled the heat generation locally. Doyle combined his electrochemical approach with the local heat generation of Song and Evans and Wang et al. to be more accurate in predicting cell temperature.

Today Newman's model is a base for further understanding of processes inside of the battery and creates a platform for discussions and comparisons. For example, Lai et al. compared Poisson-Nernst-Planck equation with Newman's model showing only equations without any simulations [47]. Also, Botte et al. made a summary of battery modeling, comparing different model approaches and mathematical solutions [32]. Santhanagopalan et al. made a review on models for predicting the cycling performance of lithium batteries [48]. Fuller et al. modeled relaxation phenomena for cells with lithium foils as anode [49]. Later they extended their

model by replacing the lithium foil by an intercalation material like graphite [50]. Further developments of models needed the incorporation of more specific behavior of the active materials, like conduction phenomena. This was reviewed by Park et al. concerning lithium-ion batteries [51]. Even step by step the material's behavior was investigated and could be involved in battery models. The time-resolved history of new approaches, concerning cathode materials and their behavior, is given in the review of M. S. Whittingham [52].

Due to the complex processes occurring inside the battery at different times and different locations, multi-scale approaches are necessary to describe the complete battery. The temperature variation during cycling can be described on macro-scale. The micro-scale is necessary to get the contributions of generated heat and transport phenomena between the electrodes. On the atomistic scale reactions take place, for example adsorption on the surface of particles and the intercalation into the host material. The first models were simply developed using lithium metal as anode electrode, where intercalation can be neglected and surface reaction assumed to be very fast. Later graphite as anode material was modeled with one-electron step as transfer mechanism which can be described with the Butler-Volmer equation. Here the adsorption and intercalation reaction are lumped together into a single step. Recent results show that the intercalation process is more complex. Colclasure et al. proposed that the reaction on the surface of each particle should be described with elementary kinetics instead of the Butler-Volmer expression [53].

As the computer performance is continuously improving, it allows to calculate more complex systems and to obtain results in shorter times. Further investigations must be done to improve the understanding of the electrochemical and thermal behavior of a battery under normal conditions right up to extreme situations like thermal runaway due to side reactions.

2.5.2 Electrolyte

The liquid electrolyte with its conducting salt $LiPF_6$ is responsible for mass and charge transport between the active materials of each electrode. To describe the transport phenomena a set of equations are used in literature [47]:

$$J_i = -D_i^{eff} \nabla c_i - \frac{D_i^{migr,eff}}{z_i F} \nabla \phi \ , \tag{1}$$

$$\frac{\partial c_i}{\partial t} = -\nabla J_i \ , \tag{2}$$

$$0 = \sum_i z_i c_i \ . \tag{3}$$

In equation 1 the flux J_i of species i is described using Nernst-Planck equation, where z_i is the charge of species i, F is the Faradaic constant, D_i^{eff} is the effective chemical diffusivity, c_i is the concentration, $D_i^{migr,eff}$ is the effective migration diffusion and ϕ is the electric potential. This equation expresses the transport via diffusion (gradient of the concentration) and migration (gradient of the potential). The continuity of species i is given in equation 2, where the concentration variation with time depends on the ionic flux of species i. Usually electroneutrality is assumed to determine the electric potential using equation 3, where z_i is the charge of species i. In dilute solutions the migration coefficient D_i^{migr} is given as a function of the diffusion coefficient D_i according to [47]

$$D_i^{migr} = \frac{z_i F}{RT} c_i D_i \ . \tag{4}$$

The theory of concentrated solutions assumes interactions between anion and cation, and therefore it requires more parameters. Restricting to binary salts ($z_+ = |z_-|$) with a single cation and single anion without convection, it can be described by the equations [47]:

$$\frac{\partial c}{\partial t} = \nabla\left(D_{LiPF_6} \nabla c\right) + \frac{i t_+}{z_+ F} \ , \tag{5}$$

$$i = -\frac{2}{z_+ F}(t_+ - 1)\frac{\partial \mu_+}{\partial c} \nabla c - \sigma \nabla \phi \ , \tag{6}$$

In the continuity equation 5 the concentration changes depends on the diffusion term with the diffusion coefficient of LiPF$_6$ D_{LiPF_6} and an additional term consisting of the transfer number of the cation t_+ and the current i. The current is described in equation 6 depending on the local electric potential ϕ and the chemical potential μ_+ of the cation, where σ is ionic conductivity.

In literature many measurements and simulations can be found concerning liquid electrolytes. Variation of components of electrolytes, conducting salts and their concentrations were performed to estimate the influence on the performance on a cell. Therefore full cells or half-cells were investigated. In theoretical work equations of the concentrated solution theory are used frequently [8,32,40,42–44,46,47,49,53–64]. For example, Nyman et al. regarded the mass transport only in the electrolyte [62]. To characterize the mass transport, measurements on concentration cells and galvanostatic polarization experiments were performed supported by electrochemical impedance measurements. Due to the fact that the diluted solution theory assumes an ideal behavior, the use is less often compared to the concentrated solution theory.

For example, Danilov et al. shows in his work the concentration gradient of the conducting salt in the region of the separator [65,66]. In this model the domains of anode and cathode are not resolved. Independent on the theory, which is used, all simulations show a concentration gradient occurring along the transport direction increasing with time of operation. The transport is influenced by the composition of the electrolyte, the choice of conducting salt and its concentration, respectively. Table 1 shows a choice of the diffusion coefficients which were measured or calculated in literature. It can be seen that the values spread over a wide range of magnitude.

Table 1: List of diffusion coefficients of lithium-ion salts within liquid electrolytes

Range of used diffusion coefficients /m²/s	Salt	Electrolyte	Temp. / K	Comments	Ref.
$1.07 \cdot 10^{-10} - 8.06 \cdot 10^{-12}$	$LiN(CF_3SO_2)_2$	EC / DEC	$238 - 343$	Exp.	[67]
$1 \cdot 10^{-8} - 1 \cdot 10^{-9}$	$LiPF_6$	EC / DMC	293	Sim.	[68]
$4.112 \cdot 10^{-9}$	$LiPF_6$	EC / DMC	293	Sim.	[68]
$2 \cdot 10^{-11}$	$LiPF_6$	Not specified	298	Sim.	[65]
$1.07 \cdot 10^{-11}$	$LiPF_6$	Not specified	298	Sim.	[65]
$4 \cdot 10^{-10} - 4 \cdot 10^{-11}$	$LiPF_6$	EC / EMC	298	Sim.	[62]
$4.2 \cdot 10^{-12}$	$LiBF_4$	EC / DMC	299	Sim.	[39]
$5.4 \cdot 10^{-12}$	$LiBF_4$	EC / EMC	299	Sim.	[39]
$3.1 \cdot 10^{-12}$	$LiBF_4$	EC / DEC	299	Sim.	[39]
$1 \cdot 10^{-10} - 7 \cdot 10^{-10}$	$LiPF_6$	EC / EMC	333	Sim.	[69]
$5 \cdot 10^{-11} - 2 \cdot 10^{-10}$	$LiPF_6$	EC / DEC	273	Sim.	[69]
$7.5 \cdot 10^{-11}$	$LiPF_6$	EC / DEC	298	Sim.	[70]
$5.34 \cdot 10^{-10} \cdot exp(-0.65c)$	$LiPF_6$	EC / DEC	$-$	Sim.	[70]
$7.5 \cdot 10^{-11}$	$LiPF_6$	EC / DEC	298	Sim.	[71]
$1.27 \cdot 10^{-11}$	$LiClO_4$	PEO	393	Sim.	[72]
$2.6 \cdot 10^{-10}$	$LiPF_6$	EC / PC	298	Sim.	[5]
$2 \cdot 10^{-10}$	$LiPF_6$	EC / DMC	$-$	Sim.	[73]
$2.7 \cdot 10^{-10}$	$LiPF_6$	EC / DMC	$-$	Sim.	[73]
$2.3 \cdot 10^{-10}$	$LiPF_6$	EC / DMC	$-$	Sim.	[73]
$3.35 \cdot 10^{-10}$	$LiPF_6$	EC / DMC	294	Sim.	[74]
$2.65 \cdot 10^{-10}$	$LiPF_6$	EC / DMC	294	Sim.	[74]
$1.85 \cdot 10^{-10}$	$LiPF_6$	EC / DMC	294	Sim.	[74]
$1.2 \cdot 10^{-10}$	$LiPF_6$	EC / DMC	298	Sim.	[75]

$2.58 \cdot 10^{-10}$	$LiClO_4$	EC / DMC	298	Sim.	[75]
$8 \cdot 10^{-12}$	$LiCF_3SO_3$	PEO	363	Sim.	[45]
$2.6 \cdot 10^{-10}$	$LiBF_4$	PC	298	Sim.	[76]
$2.6 \cdot 10^{-10}$	Not specified (Li^+)	Not specified	−	Sim.	[77]
$1.9 \cdot 10^{-11} - 7 \cdot 10^{-11}$	$LiPF_6$	PC	298	Sim.	[41]
$5 \cdot 10^{-11} - 1.71 \cdot 10^{-10}$	$LiPF_6$	PC	298	Sim.	[41]
$2 \cdot 10^{-12} - 2.6 \cdot 10^{-11}$	$LiPF_6$	PC	298	Sim.	[41]
$3.5 \cdot 10^{-11} - 9.2 \cdot 10^{-11}$	$LiPF_6$	EC / DMC	298	Sim.	[41]
$9 \cdot 10^{-11} - 25.3 \cdot 10^{-11}$	$LiPF_6$	EC / DMC	298	Exp.	[41]
$6.1 \cdot 10^{-11} - 24.1 \cdot 10^{-11}$	$LiPF_6$	EC / DMC	298	Sim.	[41]
$22.6 \cdot 10^{-11} - 31.1 \cdot 10^{-11}$	$LiPF_6$	EC / DMC	298	Exp.	[41]
$2 \cdot 10^{-12} - 3.4 \cdot 10^{-11}$	$LiPF_6$	EC / DMC	298	Sim.	[41]
$7.5 \cdot 10^{-10}$	$LiPF_6$	EC / DMC	298	Sim.	[63]
$5 \cdot 10^{-13}$	$LiCF_3SO_3$	PEO	−	Sim.	[60]
$7.5 \cdot 10^{-10}$	Not specified	Not specified	298	Sim.	[48]
$1.1 \cdot 10^{-11} - 1.3 \cdot 10^{-10}$	$LiBF_4$	PC	295	Exp.	[78]

2.5.3 Electrode materials

2.5.3.1 Introduction

The behavior of a battery strongly depends on the active materials used as electrodes. Therefore it is necessary to know the corresponding thermodynamic and kinetic parameters quite well. Unfortunately these parameters are difficult to measure or to gain and the half-cell potential does not simply correlate between potential and state-of-charge. The following chapter will present some handlings and solutions in literature how to deal with these challenges.

2.5.3.2 Graphite-based anodes

In literature different approaches for the anode electrode can be found. This depends on the active material. There are pure lithium metal or combinations of diverse graphite types, which results therein, that, for example, the half-cell potential shows different behavior.

In some literature the anode is treated as pure lithium-metal anode [5,58–60]. If done so, rate-limiting reactions due to transport phenomena within the anode particles and concentration limitations can be neglegted. In these papers, the surface morphology is assumed to be ideal and changes due to rough structures or blocking of adsorption sites are neglected. The main

advantage of this approach is the constant half-cell potential, which is 0.0 V versus Li/Li$^+$. Graphite as active material, instead, shows a distinct behavior in the half-cell potential which can be explained with its structure. This special behavior is visible in the discharge curves. The potential does not change continuously with state-of-charge (see chapter 2.2.3). To simulate the half-cell potential of this material accurately, different possibilities were taken: Using a look-up table, where experimental data were deposited and other required values were interpolated. With this method the code stays very flexible for simulating different active materials. Additionall values, like half-cell enthalpy and entropy, can be included as it is done in this work. Also the use of polynomial expressions can be found in literature [63,79]. Mostly these expressions are complicated and contain an exponential term and a polynomial of higher order. Also these methods fit well to the experiments. Colclasure et al. used the Redlich-Kister expansion to fit the half-cell potential $E_{\text{ref}}^{\text{eq}}$ assuming that both vacancies and intercalated lithium have an activity which is not ideal (not unity) [53]:

$$E_{\text{ref}}^{\text{eq}} = \frac{\Delta G}{F} + \frac{RT}{F} \ln\left(\frac{\left(1 - x_{\text{Li}^{\text{I}}}\right)\gamma_{\text{Li}^{\text{V}}}}{x_{\text{Li}^{\text{I}}}\gamma_{\text{Li}^{\text{V}}}} \right). \qquad (7)$$

Here $\gamma_{\text{Li}^{\text{V}}}$ is the activity of the lithium vacancies and $x_{\text{Li}^{\text{I}}}$ the stoichiometry of intercalated lithium.

The most important electrochemical step in the battery is the mass and charge transfer at the electrode surface. Therefore equations are needed which treat mass and charge transfer. Usually a correlation between mass transfer and charge transfer in form of current is used. Due to the fact that lithium has only one electron, most processes on the surface can be assumed as one-step electron transfer processes. The rate of charge transfer is usually modeled with the Butler-Volmer equation.

$$i = i_0 \cdot \left(\exp\left(\frac{\alpha_{\text{a}} F}{RT} \eta_{\text{act}} \right) - \exp\left(-\frac{\alpha_{\text{c}} F}{RT} \eta_{\text{act}} \right) \right). \qquad (8)$$

Here is i the current density, i_0 the exchange current density, α_{a} the anodic and α_{c} the cathodic symmetry factor, η_{act} the activation overpotential, F the Faraday constant, R the ideal gas constant and T the temperature. For an elementary reaction the sum of the symmetry factors is unity. The first exponential term represents the anodic reaction, i.e. producing electrons, and the second term the cathodic reaction, i.e. consuming electrons, respectively. This formulation represents a global kinetic reaction which means, that a single rate-limiting step is assumed. Competitive, parallel occurring reactions cannot be regarded.

Modeling charge transfer chemistry with elementary kinetics enables the incorporation of multiple parallel pathways. With this, combinations with other side reactions, like SEI for-

mation or Li plating, are possible.

After the charge transfer reaction and the intercalation reaction, the lithium ions move within the particle. This movement can be assumed to occur via a hoping mechanism [80,81]. First-principles calculations get different energy barriers depending on the structure of the host material. Regularly the movement of lithium ions is modeled assuming simple diffusion due to concentration gradient as driving force and using Fick's diffusion law [53]. There is much literature estimating the diffusion coefficient. Frequently it is assumed to be constant. Some literature shows a dependence on stoichiometry. But no homogenous consequence can be drawn concerning different velocity of migration of lithium ions within the particle due to different experimental setups, different production processes of graphite (natural or synthetic) and their particles (size). A list of different diffusion coefficients in literature is given Table 2.

Table 2: List of diffusion coefficients in anodic active material

Range of used diffusion coefficients / m²/s	*Graphite type*	*comments*	*Ref.*
$1\cdot10^{-11} - 1\cdot10^{-14}$	MCMB		[68]
$1\cdot10^{-13} - 1\cdot10^{-14}$	Natural graphite	Different measurement techniques	[51]
$1\cdot10^{-11} - 1\cdot10^{-15}$	MCMB	Different measurement techniques	[51]
$2.2\cdot10^{-13}$	MCMB		[82]
$1.12\cdot10^{-14}$	Graphite powder (1-2μm)	at 25 °C SOC 0%	[83]
$6.51\cdot10^{-15}$	Graphite powder (1-2μm)	at 25 °C SOC 30%	[83]
$1.35\cdot10^{-14}$	Graphite powder (1-2μm)	at 55 °C SOC 0%	[83]
$1\cdot10^{-13} - 1.8\cdot10^{-12}$	Petroleum coke		[83]
$1\cdot10^{-16} - 1\cdot10^{-14}$	Carbon fiber		[83]
$1\cdot10^{-15} - 1\cdot10^{-14}$	Pith-based carbon fiber		[83]
$1\cdot10^{-11.7} - 1\cdot10^{-10.4}$	Carbon fiber		[83]
$1\cdot10^{-12.5} - 1\cdot10^{-11.4}$	Artificial graphite		[83]
$1\cdot10^{-14}$	Carbon fiber	Sim.	[83]
$5.5\cdot10^{-14}$	MCMB		[5]
$3.9\cdot10^{-14}$	MCMB		[84]
$2\cdot10^{-14}$	MCMB 25-28		[74]
$2.2\cdot10^{-13}$	Carbon fiber		[46]
$3.9\cdot10^{-14}$	MCMB 25-10 petroleum coke		[75]

$1 \cdot 10^{-15} - 1 \cdot 10^{-16}$	MCMB		[85]
$3 \cdot 10^{-14}$	graphite		[86]
$9 \cdot 10^{-14}$	Graphite	Sim.	[87]
$3.9 \cdot 10^{-14}$	Graphite	Sim.	[33]
$2 \cdot 10^{-16}$	Graphite	Sim.	[77]
$1 \cdot 10^{-15}$	Graphite	Sim.	[88]
$5 \cdot 10^{-13}$	Graphite	Sim.	[49]
$3.89 \cdot 10^{-14}$	Graphite	Sim.	[6]
$1 \cdot 10^{-12}$	MCMB 25-28		[8]
$5 \cdot 10^{-15}$	MCMB 6-10		[8]
$3.9 \cdot 10^{-14}$	Graphite	Sim.	[48]
$4 \cdot 10^{-10}$	MCMB		[89]

2.5.3.3   LiFePO$_4$-based cathode

Due to the scientific impact of LiFePO$_4$-based batteries, many models concerning LiFePO$_4$ (LFP) were presented in literature in the recent years. This section gives a short overview on existing modeling activities.

Core-shell model.   The first continuum model was reported by Srinivasan and Newman [90]. It is based on the core-shell concept, initially proposed by Padhi et al.[91]. This model describes the growing of LFP (Li-rich phase) which surrounds a shrinking core of FP (Li-poor phase). Lithium diffusion through the growing outer-shell and a fast lithium transfer across the phase boundary were considered. The authors describe the diffusion in a spherical particle using

$$\frac{\partial c}{\partial t} = D_{Li} \frac{\partial^2 c}{\partial r^2} + \frac{2D_{Li}}{r} \frac{\partial c}{\partial r}. \tag{9}$$

Where the initial and boundary conditions are set as following

$$c = c_0 \quad \text{at} \quad t = 0, \tag{10}$$

$$D_{Li} \frac{\partial c}{\partial r} = \frac{i}{F} \quad \text{at} \quad r = r_0, \tag{11}$$

$$c = c_{eq} \quad \text{at} \quad r = r(t), \tag{12}$$

where c is the concentration of lithium in the bulk and c_0 is the initial concentration, D_{Li} is the diffusion coefficient, r the radius of the particle, F means the Faradaic constant, i the current, c_{eq} is the concentration at equilibrium. It has to be noted that the half-cell potentials were giv-

en as polynomial expression. Srinivasan et al. report that their simulations suggest the need of a current dependent-diffusion coefficient, which was suggested in other publications, too [74,90,92,93]. Two possible reasons for this phenomenon are a diffusion coefficient which is a function of concentration, which manifests itself as a rate-dependent diffusion coefficient, or the existence of a particle size distribution. A concentration dependent diffusion coefficient was introduced:

$$D_{Li} = (D_0 - D_1)\left(\frac{c_{max} - c}{c_{max} - c_{eq}}\right)^n + D_1, \tag{13}$$

where D_1 and D_o are constant diffusion coefficients of lithium which were fixed at the concentration limits. c_{max} is the maximum concentration in the LFP lattice and c_{eq} the concentration in the shell at the phase-interface. Despite of using a flexible diffusion coefficient, the simulations could not match the experiments well. Good agreements with experiments up to 65 A/m², which corresponds to around 5C, were only found using a particle-size distribution. Also Striebel et al. studied LFP from different sources using the core-shell model of Newman and a binary diffusion coefficient [94]. They observed a strong variation of the discharge behavior of a cell. They concluded that the carbon coating is very important as well as the carbon material itself. Wang et al. presented their work using the COMSOL multi-physics package (Version 3.2) for Li/PEO-LiClO$_4$/LiMn$_2$O$_4$-battery [95]. This battery model consists mainly of the work of Newman et. al [55]. Yamada et al. confirm the shrinking core model of Newman and Srinivasan using crystallographic data from X-ray diffraction (XRD) of Li$_x$FePO$_4$ phases with $0 \leq x \leq 1$ [96]. In contrast to Yamada et al., using the Avrami-Johnson-Mehl-Eroofev equation, Allen et al. determined an Avrami exponent which supports a linear, 1D-growth mechanism instead of a 3D shrinking core model [97]. Their analysis of the Avrami exponent suggests a phase boundary controlled mechanism. For the nano-scale material they estimate an activation energy of around 13 kJ/mol.

Domino-cascade model.   The present work supports another approach, which focuses on the idea of a 1D-transport mechanism of lithium-ions: the domino-cascade model by Delmas et al. They examined nano-sized particles evaluating X-ray diffraction and electron microscopy measurements [98]. They observed two coexisting single phases of LFP and FP [99]. In order to describe this phenomenon, they developed the so-called domino-cascade model. This describes the movement of the phase front through the particle. Due to the fact that LFP is a 1D-lithium-ion conductor, lithium ions diffuse along one of the cartesian coordinates (in [010] b direction). Along this axis lithium ions diffuse from the center to the surface of the particle.

41

This leads to a crystal-monolayer of FP. First of all this monolayer has to be freed of lithium ions. Then the monolayer next to the freed one will be emptied. This means that the area of the phase front propagates perpendicular to the diffusion direction. This proposition is supported by the work of Islam et al. [100]. They predict that the lowest lithium ion migration energy of 0.55 eV is found for the pathway along the [010] direction. This means that this direction should be preferred to other ones. This is in agreement with the experiments of Delmas et al. (domino-cascade model) [14]. Also Laffont et al. examined a LFP crystal using high-resolution electron energy loss spectroscopy [99]. Like Delmas et al., they found that the crystal contains both single-phases, LFP and FP. In contrast to Delmas et al., who suggest that between these pure phases no stoichiometric mixture of LFP and FP exists, Laffont et al. propose that the interface of these phases consists of Li_xFePO_4 which is the superposition of these two end members rather than a solid solution. This result could explain why a current dependence for different discharge rates can be found and why the shrinking core model and the cascade model cannot describe the behavior by themselves alone.

Ramana et al. invalidates both the core-shell model and the domino-cascade model [101]. Using high-resolution transmission electron microscopy and Raman spectroscopy structural properties of LFP were studied. They found that LFP and FP phases exist concurrently in the shell at a delithiated state of 50 %.

Multi-particle model. Dreyer et al. add a further model to these two competing models [21]. They postulate another scenario for lithium extraction from a Li-rich phase. Usually in literature it is widely accepted that slightly delithiated particles are stable. Dreyer et al. predict that this slightly delithiated particle is unstable. A rearrangement takes place where the lithium content is distributed to particles that are totally filled and other particles that are totally unfilled. It should be noted, that this mechanism may be valid for scenarios near equilibrium, this means for extremely low discharge rates.

Safari et al. presented a model based on Subramanian et al. and Santhanagopalan et al. [48,58]. Additionally they introduced a four-particle model at the cathode which represents particles that are connected differently with an electron conducting material [102–104]. Using normal Butler-Volmer kinetics, polynomial half-cell potentials and a current correction factor they achieved a good agreement with the experiments for discharge rates up to 1C.

Phase-field model. A common method to describe phase transitions is the phase-field model. Tang et al. describes the phase transition introducing a diffusive interface (phase field)

model [105,106]. Here, the total free energy of a cathode particle can be expressed as a functional of electric potential Φ, concentration c, crystallinity n and a displacement vector u. The general equation is given as:

$$F(c,n,u,\phi) = A + B + C,$$ (14)

where A is the chemical free energy which depends on concentration, crystallinity, electric potential and temperature, B is the elastic strain energy, which depends on concentration, crystallinity and the elastic strain tensor, and C is the chemical and structural gradient energies which depend on concentration and crystallinity gradients along the radius of the particle. With their work they obtained three central conclusions: The first conclusion is that an initially crystalline phase may undergo amorphization during cycling. The second one is that applied electric overpotentials have an immense influence on the phase stability and on the phase transition pathways of small particles. The third one is that the tendency of amorphization depends on the amount of misfit strains between lithiated and delithiated crystalline phases.

Using a spherical particle they confirm the approaches of Newman that an amorphous phase may occur. Also Han et al. used a phase field model for electrochemical modeling of an intercalation process in LFP [107]. They measured the diffusion coefficient depending on stoichiometry between $1 \cdot 10^{-15}$ and $3 \cdot 10^{-17}$ m^2/s using GITT and PITT. Chiang et al. propose a mechanism change in transition of FP to LFP [108]. Using phase field modeling they showed that under moderate overpotentials (e.g. 25 mV) misfit stress causes LFP to grow along the longitudinal direction [100] which is perpendicular to the fast-diffusion direction. Another behavior is seen at increasing overpotentials like 100 mV. They show that the particle will be filled in [010]-direction which has the highest Li-ion diffusion. This is indirectly supported by Islam et al. who calculated the energy for every migration direction [100].

Atomistic model. Morgan et al. calculated the activation barriers of lithium-ion motion and estimated the lithium-ion diffusion constants using first-principles methods [109]. Their conclusion is that the rate problems in LFP materials are due to electron-conductivity limitations. Interestingly the differences between the olivine materials LiMPO$_4$ (M=Fe, Mn, Co, Ni) are very small. For LFP they estimated a diffusion coefficient of $1 \cdot 10^{-12}$ m^2/s and an activation energy of 270 meV using following equation:

$$D = l^2 \upsilon \cdot \exp\left(\frac{-E_{act}}{k_b T}\right),$$ (15)

where D is the diffusion coefficient, υ is the hopping frequency from a filled to a vacant site, l

the hopping length, E_{act} the hopping activation energy, k_b the Boltzmann constant and T the temperature. Beside the discussion of the coexistence of two phases the stability of the single phases is studied, too. Tang et al. reports that LFP is more stable than FP or lithium metal using electron density calculations [110]. Zhou et al. reports on a significant failure of the local density approximation (LDA) and the generalized gradient approximation (GGA) to reproduce the phase stability and thermodynamics of mixed-valence Li_xFePO_4 compounds [111]. They concluded that there is no phase separation.

Harinipriya et al. used a Monte Carlo strategy to simulate the performance of LFP based cathode batteries [112]. Their methodology takes into account micro-scale properties, e.g. diffusion of spherical electrode particles, solvation effects, diffusion coefficients and concentration gradient to determine the diffusion of Li ions. For LFP they are using a diffusion coefficient of $8 \cdot 10^{-18}$ m^2/s.

Semi-empirical models. Roscher et al. published an electric equivalent-circuit model using an analytical approach for the 1D-movement of lithium-ions within particles where the particle shape and size distribution are taken into consideration [113]. They demonstrated the shell development which is dependent on adjusted currents, period durations and temperatures. Especially at low temperatures the influence of the shell development on the internal resistance becomes more and more important. Schmidt et al. performed impedance spectroscopy on LFP and compared it to results from equivalent circuit simulations [114,115]. They postulated three main losses: The first loss is the solid-state diffusion or intercalation. The second loss is the charge-transfer at the cathode/aluminum interface. The last loss is probably the charge transfer at the cathode/electrolyte interface. Unfortunately the frequency domain, where diffusion processes can be regarded, cannot be simulated.

Many investigations were performed to describe the diffusion correctly via using a diffusion coefficient. To describe discharge curves of LFP, Pasquali et al. fitted data (diffusion resistance of electrolyte, exchange current density and constant diffusion coefficient in LFP) to EIS and CV spectra gaining good agreements up to 30C [116]. They used the Nernst equation with an additional term which depends on the diffusion resistance. Using impedance measurements, Joachin et al. calculated diffusion coefficients for different SOC [117]. They spread from $2.46 \cdot 10^{-22}$ m^2/s (SOC 0 %) up to $1.26 \cdot 10^{-18}$ m^2/s (SOC 40 %) followed by a decrease to $8.57 \cdot 10^{-18}$ m^2/s (SOC 100 %). Using the following equation

$$D_{Li} = \frac{1}{2}\left[\left(\frac{V_m}{SFA}\right)\left(\frac{dE}{dx}\right)\right]^2 ,$$ (16)

where D_{Li} is the diffusion coefficient, V_m the molar volume of the active material, S the contact area between electrolyte and sample, F Faraday's constant, dE/dx is the slope, obtained from the plot of lithium content versus open-circuit voltage, and A is the pre-exponential factor calculated from the Warburg-impedance. Using this equation proposed by Ho et al. the deviation of the diffusion coefficient from low to high SOC shows nearly the reciprocal behavior which Safari et al. measured [103,118]. Prosini et al. determined the diffusion coefficient depending on the stoichiometry of L_xFP using GITT measurements and the equation derived by Weppner and Huggins using the following equation

$$D_{Li} = \frac{4}{\pi} \left(\frac{V_m}{SF} \right)^2 \times \left[I^0 \left(\frac{\partial E}{\partial x} \right) \middle/ \left(\frac{\partial E}{\partial \sqrt{t}} \right) \right]^2, \tag{17}$$

where V_m is the phosphate molar volume (44.11 cm³ mol^{-1}), S the contact area between electrolyte and sample (14.38 cm²), F the Faraday constant, I^0 the applied constant electric current and $\delta E/\delta x$ is the slope of the coulometric titration curve while $\delta E/\delta t^{1/2}$ is the slope of the short-time transient voltage change [119,120].

Beside the transport properties within the particles, the flat half-cell potential, due to two existing phases, is tried to be considered in different approaches. Prosini et al. modeled the voltage profile for LFP using a general equation based on a model requiring phase segregation, with the delithiated phase inside the grain and with electronic diffusion lower than ionic diffusion [121]. They separated the discharge curve into three domains: Domain I contains the first drop from OCV to the plateau, domain II is the flat plateau and domain III shows the drop from the nearly constant voltage to the switch-off-voltage at 2.0 V. For each domain they defined an equation to describe the potential variation. They concluded that the slow electronic diffusion is responsible for the decrease of electro-chemical performance of the material with increasing currents. Their model is able to describe the behavior of the insertion of Li in FP up to 10C rates. Kasavajjula et al. presented a discharge model for LFP accounting for solid solution range [122]. They assume three different domains of discharge. The first domain describes the voltage loss coming from the OCV to the constant voltage. The second domain describes the constant voltage. The last voltage drop is described by the third domain. For each domain they use a polynomial expression to fit the experiments. Simulations match experiments very well from 0.1C to 20C. Originally described by Wang et al. this model is extended by adding diffusion to both phases (LFP, FP) [95,123].

Diffusion model.   Independent of the assumed models in literature, many investigations

were carried out to estimate the diffusion coefficient of lithium in FP or LFP, respectively. Unfortunately the diffusion coefficients spread over a wide range this means ca. five orders of magnitude. This is due to the experimental setup and the investigation method. In Table 3 different diffusion coefficients from literature are shown.

It has to be mentioned that the diffusion coefficient is mostly assumed to be constant. In few published papers it can be found that the diffusion coefficient changes with stoichiometry. Safari et al. measured the diffusion coefficients with GITT or PITT and achieved a correlation, which is shown in Figure 11 [103]. There it can be seen that the diffusion coefficient is very low within a stoichiometry range of 0.1 and 0.9. At the outer-shell areas the diffusion coefficient rises extremely over around two orders of magnitude. It has to be mentioned that this behavior may be influenced by the phase-change of LFP. Then the low diffusion coefficient can be interpreted as a very slow phase-change reaction, which is rate-determining. This is acceptable, because the titration technique only regards the concentration of ions at the surface.
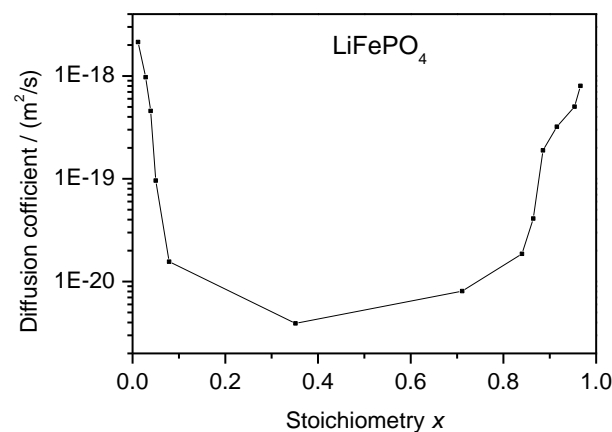

Figure 11: Diffusion coefficient of the cathode depending on the stoichiometry measured by Safari et al. [103].

Interestingly Joachin et al. show values at different SOCs and therein a reciprocal behavior compared to the results of Safari et al. [103,117]. The fastest diffusion is observed near SOC 50 % and the lowest at SOC 0 % or SOC 100 %. In contrast, Safari et al. measured that at the boundary of SOC the diffusion is the fastest. Between SOC 10 % to 90 % the diffusion is very slow. The diffusion coefficients, measured by Prosini et al., show the same order and behavior along SOC like those in the work of Safari et al. [119].

It can be concluded that further investigations have to be done explaining the transport of lithium in LFP. A few models were presented but unfortunately none of them can explain the behavior in all variations (different currents, capacity losses, etc.). The most controversially

discussed model is the one of Newman et al. based on the core-shell assumption. Also the domino-cascade model seems reasonable. The phase field model is also common as well as other research based on semi-empirical expressions.

Table 3: List of different diffusion coefficients for LiFePO$_4$ in literature

Diffusion coefficient / m²/s	Comments	Ref.
$1.8 \cdot 10^{-18}$ (LFP) – $2.2 \cdot 10^{-20}$ (FP)	GITT measurement	[119]
$9.13 \cdot 10^{-19}$	Li$_{1-x}$FePO$_4$, x = 0.1, GITT	[119]
$9.32 \cdot 10^{-20}$	Li$_{1-x}$FePO$_4$, x = 0.2, GITT	[119]
$6.48 \cdot 10^{-21}$	Li$_{1-x}$FePO$_4$, x = 0.4, GITT	[119]
$4.47 \cdot 10^{-20}$	Li$_{1-x}$FePO$_4$, x = 0.5, GITT	[119]
$4.97 \cdot 10^{-20}$	Li$_{1-x}$FePO$_4$, x = 0.9, GITT	[119]
$1.29 \cdot 10^{-18}$	Li$_{1-x}$FePO$_4$, x = 0.1, IS	[119]
$1.08 \cdot 10^{-19}$	Li$_{1-x}$FePO$_4$, x = 0.2, IS	[119]
$7.68 \cdot 10^{-21}$	Li$_{1-x}$FePO$_4$, x = 0.4, IS	[119]
$7.39 \cdot 10^{-20}$	Li$_{1-x}$FePO$_4$, x = 0.5, IS	[119]
$1.91 \cdot 10^{-19}$	Li$_{1-x}$FePO$_4$, x = 0.9, IS	[119]
$1.0 \cdot 10^{-18}$ – $8.0 \cdot 10^{-22}$	Averaged values	[51]
$1.6 \cdot 10^{-13}$	LiFePO$_4$, [001], c direction at 147 °C, DC-polarization	[51]
$<1.0 \cdot 10^{-14}$	LiFePO$_4$, [100], a direction at 146 °C, DC-poarization	[51]
$2.4 \cdot 10^{-13}$	LiFePO$_4$, [010], b direction at 146 °C, DC-polarization	[51]
$4.97 \cdot 10^{-20}$ – $9.13 \cdot 10^{-19}$	Li$_{1-x}$FePO$_4$, 0.1<x<0.9, GITT	[51]
$1.91 \cdot 10^{-19}$ – $1.29 \cdot 10^{-18}$	Li$_{1-x}$FePO$_4$, 0.1<x<0.9, EIS	[51]
$1.0 \cdot 10^{-19}$	LiFe$_{0.25}$Mn$_{0.25}$Co$_{0.25}$Ni$_{0.25}$PO$_4$, GITT	[51]
~$1.0 \cdot 10^{-17}$ – ~$1.0 \cdot 10^{-16}$	LiFe$_{1-x}$Mn$_x$PO$_4$, 0<x<0.2, CV	[51]
$6.0 \cdot 10^{-12}$	Al-doped LiFePO$_4$, [001], c direction at 180 °C, DC-polarization	[51]
$1.0 \cdot 10^{-13}$	Al-doped LiFePO$_4$, [100], a direction at 180 °C, DC-polarization	[51]
$7.0 \cdot 10^{-12}$	Al-doped LiFePO$_4$, [010], b direction at 180 °C, DC-polarization	[51]
$2.9 \cdot 10^{-14}$ – $1.1 \cdot 10^{-15}$	Li$_{1-x}$FePO$_4$ / C composite, 0<x<1, EIS	[51]
$1.27 \cdot 10^{-20}$	C-coated Li$_x$FePO$_4$, x = 0, EIS	[51]
$8.82 \cdot 10^{-22}$	C-coated, Li$_x$FePO$_4$, x = 0.9, EIS	[51]
$5.95 \cdot 10^{-21}$	C-coated, Li$_x$FePO$_4$, 5th cycle, EIS	[51]
$5.44 \cdot 10^{-21}$	C-coated, Li$_x$FePO$_4$, 50th cycle, EIS	[51]

$1.0 \cdot 10^{-12}$	DFT-Sim.	[100]
$1.8 \cdot 10^{-18}$	GITT	[100]
$8.0 \cdot 10^{-18}$	Sim.	[70]
$1.0 \cdot 10^{-17} - 1.0 \cdot 10^{-22}$	Impedance technique	[70]
$2.7 \cdot 10^{-21} - 8.1 \cdot 10^{-22}$	$FePO_4$, GITT	[70]
$1.0 \cdot 10^{-17} - 1.0 \cdot 10^{-18}$	$LiFePO_4$, GITT	[70]
$5.0 \cdot 10^{-18}$	Sim.	[70]
$8.0 \cdot 10^{-18}$	Sim.	[112]
$3.2 \cdot 10^{-13} - 8.0 \cdot 10^{-17}$	Sim.	[122]
$1.0 \cdot 10^{-11} - 1.0 \cdot 10^{-12}$	Sim.	[109]
$8.0 \cdot 10^{-18}$	Sim.	[124]
$3.8 \cdot 10^{-19}$	Sim.	[87]
$8.0 \cdot 10^{-18}$	Sim.	[125]
$2.46 \cdot 10^{-22}$	Li_xFePO_4, x $=0$	[117]
$1.49 \cdot 10^{-18}$	Li_xFePO_4, x=0.18	[117]
$1.26 \cdot 10^{-18}$	Li_xFePO_4, x=0.36	[117]
$6.35 \cdot 10^{-19}$	Li_xFePO_4, x=0.55	[117]
$3.32 \cdot 10^{-19}$	Li_xFePO_4, x=0.73	[117]
$8.57 \cdot 10^{-22}$	Li_xFePO_4, x=0.91	[117]

2.5.4 Thermal behavior

Thermal management is very important for performance and aging of the battery. In case of abuse or uncontrolled operation malfunctions may occur. The risk of thermal runaway is known latest from the time when the first accidents with fire occurred in laptops caused by malfunction of batteries. Due to this, controlling of the battery in terms of current, voltage and temperature is an important task. For an adequate controlling, a better understanding of the reasons for thermal runaway is necessary. Therefore many investigations were performed experimentally and theoretically to get further indications preventing accidents caused by thermal runaway.

Nearly all thermal models applied to batteries use following classical equation to treat energy conservation:

$$\rho \cdot c_P \cdot \frac{\partial T}{\partial t} = \lambda \cdot \nabla T + \dot{Q} \ , \tag{18}$$

where ρ is the density, c_P is the heat capacity, T is the temperature, t is the time, λ is the

heat conductivity and $\dot{Q}$ is the heat source term. This equation accounts for heat accumulation on the left hand side and on the right hand side the heat conduction and heat generation, respectively. The latter can be distributed into heat sources due to ohmic resistance of current collectors and electrolyte, due to kinetic processes, like electron-transfer reactions and diffusion processes, and due to reversible entropy contributions of the thermodynamics caused by the active materials.

In literature many models can be found focusing on different battery types. Already 1994 Chen et al. presented a 3D-model of a simplified pouch cell containing graphite as anode material and TiS_2 as cathode material [126]. Although their model does not regard electrochemical processes, it gives the same tendencies like model including electrochemistry. They show anisotropic thermal conductivity within the cell, which has an important influence on the cell performance: the thermal conductivity is low through the layers and is large along width and height directions. As consequence, they predict that heat removal is more effective using latter directions. In 1995, Pals et al. presented a 1D model of a battery containing lithium metal and TiS_2 [127]. Their model is coupled with detailed electrochemistry developed by Doyle et al. [42]. They show that the cell voltage rises with increasing temperature along with the active-material utilization at the interrupting voltage. Also they demonstrate that the heat generation decreases with increasing temperature. They predict that cells, used above 90 °C, operate isothermally and are limited ohmically.

Especially $LiCoO_2$-containing lithium-ion batteries have been in the focus of research. Al Hallaj et al. presented a 1D-model of a Sony US 18650 cell [128]. They demonstrate that at low rates the temperature distribution is uniform. At higher rates all temperatures rise significantly, risking thermal runaway. Chen et al. showed a 3D-model, in which each material has its own value for density, heat conductivity and heat capacity [129]. They also claimed that the heat conduction through the sheets is less than in the other directions. Additionally they showed the temperature variation at different convection conditions. Under natural convection conditions the temperature rises nearly linearly. Increasing of the convection leads to a strong decrease of the maximum temperature and a more distinguished temperature variation. Guo et al. modeled a battery pack of eight coupled cells including detailed electrochemistry [130]. In this model self-balancing of the batteries is implied. The results show that by parallel connection the SOC becomes uniform only at the surface sheets, but the deviation in individual electrode surfaces is not necessarily reduced. Kumaresan et al. published a combined electrochemical and thermal model using concentrated solution theory for transport properties within the liquid electrolyte [131]. For isothermal simulations they achieve a good agreement with

experiments at different temperatures. Among other, they compared the temperature dependence of some parameters and their influence on discharge curves for non-isothermal conditions. They show that the thermodynamic factor, the diffusion of ions within the electrolyte and the solid state diffusion of lithium within graphite have an effect on discharge curves leading to a better performance of the battery, except the ionic conductivity, which has no visible influence. Kim et al. presented a 3D-model using the finite volume method applied on a $LiCoO_2$-battery [132]. They predict a significant heat accumulation within the center core of the battery, which can lead to thermal runaway. Hatchard et al. presented a 1D-model for cylindrical and prismatic cells using properties of $LiCoO_2$ and $LiMn_2O_4$ as cathode material to investigate the behavior while an oven exposure is applied [34]. Huang et al. measured experimentally enthalpy and entropy contributions in a potentiostatic mode [133]. They observed that the cathode side has a small exothermal effect in opposite to the anode, which has a small endothermal effect. They show that the cathode has a three times larger heat production than that of the overall battery reaction. In comparison to this, Williford et al. published a 1D-thermal model of a prismatic cell using entropy values for different active materials [134], which were measured by Viswanathan et al. for different SOC [135]. They state that the entropy contribution has an immense effect on the thermal management of a battery. They show that the positive terminal has a higher temperature than the negative terminal, which is in agreement with the statement of Huang et al. They also demonstrate that the use of a battery-averaged entropy overestimates the predicted temperature compared to the use of individual entropies for anode and cathode. Srinivasan et al. published a 2D model coupled with detailed electrochemistry applied to a $LiMn_2O_4$-based battery [30] . They claimed that the reversible heat is important for all C-rates. Especially at high rates, the non-uniform reaction distribution is significant, which in turn introduces error in estimating the heat generation based on the averaged cell voltage and OCV. Concerning the same active material, Somasundaram et al. presented a 2D-model for a cylindrical cell [136]. Their results show the total heat generation split in their contributions due to reversible or irreversible heat and ohmic resistance. Also the heat contribution separated in the different layers is shown. It could be concluded that the active materials contribute the most to the total heating. At low C-rates the influence of the reversible heat is more significant that at higher rates, where heat generation due to ohmic resistance dominates. Unfortunately a comparison with experiments is not carried out. Their work is in agreement with the reports of Williford et al., Pals et al. and Ye et al. The latter examined a $LiMn_2O_4$ containing battery, too [137]. Using a coupled electrochemical and thermal model, they concluded that at high temperatures the reversible heat has more influ-

ence on the performance of a battery than at low temperatures, where the gradient of lithium-ions within the liquid electrolyte dominates. At high C-rates the reversible heat can be neglected, because the kinetic contribution domiates the total heat generation.

In the recent years LiFePO$_4$ as cathode material has come into the focus of research. Guo et al. published a 3D model of a cylindrical cell using a finite element method without a detailed electrochemical model [138]. They studied the thermal abuse of this battery and concluded that the gradient, occurring along the thickness of the battery, has the most important effect on heating. The other directions have a higher thermal conductivity, so that they are not the limiting factor. This is in agreement with other reports, like those of Chen, S. et al. and Chen, Y. et al. Also Forgez et al. examined a LiFePO4 battery with a 1D or 2D model, unfortunately without detailed electrochemical behavior [36]. They show that the temperature increases while discharging from 25 °C to 45 °C. Their model fits well to the experiments taken at the surface of the battery. They predict that the internal temperature is around 10 °C higher than the surface temperature. Other materials were examined, too, like Ni-MH battery by Gu et al. and CaCrO4 by Freitas et al. using a CFD software, but which are not explained in detail here [61,139]. Finally Botte et al. gives a nice overview over thermal and electrochemical models including governing equations and methods to solve these equations [32].

3 Experiments

3.1 Motivation

Experimental data of LiFePO$_4$-based batteries are sparse. The data sheet of the battery used in the present work, which is given by the producing company, does not contain a lot of information about the performance of the battery. In this work, experimental investigations were performed. It allows specifying definite operation conditions, such as applied current or ambient temperature, which were needed to validate the model exactly. Therefore, a wide range of operation conditions can be investigated which may also include extreme situations in which a battery normally is not used. Furthermore, experimental results provide a basis for comparison with simulations under different conditions. Occurring agreements or differences between them can be used to optimize the model and to improve the understanding of a battery.

3.2 Investigated cell

The investigated cell in this work is a LiFePO$_4$-based lithium-ion battery of the company A123 systems (Figure 12). It is a 26650 cylindrical high-power cell with a nominal capacity of 2.3 Ah and a nominal cell voltage of 3.3 V. Further information is given in the official data sheet of the company A123 systems in Figure 13.
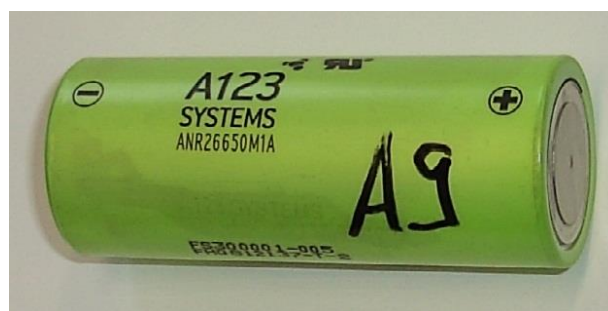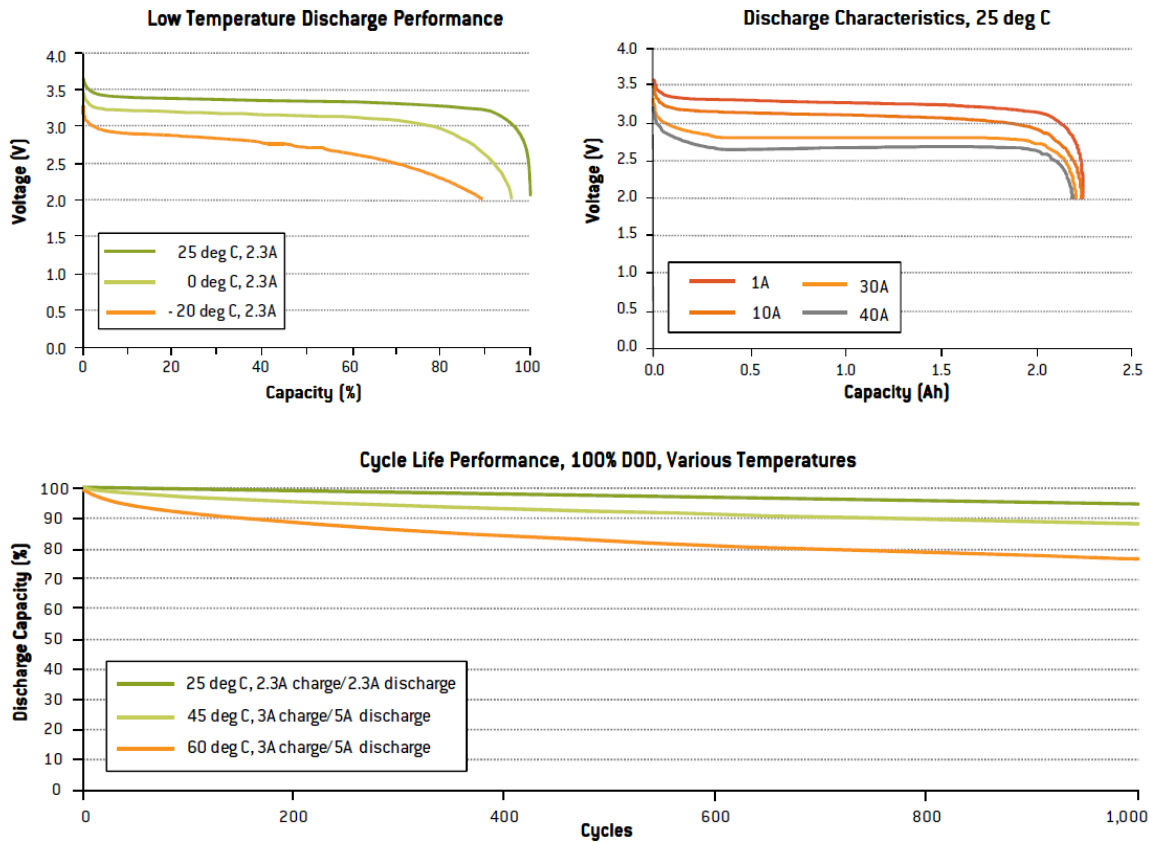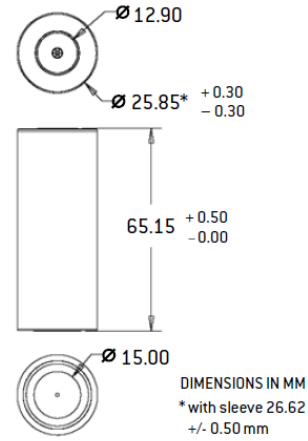

Figure 12: Investigated cell of the company A123 systems. Declaration "A9" is for DLR-internal investigation record.

High Power Lithium Ion ANR26650*m1*A

A123Systems' lithium ion rechargeable ANR26650*m1*A cell is capable of very high power, long cycle and calendar life, and has excellent abuse tolerance due to its use of patented Nanophosphate™ technology.

Nominal capacity and voltage	2.3 Ah, 3.3 V
Internal impedance (1kHz AC)	8 mΩ typical
Internal resistance (10A, 1s DC)	10 mΩ typical
Recommended standard charge method	3A to 3.6V CCCV, 45 min
Recommended fast charge current	10A to 3.6V CCCV, 15 min
Maximum continuous discharge	70A
Pulse discharge at 10 sec	120A
Cycle life at 10C discharge, 100% DOD	Over 1,000 cycles
Recommended pulse charge/discharge cutoff	3.8V to 1.6V
Operating temperature range	-30°C to +60°C
Storage temperature range	-50°C to +60°C
Core cell weight	70 grams

Ø 12.90

Ø 25.85* $^{+0.30}_{-0.30}$

65.15 $^{+0.50}_{-0.00}$

Ø 15.00

DIMENSIONS IN MM
* with sleeve 26.62
+/- 0.50 mm

Low Temperature Discharge Performance
- 25 deg C, 2.3A
- 0 deg C, 2.3A
- -20 deg C, 2.3A

Discharge Characteristics, 25 deg C
- 1A
- 10A
- 30A
- 40A

Cycle Life Performance, 100% DOD, Various Temperatures
- 25 deg C, 2.3A charge/2.3A discharge
- 45 deg C, 3A charge/5A discharge
- 60 deg C, 3A charge/5A discharge

A123 SYSTEMS

Figure 13: Data sheet of a 26650 LiFePO$_4$-battery of A123 systems, downloaded in 2009.

3.3 Discharge / charge measurements

To characterize the cell electrochemically, charge and discharge measurements were performed using a Zahner IM6 frequency response analyser [140–142]. The measurements were taken in a climate chamber to ensure constant ambient temperature. Two different conditions were chosen. The first set of charge / discharge curves was taken at room temperature applying different currents. The second set was performed at different temperatures using one defined current (1C rate[1]). For the first set at room temperature, discharge measurements were performed using constant current in a range of 0.23 to 23 A after constant-current constant-voltage (CC-CV) charge. To set the same initial conditions, always a charge current of 1C (2.3 A) at room temperature was chosen, also a cut-off-voltage of 3.6 V for changing into the constant voltage mode. This voltage was kept until the current reduced to 0.1C (0.23 A). Then the load was turned off and the charging was finished. After a rest of minimum 60 minutes the measurements were taken. The charge curves were performed after reaching the initial point of a fully charged battery described above and discharging with 1C rate to the cut-off voltage of 2 V. Then it was charged with different currents in the range of 0.23 A to 10 A. The second set of charge and discharge curves was taken using 1C rate for different temperatures in the range of − 10 °C to 50 °C. Reaching a comparable starting point, same conditions were taken as described above, in addition that the temperature was returned to room temperature while returning to the starting point.

In Figure 14 a) a set of discharge curves at room temperature is shown. The open-circuit voltage (OCV) is around 3.6 V (not visible in the figure) and the cut-off voltage is 2.0 V. The capacity is around 2.3 Ah which is reached by all curves. All curves have in common that between a capacity of 0.25 Ah and 2.0 Ah the voltage is nearly constant which is due to the behavior of the cathode material. This plot shows the current dependence of the discharge voltage. The higher the applied current is, the lower the cell voltage is.

In Figure 14 b) a set of charge curves at room temperature is shown using different charge currents from 0.1 C to 5 C (0.23 A to 11.5 A). The curves start at around 2.4 V (not visible in Figure 14 b) which correlates to the relaxed cell potential after discharging with 1C, reaching the cut-off voltage of 2.0 V and switching off the current immediately. After the charge process and reaching 3.6 V the voltage was kept constant until the current dropped down below 0.1C (0.23 A). It can be seen that the charge voltage depends on current, too.

---

[1] Discharging with a 1C rate means that the battery is discharged after 1 h. The applied current depends on the capacity. For example, a battery with 2.3 Ah is discharged within 1 h applying a current of 2.3 A.
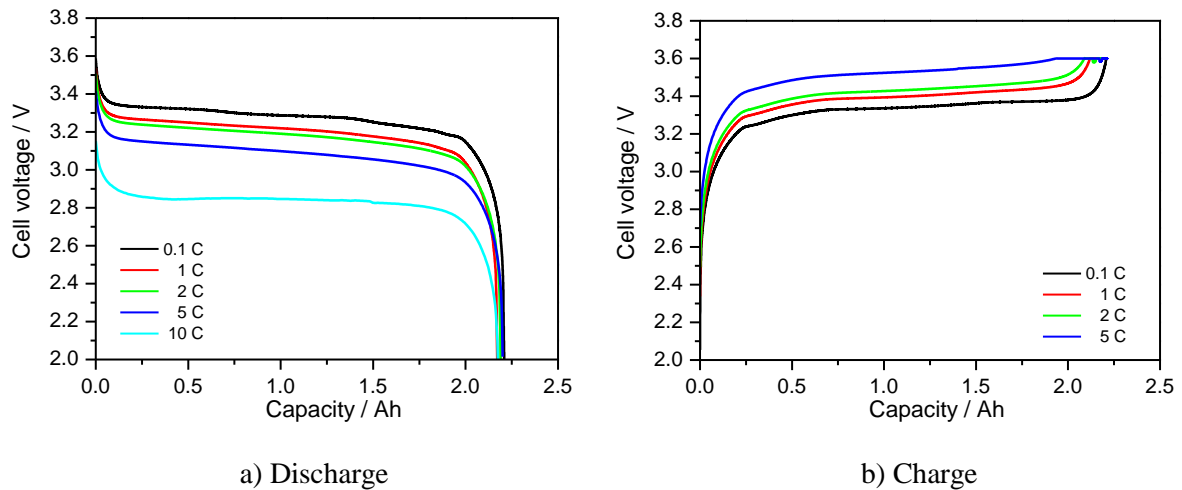
a) Discharge   b) Charge

Figure 14: Discharge and charge curves at different currents at room temperature
[141,142].

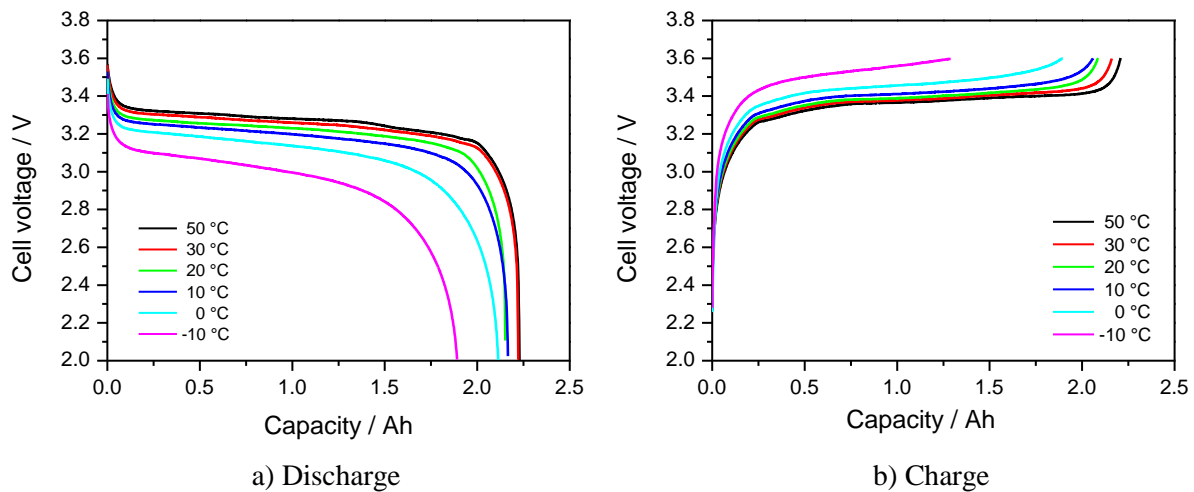a) Discharge   b) Charge

Figure 15: Discharge and charge curves at different temperatures at 1C [141,142].

As already known, the temperature influences the performance of the battery immensely. In Figure 15 a), a set of 1C discharge curves at different temperatures in the range of −10 °C to 50 °C is shown. The most immense effects are the increase of overpotentials and the loss of the capacity with decreasing temperature.

At lower temperatures the curves show more smooth behavior, due to kinetic effects, than at high temperatures, e.g. 50 °C. At lower temperatures the overpotentials become higher and cover the characteristics of the thermodynamics. At high temperatures the overpotentials are lower and the thermodynamics of the half cells becomes more important.

In Figure 15 b) a set of 1C charge curves at different temperatures is shown. The initial OCV is around 2.2 V. The cut-off voltage is 3.6 V. The charge curves show a temperature dependence with the same characteristics as in the discharge mode, such as the intensification of overpotentials and increasing smoothness of curves with decreasing temperature.

55

3.4 Impedance measurements

Electrochemical impedance spectra (EIS) give more detailed information about processes occurring within the battery. Due to time or frequency dependence, respectively, information about relaxation times of processes and, depending on the magnitude of resistance, the importance can be estimated. Two representations are typically used, either the Bode plot, which shows the spectra versus the frequency separated in the real part and the imaginary part or the magnitude and phase of the signal, or the Nyquist plot which displays the real part versus the imaginary part. All electrochemical impedance spectra were recorded in potentiostatic mode with 2 mV excitation amplitude in the frequency range of 1.2 mHz – 100 kHz. A four-wire setup was used. All measurements were performed at room temperature using a Zahner IM6 frequency response analyser [140–142].

Impedance spectra were measured at different states of charge (SOC[2]). To ensure the reproducibility in obtaining defined SOC, the following methodology was used. The climate chamber was brought to 20 °C and the battery was charged with 1 C (2.3 A) till the voltage of 3.6 V was reached. Then the voltage was kept constant until the current dropped below 0.1 C (0.23 A). For relaxation of inner-gradients a rest of minimum 60 minutes was added. Afterwards the battery was discharged with 1C (2.3 A) at 20 °C to the chosen SOC. After an additional rest of 60 minutes the impedance measurement was taken. For each SOC the methodology was repeated starting with charging with 1C at 20 °C to a SOC of 100%.

In Figure 16 a) and b) the Bode plot of the impedance spectra for different SOC are shown. The real part of the resistance versus the frequency is shown in Figure 16 a). The lowest impedance can be found at a frequency of 10^4 Hz. At a frequency of around 10^5 Hz an increase of the resistance is assumed due to inductance. Going to lower frequencies, further increases of the impedance can be observed. The next important increase of the resistance is at around 10^2 Hz which results from electron transfer reactions. At a low frequency of 10^{-2} Hz an immense increase of the impedance occurs. This can be attributed to slow processes like diffusion or phase transition.

The imaginary part of the impedance versus the frequency is shown in Figure 16 b). In the range of 1 Hz to 10^3 Hz the imaginary part is nearly constant. At higher frequencies it decreases for all SOCs equally. This can be attributed to induction. At lower frequencies the impedance increases depending on the SOC. The SOC of 90 % to 30 % show nearly the same

---

[2] The state of charge (SOC) describes the loading of a battery. A full battery has the SOC of 100 %, an empty one has a SOC of 0 %.

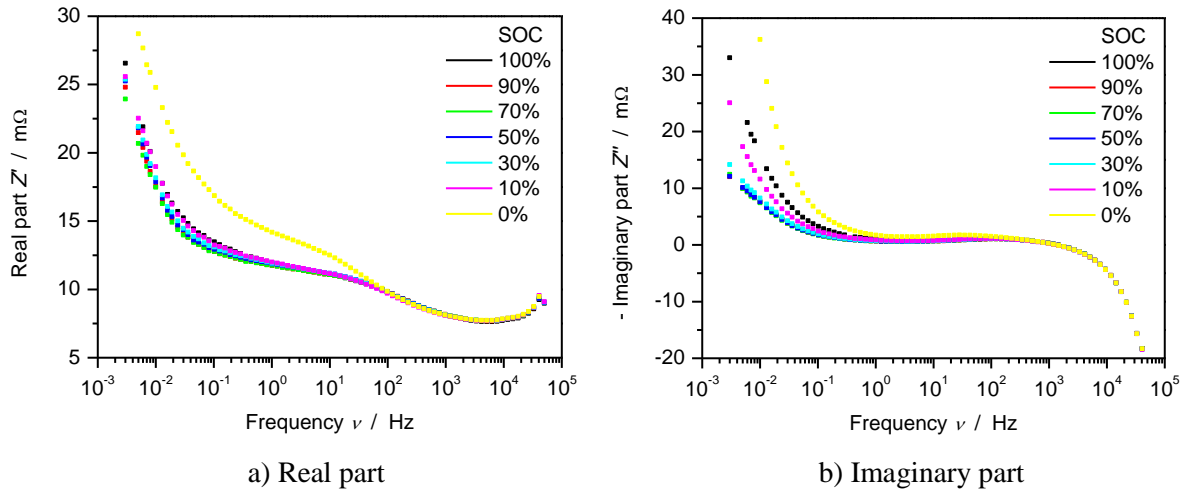a) Real part   b) Imaginary part

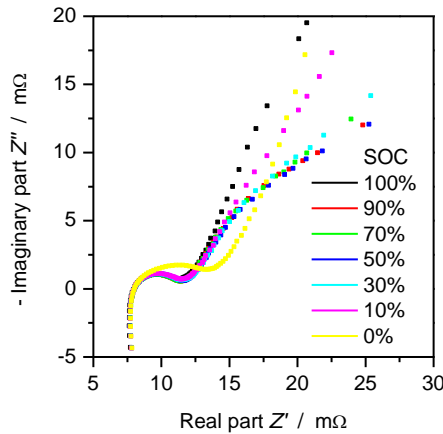Figure 16: Impedance spectra vs. frequency (Bode plot) [141,142].

Figure 17: Nyquist-plot of an impedance spectra [141,142].

increase, compared to the SOC of 100 %, 10 % and 0 % which show an immense increase. The rise is caused by capacitive behavior.

In Figure 17 a Nyquist plot of the same impedance spectra is shown. Here, the imaginary part of the impedance is displayed against the real part. The curves for different SOC all show different behavior, but they have in common that at around 8 mΩ the imaginary part crosses 0.0. Afterwards a stretched semi-circle occurs which is due to electron transfer processes of both electrodes. Then starting around a real part of 12 mΩ the real and imaginary part increase nearly equally. Due to the fact that the other curves do not show this behavior, and especially the curves of SOC 30 % − 70 % show a beginning semi-circle, it can be assumed that another slow reaction takes place, e.g. phase transition.

3.5 *Thermal measurements*

Temperature measurements were also performed. During cycling of the battery, the temperature of the battery surface was recorded. Therefore, the plastic envelope of the cell was removed on one side creating an area of ca. 1 cm² of pure container metal. On this area the temperature sensor (TP100) was installed. At room temperature different C-rates were applied and the temperature change was recorded. Also at different ambient temperatures the battery was cycled and its temperature change on the surface was measured. As experimental setup a multi-channel battery cycler Evaluater B from FuelCon and a climate chamber WK 360/40/5 from Weiss GallenKamp were used [141,142].

3.6 *Computer tomography*

For determination of macro-structural parameters, X-ray computer tomography (CT) was performed using a Phoenix v-tome-x L450 with a nominal voxel size of 5 μm [143]. The practical resolution in the current experiments was around 8 μm. Results of the measurements are shown in Figure 18 and Figure 19.

In Figure 18a, a cross section of the complete battery is shown. On the left side there is the cathode pole cap and on the right side the anode pole cap. In this picture the inner design can be analyzed. The gray rectangular regions are the windings of the repeat units and its active materials. Within these windings some bigger current collector stripes are included to improve the electric current to the pole caps. On the cathode side the current collector consists of aluminum which is displayed in gray in the picture and can be found on the left side above. On the anode side the current collector is consisting of copper, on the right side below. For each electrode there is more than one current collector leading to the pole caps. In Figure 18b, a zoom of picture a) shows the domain of the anodic current collector. At three different positions current collectors, leading to the pol-cap, are inserted into the repeat units. The brighter lines represent the current collectors of a repeat unit. The gray areas represent the active material. Due to resolution and nearly the same gray values, not all sheets of the repeat unit can be resolved.

Figure 19 shows three cross sections parallel to the pole caps. In panel a) the cross section of a whole battery, parallel to the pole caps near the anode pole, is shown. The construction shows a spiral configuration of the windings. The bright lines represent the current collectors which are inserted into the windings. In panel b) a zoom of the outer-shell was taken. The gray displayed areas are the active materials; the bright lines are the current collectors. At the end of

the windings the active material ends while the distance decreases. A short distance remains, which is due to the existence of the separator. In panel c) a zoom of the inner-section was taken. In the dark region the end of the active material is visible. In dark gray the separator can be observed which continues into the center hole of the cell.
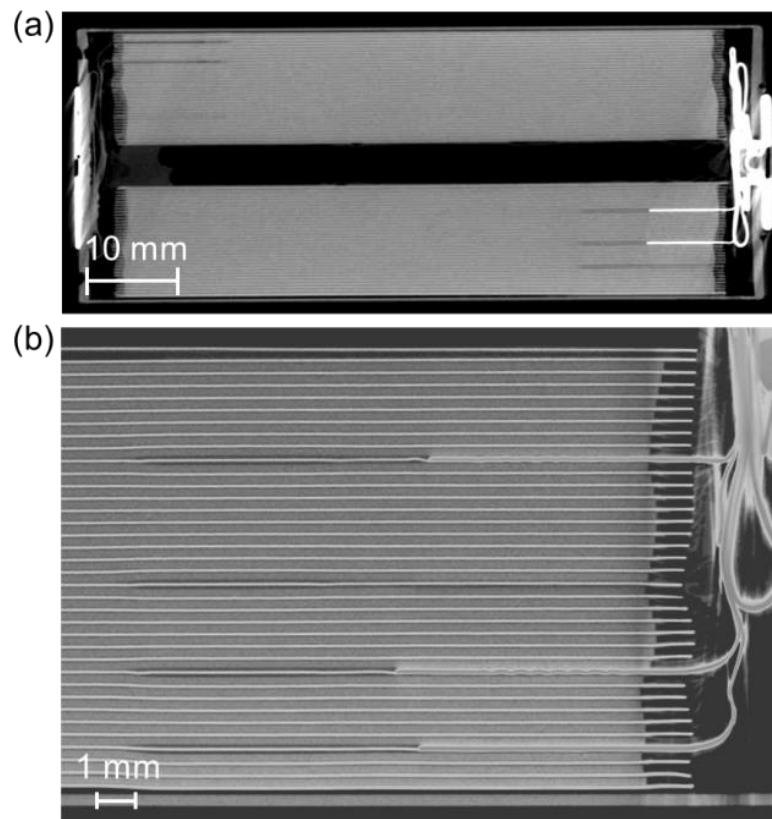

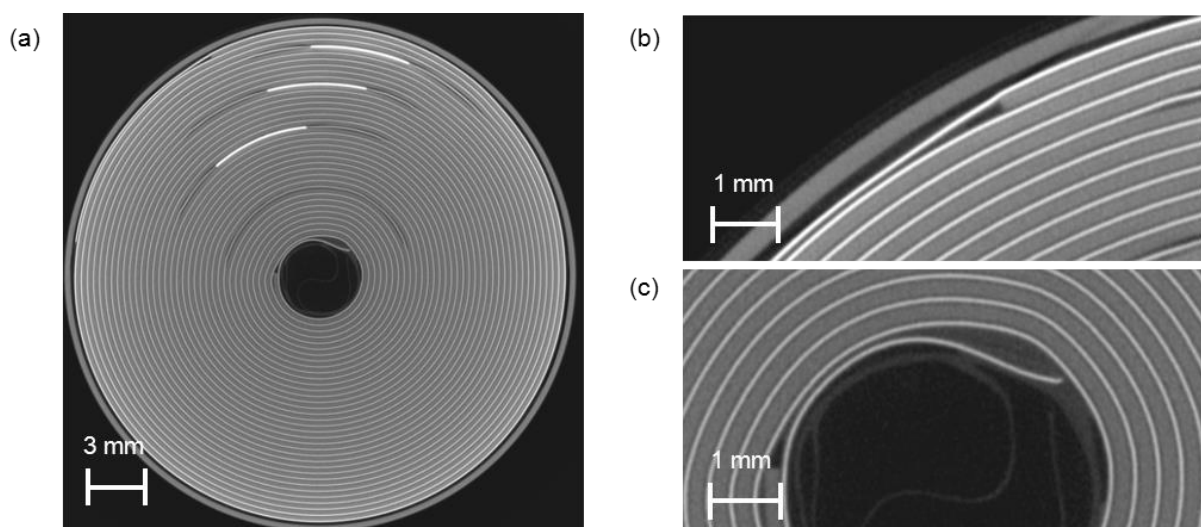Figure 18: Computer tomography measurements. a) Cross section perpendicular to pole caps, b) zoom [143].

Figure 19: Computer tomography measurements. a) cross section parallel to pole caps, b) zoom of outer shell, c) zoom of inner shell [143].

3.7 Scanning electron microscopy

For more detailed information about the construction and particle sizes, scanning electron microscopy measurements were performed using a Zeiss ULTRA plus scanning electron microscope [144]. For measuring the thickness of the sheets, a current collector, coated with active material on both sides, was prepared by fixing it in a polymer and polishing the cross section.

For estimating the averaged particle size, SEM-pictures of a cross section and of the surface of the active material were used. To determine the porosity of each electrode, a simple gray-value method was applied. The procedure was the following: a SEM-picture was taken and converted into three different gray-value types (white, gray and black). To be more exact and to get clearer phase borders, the fields with the same gray-values were homogenized [145]. The pixels of the picture with the same gray-value were counted. It was assumed that the darkest gray-value (black) represents the holes and the pores within the electrode. The percentage of this contribution is used as porosity. It has to be noted that SEM measurements are surface-specific measurements. However, depending on the energy of the electrons used in the setup, the depth of penetration of the electrons changes. This results in the effect that particles below the observed surface are assumed being on the surface due to a brighter reflection within the picture. With the gray-value method these particles are counted to the surface and therefore the porosity depends on the SEM-measurement parameters.

In Figure 20, a cross section of the anode current collector is shown. It can be seen in the center of the picture as a big white bar. Below and above, the current collector is coated with active material. Within the active material layers, particles of different sizes are visible. Some of them have a size up to 10 µm, while others are very small with around 4 µm. The thickness of the electrode is 35.5 µm. For estimating the averaged particle size, Figure 21 was used which shows a zoom of the cross section. The averaged particle radius was estimated as 2.46 µm. The porosity was estimated with 33 % using the gray-value method described above.

In Figure 22 a cross section of the cathode electrode is shown. Within this picture the current collector is on the bottom, and the porous electrode fills most of the picture. The thickness of the electrode is around 79.5 µm. For estimating the averaged particle size Figure 23 was used. A radius of 36.5 nm was estimated, which is consistent with measurements of Safari et al. [103]. Also this picture was used to determine the porosity with the gray-value method described above. The porosity was estimated to be 33 %.
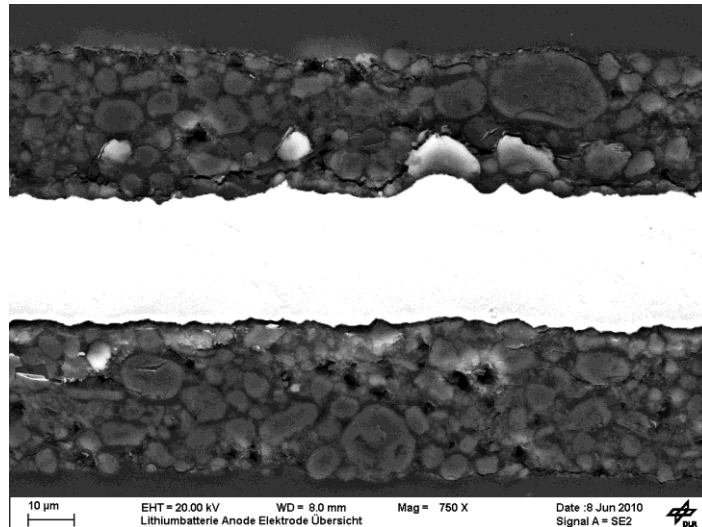
Figure 20: Cross section of an anodic current collector coated with active material [144].
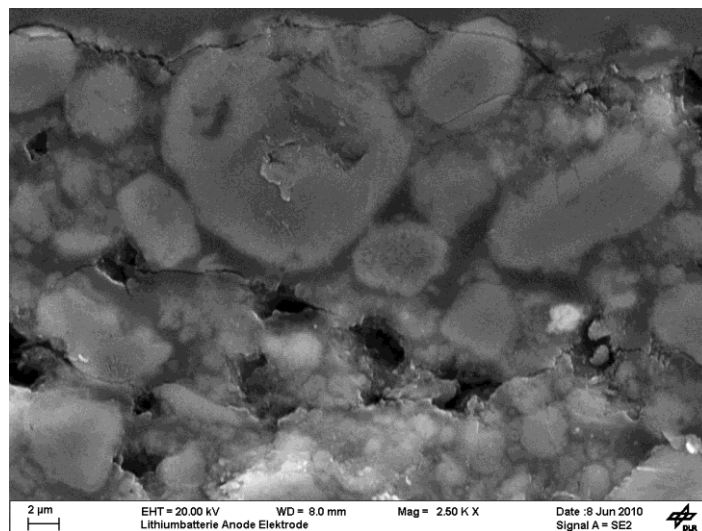

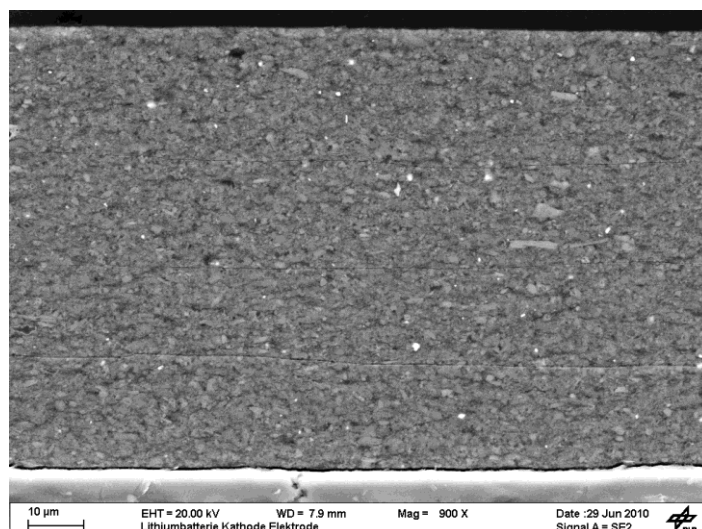Figure 21: Cross section of the anode active material taken by SEM [144].

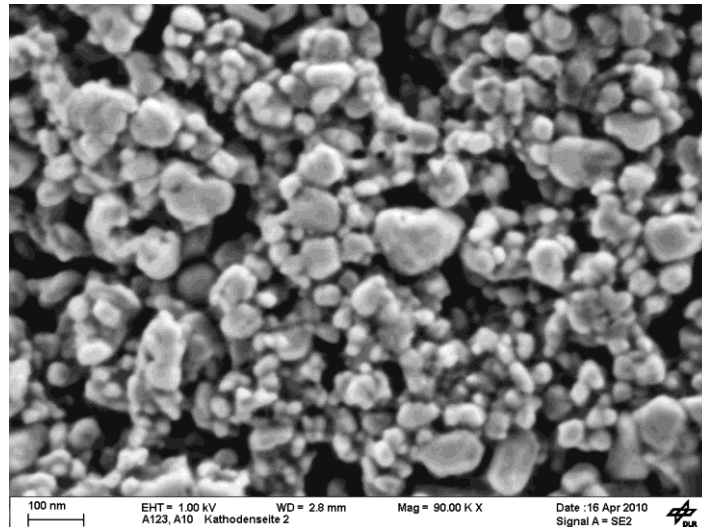Figure 22: Cross section of the cathode [144].

Figure 23: LiFePO$_4$ particles used as cathode active material [144].

3.8 Opened battery

For the determination of some parameters, like thickness of electrodes, particle sizes and porosity, the battery was opened [141]. Figure 24 shows the battery without the cylindrical can. From the left to the right the construction can be observed. The cathode pole cap, consisting of aluminum, is connected to the big current collector stripe of aluminum which is led through a plastic holder. Afterwards the "heart" of the battery consists of the windings of repeat units. The separator is the white foil overlapped by an electrode sheet. The latter is covered by the black active material. While opening the battery, the outer-windings are affected which can be seen as a cut in the center of the battery. To the right the anode current collector consisting of copper leads through a plastic holder to the anode pole cap. The contact of the pole cap with the current collector is different for both electrodes. The contact on the cathode side is very simple. The pole cap and the current collector are pressed together. On the anode side it is more complex due to the usage of a vent. In Figure 24 on the right side of the picture the vent can be seen as small blue dot within the pole cap of the anode.


Figure 24: Opened battery without container. [141]

4 Modeling and simulation

4.1 Simulation methodology

The electrochemical and thermal behavior of a cell is based on processes which occur at different time and length scales. A multi-scale approach for modeling is used to describe this behavior, which is shown in Figure 25. The atomistic structure represents the lowest scale. Here, information about binding and activation energies can be used for simulations on higher scales. The next higher scale is represented by the particle. Here, lithium diffusion within the bulk material, (de-)intercalation and surface reactions take place. The next level is represented by the composite electrodes consisting of different phases or materials which influence the behavior of a cell, too. The repeat unit represents the next scale where all processes between the electrodes are considered, in particular mass and charge transport. All repeat units combined form the single cell where temperature gradients occur. They influence all lower scales due to the fact that all processes are temperature dependent. The highest scale, presented in Figure 25, is a battery pack used in mobile applications. On this scale further requirements are regarded such as cooling or heating, concepts, electrical connections, battery management system, etc.
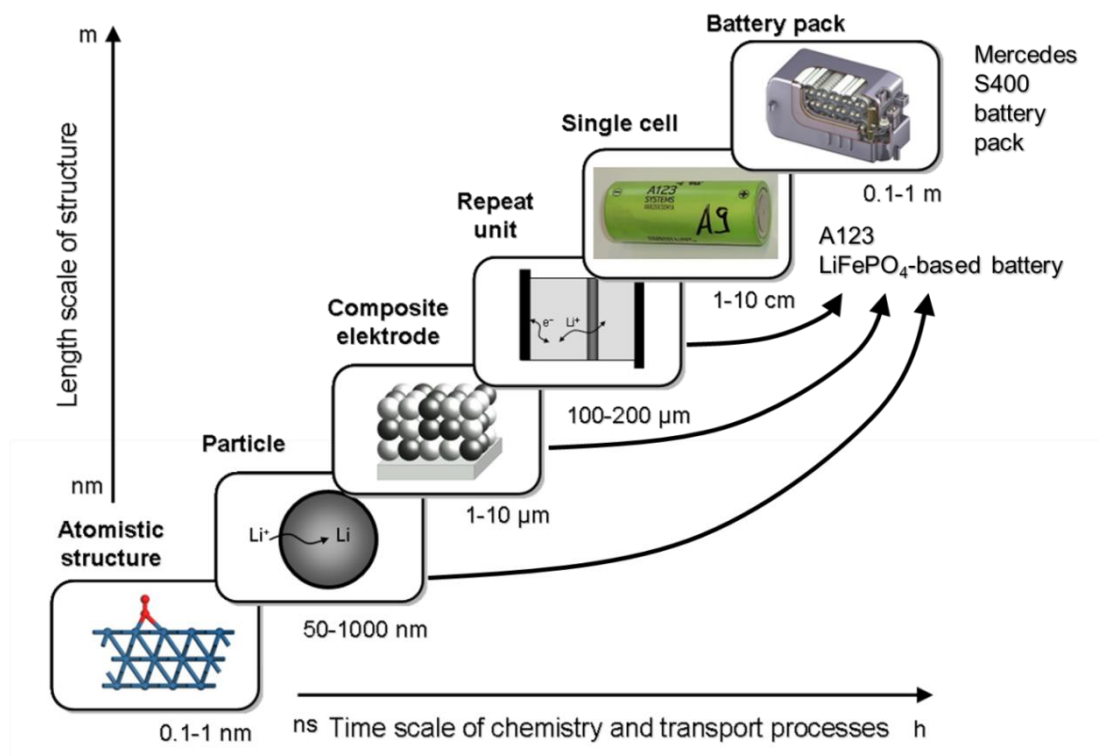
Figure 25: Different time and length scales of processes occuring in a battery. The picture of the battery pack is taken from literature [146].

In this work all scales are considered except the atomistic scale and the battery pack. In Figure 26 the three important scales are shown. On the first scale is the single cell (mm – cm). On this scale the thermal behavior of the battery is simulated. The thermal behavior and its temperature contribution depend on the transport processes on this scale and on the heat sources coming from lower scales. Therefore, this scale is coupled to a smaller scale (μm) which is represented by a repeat unit. On this scale mass and charge transport mechanisms are considered, like diffusion and migration of lithium ions within the liquid electrolyte. For describing the thermal and electrochemical behavior of a battery, the (de-)intercalation process and the lithium storage within the active material of both electrodes must be considered. Therefore, the smallest scale in this work consists of spherical particles surrounded by liquid electrolyte and an electron-conducting material (like particles coated with carbon black). On the surface of these particles the electron-transfer reaction takes place which involves the (de-) intercalation of lithium ions. Additionally the transport of lithium within the particles is described by an ordinary Fickian diffusion. Due to (de-) intercalation and transport of lithium within the particles the concentration of lithium changes with operating time. This has a strong influence on the thermodynamics of each active material, i.e., the thermodynamics are not constant. Depending on the intercalated concentration of lithium the thermodynamics change which results in different enthalpy and entropy contributions. Due to this the total cell voltage has a characteristic shape depending on the state of charge. All these effects are described in more detail in the following subchapters.

In general, this work is separated into two model approaches depicted in Figure 26. The first model contains the largest scale of a full battery, where a temperature gradient along the windings occurs. It is coupled to the scale of a repeat unit. There, lithium ion diffusion in the liquid electrolyte takes place as well as lithium intercalation into the active materials. This model is called "macro-model" and it describes the thermal and electrical behavior of a cell, based on global kinetics.

The second model is called "micro-model". Here, the scale of a repeat unit and the scale of particles are coupled. The particles are assumed to be spherical and they are surrounded by electronically conductive coating. Processes such as lithium diffusion or phase transition are described occurring within the particles. The micro-model describes the electrical behavior of an isothermal cell based on elementary kinetics.

A list of the model equations are given in Table 4.
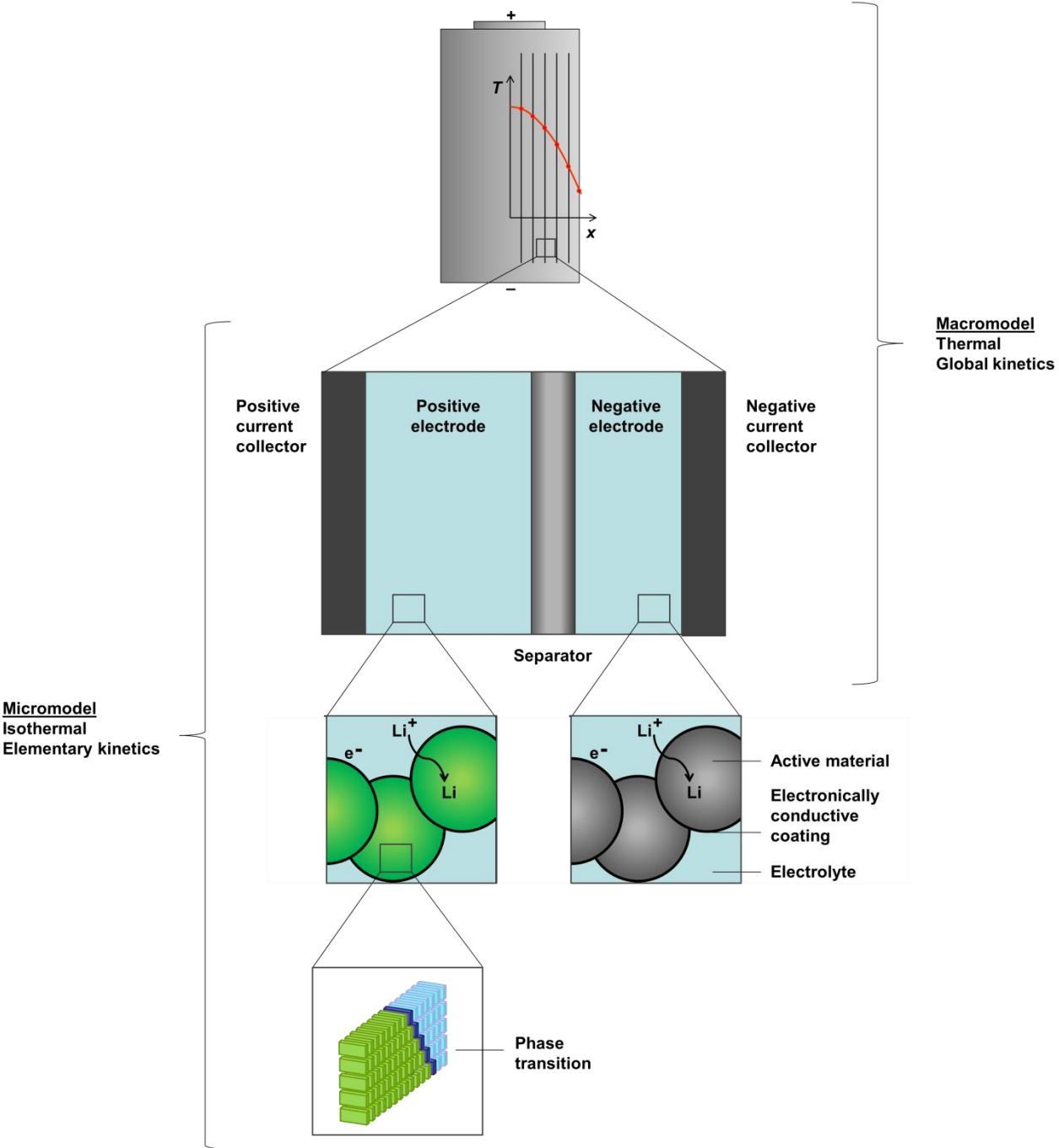
Figure 26: Three main scales are represented in this work. The lowest scale describes spherical particles. The next scale represents the repeat unit. The largest scale is used to represent a complete single cell.

Table 4: List of model equations

Physicochemical process	Model equation	Equation
Thermodynamics (anode and cathode)		
Half-cell equilibrium potential	$\Delta\phi_{eq}(c_{Li}) = -\dfrac{\Delta G(c_{Li})}{zF} = -\dfrac{\Delta H(c_{Li}) - T\Delta S(c_{Li})}{zF}$	(19)
Kinetics (anode and cathode)		
Butler-Volmer kinetics	$i_F^V = i_0 \cdot \left(\exp\left(\dfrac{\alpha_a F}{RT}\eta_{act} \right) - \exp\left(-\dfrac{\alpha_c F}{RT}\eta_{act} \right) \right)$	(28)
Exchange current density	$i_0 = i_{00} \cdot c_{Li,EL}^a \cdot c_{Li,bulk}^b \cdot (1 - c_{Li,bulk})^c$	(29)
Activation overpotential	$\eta_{act} = \Delta\phi - \Delta\phi_{eq}(c_{Li}) - \eta_{conc}$	(22)
Potential step	$\Delta\phi = \phi_{elde} - \phi_{elyt}$	(21)
Concentration overpotential	$\eta_{conc} = \dfrac{RT}{zF}\ln\left(\dfrac{c_0}{c(t)} \right)$	(23)
Total current density	$i = \displaystyle\int_{y=0}^{L_{elde}}\left(i_F^V + i_{dl}^V \right)dy$	(24)
Current density due to electrochemical double-layer	$i_{dl}^V(t) = A_{dl}^V\, C_{dl}(\Delta\phi)\,\dfrac{\partial(\Delta\phi)}{\partial t}$	(25)
Cell voltage		
Cell voltage	$E(i) = \phi_{ca}(i) - \phi_{an}(i) = E_{eq} - \eta(i)$	(20)
Solid-state transport		
Spherical diffusion in anode particle	$\dfrac{\partial\rho_{Li}}{\partial t} = \dfrac{1}{r^2}\dfrac{\partial}{\partial r}\left(r^2 D(x_{Li})\dfrac{\partial\rho_{Li}}{\partial r} \right)$	(49)
Fickian diffusion in cathode particle	$\dfrac{\partial\rho_{Li}}{\partial t} = \dfrac{\partial}{\partial z}\left(D(x_{Li})\dfrac{\partial\rho_{Li}}{\partial z} \right)$	(51)
Interfacial area	$A_{LFP,FP}^V = A_0^V \cdot f\left(i^V, x_{Li} \right)$	(52)
	$f\left(i^V, x_{Li} \right) = \left(7.0 \cdot 10^4 \cdot \left(\dfrac{i^V}{10^4\,\frac{A}{m^3}} \right)^2 + 0.02 \cdot \left(\dfrac{i^V}{10^4\,\frac{A}{m^3}} \right) \right) \cdot x_{Li} + 1.0$	(53)
Electrolyte transport (diluted solution theory)		
Mass conservation	$\dfrac{\partial(\varepsilon\rho_i)}{\partial t} = \nabla(D_i\nabla\rho_i) + \nabla\left(D_i^{migr}\nabla\phi \right) + M_i\dot{s}_i^V$	(35)
Migration coefficient	$D_i^{migr} = \dfrac{z_i F}{RT}D_i\rho_i$	(36)
Charge conservation	$\nabla(\sigma\nabla\phi) = b \;,$	(38)
		(91)

$$\sigma = \sum_i \left(\frac{z_i^2 F^2}{RT} \frac{D_i \rho_i}{M_i} \right),$$

$$b = -\sum_i \left(\nabla \left(\frac{z_i D_i F}{M_i} \nabla \rho_i \right) \right) - \sum_i z_i F \dot{s}_i^{\mathrm{V}} \tag{92}$$

Electrolyte transport
(concentrated solution theory)

Diffusion coefficient	$D_{\pm}^{\mathrm{eff}} = \varepsilon_{elyt}^{\beta_{\pm}} D_{elyt} + \frac{t_{\pm}}{z_{\pm} F} \frac{\sigma_D^{\mathrm{eff}}}{c_{\pm}}$	(41)
	$D_{\pm}^{\mathrm{migr,eff}} = +\frac{t_{\pm}}{z_{\pm} F} \sigma^{\mathrm{eff}}$	(42)
	$\ln\left(D(c,T)\right) = D_i(T) + D_{i+1}(T) \cdot c$	(45)
	$D_i(T) = D_{i0} + \dfrac{D_{i1}}{T - \left(T_{g0} - T_{g1} c\right)}$	(46)
Effective ionic conductivity	$\sigma_D^{\mathrm{eff}} = \dfrac{2RT}{F} \sigma^{\mathrm{eff}} (t_+ - 1) \left(1 + \dfrac{d \ln \gamma_{\pm}}{d \ln c_{elyt}} \right)$ $\sigma^{\mathrm{eff}} = \varepsilon^{\beta_k} \sigma$	(43) (44)
Ionic conductivity	$\sqrt{\sigma(c,T)} = \alpha c \sum\limits_{i=0}^{2} \sum\limits_{j=0}^{2} \sigma_{ij} c^i T^j$	(47)
Activation coefficient	$\ln(\gamma_{\pm}) = \dfrac{1}{1-t_+} \sum\limits_{j=1}^{3} \dfrac{2}{j} a_{j0}\left(1 + a_{j1}(T - 293)\right) c^{j/2}$	(48)

Heat transport

Heat conduction and convection	$\rho^{\mathrm{eff}} c_{\mathrm{p}}^{\mathrm{eff}} \dfrac{\partial T}{\partial t} = \nabla\left(\lambda^{\mathrm{eff}} \nabla T\right) + \sum\limits_{j} \dot{q}_j^{\mathrm{V}} + \dot{q}_{chem}^{V} + \dot{q}_{res}^{V} + \dot{q}_{ohm}^{V}$	(54)
Reversible heat source	$\dot{q}_{\mathrm{rev}}^{\mathrm{V}} = \dfrac{i^{\mathrm{V}}}{zF} \left(\sum\limits_{e} \left(-T \cdot \Delta_R S_e^{\mathrm{m}}\right) \right)$	(57)
Heat source due to polarization	$\dot{q}_{\mathrm{pol}}^{\mathrm{V}} = i^{\mathrm{V}} \left(\sum\limits_{e} \left(\eta_{\mathrm{act},e} + \eta_{\mathrm{conc},e}\right) \right)$	(58)
Heat source due to resistivity	$\dot{q}_{\mathrm{res}}^{\mathrm{V}} = i^{\mathrm{V}} \left(\sum\limits_{h} \left(\eta_{\mathrm{res},h}\right) \right)$	(60)
Heat source due to ohmic resistance	$\dot{q}_{\mathrm{ohm}}^{\mathrm{V}} = i^{\mathrm{V}} \left(\sum\limits_{l} \left(\eta_{\mathrm{ohm},l}\right) \right)$	(61)
Heat source due to electrochemistry	$\dot{q}_{\mathrm{chem},e}^{\mathrm{V}} = \dot{q}_{\mathrm{rev},e}^{\mathrm{V}} + \dot{q}_{\mathrm{pol},e}^{\mathrm{V}} = i^{\mathrm{V}} \left(\dfrac{\Delta H}{zF} + \Delta\phi_e \right)$	(59)

4.2 Electrochemistry

4.2.1 Thermodynamics

The cell voltage of the battery is mainly influenced by the half-cell contributions of both electrode materials. With changing lithium content within the active material, the half-cell potentials are not constant over the whole range of discharge or charge operation. Each active material has its own characteristics which contribute to the total behavior. This has to be considered. As mentioned above, LiCoO$_2$ as cathode material shows a stronger slope in the half-cell potential than LiFePO$_4$ does. Usually the half-cell potential itself is used in literature to describe the contribution of the electrode to the complete battery. In this work the separation of the half-cell potential into an enthalpy and entropy contribution is preferred in order to describe the electrochemical performance of a battery and the thermal behavior additionally [147]. This can be done using the following expression

$$\Delta\phi_{eq}(c_{Li}) = -\frac{\Delta G(c_{Li})}{zF} = -\frac{\Delta H(c_{Li}) - T\Delta S(c_{Li})}{zF} \quad , \tag{19}$$

where $\Delta\phi_{eq}(c_{Li})$ is the equilibrium half-cell potential which depends on the concentration of intercalated lithium, $\Delta G(c_{Li})$ is the Gibbs Energy, z the number of transferred electrons, F the Faradaic constant. The half-cell potential can be derived by dividing the negative Gibbs energy by z and F. Using the Gibbs-Helmholtz equation, the Gibbs energy can be separated into two contributions: the enthalpy $\Delta H(c_{Li})$ and entropy contribution $\Delta S(c_{Li})$, which also depend on the concentration of intercalated lithium.

In the following subchapters the half-cell potentials and their enthalpy and entropy contributions are derived, based on available literature.

Anode. In this work the active material of the anode is graphite. As already shown, the half-cell potential of the anode varies depending on the graphite material. It is assumed that in the experimental A123 battery, natural graphite as active material is used which shows best agreement with experimental data as compared to other graphites. The half-cell potential of the anode versus the stoichiometry is shown in Figure 27. The half-cell potential shows characteristic potential changes which correlate to a change in the occupied sites in the host material (see chapter 2.2.3). The first change is at a stoichiometry of around 0.08, followed at 0.2, 0.5 and 0.6. These potential changes can be observed in the experimental measurements, too. Due to the fact that the half-cell potential of LiFePO$_4$ is nearly constant over a wide range, the voltage changes can be mainly attributed to the anode material. To obtain a good agreement

between simulation and experiments concerning these characteristic potential steps, the range of stoichiometry was restricted. This means that not the full range of stoichiometry is used, which would be here from $x = 0.0$ to around $x = 0.8$. A good agreement was achieved using the range of $x = 0.01$ to $x = 0.57$ (cf. chapter 5.1) [148].
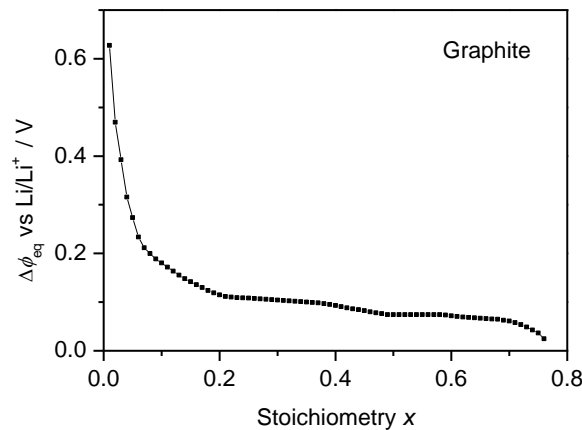

Figure 27: The half-cell potential $\Delta\phi_{eq}$ of the anode versus stoichiometry x in Li_xC_6 is used in the simulations.
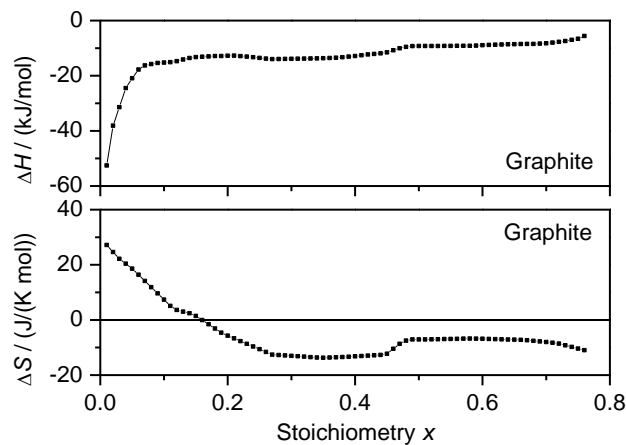

Figure 28: Enthalpy and entropy contribution versus the stoichiometry [3,102].

To obtain the enthalpy and entropy contributions, the half-cell potential, which was measured by Safari et al. [102], was converted to the Gibbs energy. From this the entropy contribution measured by Reynier et al. [3] was subtracted, yielding the enthalpy contribution using equation (19). Both contributions are shown in Figure 28.

The enthalpy contribution shows no further relevant characteristics apart from the potential steps. The entropy contribution shows two relevant features. The first one is the sign change of the absolute entropy value when going from low stoichiometry to a higher one ($x = 0.0$ to 0.2). The second feature is at around $x = 0.5$ where the entropy increases again and keeps

nearly constant going to higher stoichiometry of 0.8. This change around a stoichiometry of 0.5 can be correlated to the stage change of intercalation (LiC_{12} to LiC_6), which was reported in chapter 2.2.3. These two effects have a strong influence on the heat generation during operation and can be used as explanation for the temperature contribution shown in experimental measurements.

It has to be noted that the sign change of the entropy is due to the measurement of this active material versus pure lithium metal using a half-cell set-up. This effect is widely discussed in the paper of Reynier et al. [3]. They concluded that lithium ions within the active material have a higher order than lithium metal and therefore the entropy contribution becomes negative.
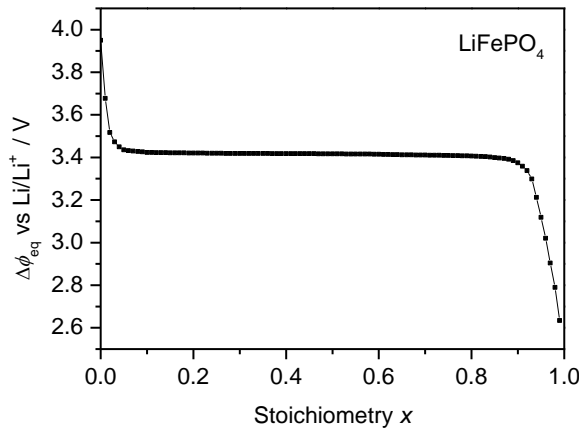

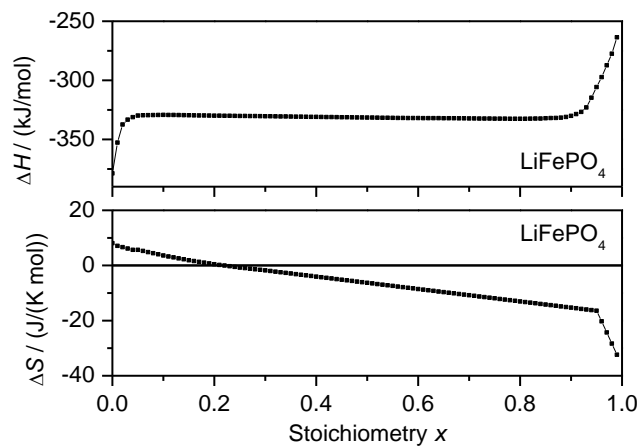Figure 29: Half-cell potential of $LiFePO_4$ used in the simulations.

Figure 30: Enthalpy and entropy contribution versus stoichiometry for $LiFePO_4$ [11,103].

Cathode. The active material on the cathode side is $LiFePO_4$ (LFP). As mentioned in chapter 2.2.4, LFP acts like a conversion material due to the fact that a phase change from LFP to FP occurs. The structural rearrangement is mainly caused by the electron-transfer re-

action of Fe(II) and Fe(III) accompanied by the (de-)intercalation of lithium. This behavior is visible in the half-cell potential which is shown versus stoichiometry in Figure 29. The half-cell potential starts at around 3.9 V vs. Li/Li$^+$, decreases to around 3.4 V, and stays nearly constant over a wide range of the stoichiometry ($x = 0.1 - 0.8$). Then the voltage drops down to around 2.6 V. This half-cell potential was measured by Safari et al. and used in this work [103]. In order to separate into enthalpy and entropy contributions, the entropy versus stoichiometry, measured by Dodd et al. [11], was used to determine the enthalpy contribution using equation (19). Both contributions versus stoichiometry are shown in Figure 30. As seen in Figure 29, the half-cell potential slightly decreases with rising stoichiometry. The enthalpy contribution in Figure 30 shows a slightly different behavior. In the stage of the plateau, this means between the stoichiometry of 0.1 and 0.8, the enthalpy decreases with rising stoichiometry. This might be due to the converting calculations getting the enthalpy contribution. But it could be reasonable as Dreyer et al. suggested that there is a slope in the thermodynamics [21]. Important to emphasize is the behavior of the entropy contribution. With rising stoichiometry the entropy decreases. At a stoichiometry of around 0.2 a sign change occurs. This has a strong effect on the heat generation during operation which leads to a characteristic temperature behavior as seen in experiments. As in the case of graphite, the entropy of LFP is measured against pure lithium metal. Due to the fact that lithium has to be included into a well-ordered structure, the entropy decreases [3].

4.2.2 Kinetics

The cell voltage is determined by the half-cell potentials with the following correlation [147]:

$$E(i) = \phi_{ca} - \phi_{an}(i) = E_{eq} - \eta(i) \ , \tag{20}$$

where E is the cell voltage, ϕ_{ca} and ϕ_{an} the electric potential of the cathode or the anode, respectively. ϕ_{ca} is set to zero as reference while ϕ_{an} depends on the current which is applied to the battery. The dependence can also be described with the difference of the equilibrium cell voltage E_{eq} and the overpotential η. The equilibrium cell voltage E_{eq} is the difference of the equilibrium half-cell potentials $\Delta\phi_{eq}(c_{Li})$ of both electrodes which are defined in equation 19. To obtain all kinetic contributions the potential step at each electrode is given by

$$\Delta\phi = \phi_{elde} - \phi_{elyt} \ , \tag{21}$$

where ϕ_{elde} and ϕ_{elyt} are the potentials of the electrode or electrolyte, respectively. Further, especially for using the Butler-Volmer equation, the activation overpotential η_{act} is defined

using the following expression:

$$\eta_{act} = \Delta\phi - \Delta\phi_{eq}(c_{Li}) - \eta_{conc} , \tag{22}$$

while the concentration overpotential η_{conc} due to electrolyte transport is defined as

$$\eta_{conc} = \frac{RT}{zF} \ln\left(\frac{c_0}{c(t)}\right) , \tag{23}$$

where R is the ideal gas constant, T the temperature, c_0 is the reference concentration of lithium ions in the electrolyte and $c(t)$ the concentration at a certain time-step.

The thermodynamics of the active materials influence the behavior of the cell strongly which can be seen in discharge or charge curves at low currents. However, with increasing current the performance and behavior of a cell change due to the kinetics which become more important. The most important reaction step is the intercalation of lithium into the active material. This can be described by a global kinetic expression like the Butler-Volmer equation where an exponential correlation between current and overpotential is assumed and forward and backward pathway of this reaction is considered. This simple global reaction can be split into a number of elementary reactions, like the adsorption of lithium ions from the electrolyte on the particle surface and the intercalation reaction. In the next subchapters both, global and elementary kinetic models are described in more detail.

In general, the total current of a porous battery electrode is calculated using the following equation published by Bessler et al. [149]

$$i = \int_{y=0}^{L_{elde}} \left(i_F^V + i_{dl}^V\right) dy , \tag{24}$$

where i is the total area-specific current, i_F^V the volumetric faradaic current, i_{dl}^V is the volumetric current coming from the electrochemical double-layer and y is the distance depending on the discretization.

The double layer current is determined by

$$i_{dl}^V(t) = A_{dl}^V C_{dl}(\Delta\phi) \frac{\partial(\Delta\phi)}{\partial t} , \tag{25}$$

where A_{dl}^V is the volumetric surface area, C_{dl} the double-layer capacity, $\Delta\phi$ the potential step and t the time.

In this work, i_F^V is differently calculated depending on the applied model. In case of the macro-model, the current is expressed as global kinetics while the current in the micro-model is due to elementary kinetics. This is described in more detail in the following.

Macro-model. The most important electrochemical step in the battery is the charge transfer at the electrode surface. Therefore equations are needed which treat charge-transfer reactions. Due to the fact that lithium has only one electron in its outer shell, most processes on the surface can be assumed as single electron transfer reactions. On the anode side the reaction can be described as followed [147]

$$LiC_6 \rightleftarrows C_6 + Li^+ + e^- \tag{26}$$

On cathode side the following reactions takes place [147]:

$$Li^+ + e^- + FePO_4 \rightleftarrows LiFePO_4 \tag{27}$$

The rate of a charge transfer process is usually modeled with the Butler-Volmer equation:

$$i_F^V = i_0 \cdot \left(\exp\left(\frac{\alpha_a F}{RT} \eta_{act} \right) - \exp\left(-\frac{\alpha_c F}{RT} \eta_{act} \right) \right). \tag{28}$$

Here, i is the current density, i_0 the exchange current density, α_a the anodic and α_c the cathodic symmetry factor, η_{act} the activation overpotential, F the Faraday constant, R the ideal gas constant and T the temperature. For an elementary reaction the sum of the symmetry factors is one. The first exponential term represents the anodic reaction, i.e., producing electrons, and the second term the cathodic reaction, i.e., consuming electrons. This formulation represents a global kinetic reaction which means that a single rate-limiting step is assumed. Competitive parallel reactions are not considered.

The Butler-Volmer equation needs to be extended to include the influence of changes in the solid-phase and liquid concentrations which leads to following equation:

$$i_0 = i_{00} \cdot c_{Li,el}^a \cdot c_{Li,bulk}^b \cdot (1 - c_{Li,bulk})^c \cdot e^{\left(\frac{E_{act}}{RT} \right)}, \tag{29}$$

where i_{00} is a constant, $c_{Li,el}$ the dimensionless, relative concentration of lithium ions within the electrolyte solution and $c_{Li,bulk}$ the dimensionless, relative concentration of lithium at the particle surface [53]. The term $(1 - c_{Li,bulk})$ describes the vacancies in the particle bulk. The factors a, b and c are constant parameters which are fitted for reproducing experimental results. The factor a is set to 0.5 according to literature [53]. The factors b and c are set to 0.1. Furthermore, E_{act} is the activation energy, R the ideal gas constant and T the temperature. The parameters are given in Table 5. For some simulations the Butler-Volmer equation was modified to include other effects causing additional ohmic resistances like the existence of a solid electrolyte interface (SEI) [150]. Then the equation is given as

$$i_F^V = i_0 \cdot \left(\exp\left(\frac{\alpha_a F}{RT} \left(\eta_{act} - R_{SEI} \cdot i_F^V \right) \right) - \exp\left(-\frac{\alpha_c F}{RT} \left(\eta_{act} - R_{SEI} \cdot i_F^V \right) \right) \right), \tag{30}$$

where R_{SEI} is the ohmic resistance of the SEI. This added resistance influences only the cur-
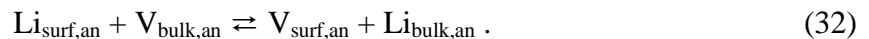
rent distribution and not, for example, the SEI-layer thickness which, in turn, changes the diffusion process. So, it is not an appropriate way to describe further processes affecting additional ohmic resistances. It has to be noted, that resistances can also be caused by other effects apart of the SEI. Nevertheless using the Butler-Volmer equation is appropriate to model pure metal surfaces where only adsorption of ions and electron transfer take place. If intercalation materials as electrode are used, then the Butler-Volmer equation has to be modified with the result that all other occurring processes, such as ion diffusion in crystal lattice or phase transition, are lumped into the single kinetic expression. To improve the understanding of all these processes the contribution of each occurring reaction in form of elementary kinetic mechanisms can be considered.

Table 5: Macro-model related parameters used in the Butler-Volmer equation

Parameter	Anode	Cathode	Ref.
i_{00} (A/m²)	$3.12 \cdot 10^{15}$ [f*]	$1.79017 \cdot 10^{12}$ [f*]	[148,151]
E_{act} (J/mol)	53411.0 [f*]	41367.0 [f*]	[148,151]
α	0.5 [l*]	0.5 [l*]	[42,148,151]

*f means fitted and l means literature.

Micro-model. Modeling charge transfer chemistry with elementary kinetics enables the incorporation of multiple sequential and / or parallel pathways. In this work, CANTERA, developed by Goodwin et al., is used to evaluate thermodynamic properties and reaction rates of elementary reaction mechanisms [152]. On the anode side two reactions are assumed: the adsorption of dissolved lithium ions onto the anode surface (31) and the intercalation within the active material (32),

$$\text{Li}_{el}^+ + \text{V}_{surf,an} + \text{e}^- \rightleftarrows \text{Li}_{surf,an} , \tag{31}$$

$$\text{Li}_{surf,an} + \text{V}_{bulk,an} \rightleftarrows \text{V}_{surf,an} + \text{Li}_{bulk,an} . \tag{32}$$

Parallel to the adsorption process the electron transfer takes place, where Li_{el}^+ is the lithium-ion solved in the electrolyte, $\text{V}_{surf,an}$ is the vacancy for adsorption on the particle surface, e^- is the transferred electron and $\text{Li}_{surf,an}$ is the adsorbed lithium atom on the particle surface. After the adsorption the intercalation occurs, where $\text{V}_{bulk,an}$ is the vacancy within the particle and $\text{Li}_{bulk,an}$ is the lithium atom occupying the host lattice space. These two reactions were also postulated by Colclasure et al. [53]. The parameterization is given in Table 6 and Table 7. This formulation allows further implementation of side reactions like lithium plating or SEI-formation starting from adsorbed species.

On the cathode side we have developed a model inspired by the work of Delmas et al. [14]. They developed a so-called domino-cascade model which describes the phase-change from LFP to FP within a particle. In Figure 31 the domino-cascade model with its phase-front propagation is shown. The main assumption is that lithium-ions diffuse into the material perpendicular to the phase-front propagation. This is very important, because the first guess would be that the diffusion direction is parallel to the phase-front propagation, due to the fact that LFP, or FP respectively, is a 1D-conductor. The second assumption is that only at the interface (dark-blue) between LFP (green) and FP (light-blue) lithium ions are intercalated accompanied by the electron-transfer reaction (red arrows). For representing this behavior, the following model is developed. As shown in Figure 32 there are two bulk-phases LFP and FP, respectively. Between them an interface is assumed. Within this interface lithium diffusion is assumed using an ordinary fickian diffusion approach. This implies that the transport of the lithium atoms depends on a concentration gradient along the diffusion direction. The electron-transfer reaction occurs only at the boundary between liquid electrolyte and FP/LFP interface which can be described as followed:

$$Li^+_{el} + V_{surf,ca} + e^- \rightleftarrows Li_{surf,ca} \ , \tag{33}$$

where lithium-ions from the electrolyte Li^+_{el} react with a vacant interface site $V_{surf,ca}$ to an interfacial species $Li_{surf,ca}$. After this reaction the diffusion into the bulk material takes place where the bulk reaction i.e., phase-change reaction, occurs. This is described as:

$$Li_{surf,ca} + V_{bulk,ca} \rightleftarrows V_{surf,ca} + Li_{bulk,ca} \ , \tag{34}$$

where lithium of the internal surface $Li_{surf,ca}$ reacts with a vacancy of bulk FP $V_{bulk,ca}$ to form LFP $Li_{bulk,ca}$ and a free interfacial site $V_{surf,ca}$. The parameterization is given in Table 7.

It can be seen that there is a strong correlation between diffusion and creating or consuming free vacancies by phase change reaction along the diffusion pathway. This method offers an improved understanding of this material's behavior by separating electron transfer and transport processes from the phase-change reaction.

Table 6: Micro-model related parameters

Parameter	Anode	Cathode	Ref.
Active surface area (m²/m³)	$4.02 \cdot 10^{5,e*}$	$6.7 \cdot 10^{6,e*}$	
Three phase boundary length (m/m³)	$1.0 \cdot 10^{12,e*}$	$3.72 \cdot 10^{14,e*}$	
Site density (mol/cm²)	$2.6 \cdot 10^{-9,l*}$	$2.6 \cdot 10^{-9,l*}$	[53]

*e means estimated and l means literature.

75
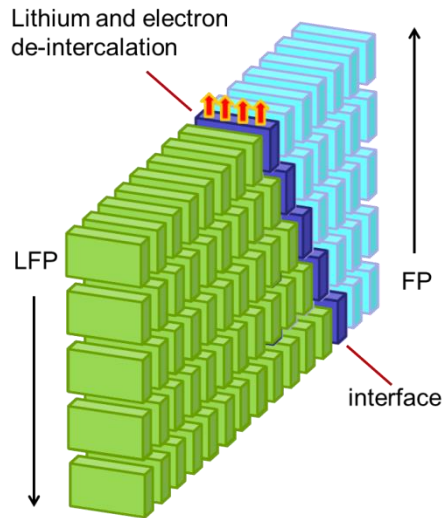
Figure 31: Phase-front propagation from FP (light-blue) to LFP (green) where lithium and electron de-intercalation (red arrows) take place into the distorted region (dark-blue). This domino-cascade model is inspired by the work of Delmas et al. [14].
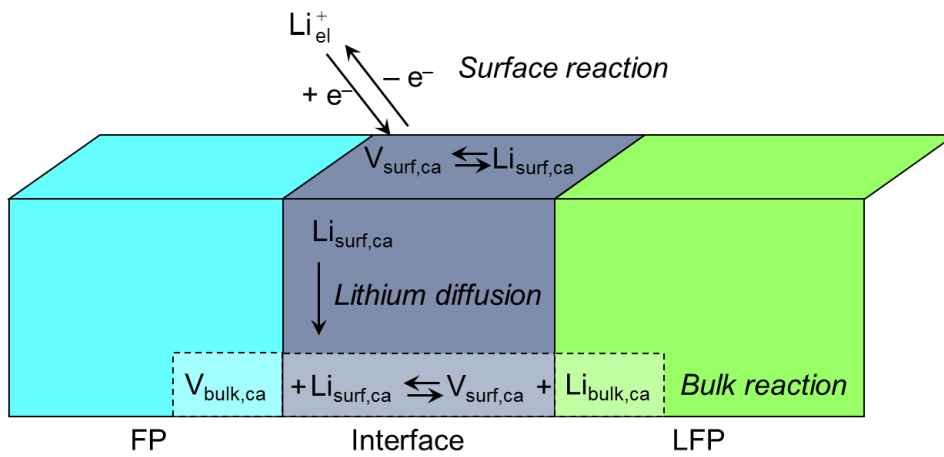
Figure 32: The modeled elementary reactions occurring at the phase boundary of LiFePO$_4$ (LFP) and FePO$_4$ (FP) and an interface, where lithium transport into the bulk material takes place.

Table 7: Elementary reaction mechanisms of micro-model

Reaction	Preexponential factor	Activation energy / J/mol	Equation
$Li^+_{el} + V_{surf,an} + e^- \rightleftarrows Li_{surf,an}$	$5.0 \cdot 10^{-1}$	9200.0*	(31)
$Li_{surf,an} + V_{bulk,an} \rightleftarrows V_{surf,an} + Li_{bulk,an}$	$2.34 \cdot 10^4$	2450.0*	(32)
$Li^+_{el} + V_{surf,ca} + e^- \rightleftarrows Li_{surf,ca}$	$4.0 \cdot 10^{16}$	1.0	(33)
$Li_{surf,ca} + V_{bulk,ca} \rightleftarrows V_{surf,ca} + Li_{bulk,ca}$	$8.0 \cdot 10^{-7}$	1.0	(34)

*The activation energies of the anode reactions (Eqs. 31,32) are given by Colclasure et al. [53].

Table 8: List of parameters

Parameter	Anode	Separator	Cathode	Ref.
Geometry				
Thickness current collector (µm)	15 [m*]		15 [m*]	
Thickness of active material (µm)	35.5 [m*]	20.0 [m*]	79.5 [m*]	
Porosity / Tortuosity	0.33 [m*] / 1.2 [e*]	0.5 [m*] / 1.0 [e*]	0.33 [m*] / 1.2 [e*]	
Density (kg/m³)	2420.0 [f*]		1440.0 [f*]	
Particle radius (nm)	3580 [m*]		37.0 [m*]	
Electrolyte				
Initial concentration LiPF$_6$ (mol/l)	1.2 [l*]	1.2 [l*]	1.2 [l*]	[29]
Double layer capacity (F/m³)	$2.0 \cdot 10^4$ [f*]		$1.0 \cdot 10^5$ [f*]	
Global parameters				
Serial resistance (Ω·m²)		$5.0 \cdot 10^{-4}$ [f*]		
Inductance (Ω·cm²·s)		$1.5 \cdot 10^{-4}$ [f*]		

*m means measured, e means estimated, l means literature and f means fitted.

Both models presented here use the same parameter set for the battery construction and other global settings, such as initial salt concentration, double-layer capacity, etc. These parameters are given in Table 8.

4.3 Mass and charge transport

4.3.1 Electrolyte

Diluted concentration theory. Within the liquid electrolyte the transport of ions takes place. We use the Nernst-Planck-equation to describe the transport process by coupled diffusion and migration [147]. A general multi-component formulation is developed that can accommodate spatially varying diffusion coefficients. As common in computational fluid dynamics approaches, the mass density ρ (kg/m³) instead of concentration c (mol/m³) as conservation variable is used.

The Nernst-Planck equation describes ionic transport based on diffusion and migration,

$$\frac{\partial(\varepsilon \rho_i)}{\partial t} = \nabla\left(D_i^{\mathrm{eff}} \nabla \rho_i\right) + \nabla\left(D_i^{\mathrm{migr,eff}} \nabla \phi\right) + M_i \dot{s}_i^{\mathrm{V}}, \tag{35}$$

with

$$D_i^{\mathrm{migr,eff}} = \frac{z_i F}{RT} D_i^{\mathrm{eff}} \rho_i \,, \tag{36}$$

where ε is the porosity (depending on the location within the repeat unit), D_i^{eff} is the effective diffusion coefficient of the species i, $D_i^{\mathrm{migr,eff}}$ the effective migration coefficient, z_i the charge of species i, F the faradaic constant, R the ideal gas constant, T the temperature, ϕ the electric potential, M_i the molar mass and $\dot{s}_i^{\mathrm{V}}$ a chemical source term due to lithium (de-)intercalation or chemical reactions in the electrolyte (e.g., ion association, SEI formation). For n species, there are n equations (35), but $n+1$ unknowns (n densities ρ_i plus the electric potential ϕ). In order to close the equation system, we assume charge neutrality [147]

$$\sum (\varepsilon c_i z_i) = 0 \,. \tag{37}$$

For charge conservation, we use

$$\nabla(\sigma \nabla \phi) = b \,, \tag{38}$$

where σ is the ionic conductivity of the electrolyte and b is a source term due to transport and chemical reactions of charged species [147]. Thus, we have mathematically cast the charge neutrality condition into a form that can be easily implemented into simulation software. The derivation is given in Appendix 7.1. Note that this formulation (equation 35 and 38) is applicable to multi-component mixtures of both charged and uncharged species. For uncharged species ($z = 0$), the Nernst-Planck Equation is reduced to an ordinary diffusion equation and the charge conservation equation is unaffected.

In case of diluted solution theory, the effective diffusion coefficient is described as followed:

$$D_i^{\mathrm{eff}} = \frac{\varepsilon_i}{\tau_i^2} D_i \,, \tag{39}$$

where ε is the porosity, τ the tortuosity and D the diffusion coefficient of species i. Also, the effective conductivity depends on porosity and tortuosity according to

$$\sigma_i^{\mathrm{eff}} = \frac{\varepsilon_i}{\tau_i^2} \sigma_i \,, \tag{40}$$

where σ is the conductivity of species i, which is given by the left-hand side of equation 37. The implementation is done to ensure the most flexibility in enabling to give the diffusion coefficient as constant of as function depending on concentration, which is read in as look-up table.

Concentrated solution theory.   In case of high concentrations of conducting salt, the ions interact with each other resulting in different diffusion behavior [153]. Therefore, also using the equations 35 and 38 as in diluted solution theory [154], we consider the change of

diffusion using dependencies of a Bruggemann coefficient β and an effective ionic conductivity σ_D^{eff} according to

$$D_\pm^{\text{eff}} = \varepsilon_{elyt}^{\beta_\pm} D_{elyt} + \frac{t_\pm}{z_\pm F} \frac{\sigma_D^{\text{eff}}}{c_\pm} \quad . \tag{41}$$

Here, the diffusion coefficient depends on the transference number t additionally (thereby is $t_- = 1 - t_+$ and $\text{Li}^+ \hat{=} +$ and $\text{PF}_6^- \hat{=} -$) [154]. Also, a change of the migration coefficient is considered yielding [154]:

$$D_\pm^{\text{migr,eff}} = + \frac{t_\pm}{z_\pm F} \sigma^{\text{eff}} \quad . \tag{42}$$

The effective ionic conductivity of diffusion derives from the partial derivation of the chemical potential by the electrolyte concentration of the dissolved species according to

$$\sigma_D^{\text{eff}} = \frac{2RT}{F} \sigma^{\text{eff}} (t_+ - 1)\left(1 + \frac{d\ln\gamma_\pm}{d\ln c_{elyt}}\right) , \tag{43}$$

where $\gamma_\pm$ is the activity coefficient describing the deviation from the ideal behavior which in turn is no interaction between ion and electrolyte molecules [154]. The effective ionic conductivity is calculated by

$$\sigma^{\text{eff}} = \varepsilon^{\beta_k} \sigma \quad , \tag{44}$$

using the ionic conductivity σ [154]. The diffusion coefficient D_{elyt} is calculated by

$$\ln(D(c,T)) = D_i(T) + D_{i+1}(T) \cdot c \text{ with } i = 0,1 , \tag{45}$$

depending on concentration c and temperature T [69,151]. The temperature dependent diffusion coefficient is described as

$$D_i(T) = D_{i0} + \frac{D_{i1}}{T - (T_{g0} - T_{g1}c)} , \tag{46}$$

where T_{g0} is the glass temperature [69] [151]. The conductivity is given by

$$\sqrt{\sigma(c,T)} = \alpha c \sum_{i=0}^{2} \sum_{j=0}^{2} \sigma_{ij} c^i T^j \quad . \tag{47}$$

The activity coefficients of the ions is calculated using the following equation

$$\ln(\gamma_\pm) = \frac{1}{1-t_+} \sum_{j=1}^{3} \frac{2}{j} a_{j0}(1 + a_{j1}(T - 293))c^{j/2} , \tag{48}$$

where t_+ is the transference number of the positive ion [69,151]. The parameters that are used to calculate the coefficients of diffusion, conductivity and activity are given in Table 9 [69,151].

Table 9: Concentrated solution theory [69,151]	
Parameter	Value
Diffusion coefficient / (m, s, mol, l, K)	
D_{00}	$-4.43 \cdot 10^{-4}$
D_{01}	$-54.0 \cdot 10^{-4}$
D_{10}	$-2.2 \cdot 10^{-8}$
D_{11}	0.0
T_{g0}	229.0
T_{g1}	5.0
t_+	0.38
$\beta_\pm$	1
Activity coefficient / (mol, l, K)	
a_{00}	0.601
a_{01}	0.0
a_{10}	-0.24
a_{11}	0.0
a_{20}	0.0
a_{21}	0.0
a_{30}	0.982
a_{31}	$-5.2 \cdot 10^{-2}$
Ionic conductivity / (Ω, m, mol, l, K)	
σ_{00}	-1.05
σ_{01}	$7.4 \cdot 10^{-3}$
σ_{02}	$-6.96 \cdot 10^{-6}$
σ_{10}	$6.68 \cdot 10^{-2}$
σ_{11}	$1.78 \cdot 10^{-3}$
σ_{12}	$2.80 \cdot 10^{-6}$
σ_{20}	$4.94 \cdot 10^{-2}$
σ_{21}	$-8.86 \cdot 10^{-5}$
σ_{22}	0.0
β_κ	1.0

4.3.2 Particle

Anode. The active-material particle plays an important role in the transport of lithium ions towards or away from the surface where the electron-transfer process takes place. To describe the transport within this particle, further assumptions are necessary which are applied in the micromodel. In this work the particles are assumed being spherical and having the same particle size. The complete particle surface is active for (de-)intercalation of lithium-ions.

To describe the transport of lithium within the particle a simple Fickian diffusion is assumed according to:

$$\frac{\partial \rho_{Li}}{\partial t} = \frac{1}{r^2} \frac{\partial}{\partial r}\left(r^2 D(x_{Li}) \frac{\partial \rho_{Li}}{\partial r} \right) . \tag{49}$$

It describes the change of the density of lithium ρ_{Li} with time t depending on the diffusion in radial coordinate r and the diffusion coefficient D which depends on the stoichiometry. The stoichiometry describes the amount of intercalated lithium relative to the maximum concentration and has values between 0 and 1. As boundary condition a source term is used:

$$\dot{s}_{Li}^V = \frac{M_{Li}}{zF} i , \tag{50}$$

which is valid for the position $z = 0$ and describes the (de-)intercalation of lithium ions at the particle surface. At the center $z = r$, the source term is per definition 0.

As shown in previous chapters, the diffusion coefficients within particles reported in literature are mostly assumed to be constant. Few studies reported a change of the diffusion coefficient depending on the stoichiometry for both electrode materials. In this work stoichiometry-dependent diffusion coefficients are used, because constant diffusion coefficients did not represent the impedance behavior correctly. They are extracted from literature and used in form of a look-up table with interpolation between given entries.
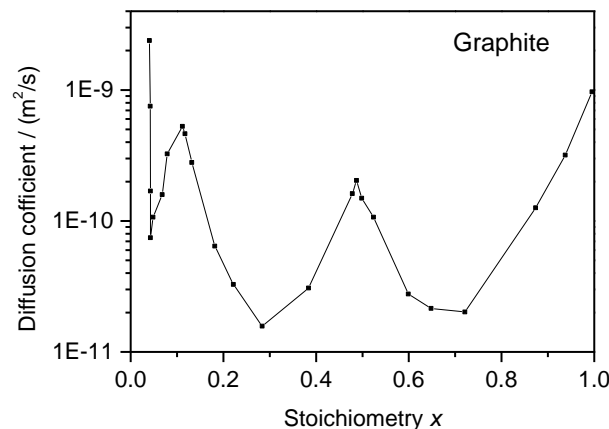
Figure 33: Diffusion coefficient of the anode depending on the stoichiometry measured by Levi et al. [155].

Using the macro-model (cf. chapter 5.2.1), processes within the particle are neglected. Only in case of using the extended macro-model (cf. chapter 5.2.2) and the micro-model (cf. chapter 6), the diffusion coefficients of Levi et al. were used to describe the transport within particles on the anode side [155]. These are shown in Figure 33. It can be seen that the diffusion coefficient decreases with increasing stoichiometry and rises again when the stoichiometry reaches one. Interestingly at a stoichiometry of around 0.5, the diffusion coefficient increases shortly but over a range of one order of magnitude. This correlates with the stoichiometry point in the thermodynamics. At this point the potential of the anode (Figure 27) shows a characteristic step, which is very well to see in the thermodynamics, especially in a change of the entropy contribution at this stoichiometry in Figure 28. This characteristic potential step is more concise in the half-cell potential of natural graphite (Figure 5). In this work the diffusion coefficient of the anode is linearly interpolated between $x = 0.02$ ($D = 2.5e-9$ m²/s) and $x = 0.11$ ($D = 5.5e-10$ m²/s) to improve the numerical stability of the calculations [148].

Cathode.   Using the extended macro-model (cf. chapter 5.2.2) and the micro-model (cf. chapter 6), processes within the active material are considered. Only the general macro-model neglects transport properties within the active material. In case of the extended macro-model, the bulk diffusion is described as on the anode side using equations (49) and (50). The diffusion coefficient is assumed to be stoichiometry dependent as described in chapter 2.5.3.3, section "diffusion model". The values are taken from Safari et al. (cf. Figure 11) [103].

In case of the micro-model the diffusion of lithium and the phase-transition reaction are considered. The diffusion takes place at the FP-LFP interface and not in a spherical particle as it is assumed on the anode side (Figure 31, Figure 32). For diffusion, two assumptions are made. The first one is that the diffusion can be expressed as simple Fickian diffusion in the following form:

$$\frac{\partial \rho_{\mathrm{Li}}}{\partial t} = -D \frac{\partial^2 \rho_{\mathrm{Li}}}{\partial z^2} \ , \tag{51}$$

where D is the diffusion coefficient, ρ_{Li} is the density and z the diffusion direction. The diffusion coefficient is assumed to be constant. The second assumption is that the interfacial area between the LFP and FP phases $A_{\mathrm{LFP,FP}}^{\mathrm{V}}$ changes depending on the current i^{V} and on the stoichiometry of lithium x_{Li} in order to investigate the size flexibility and size growth of the FP-LFP interface. Therefore, following expression is used:

$$A_{\mathrm{LFP,FP}}^{\mathrm{V}} = A_0^{\mathrm{V}} \cdot f\left(i^{\mathrm{V}}, x_{\mathrm{Li}}\right), \tag{52}$$

where A_0^{V} describes the initial interfacial area, or expressed in other words, it describes the

interfacial area at equilibrium. The change, depending on current and concentration, is expressed as:

$$f\left(i^{\mathrm{V}}, x_{\mathrm{Li}}\right) = \left(7.0 \cdot 10^4 \cdot \left(\frac{i^{\mathrm{V}}}{10^4 \frac{A}{m^3}}\right)^2 + 0.02 \cdot \left(\frac{i^{\mathrm{V}}}{10^4 \frac{A}{m^3}}\right)\right) \cdot x_{\mathrm{Li}} + 1.0 \ , \tag{53}$$

where x_{Li} takes values between zero and one. This will be discussed in more detail in chapter 6.2.

4.4 Heat transport

4.4.1 Model equations

Only a part of the energy that is stored in the active material can be used as electric energy. The difference between theoretically possible (ΔH) and actually used energy (ΔG) is released in form of heat, besides heat due to kinetic contributions. This heat accumulates within the battery and dissipates at the battery surface. This results in a temperature gradient within the battery. This temperature gradient depends on the heat transport through the battery and is modeled with the following equation [151]:

$$\rho^{\mathrm{eff}} c_{\mathrm{p}}^{\mathrm{eff}} \frac{\partial T}{\partial t} = \nabla\left(\lambda^{\mathrm{eff}} \nabla T\right) + \sum_j \dot{q}_j^{\mathrm{V}} \ , \tag{54}$$

where ρ^{eff} is the effective density of the material, $c_{\mathrm{p}}^{\mathrm{eff}}$ the effective specific heat capacity, T the temperature, t the time, λ^{eff} the effective heat conductivity and $\dot{q}_{\mathrm{sour},j}^{\mathrm{V}}$ the volumetric heat source. As initial condition for $t = 0$, the internal temperature equals the ambient temperature. The heat release at the boundaries cell center "0" and battery surface "s" is described by Neumann boundary condition. The cell center equals the left boundary of the heat release resulting in a conductive heat flux according to

$$n \cdot \dot{q}_{cond}\big|_0 = -\lambda^{eff} \nabla T\big|_0 = 0 \ , \tag{55}$$

On the right hand side, the heat flux equals the heat release at the battery surface caused by convection and radiation, according to

$$n \cdot \dot{q}_{cond}\big|_s = -\lambda^{eff} \nabla T\big|_s = \alpha_{conv}\left(T_s - T_{amb}\right) + \varepsilon_s k_B\left(T_s^4 - T_{amb}^4\right) , \tag{56}$$

where α_{conv} is the convective heat-transfer coefficient, ε_s the electro-magnetic emission coefficient, k_B the Stefan-Boltzmann constant, and T_s and T_{amb} are the temperature of the battery surface or the ambient temperature, respectively.

On the left hand side of equation 54 the heat accumulation is described which depends mainly on the effective specific heat capacity. The change of the thermal energy with time is described on the right hand side. Three main processes affect temperature variation: the heat conduction through the cell, the heat generation and the heat dissipation in form of radiation or convection at the outer-shell of the battery. The latter one is strongly influenced by the temperature difference between surface and environment. The heat generation can be formulated as a sum over all processes taking place which consume or produce heat. The sources for heat can be split into different contributions.

The reversible heat due to electrochemistry can be described with the following equation:

$$\dot{q}_{\text{rev}}^{\text{V}} = \frac{i^{\text{V}}}{zF}\left(\sum_e \left(-T \cdot \Delta_R S_e^{\text{m}}\right)\right) \text{ with } e = [\text{an, ca}], \tag{57}$$

where i^{V} is the volumetric current, z the transferred electrons, F the Faradaic constant, T the temperature, $\dot{q}_{\text{ref}}^{\text{V}}$ the reversible, volumetric heat source term and $\Delta_R S_e^{\text{m}}$ the molar reaction entropy of anode or cathode, respectively. These entropies depend on the stoichiometry of lithium ions within the active material and show sign changes depending on stoichiometry (cf. chapter 4.2.1). Consequently, a change of the temperature gradient within the battery occurs.

Furthermore, there are irreversible heat sources which contribute to heat generation. These are due to overpotentials, such as activation overpotential η_{act} and concentration overpotentials η_{conc}, which are directly dependent on current. The heat source due to polarization can be described with

$$\dot{q}_{\text{pol}}^{\text{V}} = i^{\text{V}}\left(\sum_e \left(\eta_{\text{act},e} + \eta_{\text{conc},e}\right)\right) \text{ with } e = [\text{an, ca}]. \tag{58}$$

Reversible heat and polarization heat can be described in a combined way according to

$$\dot{q}_{chem,e}^{\text{V}} = \dot{q}_{\text{rev},e}^{\text{V}} + \dot{q}_{\text{pol},e}^{\text{V}} = i^{\text{V}}\left(\frac{\Delta H}{zF} + \Delta\phi_e\right) \text{ with } e = [\text{an, ca}], \tag{59}$$

where $\Delta\phi_e$ is the half-cell potential of the anode (an) or cathode (ca), respectively. This expression is used in this work applying the macro-model. The details of the derivation can be found in the Appendix.

Further heat generation is due to resistivity within liquid electrolyte and due to ohmic resistance within the current collectors. The heat source due to resistivity can be described therefore as

$$\dot{q}_{\text{res}}^{\text{V}} = i^{\text{V}}\left(\sum_h \left(\eta_{\text{res},h}\right)\right) \text{ with } h = [\text{an, sep, ca}], \tag{60}$$

where the resistivity depends on the location within the battery. The metal components only have an ohmic resistance which can be handled separately:

$$\dot{q}_{ohm}^{V} = i^{V}\left(\sum_{l}\left(\eta_{ohm,l}\right)\right) \text{ with } l = [\text{ac, cc}].\qquad(61)$$

This is valid for the current collectors on the anode (ac) or cathode side (cc).

4.4.2 Model reduction and implementation

In the present work, two different implementations of the heat transport equation (54) are used, a full model and a reduced model [151]. Both approaches are shown in Figure 34. They have in common that the heat source comes from the repeat unit which represents the micro-scale behavior with its different heat sources (electrochemistry, ohmic resistance, etc.). The difference between them is the number of used repeat units to get the correct heat and temperature contribution. This is explained in more detail in the following section.

In Figure 34 a) a battery cell is shown. To resolve the temperature distribution across the windings, the full model is used first which is shown in Figure 34 b). Using the heat sources coming from the repeat unit, the temperature can be calculated using the equation (54) shown above.

In general, only one single repeat unit could be used for the calculation of the heat source. But this implies that the heat source is averaged over the complete cell. To avoid this, more repeat units are necessary. But due to the fact that the repeat unit is very small compared to the radius of the battery and the heat source is volumetric, it is necessary to use all repeat units to represent all existing windings within the battery which are electrically and thermally coupled. Then the number of repeat units increases to around 37. Unfortunately this leads to very time-consuming simulations. Due to this, the effective number of repeat units has to be reduced without losing information about the heat or temperature contribution. The developed reduced model only needs few repeat units (around 7) to gain the same agreement and information density as the complete set of repeat units. For this, an additional dimension was included which is the w-dimension, as shown in Figure 34 c). This dimension can be highly discretized gaining a smooth temperature curve compared to the scale of the heat sources. Both scales have the same dimension (radius of the battery) and direction (from the inner shell to the outer shell of the battery). To correlate both scales, it is assumed that all grid points (nw) of the temperature scale (w-scale), occurring in a grid point (nx) of a heat source scale (x-scale), have the same heat production.
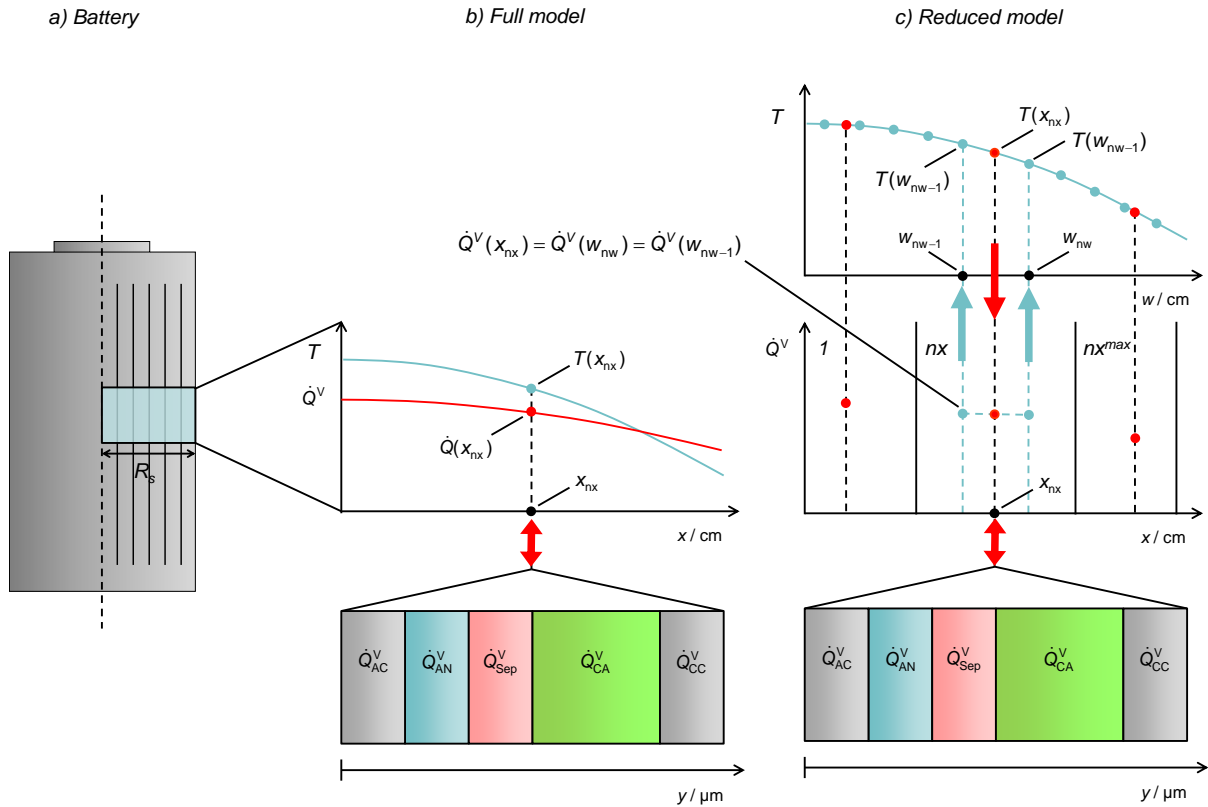
Figure 34: Comparison of two thermal models: a) Cylindrical battery cell, b) full model
with macro scale *x* and c) reduced model with an additional macro scale *w* [151].

Assignment of scales. To calculate the energy-balance equation (54), it must be assigned
a temperature in the *w*-scale $T(w)$ for each grid point *nw* and a correlated heat source of the *x*-
scale $\dot{q}_{w}^{V}(x)$ [151]. An exact determination of the correlating positions is required to couple
heat production and heat transport yielding a smooth temperature profile along the macro-
scale *w*. The coupling includes four calculations steps.

To determine the exact position of a *nx* grid point, after definition of the number of *nx* grid
points to calculate the heat sources, their exact positions on the *x*-scale have to be determined.
Therefore, all layer thicknesses l_m of elements *m* to *nx* are summed. Due to the evaluation of
all state variables in the grid-point center (finite-volume approach), the half thickness of the
regarded grid point *nx* has to be subtracted after summing according to

$$x_{nx} = \sum_{m=1}^{m \leq nx}(l_m) - \frac{l_{nx}}{2} \quad \text{with} \quad nx = [1 \ldots nx^{\max}]. \tag{62}$$

After determination of the exact position of grid point *nx*, a temperature must be given to cal-
culate the heat source. The heat balance can be solved only by computation of a correlating
heat source of the *x*-scale for each temperature of the *w*-scale. Due to different discretizations
of both scales, the temperatures on the *x*-scale have to be interpolated. The linear interpola-
tions is carried out by knowing the temperatures of the adjacent grid points of the *w*-scale

86

$(T(w_{nw-1}), T(w_{nw}))$ yielding the temperature $T(x_{nx})$. The exact positions of two adjacent temperatures were calculated according to

$$w_{nw} = \sum_{m=1}^{m \leq nw} (l_m) - \frac{l_{nw}}{2} \quad \text{with} \quad nw = [1 \dots nw^{\max}]. \tag{63}$$

All layer thicknesses were summed up until the condition $([w_{nw} \leq x_{nx}])$ is no longer fulfilled. To convert the temperature from the w to the x-scale, while being flexible in discretization of scale, the determination of the temperature of a nx-grid point is carried out by linear interpolation, in general $([w_{nw-1} < x_{nx} \leq w_{nw}])$ according to

$$T(x_{nx}) = T(w_{nw-1}) + \frac{T(w_{nw}) - T(w_{nw-1})}{w_{nw} - w_{nw-1}} \cdot (x_{nx} - w_{nw-1}) \ . \tag{64}$$

In case of a left border that the nx-element is smaller or similar to the first nw-grid point $([x_{nx} \leq w_{nw=1}])$ we use

$$T(x_{nx}) = T(w_{nw=1}) \ . \tag{65}$$

In case of a right border that the postion of a nx element is bigger or similar to the last nw-grid point $([x_{nx} \geq w_{nw=nw}{}^{\max}])$, it follows:

$$T(x_{nx}) = T(w_{nw=nw^{\max}}) \ . \tag{66}$$

To convert the heat source of the x-scale into the w-scale, the heat source $\dot{q}^V(T(x_{nx}))$ at position x_{nx} is determined. Here, a coupling of the micro-scale y and macro-scale x takes place. The following applies

$$\dot{q}_x^V(T(x_{nx})) = \left\langle \dot{q}_y^V(T(x_{nx})) \right\rangle \ . \tag{67}$$

The produced heat per volume of a nx grid point equals the averaged value of heat sources of different repeat-unit layers. Here, the heat source within a nx-grid point is constant and the determined point nw is located there, it also follows

$$\dot{q}_w^V(x) = \dot{q}_x^V(T(x_{nx})) = \dot{q}_w^V(T(w_{nw})) \ . \tag{68}$$

Now, the temperature $T(w_{nw})$ and the correlating heat source are determined. The energy balance is solved for each time step.

Parameterization. To simulate the heat transport on the macro-scale, four parameters have to be defined [151]. On the left-hand side of Eq. 54 the volume-specific parameter $\rho^{\text{eff}} c_p^{\text{eff}}$, consisting of the effective heat capacity c_p^{eff} and the effective density ρ^{eff}, can be estimated with the arithmetic average of volume-specific heat capacity of each compound using:

$$\rho^{\text{eff}} c_{\text{p}}^{\text{eff}} = \frac{\sum_k l_k \left(\rho_k c_{\text{p},k} \varepsilon_k + \rho_{\text{elyt}} c_{\text{p,elyt}} \left(1 - \varepsilon_k\right)\right)}{\sum_k l_k} \, , \tag{69}$$

where ε_k is the porosity of each compound k and l the length. Due to the fact that all porous components are saturated with liquid electrolyte, its properties must be also taken into account. Using the parameters given in Guo et al. [138], $\rho^{\text{eff}} c_{\text{p}}^{\text{eff}}$ can be estimated as $1.85 \cdot 10^6$ J/(m³·K).

Also the heat conductivity has to be defined. In case of a cylindrical battery the heat flows orthogonal to the windings. This means that the transport resistance is dominated by the compound with the lowest heat conductivity. Therefore a harmonic average is used instead of an arithmetic one:

$$\lambda^{\text{eff}} = \frac{\sum_k l_k}{\sum_k \left(\dfrac{l_k}{\lambda_k \varepsilon_k + \lambda_{elyt}\left(1 - \varepsilon_k\right)}\right)} \, , \tag{70}$$

where λ^{eff} is the effective heat conductivity and λ_k is the heat conductivity of each compound k. Hence λ^{eff} has the value of 1.02 W/m/K using values of each component published by Guo et al [138].

The emissivity of the battery is estimated as 0.8 [138]. For typical steel casing the literature values spread between 0.7 and 0.9 [136,138,149]. Therefore the mean value is chosen.

The last parameter for the heat transport which has to be defined is the heat transfer coefficient α_{conv}. Usually this value can be estimated roughly using semi-empirical approaches like the Nusselt correlation. In this work this methodology cannot be applied due to the unknown flow properties inside the cell test bench. Therefore this parameter is fitted to the experimental data to achieve a good agreement with measured surface temperature. Here a value of 55 W/m² was found. Usually, lower values are reported in literature (5 − 10 W/m² assuming natural convection [156]). Higher values stand for forced convection. For the high value observed in this work there are two possible explanations. The first explanation could be that the model in this work only includes heat transport across the windings and heat emission to the ambient atmosphere at the battery surface. Kim et al. report that a significant part of the heat is dissipated by the current collectors and the pole caps [132]. This possible heat transfer is not included in our model and has to be compensated by a higher radial heat loss. The second explanation could be that this high value is due to the experimental setup. The battery is cycled in a climate chamber of that comes with a ventilator to ensure constant temperatures. We

have not investigated how strong this fan works and how it affects higher heat flow on the battery surface. Probably both explained effects contribute to the thermal characteristics which are found in this work. A summary of the parameters used in thermal simulations are given in Table 10.

Table 10: Heat-related parameters		
Parameter	**Value**	**Reference**
λ^{eff} / W/m/K	$1.02^{\text{ e*}}$	[138,151]
$\rho^{\text{eff}} c_{\text{p}}^{\text{eff}}$ / J/m³/K	$1.85 \cdot 10^{6 \text{ e*}}$	[138,151]
α_{conv} / W/m²	$55^{\text{ f*}}$	[151]
ε_{surf} / −	$0.8^{\text{ l*}}$	[138,151]

*e means estimated, f means fitted and l means literature.

4.5 Simulation tool DENIS

The detailed models and numerical simulations, described in this section, are implemented in the software package DENIS (Detailed Electrochemistry and Numerical Impedance Simulation). This in-house software was developed by Bessler et al. and is described in detail in their papers [149,154]. It describes physicochemical processes needed to simulate the behavior of fuel cells or batteries regarding thermodynamic properties, phase change management, different transports in solid, liquid or gaseous phases in form of mass or charge, etc. To convert the PDEs occurring in the transport models to a DAE system, finite-volume discretization is used in each scale (x-, y-, z- and w-dimension). To solve the equations, the LIMEX solver developed by Deuflhard et al. is used [157]. Analytic expressions for specific boundaries (Eqs. 52, 53) are evaluated using muParser [158].

In case of elementary kinetics, CANTERA, developed by Goodwin et al. [152], is used which is coupled to DENIS. Chemistry source terms for surface reactions are calculated by given chemical reaction mechanisms (pre-exponential factors, activation energies, thermodynamic properties).

5 Macro-model: Results and discussion

5.1 Parameterization

The experimental charge and discharge curves show a characteristic temperature and current behavior. Therefore, it is necessary to take the temperature influence on electrochemical reactions and on transport processes into consideration. Isothermal simulations at various temperatures build the base for model parameterization. Here, adjustments are presented concerning thermodynamics and kinetics to achieve a good agreement with the experimental results in charge and discharge curves for different C-rates and different ambient temperatures [148].

Thermodynamics. The battery consists of two electrodes. The active material of the anode is graphite and of the cathode is LFP. Unfortunately, the exact composition of both electrodes is not known. Therefore, it is assumed that on the anode side natural graphite is used as active material. Comparing different half-cell potentials, the best agreement was found using natural graphite. Usually, different graphite compounds are mixed to ensure good electric conductivity and best possible lithium storage. In this work, the half-cell contribution of the anode is assumed to consist only of one active material. On the cathode the active material is LFP. Usually the particles are coated with graphite compounds, such as carbon black, to enhance the electric conductivity. The active material in this work is assumed to be well-connected to the current suppliers. Also, it is assumed that pure LFP is used as active material which is not doped with other rare metals.

As already discussed in chapter 4.2.1, the half-cell potential is separated into enthalpy and entropy contributions. The latter contributes to the temperature behavior of the cell and it is not available for electric work. For the anode the entropy values are used from Reynier et al. and the enthalpy values from Safari et al. [3,102]. For the cathode the entropy values are used from Dodd et al. and the enthalpy contribution is used from Safari et al. [11,103].

Stoichiometry range. The discharge curves are influenced by both electrodes. Both are individually restricted by the lithium stoichiometry which is used during operation. It is assumed that the fine structure of the discharge curve is due to the anode. The cathode shows the characteristic behavior of a phase change material which is a constant voltage plateau. Therefore the slope variations must be due to the anode. The stoichiometry range of the cathode is set between 0 and one which means that the full range is used. This is reasonable, because LFP and FP are both stable phases. With this assumption, the anode range can be adjusted at low
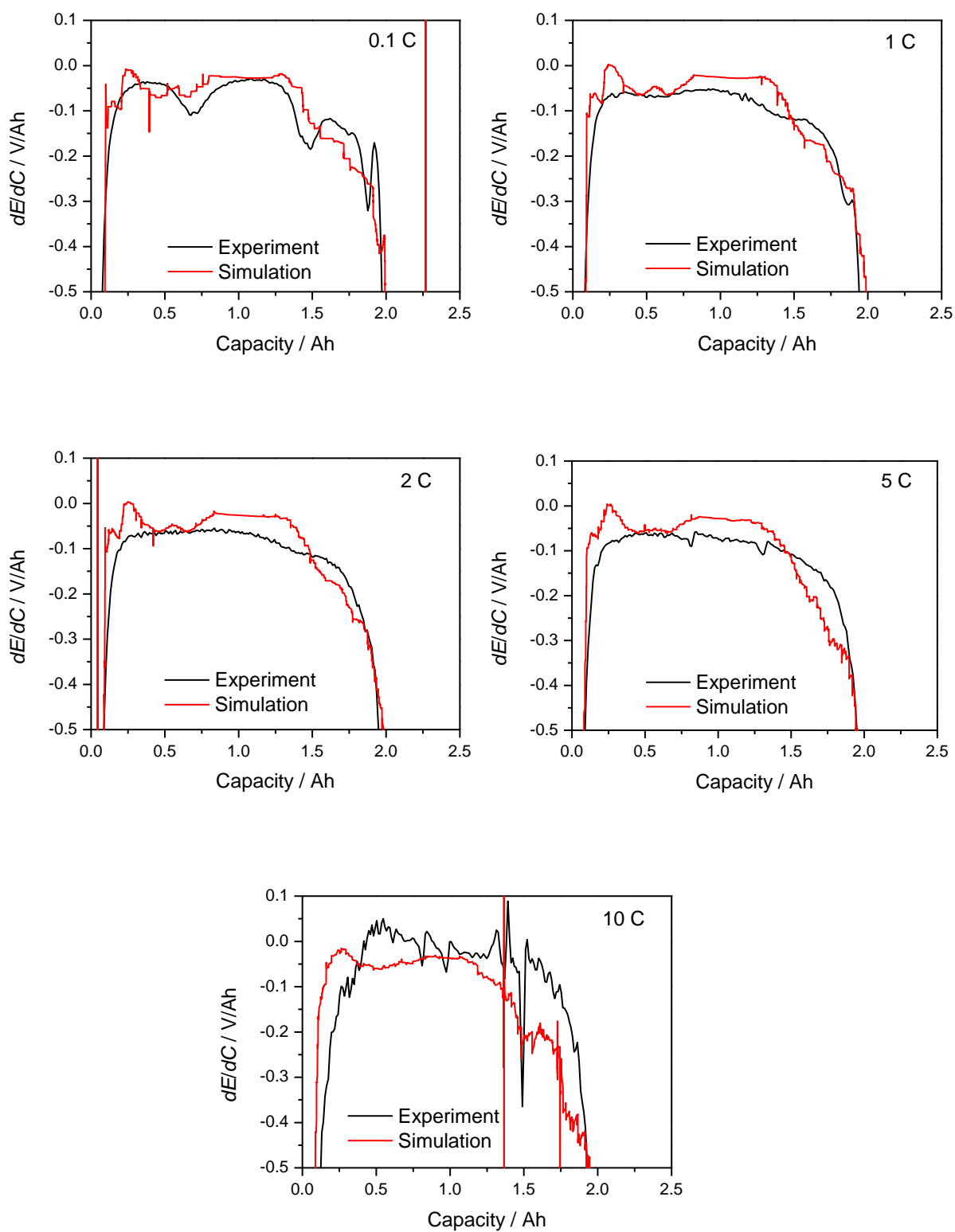
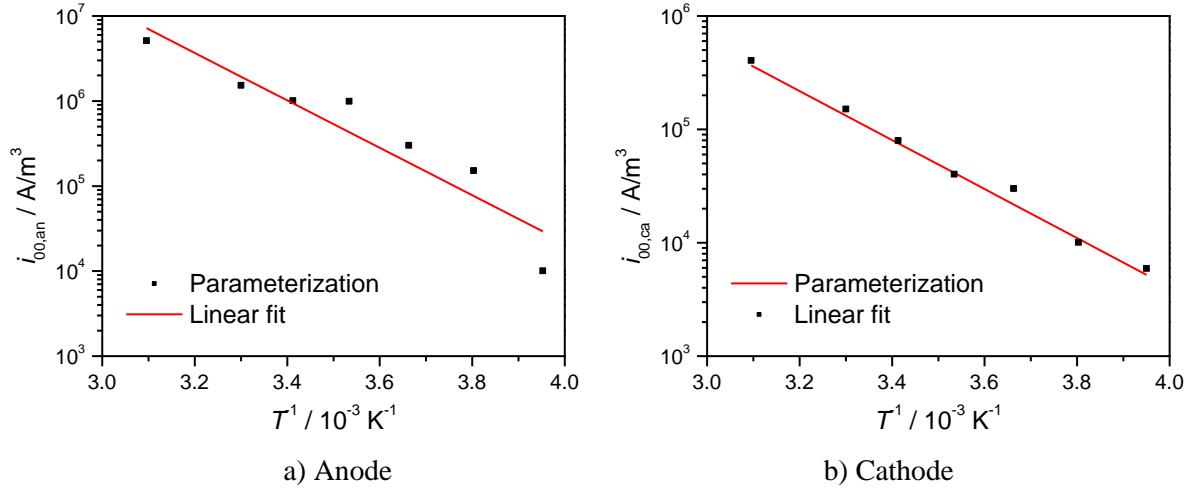Figure 35: Differential cell voltage of experiment and simulation at different C-rates.

Figure 36: Arrhenius fit to determine the activation energy of the electron transfer reactions at anode (a) [148] and cathode (b) [151].

C-rates. While applying low currents, the discharge curve shows characteristic behavior due to the thermodynamics. At higher currents, the kinetic becomes dominant which results in smooth discharge curves without any characteristic slope variations. To estimate the stoichiometry of the anode, the stoichiometry of the cathode was kept constant and the derivative of the voltage with capacity (dE/dC) was calculated to achieve best agreement with the experiments. The results are shown in Figure 35 for different C-rates. The tendency is that less slope variation is recognizable for higher C-rates. The best agreement was achieved by using a stoichiometry range of the anode between 0.57 and 0.01 [148].

The evaluation of the stoichiometry has a strong impact not only on half-cell potential or full-cell potential, but also on heat production due to entropy contributions.

Electron-transfer process. The electron-transfer reaction takes place at the surface of the particles. It is coupled with mass transfer in order to incorporate lithium ions into the active material, or the other way round, to release lithium ions from the host material. Therefore, this process influences the kinetic and the thermodynamic behavior. The kinetic behavior is influenced by this reaction due to the appearance of the activation overpotential. If the electron-transfer process is decelerated, the activation overpotential becomes higher leading to lower cell voltages in case of discharge. If the battery is charged, the cell voltage becomes higher due to this effect. Furthermore, this reaction contributes to heating due to the change of the reaction entropy. The latter depends on the entropies of each species included in the reaction according to,

$$\Delta_R S = \sum_i \nu_i s_i \quad , \tag{71}$$

92

where s_i is the molar entropy of species i and v_i the correlating stoichiometry factor. The molar entropies are given for each half-cell material in chapter 4.2.1.

In case of using global reaction kinetics, the adjustment of the exchange current density i_{00} and the activation energy E_{act} is done by the following procedure. First, the exchange current density is fitted to the experimental discharge curves at room temperature for all C-rates. Only when a good agreement was found, the parameters were made temperature dependent. At each temperature, varying between −20 °C and 50 °C, the exchange current density for both anode and cathode are fitted to get the best agreement with the experimental discharge curves. Here, the 1C discharge curves at different temperature were used. Obtaining different values for each temperature and each electrode, an Arrhenius ansatz is chosen to estimate the activation energy (cf. Figure 1 and Figure 32). The results for each electrode are shown in Figure 36 [148,151]. The parameters are given in Table 5.

It has to be mentioned that all effects, such as surface adsorption, bulk diffusion or phase transition, are lumped into the electron-transfer reaction. This is an appropriate method if only global behavior is relevant, like discharge curve or thermal characteristics. However if all effects should be reproduced time-resolved, as in the case of impedance spectra, then all effects have to be described individually and coupled.

Electrode balancing.   The battery has a capacity of 2.3 Ah. The electrodes must be balanced to obtain the same capacity. The density of each active material is used as adjustable parameter while the state of charge (SOC) suits as checking parameter. The value must fulfill the condition that at the beginning of the simulation the SOC is 100 % and reaches the 0 % at the end of discharge. This must be valid for anode and cathode. Therefore the density of the anode was found to be 2420 kg/m³ and of the cathode 1440 kg/m³. In literature the value of the graphite's density varies from 2250 kg/m³ for natural graphite to $1800 - 2100$ kg/m³ for amorphous graphite [159]. The value of the simulation is slightly higher. This can be explained by the fact that a mixture of carbons is used in the electrode of the anode, such as natural graphite, MCMB 750 and carbon black. This means that lithium can be stored by insertion into the electrode and by adsorption onto surfaces of various carbons. Due to this the storable amount of lithium increases, compared to the value of the literature. For the cathode different values can be found in literature. For FP the density spread between 2740 kg/m³ and 2580 kg/m³ [159]. For LFP the density is given as 3600 kg/m³ by Li et al. [16]. The value in the simulation is lower than in literature. Higher values and values from literature were tried but it resulted in an ending of the discharge curve at a capacity over 10 Ah. Other parameters

were changed while keeping density values from literature to decrease the capacity. But no parameter was found to compensate this effect. A possible explanation for this might be the limited utilization of a particle. Not all particles or crystals are well connected to electron-leading graphite. Additionally, there is a size distribution of particles within the electrode. This means that not all particles are used equally due to the internal composition of the particles. The minor particles are used within the whole range of SOC in contrast to the major particles. They consist of an agglomeration of crystals and inner boundaries due to crystal growth. Particle fragments which are inside of the major particles and are not connected to the electron-leading material do not contribute to the lithium storage.

Electrolyte. The discharge behavior is influenced by the transport properties of the electrolyte. As shown in chapter 2.5.2, the diffusion coefficients of electrolytes spread over a wide range depending on electrolyte composition, lead salt and its concentration and temperature. To describe the transport processes within the liquid electrolyte, concentrated solution theory was used. Parameters of Valoen et al. were chosen as listed in chapter 4.3.1 [69]. It has to be mentioned that the exact composition of the electrolyte solution is unknown. The main components are EC:EMC with a ratio of 4:6 and the conducting salt is $LiPF_6$ with a concentration of 1.2 mol/l [29]. But further additives are not known as well as their influence on transport processes. An estimation of the influence is not possible and is not available in literature. In general, additives are oxygen-containing molecules which may bond or surround the lithium ions. This leads to different solvation shells and therefore to other diffusion behavior. Also the opening of the solvation shell at the electrode surface to undergo the electron-transfer reaction is influenced by the solvating molecules regarding activation energy to open the shell. This effect influences the electron-transfer process itself. In this case the parameters of the electron-transfer reaction within the current model must be modified. It shows that various parameters depend on each other. If one parameter changes, other parameters must be adjusted. To avoid this, various parameters were fixed using literature data being aware that uncertainties remain.

Diluted and concentrated solution theory. In this work concentrated solution theory (CST) was used to describe the transport of lithium within the liquid electrolyte. It contains interaction between ion and solvent which influences the transport depending on ion concentration and temperature. In previous studies, the diluted solution theory (DST) was used which neglects ion interaction by assuming constant diffusion coefficients. At room temperature and

C-rates up to 2 C no relevant differences between both theories within this simulation could be observed. The discharge curves were nearly the same, in shape and in reaching full capacity. Differences were at higher C-rates. Using DST, the discharge curve had a stronger slope and a slight capacity loss compared to the simulations with CST. Also in impedance spectra a difference was noticeable. Within the frequency range of 10^{-1} Hz to 1 Hz the agreement between experiments and simulation was better using CST than DST.

Bulk diffusion. In case of isothermal simulations of the macro-model, additional investigations were performed regarding bulk diffusion in combination with particle-size distribution (cf. chapter 5.2). As described in chapter 4.3.2, constant diffusion coefficients and diffusion coefficients depending on stoichiometry were used. It has to be mentioned that the stoichiometry range must be the same as it is used in the thermodynamics (cf. section "stoichiometry range").

5.2 Isothermal simulations

5.2.1 General macro-model

Introduction. This chapter presents the results of the macro-model. Table 11 shows an overview of macro-model versions. The model "Macro 1" represents the base model which neglects bulk diffusion or particle size distribution. It is used for thermal simulations which are presented in chapter 5.3 and 5.4. Further investigations are shown in chapter 5.2.2 declared as extended macro-model ("Macro 2 – 5"). It includes an additional scale (bulk diffusion in a particle and particle-size distribution). The results shown there are a link to the micro-model which is presented in chapter 6.

Charge and discharge curves. Charge and discharge curves give information about the maximal capacity and the voltage distribution at different applied currents (C-rates) and temperatures. In this work isothermal and thermal simulations were performed to increase the understanding of the processes taking place and of their temperature contribution. In this chapter isothermal simulations were performed. A comparison of experiments and simulations is shown in Figure 37. The discharge curves start at a voltage of around 3.6 V and end at the cut-off voltage of 2.0 V. The characteristic shape is nearly the same for all C-rates. After applying a current, voltage drops down due to the thermodynamics of the cathode mainly and due to ohmic resistances. Then a flat voltage plateau occurs. This flat voltage characteristic is

Table 11: Overview of macro-model versions

Model name	Anode	Cathode	Chapter
Macro 1	Without bulk diffusion	Without bulk diffusion	5.2.1
	Used for thermal simulations	Used for thermal simulations	5.3, 5.4
Macro 2	Bulk diffusion, constant	Bulk diffusion, constant	5.2.2
Macro 3	Bulk diffusion, SOC dependent	Bulk diffusion, SOC dependent	5.2.2
Macro 4	Bulk diffusion, SOC dependent	Bulk diffusion, SOC and current dependent (Rubber band model)	5.2.2
Macro 5	Bulk diffusion, SOC dependent Particle size distribution	Bulk diffusion, SOC dependent Particle size distribution	5.2.2

due to the cathode material. Smaller voltage variations are due to the anode material. At the end of the discharge the curve drops down to the cut-off voltage. The voltage level of the plateau depends on the applied current: the higher the C-rate, the higher the overpotential and therefore the lower the voltage plateau. All simulated discharge curves show good agreement with experiments regarding aspects discussed above. All discharge curves reach the full capacity of 2.3 Ah. The shape of the curves is nearly the same of the experiments. Nevertheless, some differences can be observed and shall be discussed here. In general, overpotentials are marginal at low currents. Hence the shape of the discharge curve is mainly influenced by the half-cell potentials. The 0.1 C-rate shows a difference in the shape at a capacity between 1.5 Ah and 2.0 Ah. The reason is the half-cell potential of the anode. The real used active material on anode side is unknown. Therefore literature values were used which do not completely fit to the experiments. Further it can be noticed that the shape of the experimental discharge curves changes with C-rate. This can be seen in particular at a 10 C-rate. The simulation shows a negative slope overall. In contrast, the experiment shows a voltage increasing between 0.5 Ah and 1.5 Ah. An explanation for this effect is the temperature rise during operation. The temperature increases by around 40 °C at this C-rate. This temperature rise influences all processes within the battery which results in less overpotentials and therefore in a change of the discharge characteristics (cf chapter 5.3). Furthermore, it can be seen, that the 10 C-rate mismatches the experiment. A possible explanation can be the applied C-rate within the simulation. There, the current is given as current density in A/m². To obtain a reasonable value, the windings were unreeled and the visible surface area was measured obtaining

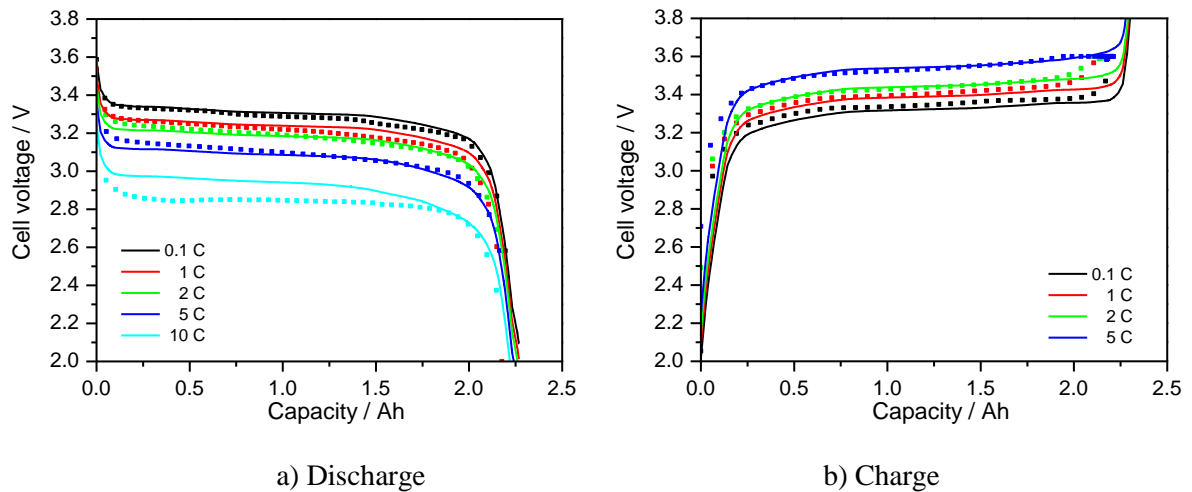a) Discharge   b) Charge

Figure 37: Discharge curves (a) and charge curves (b) at room temperature for different C-rates. Comparison of experiments (symbols) and simulation (solid line).

0.171 m². With this assumption good agreement is achieved up to 5 C.

The experimental charge curves start at around 2.0 V and end at the cut-off voltage of 3.6 V. If the cut-off voltage is reached, the charge procedure changed from constant current to constant voltage. This can be seen at a 5 C-rate. The general curve characteristic is the same for experiments and simulations. They show a strong increase of the voltage followed by the flat voltage plateau. Then the voltage increases again up to the cut-off voltage. A good agreement is achieved at 2 C and 5 C. Comparing experiment and simulation, some differences are recognizable. The simulation shows that the voltage increase at the beginning of the charge is less intense. Also, it underestimates the overpotentials at low C-rates. Furthermore, it shows a strong voltage increase near the final capacity. In contrast, the experimental curves show an earlier and smoother increase of the voltage. Due to the experimental settings, the curves end at the cut-off voltage of 3.6 V. All these effects can be attributed to the thermodynamics, because it occurs at all C-rates and especially at 0.1 C which leads to the assumption that this is not a kinetic effect. Note that the simulation of charge curves neglects the cut-off voltage of 3.6 V. The reason is to show the behavior over the total capacity range predicted by the simulation, and to ensure a comparability of the macro-model and the micro-model. To study the temperature influence 1C-rate discharge and charge curves were recorded. In Figure 38 they are shown in a range between −10 °C and 50 °C. The agreement at high temperatures is very well. Going to lower temperatures, more differences are visible. The experiments show at 10 °C, 0 °C and −10 °C stronger slopes and an earlier voltage decrease to the cut-off voltage and therefore a capacity loss. In contrast, the simulations do not show such behavior. All curves reach full capacity. An assumption is that the influence of the transport properties

97

within the active material becomes more important at lower temperatures. The deceleration of the transport towards or away from the particle surface influences the electron-transfer process. This leads to higher overpotentials resulting in an earlier decrease of the cell voltage. Due to the fact that the macro-model neglects transport within the active material, the simulation does not represent this behavior.
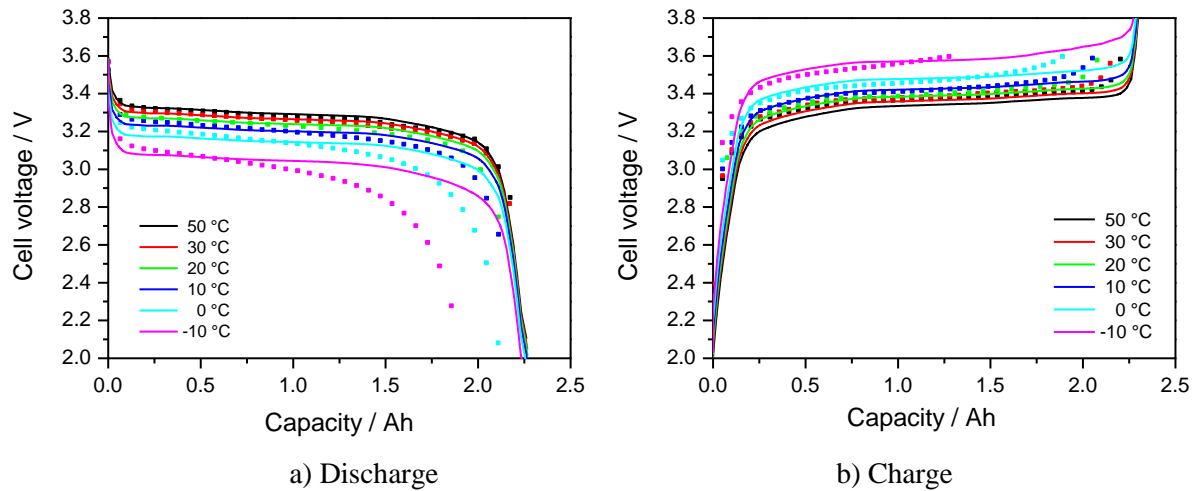

a) Discharge b) Charge

Figure 38: Discharge curves (a) and charge curves (b) at different temperatures at 1 C-rate. Simulations are shown with solid lines, experiments are in symbols.

The charge curves start at a voltage of 2.0 V. After a strong increase of the voltage, the voltage plateau is reached. Depending on the temperature the voltage rises, earlier or later, to the cut-off voltage of 3.6 V. Also here, the simulation shows the behavior in general as the experiment but with some differences. As already mentioned, the thermodynamic data causes differences in the strong voltage increase at the beginning of the charge, in the voltage plateau at high temperatures and in the voltage rise near the final capacity. The difference in the voltage plateau at 10 °C, 0 °C and −10 °C are caused by kinetics. Additionally the simulation does not show an earlier voltage rise due to low temperatures. All curves rise nearly at the same capacity to higher voltages. The reason is the same as given for the discharge curves described above.

Concentration profiles. The advantage of simulation is the ability to look at the processes occuring inside the cell. Figure 39 shows a cross section through a repeat unit. On the left side is the cathode followed by the region of the separator and completed by the anode. This figure shows a snap-shot of concentrations at a 1 C-discharge rate, at room temperature and a capacity of 1.0 Ah. The initial lithium-ion concentration is 1.2 mol/l. It shows that a gradient of the lithium-ion concentration along the repeat unit occurs. Starting from the initial ion con-

centration, the gradient becomes stronger with operation time. The characteristic during a discharge is that the concentration is higher on the anode side and lower on cathode side compared to the initial concentration. Focusing on the process at the anode side first, lithium ions de-intercalate from the active material. They dissolve in the electrolyte leading to higher concentrations. On the cathode side, this process is reversed. The ions, dissolved in the electrolyte, intercalate into the active material. This results in a decrease of the concentration in the electrolyte. The concentration leads to a diffusion process. The concentration profile shows a characteristic shape which can be separated into three sections: anode, cathode and separator. The profile of the latter shows a linear correlation. Here, only diffusion properties influence the transport of ions. On anode and cathode side, the gradient shows a particular profile. This is the combined effect of the diffusion process and the mass transfer at the electrode surfaces.
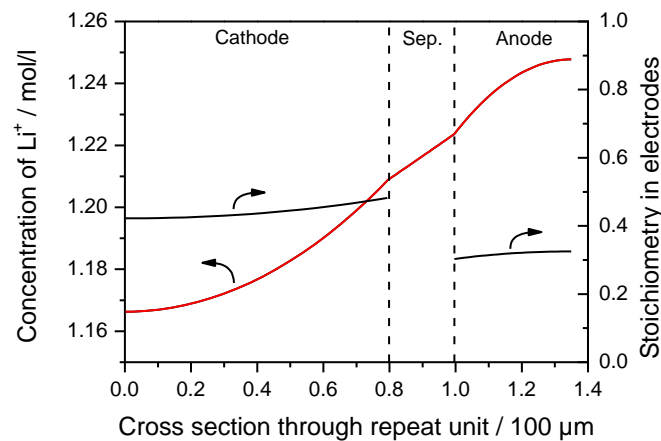
Figure 39: Concentration profiles through a cross section of a repeat unit are shown.

This ion-concentration gradient in the liquid electrolyte influences the concentration of stored lithium ions within the active material (Figure 39, black line). There, a gradient occurs along the electrode thickness, too. The concentration of lithium on the anode side shows a reduced amount near the separator than near the current collector. On the cathode side it is the other way round. Near the separator, the concentration is higher compared to the area near the current collector. Depending on C-rate, liquid electrolyte composition, initial salt concentration and temperature, the transport of ions influences the concentration within the active material. It has to be mentioned that the current distribution (C-rate) also depends on the active surface area of the particles, the (de-)intercalation and electron-transfer processes on their surfaces and the transport related parameters such as porosity, tortuosity and diffusion which affect the actual concentration at a certain area in the electrode. All these processes take place at the same time, so that a change of only one parameter influences all other parameters and therefore the global behavior of a battery cell.

The observation, that a gradient occurs within the electrode active material along one repeat unit, has an immense impact on further discussions concerning SOC determination. In general, the SOC of a whole battery is measured globally depending on total capacity, (dis)charge time and applied current. So, the SOC represents the averaged amount of stored lithium which is available for further discharging. But it does not give any information about the spatial distribution of intercalated lithium ions. Additionally, the distribution depends on temperature variation which occurs under operation, too. This influences the kinetic processes, such as transport and electron-transfer reactions. In turn, they dictate the concentration in the electrodes. For a better visualization an example is given. Regarding a battery cell, different locations are chosen, e.g., a repeat unit near the battery surface and another one in the center of the battery. While operation the battery heats up leading to different temperatures at both repeat units. The temperature influences the kinetics at both locations differently. So, it causes a different utilization of both repeat units leading to different amounts of stored lithium in the active material. The latter can be correlated to the SOC. So in turn, the SOC of both repeat units is different. Additionally, as already discussed above, the concentration of ions in the electrolyte influences the concentration of lithium in the active material, too. This means that the SOC along the thickness of the electrode is different (cf. Figure 39). So, the SOC is a function of location. Furthermore, the aging of the battery and the cycle history influence the SOC, but this is not regarded in this work.

In the following, the influence of current on the concentration of lithium in the electrodes is studied. As already remarked, the balancing of each electrode is important to fulfill few conditions. One condition is that the electrode must start at a certain stoichiometry and end at the capacity given by the experiments. Figure 40 shows the balancing of the anode (left) and the cathode (right) at a 1 C discharge at room temperature. The anode stoichiometry starts at 0.57 and reaches the stoichiometry of 0.0 at a capacity of 2.2 Ah. The cathode stoichiometry starts at 0.0 and reaches the full capacity at 1.0 (cf. chapter 5.1. section "stoichiometry range"). In Figure 40, different representative compartments along the electrode thickness are shown. They show a spreading with a characteristic distribution at certain stoichiometry points. At the anode, changes in the distribution are noticeable at a stoichiometry of around 0.4 and 0.2. For the cathode, it is at the stoichiometry of 0.9. These changes can be attributed to the thermodynamics of each active material. At these stoichiometry points, the half-cell potentials of each material change and thereby the contribution of the activation energy (cf. equation 22). The latter influence the electron-transfer reaction included in the Butler-Volmer expression. Hence, the kinetics is coupled with the thermodynamics which results in a merging of the

stoichiometry of different particles controlled by the thermodynamics. It could be described as a kind of communication or interaction between particles which was also mentioned by Dreyer et al. [21].
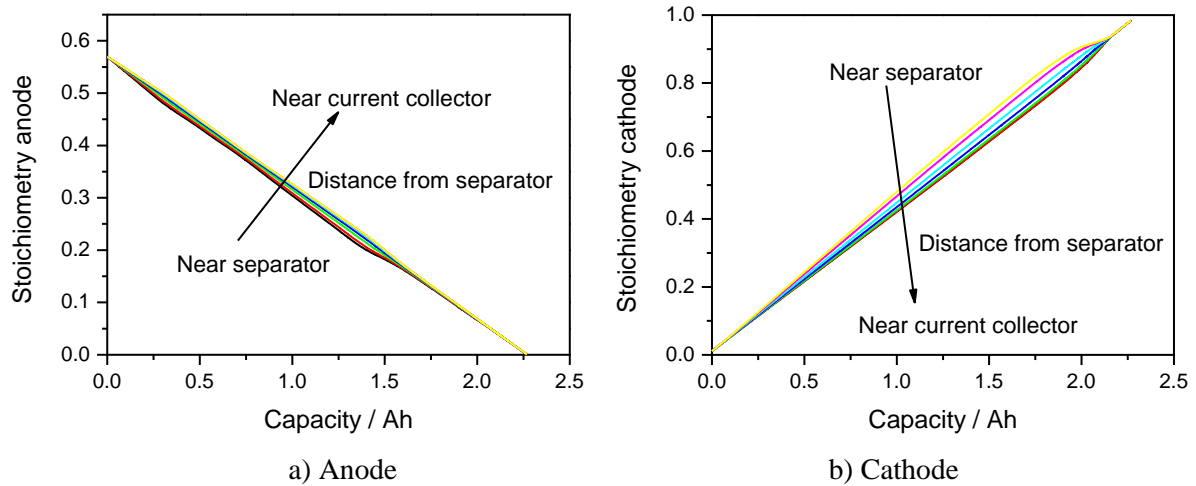

a) Anode

b) Cathode

Figure 40: Stoichiometry change for anode (a) and cathode (b) during discharge at 1 C. Seven representative locations for each electrode are chosen.
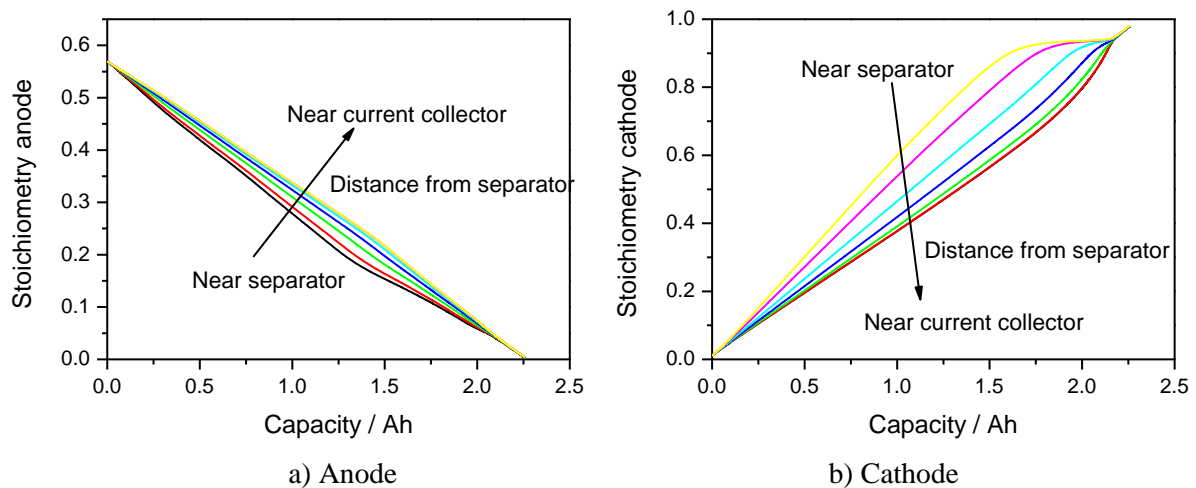

a) Anode

b) Cathode

Figure 41: : Stoichiometry change for anode (a) and cathode (b) during discharge at 5 C. Seven representative locations for each electrode are chosen.

To illustrate the characteristic behavior again, the electrode balancing is shown in Figure 41 for a 5 C-rate. The characteristic stoichiometry behavior is noticeable, too. The difference is the wider distribution due to a higher C-rate of 5 C. Anode and cathode have in common that the change of stoichiometry is the fastest in the particles near the separator. The wider the particles are far from the separator the less intense is the change. The reason is the lithium-ion gradient within the liquid electrolyte with its transport properties. Higher C-rates cause a stronger gradient. Because the electron-transfer reaction is not the rate-limiting process, the spreading of the concentration occurs along the electrode thickness.

Concerning the interaction between mass transfer and diffusion process in the electrolyte, another behavior can be observed in the simulations. If the electron-transfer reaction is assumed to be not rate limiting and to be very fast, and the diffusion of ions in the electrolyte is assumed to be very slow, then a starvation process takes place. In case of discharge, this is observed at the cathode side. The electrode intercalates lithium ions faster than the diffusion process can deliver. It results in a decrease of the lithium ions in the electrolyte reaching the concentration of 0.0 mol/l. In doing so, the simulation shows a strong increase of overpotential which leads to a strong decrease of the cell voltage reaching the cut-off voltage. This implies that not the full capacity can be used for operation. In the experiment, such a behavior was not observed. It can be assumed that this may happen at very high C-rates and this starvation is a reversible effect. But further statements cannot be given concerning safety, aging and other undesired reactions.

Overpotentials.   During operation, the measured cell voltage is different compared to the voltage at equilibrium. This difference is described as the sum of different overpotentials due to diverse kinetic processes. Overpotentials occurring at a 1C-discharge are shown in Figure 42. The overpotential due to ohmic resistance caused by current collectors, contact resistances, etc. is constant over the whole discharge time.
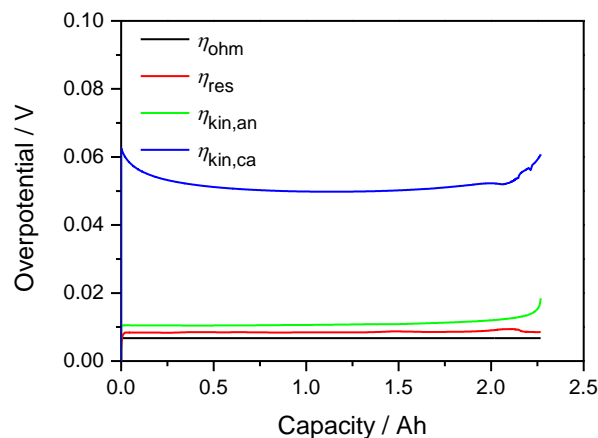

Figure 42: Overpotential contributions at 1C discharge versus capacity.

The next overpotential, which is slightly higher, is due to resistivity caused by the ion-concentration gradient in the electrolyte (cf. Figure 39). Depending on this gradient the overpotential rises quickly and is nearly constant up to the end of discharge.

More important and contributing to the total overpotential, there is the overpotential due to kinetic processes at the electrodes. This includes effects due to concentration variations and electron-transfer processes. The first one is correlated to the concentration overpotential and

the latter to the activation overpotential. Both combined are named as kinetic overpotentials in Figure 42. The concentration overpotential at the anode is around 0.4 mV and at the cathode around 0.8 mV. Due to this small difference, both combined are shown in Figure 42, named as kinetic overpotentials. Here, the kinetic overpotential of the cathode is immensely more dominant than that of the anode. The anode shows a nearly constant overpotential. But at the end of discharge, it rises slightly. The cathode shows the same behavior at the end of discharge which is an increase of the overpotential. But in contrast to the anode, the cathode shows a decrease of the overpotential at the beginning of the discharge. This relaxation ends at around 1 Ah followed by an increase lasting to the end of discharge. The relaxation can be attributed to the gradient of lithium ions in the electrolyte. The transport of the ions and the electron transfer are strongly coupled. Starting from a homogenous concentration of 1.2 mol/l, a gradient occurs. Due to the fact that transport of ions in the electrolyte is relatively faster than the electron transfer, the overpotential is shrinking.

The rise of both overpotentials at the end of discharge (2.0 Ah) is due to the spreading of the concentrations in the active material (cf. Figure 40). At the end, more and more locations along the cathode thickness reach the stoichiometry of around 95 % (cf. Figure 40) which results in a strong rise of the overpotential. This can be explained by the correlation between the local potential of the bulk material, which depends on stoichiometry, and the activation overpotential described in equation 22. At this stoichiometry point the potential of one location changes. This leads to a decrease of the activation overpotential for this location and thereby to a decrease of the current at this location described by the Butler-Volmer expression in equation 28. To ensure the total applied current, the current distribution must be transferred to other locations along the electrode whereby their activation overpotentials rise and thereby the kinetic overpotential in Figure 42. The same explanation is valid for the anode, regarding the spreading of the concentrations at a capacity of 1.5 Ah (cf. Figure 40).

Impedance spectra.   Simulation of impedance spectra enables the opportunity to look at the occurring processes in more detail. All processes are time-resolved and therefore they can be attributed to certain processes taking place. Because the SOC plays an important role, impedance spectra are taken at different SOC as described in section 3.4. Simulations were done at the same SOC and are shown in Figure 43 as Bode plots. The experiments are displayed as symbols and the simulations are shown as solid lines. Both figures show that a strong difference between simulation and experiment exists. In general, the impedance spectra can be separated into three parts regarding the frequency. The first part is the high-frequency range

(HFR) between 10^3 and 10^5 Hz. This part can be attributed to ohmic resistances. The second part, which is between 1 and 10^3 Hz and is nominated in following work as mid-frequency range (MFR), is dominated by the electron-transfer processes. The third and low-frequency range (LFR), which is lower than 1 Hz, shows slow processes like diffusion.
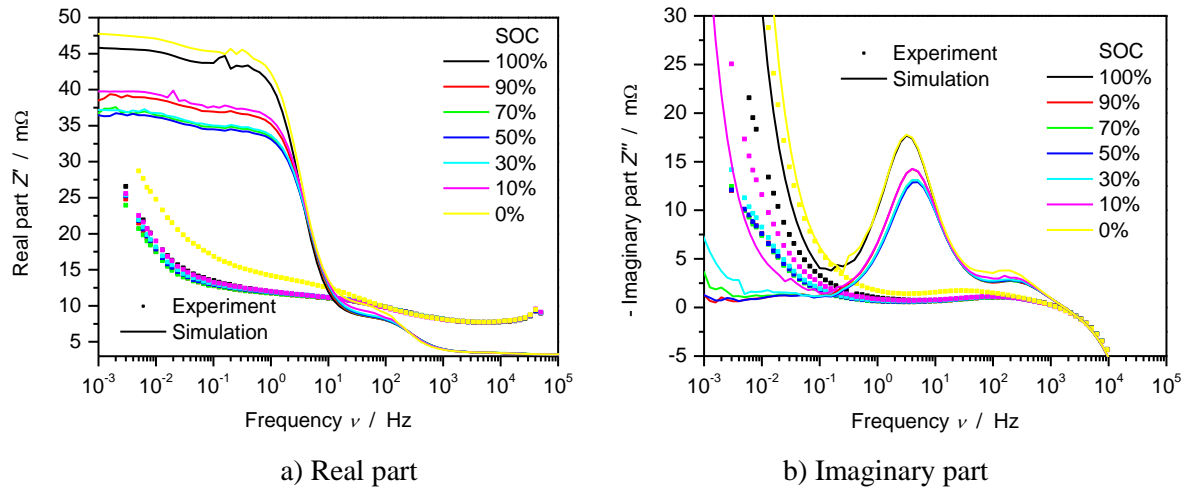

a) Real part   b) Imaginary part

Figure 43: Impedance spectra in form of a Bode plot: real part (a) and the imaginary part (b) versus frequency. Comparison between experiments (symbols) and simulations (solid lines).
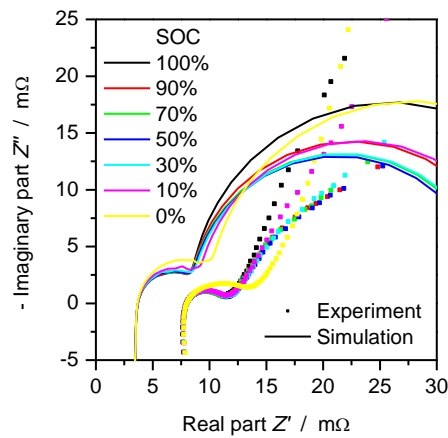
Figure 44: Impedance spectra in form of a Nyquist plot: Comparison between experiments (symbols) and simulations (solid lines).

In principle, the simulation shows the same trend as the experiment. Coming from high frequencies the real part of the impedance increases step by step. The increase is in the same frequency ranges as the experiment, but the magnitude is overestimated. Compared to the experiment the ohmic resistance of the simulation is too low in the HFR. In the MFR, the electron-transfer reactions are not described correctly. In the experiments, a smooth resistance increase is noticeable coming from higher frequencies. This increase is due to electron-transfer processes which occur at both electrodes to the same time. This results in an overlap

of the resistances of both electrodes. A separation of both contributions cannot be done in the experiments. In contrast, the simulation shows a small resistance increase at around 100 Hz and a strong increase at 10 Hz. The lower increase can be attributed to the anode, which has a high value as exchange current density used in the Butler-Volmer equation. The higher increase at around 10 Hz is due to the contribution of the cathode. The exchange current density is lower compared to the anode. This results in a higher resistance regarding the electron-transfer process. Here, the simulation predicts a strong increase of the impedance which overlaps small contributions of other processes. It has to be mentioned that the electron-transfer reaction on the cathode side is the most dominant parameter in the battery simulation using the macro-model. This parameter influences the impedance spectra and (dis-)charge curves. Regarding the discharge curves, it influences the height of the cell-voltage plateau at different C-rates. This is due to the activation overpotential. The higher the exchange current density is, the lower is the activation overpotential. If the activation overpotential is too low, the plateau of all discharge curves at different C-rates shift to higher voltages leading to a smaller spreading of the discharge curves with applied current. Additionally, this parameter influences the temperature contribution. An increasing overpotential leads to higher heat production and therefore to higher temperature. Inspite of these lacks described above, the exchange current density is set to this value obtaining a good agreement in discharge curves and thermal calculations. In the LFR the simulation shows an additional small increase of the impedance at around 0.01 Hz. Within this time frame the impedance is dominated by diffusion processes, which here is the occurrence of a concentration gradient in the liquid electrolyte.

Compared to the real part of the impedance, the imaginary part shows a better agreement with the experiments. In the HFR the inductive behavior is well described by the model. Differences are observable at the MFR, where the electron-transfer processes take place. As described above, two characteristic peaks visualize the contribution of both electrodes. The peak at 500 Hz can be attributed to the anode. The more distinct peak at around 100 Hz is due to the cathode. The height of these peaks correlates to the size of the exchange current density. The peak decreases with increasing value. Also, this indicates that the influence of the electron-transfer process of the cathode is more dominant than that of the anode. Analyzing the LFR, a controversial situation can be found. At a SOC of 100 %, 10 % and 0 %, the simulation predicts the same behavior, as seen in the experiments. The capacitive resistance increases strongly coming from high frequencies. In contrast to the experiments, the other SOC, namely the SOC between 90 % and 30 %, show no or only a slight increase of the capacitive resistance at low frequencies, which are lower than 10^{-2} Hz. This effect can be attributed to

SOC itself. If the electrodes are completely filled or emptied which is the case at 100 % and 0 %, the resistance increases at around 0.1 Hz. Here, the simulation and the experiments show a good agreement. The effect is due to the thermodynamics that the resistance increases at a SOC of 10 %. In general, the impedance spectra are sensitive to the slope of the thermodynamics. The characteristic behavior of a LFP containing battery is the flat cell voltage. Due to this plateau, all impedance spectra between SOC of 90 % and 30 % have nearly the same shape. To proof this assumption, simulations were performed wherein the thermodynamics were changed having a slope instead of a constant voltage. The result was that it also influenced the impedance spectra at the mid-SOC range showing an increase of the resistance at the LFR.

The same results are shown in Figure 44 but in form of a Nyquist plot. Here, the real and the imaginary part are plotted against each other. Each occurring process forms a semi-circle. Due to the same time range in which the processes happen an overlap may takes place. This makes an interpretation difficult and needs further knowledge coming inter alia from Bode plots, such as frequencies. It can be noticed that the simulation and the experiments have the same tendencies. They show a stretched semi-circle at low resistances and a big one at higher resistances. The latter depends clearly on the SOC. Going more into detail, the first semi-cycle starts at 4 mΩ for simulations and at 7 mΩ for experiments. This is due to different ohmic resistances. As already seen in the Bode plots, this leads to a shift of all impedance curves. The first semi-circle consists of two overlapping semi-circles from the anode and cathode. This arc can be correlated to the MFR in the Bode plots. The next arc belongs to the LFR.

If the Nyquist plot shows a slope of +45° instead of this semi-circle, it is a so-called Warburg impedance which describes diffusion processes normally. This behavior is not really distinctive in the experiments and it is not reproduced by the simulation. This means that diffusion may take place but it is not the rate-limiting process. Therefore, it can be concluded that other processes are more dominant and are highly SOC dependent. Experimental results show this SOC correlation which is not the case regarding the simulations. The latter show a big semi-circle which is SOC dependent, indeed. But the radius of the arc is too small which means that the resistance is too low. Regarding the impedance spectra, it can be said that all processes are in the same time range and not far from reality. Further adjustments are necessary to get a better agreement with the impedance spectra.

Sensitivity analysis.   To estimate the influence of parameters on the result, a sensitivity analysis was performed. This is done for each parameter used in the simulation. The method-

ology is originally presented by Vogler et al. and applied here [160]. The target parameter was the cell voltage at a capacity of 1 Ah of a discharge curve with applying a 1 C-rate. Each model parameter P_i was consecutively increased by 0.1 % from its reference value P_i^0 to P_i^+. The resulting relative change in the cell voltage $\delta E = (E^+ - E^0)/E^0$ is related to the relative change in the parameter $\delta P_i = (P_i + - P_i^0)/P_i^0 = 0.01$. The factor $f_{rel} = \delta E/\delta P_i$ is the relative sensitivity of the cell voltage with respect to changes in parameter P_i. If the relative sensitivity has a positive sign, this means that the cell voltage is higher than the reference cell voltage. If the value is negative, this means that the cell voltage is lower compared to the reference cell voltage. A value of $f_{rel} = 1$ signifies direct proportionality between model parameter and simulation target. A notable sensitivity of the model parameter (say, $f_{rel} \geq 0.01$) means that the associated physico-chemical process is rate-determining.

In Figure 45 the sensitivity analysis for the macro model is shown. It is separated into three parts: the anode, the separator and the cathode.

At the anode the most important influence shows the change of the activation energy of the Butler-Volmer equation (BV). An increase shows a significant decrease of the cell voltage due to higher activation overpotential. Further negative influences are the change of the factors b and c of the BV. They also increase the activation overpotential which leads to a decrease of the cell voltage. Positive values can be achieved by increasing the stoichiometry range. Especially the increase of the maximum stoichiometry results in a higher cell voltage, because the half-cell potential drops down later then. Also a positive result can be achieved, if the density or the electrode thickness is increased. Both parameters lead to a higher lithium content and therefore to a slower change of the stoichiometry resulting in a higher half-cell potential.

At the cathode there is one dominant parameter, which is the activation energy of the BV. The effect is the same like on the anode side. Beside other parameters, two parameters have a positive influence, which are the exchange current density and the electrode thickness. The increase of the first parameter reduces the activation overpotential. This results in a higher cell voltage. Changing the latter parameter the lithium content increases within the electrode. Having a constant density, the stoichiometry changes more moderately resulting in a higher cell potential. It has to be mentioned that the increase of the electrode thickness leads to a stronger gradient of lithium ions within the electrolyte. This increases the overpotential, usually. In this simulation the change is too small that this gradient effect has a consequence on the cell voltage. It can be assumed that this will happen if the thickness is increased drastically.
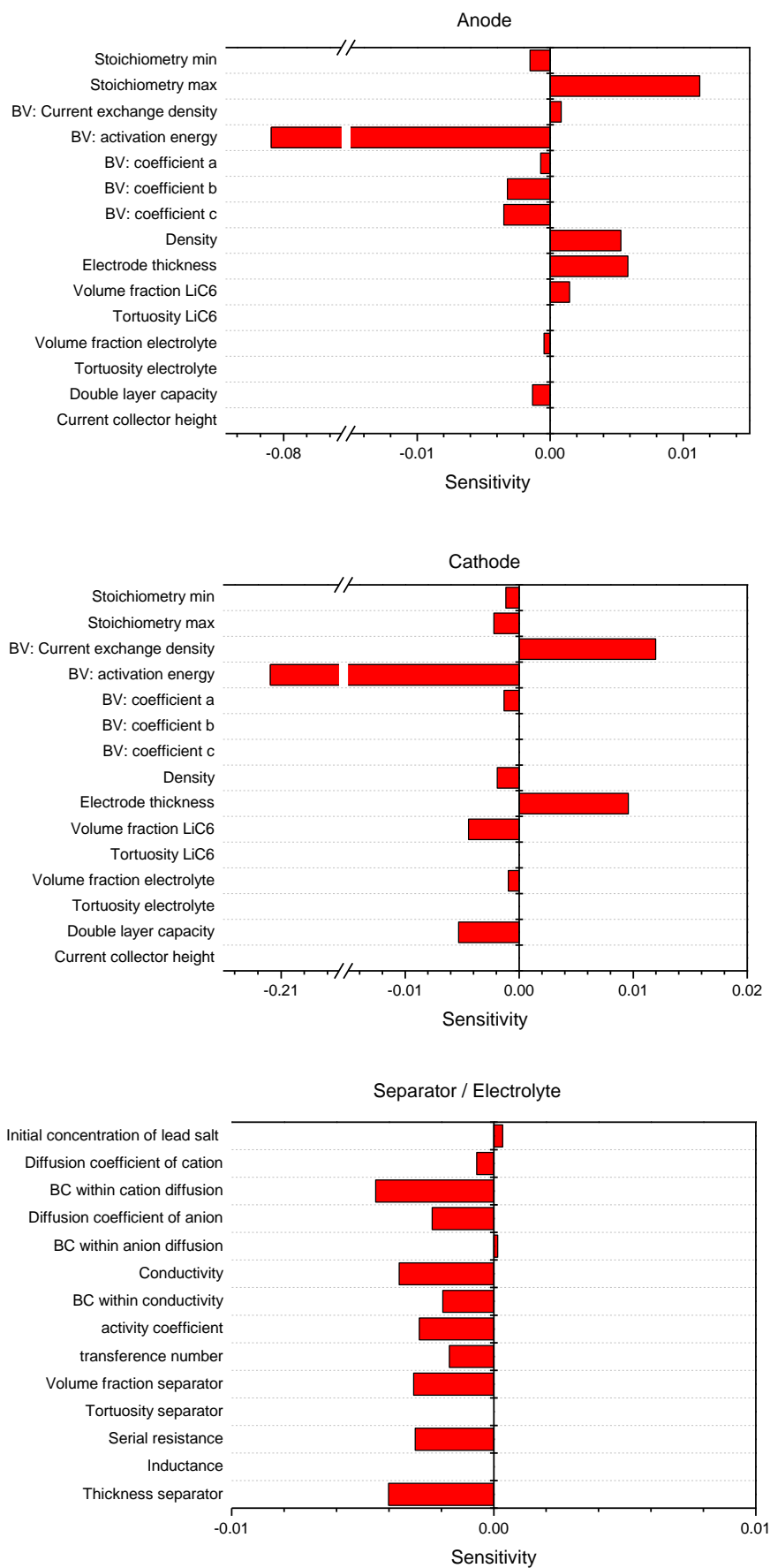
Figure 45: Sensitivity analysis. BV means Butler-Volmer equation, BC means Bruggeman coefficient.

Within the region of the separator especially the parameters of the separator itself and these of the ion transport in the electrolyte are the most important. It can be seen that all parameters have no strong influence on the cell voltage. The change of the concentration of the lead salt increases f_{rel}, because the conductivity rises. Further changes of other parameters show a negative influence such as thickness and volume fraction of the separator. Both influence the transport of ions. Therefore the gradient becomes stronger which results in a decrease of the cell voltage. Furthermore, changes of parameters belonging to transport, such as diffusion coefficients and correlating Bruggeman coefficients (BC), reduces the cell voltage by decelerating the ion transport in which the gradient becomes more intense. Furthermore, the increase of the serial resistance decreases the cell voltage, too.

5.2.2 Extended macro-model

Relationship between impedance and polarization characteristics. The simulation presented above show good agreement in discharge curves, but it predicts different behavior in impedance spectra compared to the experiments. Further model variations were performed to obtain better agreement. The focus was on impedance spectra, because it could be expected that all discharge curves fit well if all time-resolved processes were reproduced accurately. Unfortunately, gaining good agreement in impedance simulation was difficult. Regarding the Bode plot, good agreement could be obtained in the HFR and MFR up to a frequency of 1 Hz. This includes ohmic resistances and electron-transfer processes. The challenge is the LFR where slow processes take place, like diffusion. Especially this region shows a strong variation with SOC. It has to be mentioned that this LFR is difficult to describe, because there is a transition between a mode of alternating current and a continuous charging-discharging mode. The Bode plots show that all curves rise to higher resistances at a frequency of 1 mHz. Here, the duration is 1000 s which correlates to a constant current for around 15 min. Therefore, this implies a change of the SOC. Again, this has an effect on the electron-transfer process, especially when the electrodes are nearly filled or emptied. This is observable in the impedance spectra for the curves at a SOC of 0 %.

Diffusion coefficients. The LFR was in focus of research for a better understanding of the battery function. Due to the fact that this region can be allocated to slow processes, bulk diffusion was included into the model on both electrodes [148]. First, a constant diffusion was assumed (cf. Table 11, "Macro 2"). Using 10^{-14} m²/s for the anode and 10^{-18} m²/s for the cathode, no good agreement with impedance spectra could be found and still with a lack of

109

agreement in discharge curves. In the impedance spectra, the curves in the LFR showed no rise to higher resistances and discharge-curve simulations show less overpotentials with increasing C-rate.

Then, diffusion coefficients were chosen that depend on stoichiometry (cf. Table 11, "Macro 3") [148]. Levi et al. reported such behavior for graphite [155]. This was applied for the simulation. No better agreement was found in the impedance spectra, but the discharge curves showed a slightly better agreement concerning the slope. With decreasing coefficient the slope becomes more negative and with increasing the other way round. Due to the fact that the diffusion coefficient of Levi et al. shows a distinctive dependence on stoichiometry, changes in the slopes of simulated curves were also recognizable which fitted better to the experiments.
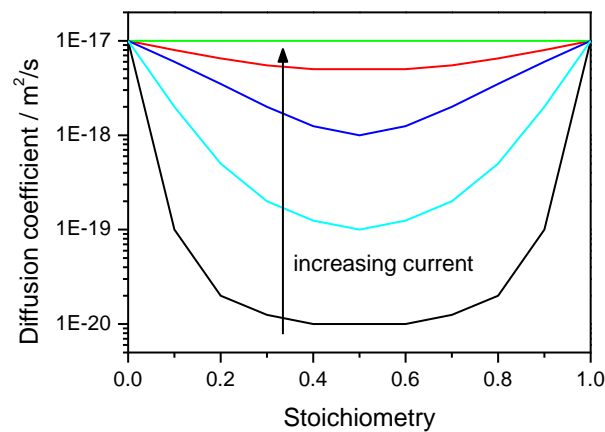
Figure 46: Sketch of the „rubber-band model".

Also, a stoichiometry depending diffusion coefficient was used on the cathode side. Safari et al. reported that the diffusion is extremely low (around 10^{-20} m²/s) in a range between a stoichiometry of 0.1 and 0.85 [103]. Between 0.0 and 0.1 and between 0.85 and 1.0, the coefficient rises up to 10^{-18} m²/s. The total change of the diffusion coefficient along the stoichiometry can be described having the shape of the letter "u" (Figure 46). Applying this no better agreement could be achieved neither in discharge curves, nor in impedance spectra. Stretching the u-shape to lower values, like 10^{-22} m²/s at stoichiometry of around 0.5, while keeping the value of 10^{-18} m²/s at the borders, an agreement could be found for impedance spectra. But the discharge curves showed at increased C-rates a stronger slope in the region of the plateau. Furthermore, the total capacity could not be reached, because the overpotentials became too strong, so that the curve dropped down at a capacity less than 1.0 Ah. At this point, the conclusion was that the diffusion coefficient has to be around 10^{-18} m²/s for discharge curves and around 10^{-22} m²/s for impedance spectra. To match both specifications, a so called "rubber-band model" was developed (cf. Table 11, "Macro 4"). This is a current-dependent model

which is sketched in Figure 46. It includes that at low C-rates the diffusion coefficient has an "u"-shape along the stoichiometry. At high C-rates, the value is constant at 10^{-18} m²/s. In between, the shape of the "u"-form becomes less intense, which means that, with increasing current, the diffusion coefficient has lower variation. The adjustment of this variation had to be done in this way that an agreement in discharge curves could be achieved for all C-rates. In doing so, the result was that the original function of the diffusion coefficient could be used at 0.1 C. For all other C-rates, the diffusion coefficient was nearly constant while obtaining not the best fits in discharge curves. The behavior could better be described as a switch: currents above 1C needed constant diffusion coefficient and below a variation. All in all, the conclusion was that there are other reasons for this behavior instead of diffusion.

Particle sizes.   Safari et al. reported a particle distribution at the cathode [103]. The particle size spread over a range between 15 nm and 370 nm. They measured that most particles have a size of 50 nm. Their d_{50}-value of this distribution is around 73 nm which means that this is the average particle size. In our model the size of the particle is 74 nm. Simulations were performed with different particle sizes combined with various diffusion coefficients (cf. Table 11, "Macro 5") [148]. In one case, different particle sizes were chosen with constant diffusion coefficients. In another case, different particle sizes were chosen with stoichiometry-dependent diffusion coefficients. Furthermore, a particle-size distribution along the cross-section of the electrode was considered including a stoichiometry dependent diffusion. In that case, various particle sizes were randomly distributed along the electrode.

Here, five particles were assumed which alternate in size and location along the cross section of the electrode. For the anode the particles have a radius of 12 µm, 8 µm, twice 3.58 µm and 2 µm. For the cathode the radius of the particles is 20 nm, 27 nm, 37 nm, 37 nm and 50 nm. In this order, the particles are stringed along the *y*-axis. When using more than five discretization compartments the size iterates in the same order. The order of the particles is given in Table 12 for anode and Table 13 for cathode. There, five different particle distributions (PD) are given exemplarily to vary the location of particles along the cross section. Furthermore, bulk diffusion is included wherein the diffusion coefficient depends on stoichiometry. Literature data by Levi et al. for the anode [155] and Safari et al. for the cathode [103] were used which were described in chapter 4.3.2. To visualize the effects more explicitly, the discretization was lowered to seventeen compartments per electrode. Using the PD_{an} A and the PD_{ca} A as reference, the influence of the PD on discharge curves is shown in Figure 47. There, the 0.1 C-rate is not affected, because kinetic processes are not rate-limiting so that there is the same result

Table 12: Anode	Position of particle within order [148]				
Particle radius / μm	12	8	3.58	3.58	2
PD$_{an}$ A	1	2	3	4	5
PD$_{an}$ B	2	3	4	5	1
PD$_{an}$ C	3	4	5	1	2
PD$_{an}$ D	4	5	1	2	3
PD$_{an}$ E	5	1	2	3	4

Table 13: Cathode	Position of particle within order [148]				
Particle radius / nm	20	27	37	37	50
PD$_{ca}$ A	1	2	3	4	5
PD$_{ca}$ B	2	3	4	5	1
PD$_{ca}$ C	3	4	5	1	2
PD$_{ca}$ D	4	5	1	2	3
PD$_{ca}$ E	5	1	2	3	4
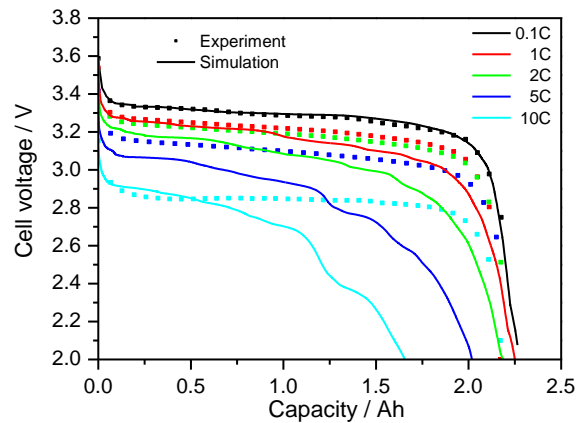
Figure 47: Influence of different particle sizes on discharge curves.

as without different particle sizes and bulk diffusion. However, if the current is increased, the shape of the curves are strongly influenced by the particle size including bulk diffusion. Characteristic voltage losses can be found which results in an earlier achievement of the cut-off voltage. Furthermore, it can be seen that specific voltage losses are shifting to lower capacities with increasing C-rate. For example, a voltage loss can be seen at a 1 C-rate at 1 Ah. At a 2 C-rate, the loss is at around 0.6 Ah and at a 4.6 C-rate, the loss is at 0.5 Ah and so on. Also, at a 10 C-rate, characteristic losses can be found at 1.2 Ah and at 1.5 Ah. These losses are recognizable in a 4.6 Ah-curve, too. To clarify the behavior, the PD was changed for one electrode while keeping the PD A of the other electrode.

112
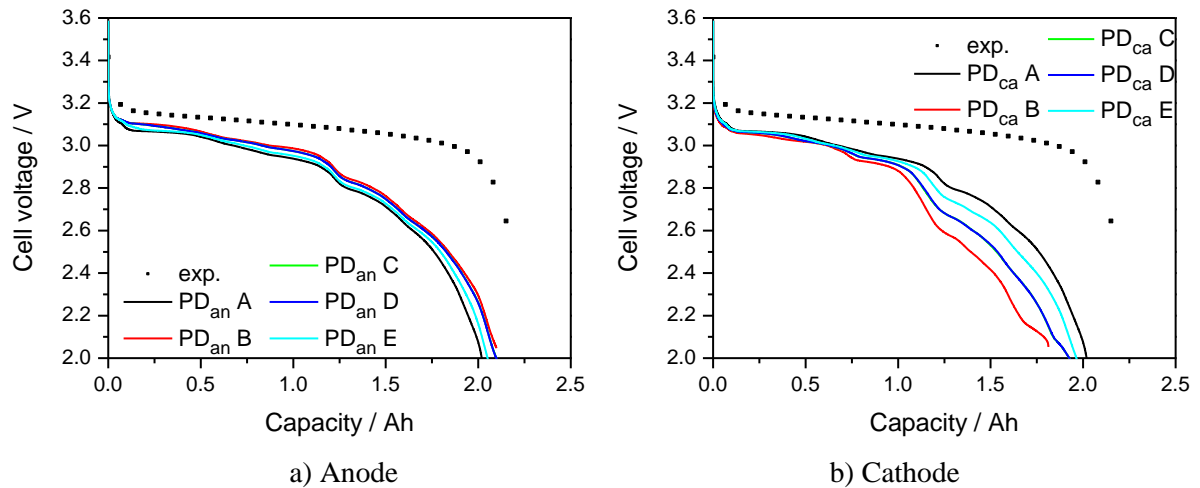
a) Anode   b) Cathode

Figure 48: The influence of a particle-size distribution for anode (a) and cathode (b) on a 5 C-rate discharge curve.
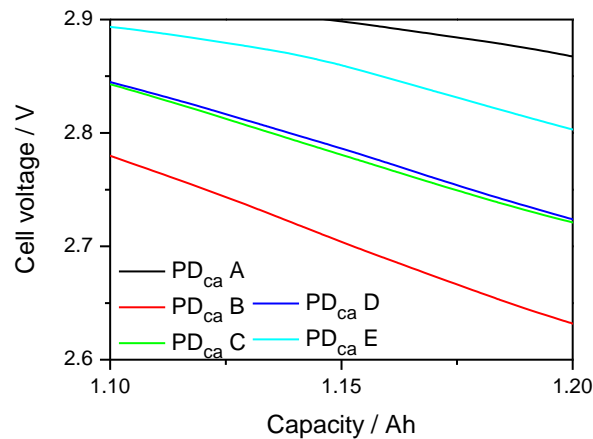

Figure 49: Zoom of the discharge curves to visualize differences between PD_{ca} C and D.

Applying a 5 C-rate, the results are shown in Figure 48. The simulated discharge curves show a strong difference to the experiments. They show stronger slopes overall and reach earlier the cut-off voltage. Also, they show distinctive voltage steps, e.g. at 1.25 Ah. Depending on the location of the particles, which is defined by using different PD (cf. Table 12 and Table 13), the curves show a spreading. This is less intense for the anode compared to the cathode. It has to be mentioned that for both electrodes the discharge curve using PD C is overlapped by the curve of PD D. There are small differences which are exemplarily shown for the cathode at a capacity of 1.15 Ah in Figure 49. Depending on location, a turning-point in a discharge curve occurs. The reason is the correlation between particle size and diffusion. If this process is too slow to free vacancies for adsorption of lithium ions, the electron-transfer is hindered. This results in an increase of overpotenials which lead to a breakdown of the cell-voltage. In general, voltage losses are higher as the particle size increases. Also, no better agreement for impedance spectra could be found which is not shown here.

5.3 Thermal simulations

During operation the battery performance is subject to thermal influences. Different ambient temperatures and internal heating lead to changes of the cell voltage. In the following section the macro-model considers heat generation in the electrodes, heat transport across the windings and heat dissipation at the battery surface as described in chapter 4.4 used model "Macro 1" in chapter 5.2 (cf. Table 11) [151,161]. Explicitly, bulk transport in active materials is not included. The conditions and their influence are explained in more detail in the following chapter.

5.3.1 1 C-rates at different ambient temperatures

The external temperature has a strong influence on the battery performance. In Figure 50, charge and discharge curves are shown at different ambient temperatures using a 1 Crate. Simulations look very similar compared to isothermal calculations. Differences can be noticed at lower ambient temperatures. The thermal simulations show less overpotential. This results in higher cell voltages at discharging and in lower cell voltages at charging. At −10 °C, the difference is most pronounced.

a) Discharge   b) Charge
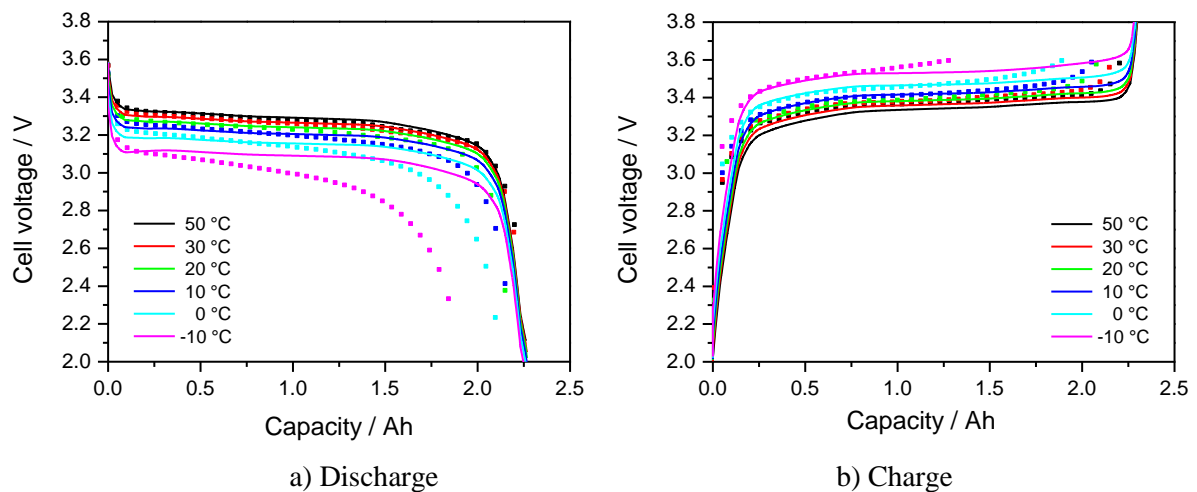
Figure 50: Discharge curves (a) and charge curves (b) at different temperatures at a 1 C-rate.

Regarding the discharge curves a general tendency is observed concerning the cell voltage at different temperatures. The lower the temperature is the lower is the cell potential and, eventually, the capacity. At high temperatures the overpotentials are less dominant and the cell voltage is mainly given by the half-cell potentials or the thermodynamics, respectively. With decreasing ambient temperature the internal resistances increase, leading to higher overpoten-

tials. These are responsible for a lower cell voltage at lower temperatures. In the experiments, especially at 0°C and − 10°C, a capacity loss can be observed, additionally. The exact origin of this capacity loss cannot be given. An assumption is that this effect is based on the intercalation reaction at the electrodes. If this reaction is hindered, the overpotential rises and leads to an earlier decrease of the cell voltage. The intercalation reaction is coupled with other processes, such as lithium transport within the electrolyte and within the bulk material, which are temperature dependent, too. Especially, the bulk transport is the bottleneck in this process cascade. If it is too slow, the electron-transfer reaction is influenced which increases the overpotential. Due to the fact that the macro-model neglects bulk-transport properties, all discharge curves reach the full capacity of 2.3 Ah.

The simulations show that heating and ambient temperature influence the performance of the battery. As already remarked, differences between isothermal and thermal simulations are visible at −10 °C. The heating leads to faster reactions at the electrodes which results in less overpotentials. Therefore, the plateau of the thermal discharge curve is above 3.1 V compared to the plateau of the isothermal simulation which is below this value.

The simulated charge curves fit quite well to the experiments. At high ambient temperatures, the cell voltage is underestimated by the simulation. Charge curves below 10°C fit well to the experiments. All simulated curves show an underestimated voltage increase at the end of the charge progress.

The reason for the underestimation of the cell voltage by the simulation could be identified. Regarding the curve at 50 °C, the cell voltage is lower compared to the experiments. In contrast, the simulation of discharge matches the experiments well at this temperature. Here, an asymmetric behavior exists. To investigate the reason, the exchange current density of the Butler-Volmer equation has been changed to get better agreements. Then, an agreement in charge curves for high temperatures could be achieved. In contrast, the discharge curves did not fit anymore. So, the conclusion was that the kinetics is not the reason for this behavior.

As already mentioned, the cell voltage at high temperatures is dominated by the half-cell potentials. In case of the cathode, the latter is dominated by the phase transition from FP to LFP (discharge) or from LFP to FP (charge), respectively. LFP is the more stable compound, because it has a lower potential. Then, it could be assumed that the transition of LFP to FP has different energies compared to the transition of FP to LFP. The energies are expressed as enthalpy and entropy contributions. Due to the underestimation of the cell voltage by charge simulations, the assumption is that the correlation between enthalpy and entropy, extracted from literature, is not really balanced to match the real behavior shown in the experiments.

Hence, it must be mentioned that some uncertainties remain regarding heating due to thermo-dynamics.

Thermal behavior. The ambient temperature influences the heating of the battery. The influence of different ambient temperatures on the average temperature of the battery is shown in Figure 51. Due to an applied 1 C discharge, the temperature increase is low resulting in a nearly constant temperature. A difference can be seen at the beginning of the discharge. At low temperatures, the battery heats up within the first minutes. The higher the ambient temperature is, the less heat generation at the beginning of discharge can be observed.

In Figure 52, the heat production at different temperatures within the range of $-10\,°C$ and $50\,°C$ is shown. The highest heat production can be observed at the lowest temperature. With increasing ambient temperature the heat production reduces. It even decreases to negative values at $50\,°C$. With operation time, an increase of the heating can be observed at all temperatures. Up to 1.0 Ah the heating is more or less constant. After 1.0 Ah the heat production rises.

In the following section, the characteristic thermal behavior is explained in more detail. Therefore, three ambient temperatures ($20\,°C$, $50\,°C$ and $-10\,°C$) are chosen to explain the contributions to the heat production and the thermal behavior.
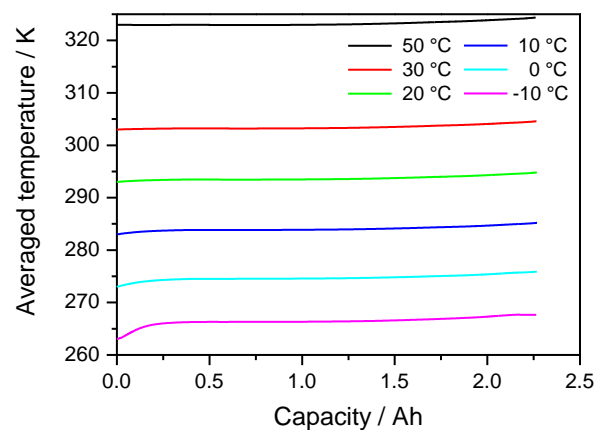
Figure 51: Averaged temperatures while discharging with 1C for different ambient temperatures.
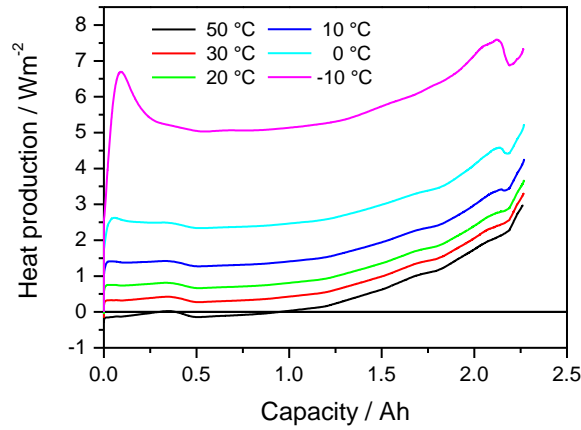
Figure 52: Heat productions of 1 C-rates at different ambient temperatures.
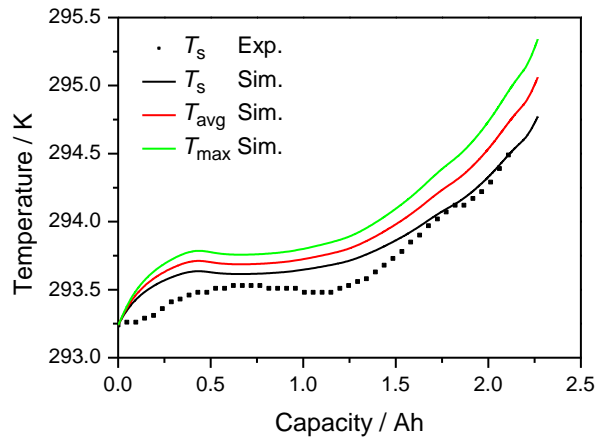

Figure 53: Temperature rise while discharging with a 1 C-rate.

Room temperature (20 °C). To explain the heat contribution and their influence on the performance of a battery, a 1 C-rate discharge at room temperature is chosen. In Figure 53, the temperature rise is shown during operation. In total, the battery heats up by around 1.25 K. The rise is nonlinear and shows characteristic behavior. The experiment shows an increase of around 0.25 K at around 0.6 Ah. Then, cooling takes place at ca. 0.8 Ah which decreases the temperature around 0.1 K. Followed by an increase, the temperature of 22 °C (295 K) is reached at the end of discharge. The simulation shows similar behavior. First, there is an increase of around 0.5 K at a capacity of ca. 0.4 Ah. Secondly, a cooling takes place between 0.5 Ah and 0.6 Ah. Thirdly, a strong increase occurs reaching the final temperature. In Figure 53, three different heating curves are shown. The lowest temperature rise occurs at the surface of the battery. In contrast to this, the maximum temperature is shown which is around 1 K higher and occurs in the center of the battery. The average temperature is in between them. Furthermore, it has to be mentioned that a characteristic temperature rise occurs at around

117

2.0 Ah seen in the experiments. The simulation shows the correct behavior qualitatively. It has the same tendency in cooling and heating as the experiment. Differences may be explained by the thermodynamic contribution of one of both electrodes.
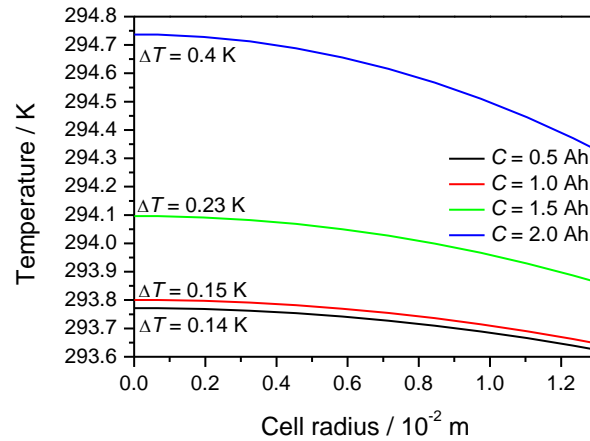

Figure 54: Internal temperature distribution along cell radius at 1 C-rate.

The temperature distribution within the battery is shown in Figure 54. With increasing operation time, a gradient occurs along the cell radius which is caused by two effects. On the one hand, the heat dissipation at the surface is determined by the heat transfer. It regulates the temperature difference between surface and ambient atmosphere. On the other hand, the heat accumulation depends on the heat generation and the heat capacity. Both effects are combined by heat-transport properties. The result is that the internal temperature is higher than that at the outer shell. This difference leads to a gradient within the battery which is rising with increasing operation time.

The temperature rise is due to different heat sources which are shown in Figure 55. The total heat production can be separated into different contributions. The smallest contribution is shown by the ohmic resistance (q_{ohm}) which is constant and less than 0.1 W/m². The heat due to resistivity (q_{res}) has a small contribution with 0.25 W/m², too. The second highest contribution is due to kinetic processes (q_{pol}). The main contribution is the heat production due to thermodynamics (q_{rev}). It is called the reversible heat, because the heat is due to the change of entropy due to intercalation of lithium in the host material. The characteristic shape of the heat production and of the temperature rise is mainly influenced by the entropy change. During discharge, first, a cooling takes place followed by a heating at around 1.5 Ah. This can be explained by the sign change of the entropy contributions of the active materials (cf. Figure 28, Figure 30).
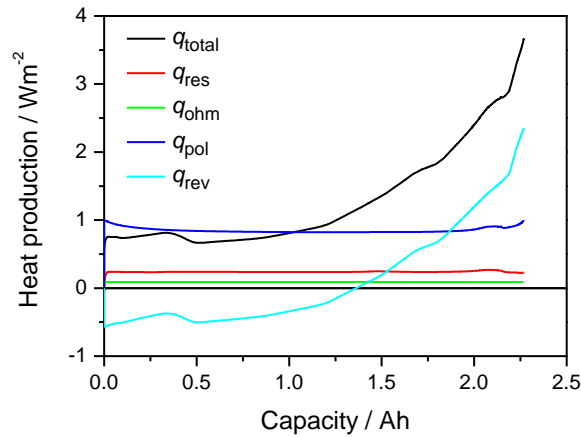
Figure 55: Different heat sources contributing to heat production

High temperature (50 °C). At high temperatures the results are different compared at room temperature, as illustrated in Figure 56. The total heating is around 1 °C after discharging. The experiment shows a distinct rise of the temperature. After a rise of 0.25 °C to 0.7 Ah, a cooling takes place of around 0.125 °C to 1.2 Ah. Then, a strong rise occurs at the end of the discharge reaching the end temperature of 50.7 °C (323.7 K). Also in the last temperature increase, characteristic fluctuations are recognizable. In comparison, the simulation shows a similar tendency beside an evident difference. The latter is that a cooling takes place immediately after starting the discharge. This lasts to 0.2 Ah and then a similar behavior takes place as seen in the experiment. The temperature rises of around 0.1 °C to 0.4 Ah, shrinks again to 0.7 Ah and starts rising to the end of discharge. The last rise is very strong and reflects the behavior of the experiment. Unfortunately, the behavior at the beginning up to 1.0 Ah is not represented correctly. The shape of the simulation can be explained by the entropy contributions of each active material. A change in the slope of the temperature reflects a sign change within the entropy contribution of LFP or graphite, respectively. The mismatch can be explained by several parameter settings. Regarding the cooling process at the beginning of the discharge, this could be a hint that the stoichiometry of the electrodes is not chosen correctly. Similarly, the entropy values extracted from literature may not fit perfectly. This may also explain the minor temperature rise or decrease during discharge. The simulation reproduces the characteristic peak of the experiment at around 0.7 Ah, but occurrence and height is different. Besides thermodynamic properties, heat capacity and heat conductivity may be a reason for this behavior. In this case, the heat capacity would be too small and the heat conductivity would be too fast. Changing both parameters, it shows the correct tendency, but it was not possible to obtain a perfect agreement. In doing so, the first characteristic peak shifted to higher capacities and rises to higher temperatures, but no match with experiments could be

achieved. Additionally, the rise at the end of discharge was too large reaching an end temperature of ca. 56 °C (324 K).

Besides, the evidence is remarkable regarding the heating due to thermodynamics which is visible in simulations. The characteristic shape of the heat production is shown in Figure 57. The thermodynamic part dominates the total heat production. Also this contribution is responsible for the cooling effect which lasts up to 1.4 Ah. Then the heat production is positive regarding only the thermodynamics. Other heat contributions are less intense and are not able to compensate the cooling effect. The reason for this low heat contribution is the high ambient temperature. At these elevated temperatures, all processes are faster resulting in less overpotentials than at room temperature.
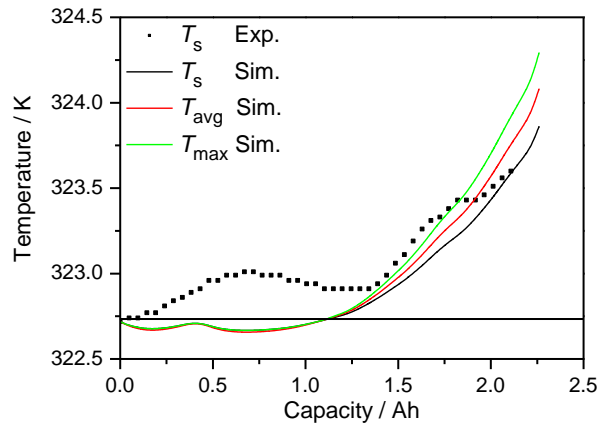
Figure 56: Temperature rise while discharging with 1 C at 50 °C.

The cell temperature along the cell radius is shown in Figure 58. The change in the inner temperature while discharging is shown in more detail in Figure 59. They show that the cell temperature decreases at the beginning of discharge. This implies that a heat flow occurs from the battery surface to the center. Due to the strong cooling, the gradient becomes more intense and reaches its maximal shape at around 0.75 Ah. Then, the thermodynamic properties change leading to an internal heating. This revises the gradient leading to higher temperatures at inner windings compared to windings at the outer-shell of the battery. Due to that, the spreading of temperatures, shown in Figure 56, occurs after reaching 1.25 Ah and is less intense.

In total, the conclusion is that at high temperatures the discharge curves are mainly influenced by the thermodynamics. Hence, heat production is due to entropy contribution of the active materials. Kinetic effects are less dominant compared to room temperature. Therefore, overpotentials are small and lead to minor heat production.
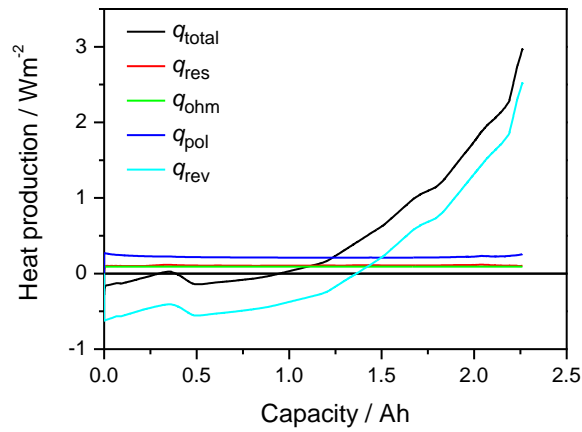
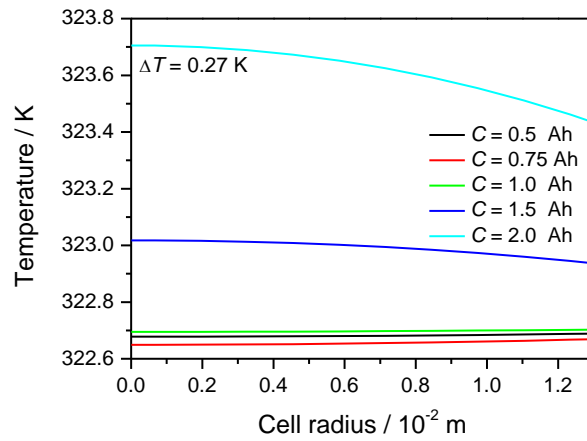Figure 57: Contributions to total heating while discharging at 1C.

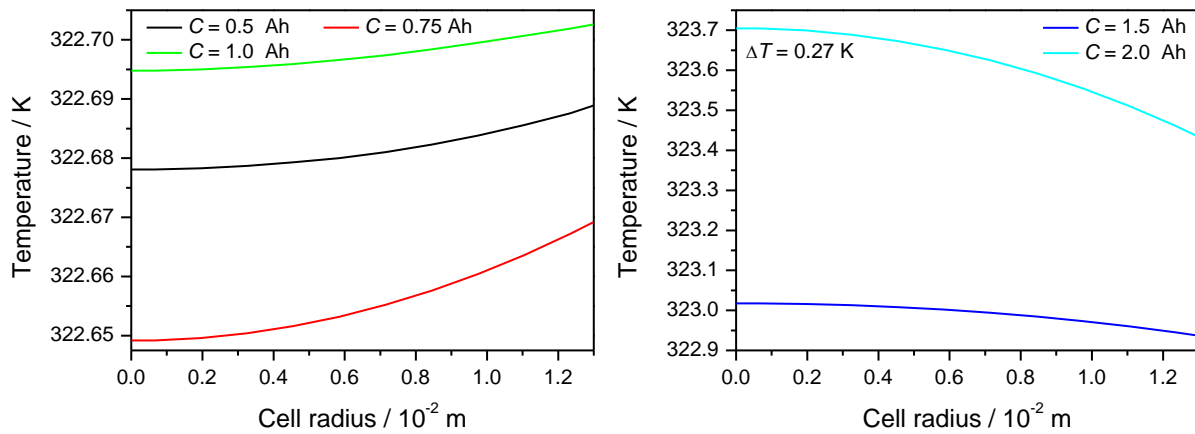Figure 58: Temperature rise along cell radius at different discharged capacities.

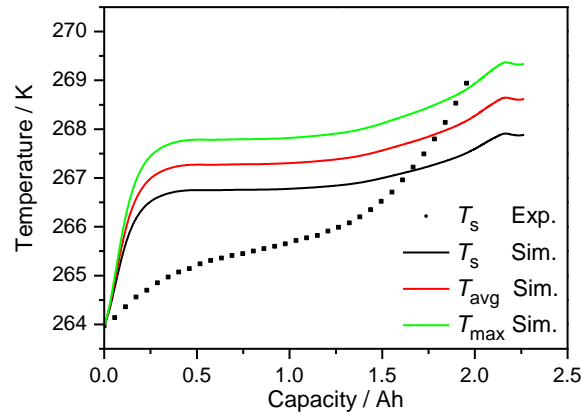Figure 59: Temperature variation within cell along cell radius at different capacities.

121

Figure 60: Temperature rise while discharging with 1 C at −10 °C.

Low temperature (−10 °C).   At lower temperatures, the experiment shows different behavior compared to higher temperatures. Compared to the curve at 50 °C, the shape is smoother and is increasing permanently which is shown in Figure 60. The experiment shows an increase of around 5 K after discharging with 1 C. The simulation has a similar augmentation. The difference is a strong temperature rise at the beginning of the discharge. Over a long time, the temperature is constant and rises then slowly to the end of discharge. The simulation shows a widening of the temperatures depending on location within the battery. The surface temperature is ca. 1 K lower than at the center. Also, this is shown in Figure 61. The temperature increases continuously while discharging with 1 C and the gradient becomes more intense with time.

The strong rise at the beginning of the discharge is caused by kinetic effects. These dominate the behavior of a cell at lower temperatures. This can be seen in Figure 62, too. Although the thermodynamics contribute with cooling to the system, kinetic effects compensate this behavior leading to a strong heating. Two heat sources can be identified which are the heat due to resistivity and due to polarization. The first occurs in the electrolyte. At these low temperatures, the ion transport is decelerated leading to stronger concentration gradients and therefore to higher overpotentials which causes higher heating. The latter is caused by the electron-transfer process at the electrodes. At low temperatures, this reaction is retarded drastically. It has to be mentioned that the strong increase, shown by the simulations, is due to the activation energy used in the Butler-Volmer expression. It seems that the activation energy is chosen too high obtaining good agreement with experimental results. But, if the energy is diminished, it could be expected that a better agreement could be obtained in heating and temperature profiles but not in discharge curves. The reason is that the activation overpotential decreases. The total heating shows a characteristic behavior while discharging which is mainly caused by the
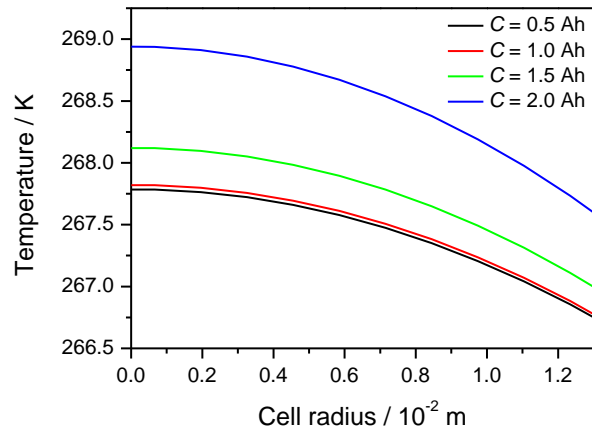
Figure 61: Temperature gradient along cell radius while discharging with 1 C at −10 °C.
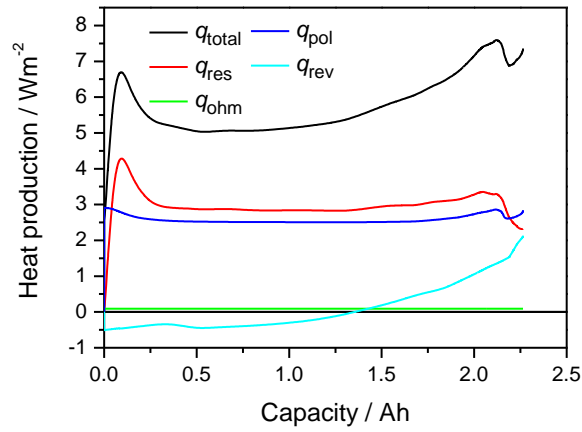

Figure 62: Heat production while discharging with 1 C at −10 °C.
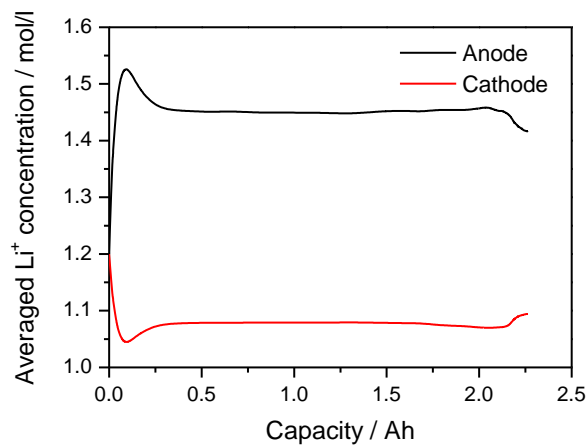

Figure 63: Averaged lithium-ion concentration on anode and cathode side while discharging with 1 C.

resistivity.

During operation the concentration gradient changes with time. Figure 63 shows the averaged concentrations of lithium ions on anode and cathode side. The gradient can be described as the difference between these both lines. Starting with a concentration of 1.2 mol/l the gradient increases drastically, meanwhile the battery heats up. Due to this heating, the transport is accelerated leading to a lower gradient and to less overpotential. Then, the gradient is nearly constant. At the end of discharge the gradient decreases which is not an expected behavior. The reason is the influence of the thermodynamics on lithium intercalation which affects itself the ion concentration within the liquid phase. As shown in Figure 40 and Figure 41, stoichiometry (lithium-ion concentration within bulk material) shows a spreading during operation. At around 2.1 Ah, the spreading is removed leading to the same stoichiometry in all particles along the cross section of a repeat unit. At this capacity point, the thermodynamics of the cathode changes causing this behavior (cf. Figure 30). This leads to lower activation overpotentials why the electron transfer is hindered. Due to this, the concentration gradient decreases within electrolyte.

5.3.2 Different C-rates at room temperature

At room temperature, thermal effects can be studied applying different C-rates. In Figure 64, discharge and charge curves are shown. The behavior is similar as in the isothermal simulations (cf. Figure 37). However, there is a remarkable difference concerning the discharge curve at 10 C. It can be noticed that, after the voltage drop at the beginning, the cell voltage rises around 0.1 V reaching the maximum at 1.25 Ah. Then the voltage decreases reaching the cut-off voltage. The voltage rise can also be observed at a 5 C-rate but in a moderate extent. Compared to isothermal simulations (cf. Figure 37), wherein no voltage rise occurs, it can be said that this rise is due to heating. This effect can be seen in the experimental 10 C-rate, too. It is noticeable at around 1.0 Ah. Comparing with experiments, the thermal simulation overestimates the heating at 10 C. There are a few possible reasons. First, the validation was performed only for 1 C-rates at different temperatures. Other C-rates were not available for validation. Therefore the chosen heat capacity could be too high, or the heat transport is too slow. Secondly, the entropy contribution of the electrodes is too high which results in a too strong heating. Thirdly, the model excludes heat dissipation at pole caps and heat transport along windings. Therefore the heat transfer coefficient is very high using 55 W/m², also caused by an unknown impact of a fan in a climate chamber.

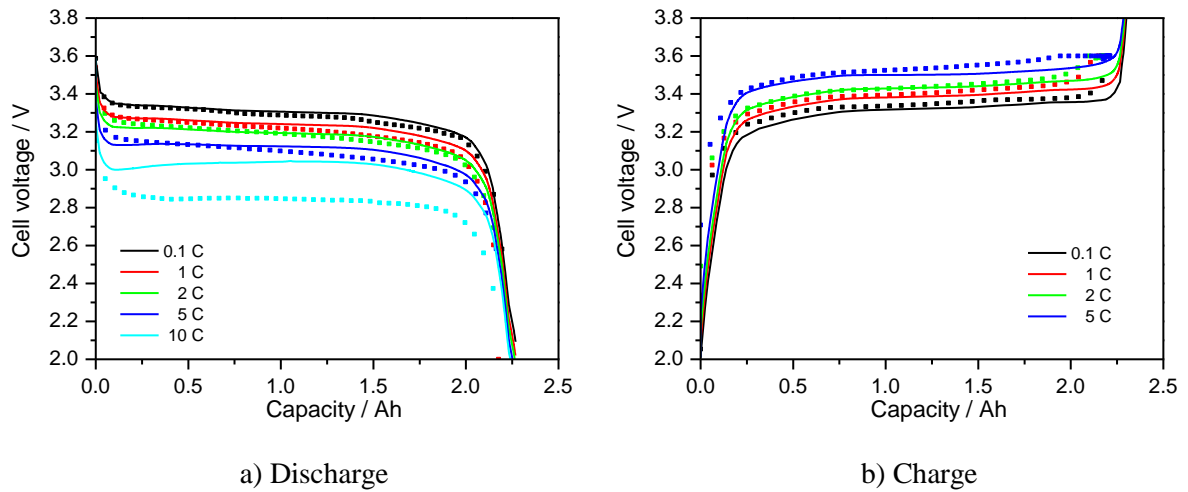a) Discharge   b) Charge

Figure 64: Discharge curves (a) and charge curves (b) at room temperature at different C-rates.
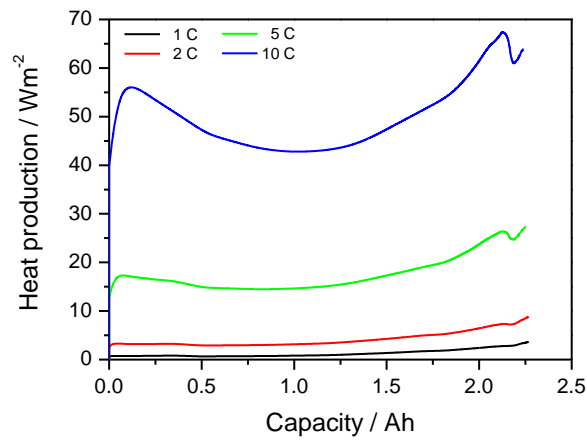

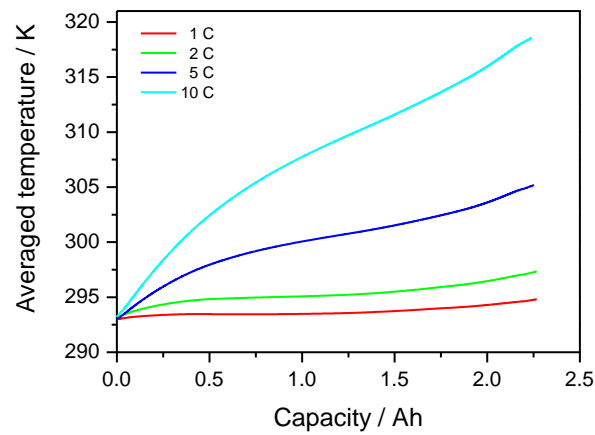Figure 65: Heat production of different C-rates at room temperature.

Figure 66: Temperature rise for different C-rates at room temperature.
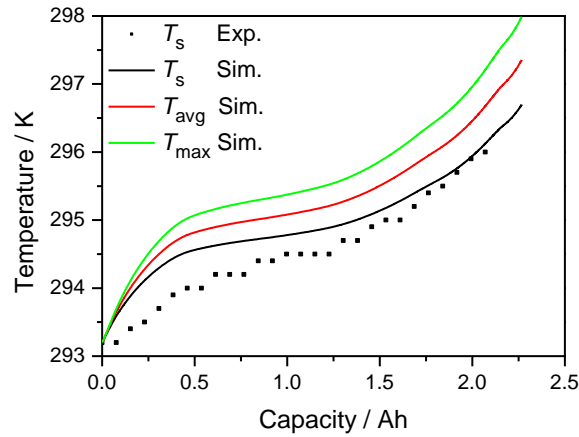
125

Figure 67: Temperature rise of a 2 C-rate at room temperature.
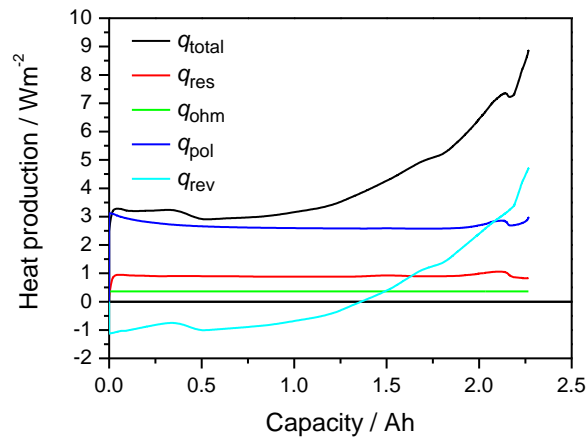
Figure 68: Heat production of a 2 C-rate at room temperature.
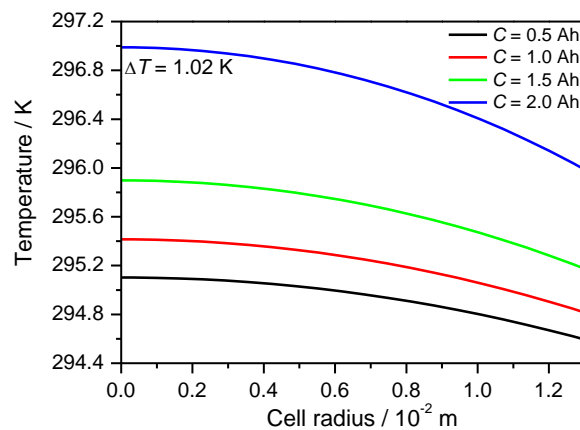
Figure 69: Temperature gradient along cell radius of a 2 C-rate at room temperature.

Thermal behavior. During operation the battery is heated by processes which correlate with applied current. A general overview of simulated temperature rises and heat productions are shown in Figure 65 and in Figure 66, respectively. There it can be seen that the heat production depends strongly on the applied current. At low C-rates, the temperature rise is marginal. Applying a 10 C-rate, the temperature increases by around 30 °C. The characteristic

shape of a 10 C-rate has the same origin as the heat production at −10 °C which is explained in the section above (cf. Figure 62).

1 C-rate. The results of a 1 C-rate at room temperature have already been shown and discussed (cf. Figure 53, Figure 54, Figure 55).

2 C-rate. The simulated temperature rise of a 2 C-rate fits quite well to the experiments. This is shown in Figure 67. The surface temperature reaches nearly the same value like the experiment does. Also, the characteristic shape of the rise is reproduced. First, it shows an increase at the beginning of discharge followed by a region wherein the rise is less intense. At the end the increase becomes more dominant. This can be explained by the heat production during operation (Figure 68). The combination of heating due to polarization overpotential and cooling due to thermodynamic properties leads to the first strong rise of the temperature. The strong rise at the end is due to the dominance of the thermodynamics. In Figure 69, the occurring temperature gradient along the cell radius is shown. It can be noticed that with increasing time, which is depicted as chosen capacity points, the temperature rises within the battery. Due to the heat dissipation at the surface of the battery, a heat flux from the center of the battery to the surface occurs leading to a gradient along the cell radius. At a capacity of 2 Ah, the temperature difference between center and surface is around 1 °C. In Figure 67 it can be seen that the simulation predicts that an internal temperature of 25 °C is around 1.5 °C higher than the temperature at the surface. The total internal temperature rise is around 5 °C.

5 C-rate. At applied 5 C, the temperature rise is more intense which can be seen in Figure 70. The simulations show a stronger temperature rise compared to the experiments leading to higher temperatures at the end of discharge. Here, the simulation predicts an inner temperature of around 34 °C which is around 4 °C higher than the surface temperature. The experiment only has an end temperature of 27 °C which is a total increase of 7 °C. Although the discharge curve, shown Figure 64, matches well the experiment, a difference in the heating can be observed. A reason for this is the strong polarization overpotential which occurs at this C-rate. Because this is too high, the heating is too intense. This can be seen in Figure 71. Besides, an important task is to estimate the internal temperature at elevated C-rates. The simulation predicts that there is a gradient occurring during operation (Figure 72). The shape is steeper compared to the profiles at 2 C. But the temperature difference between center and surface is only 3.13 °C at a capacity of 2 Ah. The heat transport through the windings and the

heat dissipation at the battery surface is fast enough to ensure a relatively constant internal temperature. But it has to be mentioned that the heat transfer coefficient, used in the simulation, is very high. The assumed reason is a working fan in the climate chamber. This means that under cooling conditions the internal temperature rises less than normally assumed. But it has to be estimated that higher temperature gradients occur if natural convection takes place.
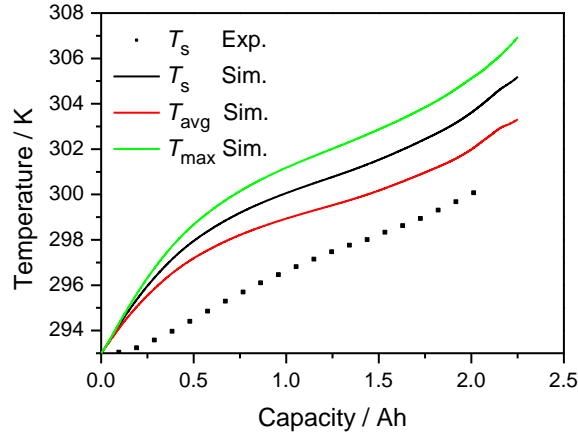
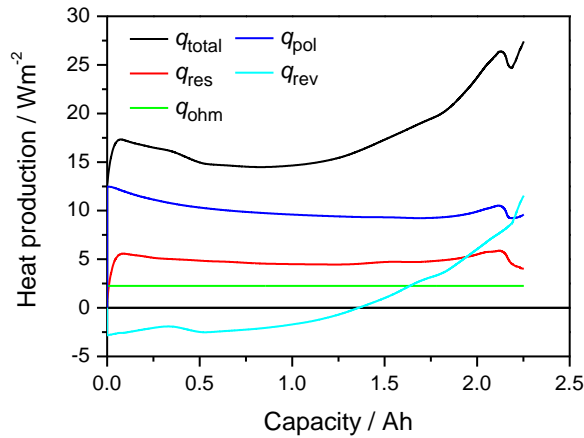Figure 70: Temperature rise of a 5 C-rate at room temperature.

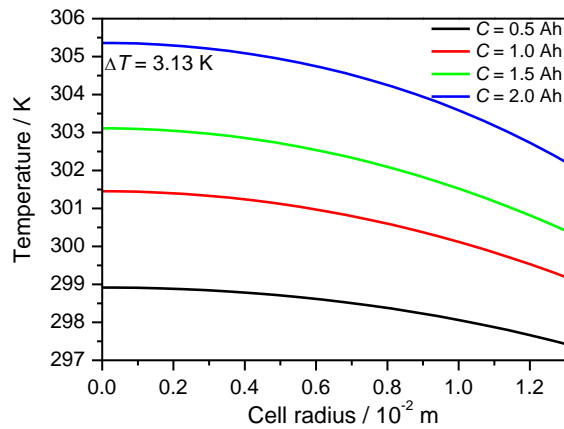Figure 71: Heat production of a 5 C-rate at room temperature.

Figure 72: Temperature gradient along cell radius of a 5 C-rate at room temperature.

5.4 Cycling behavior

In this section, cycling of a battery was performed. A full battery was discharged with constant current. After reaching the voltage of 2.4 V, the current was inversed to charge the battery without any break or relaxation time. The charging was stopped when reaching the voltage of 3.6 V. This procedure was performed at different temperatures. Results of experiments, obtained at 20 °C and 50 °C ambient temperature, are compared with simulations.

1 C-rate. In Figure 73, the results of a cycle at a 1 C-rate are shown. Voltage distribution and surface temperature variation of the simulation reproduce quantitatively and qualitatively the behavior of the experiments. Especially, the characteristic peaks occurring at current change show similar behavior. The simulated charge curves show lower cell voltage and a shift to higher time at both temperatures. The simulation shows higher end-capacity compared to the experiment. This results in a shift of the curves. Also, the overpotentials are smaller than those of the experiment. Furthermore, as already mentioned, the thermodynamics, obtained from literature and used in simulations, show a small deviation from the experiments at the end of discharge. In Figure 74, a correlation between temperature and heat production is shown. The temperature change is smooth in contrast to the heat production. Especially, this can be seen at the change between discharge and charge. The heat production changes instantaneously, decreasing to low values followed by a rise of the heat production again. In contrast, the temperature decreases with a lag of time to lower values before the temperature rises again. The reason is the specific heat capacity of the battery. The lower the capacity is the faster is the change of the temperature.

The change from heating to cooling is caused by the change of the reversible heat in terms of entropy. This effect was already described in chapter 4.2.1 and in the section above. In Figure 75, contributions of heat productions are shown versus time at 1C-rate. It can be noticed that the heat production due to thermodynamics is symmetric. Due to the sign change of the current, the entropy value changes, too. Due to the same applied C-rate, the heat production, caused by thermodynamics, have the same order of magnitude at both temperatures. In contrast to the thermodynamics, heat productions due to kinetic processes always have a positive contribution. The highest contribution is due to polarization overpotentials at the electrodes. These contributions are higher at 20 °C than at 50 °C. Due to this correlation between thermodynamics and kinetics at various temperatures, the consequence is different regarding surface temperature and cell voltage.

$T_{amb} = 20\ °C$ $T_{amb} = 50\ °C$
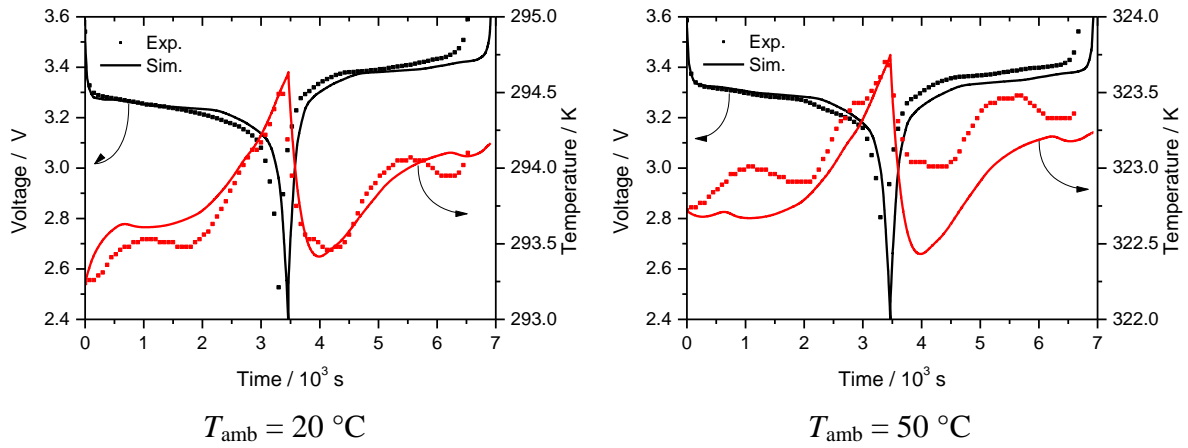
Figure 73: Comparison of experiment and simulation regarding voltage and surface temperature versus time at 1C-rate while cycling.

$T_{amb} = 20\ °C$ $T_{amb} = 50\ °C$

Figure 74: Correlation of simulated results regarding surface temperature and heating versus time at 1C-rate while cycling.

$T_{amb} = 20\ °C$ $T_{amb} = 50\ °C$

Figure 75: Contributions of heat production simulated versus time at 1C while cycling.

$T_{amb} = 20\ °C$ $T_{amb} = 50\ °C$
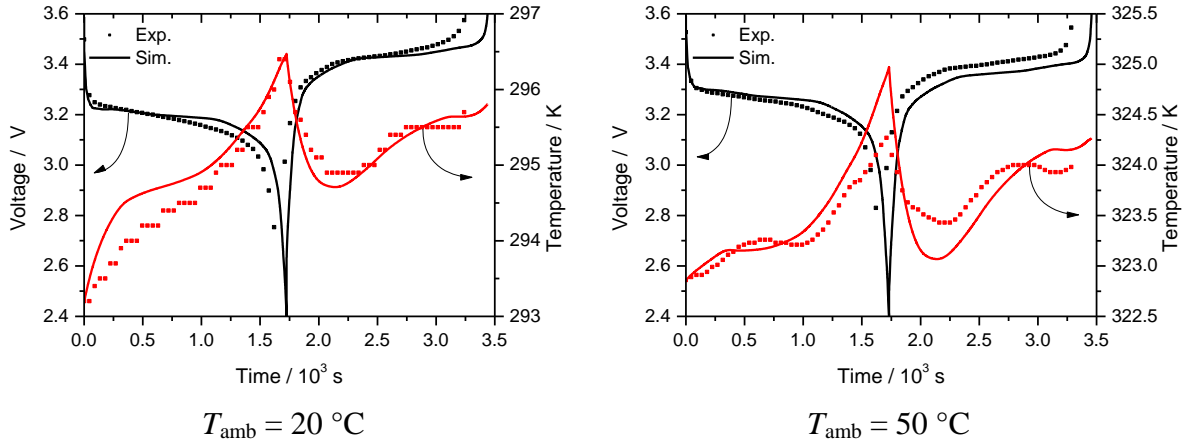
Figure 76: Comparison of experiment and simulation regarding voltage and surface temperature versus time at 2C-rate while cycling.
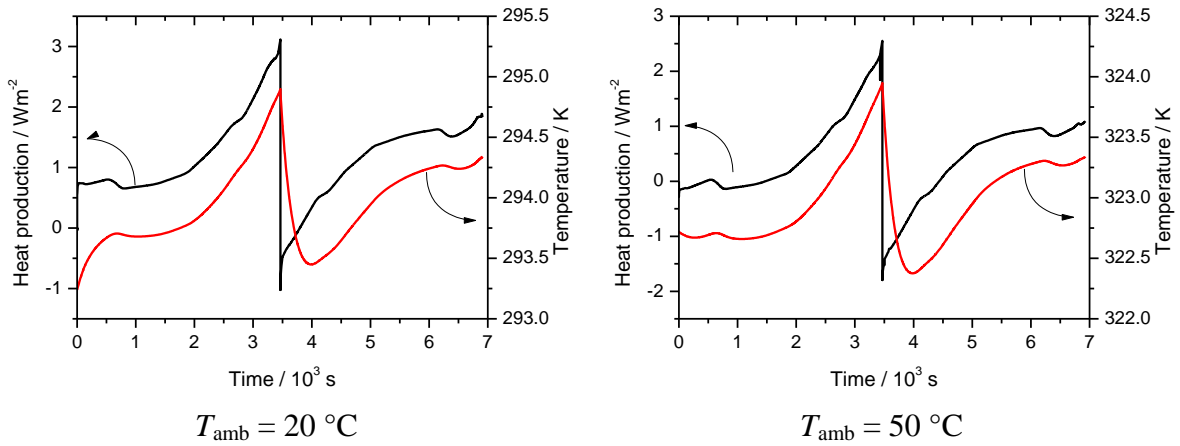

$T_{amb} = 20\ °C$ $T_{amb} = 50\ °C$

Figure 77: Correlation of simulated results regarding surface temperature and heating versus time at 2C-rate while cycling.
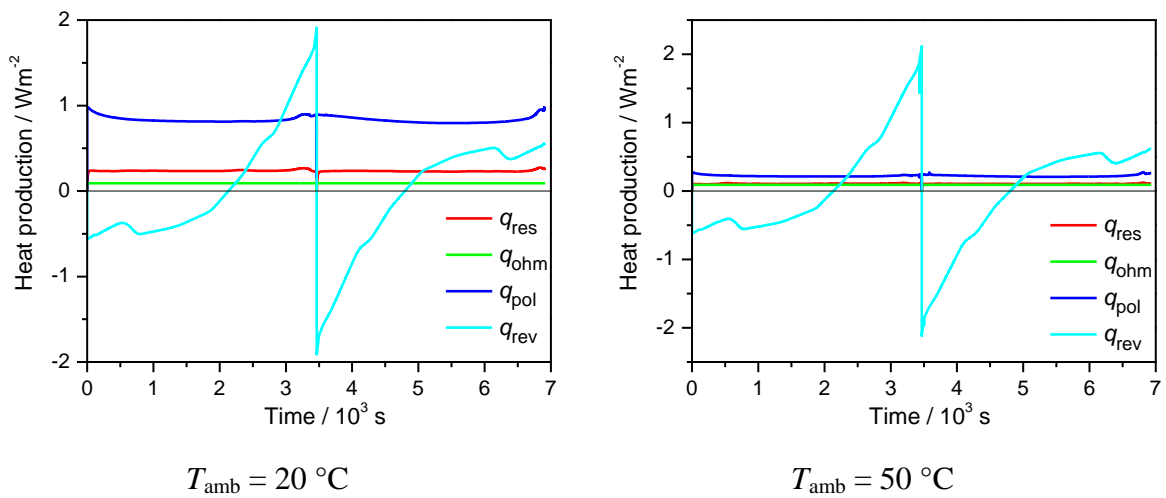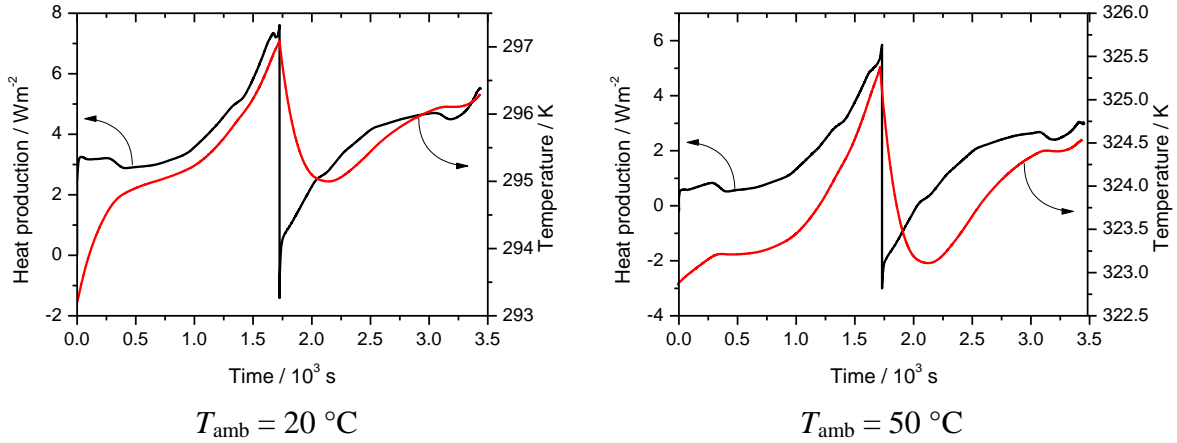

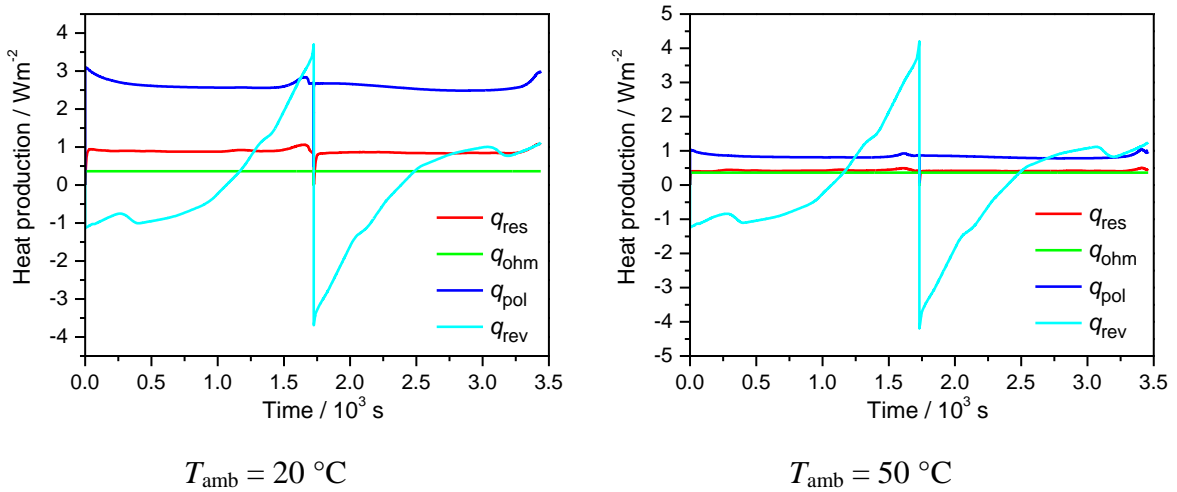$T_{amb} = 20\ °C$ $T_{amb} = 50\ °C$

Figure 78: Contributions of heat production simulated versus time at 2C while cycling.

131

2 C-rate. Nearly the same behavior can be recognized by applying a 2C-rate at 20 °C and 50 °C. In Figure 76, a comparison of voltage and surface temperature versus simulation time are shown. Also here, a good agreement is achieved concerning voltage and temperature profiles. Applying a 2 C-rate means that the battery is totally discharged after 30 min or 1800 s, respectively.

The experiments reach the cut-off voltage at 1730 s which means that the capacity is 2.25 Ah instead of the nominal capacity of 2.3 Ah. Probably the battery has aged by the time these experiments were performed. The simulation time was adjusted in order to change the current to the same time as in the experiment. So, the simulated voltage is below 2.4 V.

Compared to an applied 1C-rate, the temperature rise is higher due to a stronger heating. This is depicted in Figure 77. Also here, the delayed rise of the temperature after the heat production can be seen. At this 2C-rate, diverse ambient temperatures cause different heat rates. The temperature rise at 20 °C is around 4 °C and at 50 °C around 2.5 °C. The reason is the heating due to kinetic effects which dominates at lower temperatures. In Figure 78, the contributions of heat production are shown in more detail. The contribution due to thermodynamics is nearly doubled compared to the contribution at 1C, because the current is twice as high. The heating due to overpotentials rises at 2C, too. The polarization overpotential causes the highest heat production, followed by the resistivity overpotential. At 20 °C, both overpotentials are higher in contrast to the ones at 50 °C. Therefore, the temperature rise and its profile show differences at diverse temperatures.

Multiple cycles. This section describes the behavior of a battery while cycling with a 5C-rate at 0 °C and 20 °C. This is a representative range for operation at low or moderate temperatures. Here, the consequences within this temperature range are discussed. In the following, four cycles are shown. Increasing the cycling number was observed to have no further changes in the battery behavior.

In Figure 79, experimental and simulated results are compared. It shows the cell voltage and the temperature distribution while cycling with 5C. Differences can be recognized regarding the time for each cycle. The cycle lasts longer at room temperature than at low temperatures. This can be seen for experiment and simulation, too. Also, it is noticeable that the experimental cycles have lower cycling time in contrast to the simulations. These deviations are caused by the simulated discharge. The simulation shows higher cell potential and it achieves higher end-capacity. Furthermore, the simulation shows smaller overpotentials which result in longer cycling times. In contrast, the experiment shows a decrease of cycling time which is

noticeable at 0 °C. Here, the overpotentials rise with increasing cycling number. At 20 °C, this effect is not remarkable anymore. The simulation, however, does not show such characteristics. It can be assumed that other processes may cause a rise of overpotentials which are not regarded in the macro-model, such as solid-state diffusion.

Another reason for this deviation between simulation and experiment could be a possible altering of the investigated battery. Although it is a high-power cell, it shows especially at low temperatures that the cycling time is less than 720 s. The expected capacity is not obtained at these conditions, although the recommended cut-off voltage and charge current are used (cf. Figure 13). However, the battery shows a good efficiency at all temperatures and current requirements. The cell voltage falls below the voltage of 2.8 V tardily. Furthermore, the cell voltage rises with increasing temperature in the first cycle at 0 °C due to a decrease of overpotentials. From this, it can be derived that the internal warming can be used as mode of operation at low ambient temperatures to increase the battery efficiency.

Experiment, $T_{amb} = 0$ °C   Experiment, $T_{amb} = 20$ °C

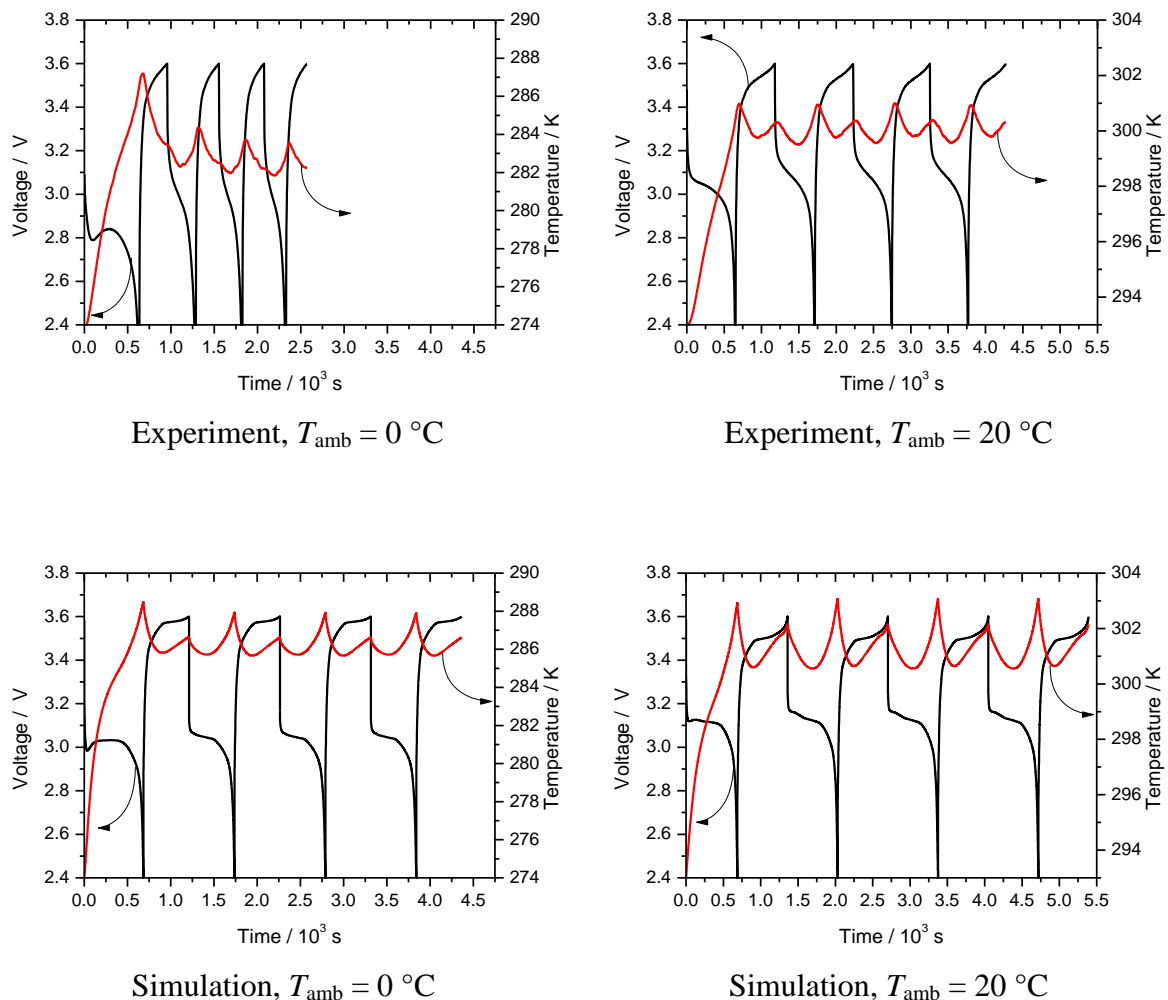Simulation, $T_{amb} = 0$ °C   Simulation, $T_{amb} = 20$ °C

Figure 79: Comparison of voltage and surface temperature between experiment and simulation at 0 °C and 20 °C while cycling with 5C.

133

The surface temperature rises strongly within the first discharge. Then a cooling occurs while charging which is due to thermodynamics. After the first cycle, the temperature shows an oscillation while cycling. The experiment at 0 °C shows also an oscillation which occurs later stabilizing around the fourth cycle. With increasing cycle number, the temperature variation becomes less intense. This can be explained using Figure 80. The change in heat, and therefore in temperature, is due to the change of polarization and resistivity overpotentials. Within the first discharge, the overpotential rises immensely leading to a warming of the battery. The latter results in less overpotentials which, in turn, produces less heat. A quasi-equilibrium is reached after the first cycle. At low temperatures, this effect is more distinctive. The reversible heat production remains the same within all cycles. Due to the dependence on temperature, the reversible heat source is higher in total at 20 °C compared to 0 °C.

a) $T_{amb} = 0$ °C   b) $T_{amb} = 20$ °C
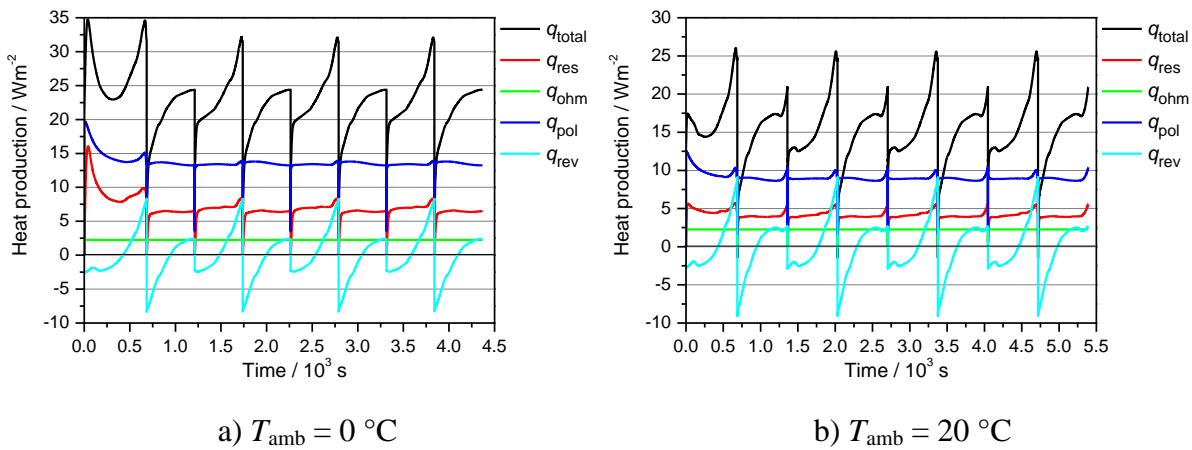
Figure 80: Heat-source variation during cycling with 5C.

5.5 Conclusions and outlook

Conclusion. The macro-model, presented here, is able to represent discharge curves, charge curves and thermal behavior in good agreement with experimental results. Especially, regarding temperature profiles, it is not necessary to go into further details, like bulk diffusion, phase transition, etc. However, because all micro-scale information is lumped into the global Butler-Volmer equation, electrochemical impedance spectra cannot be reproduced quantitatively. This motivated the development of the micro-model. Depending on a lithium-ion concentration gradient within the liquid electrolyte, a concentration variation of lithium in the active material along a cross section could be observed. Therefore the SOC is time and location dependent.

It was shown that, in the experimental commercial cell by A123, natural graphite is used as active material of the anode. The exact composition could not be clarified. Furthermore, it

was shown that not the total possible stoichiometry range of the anode is used. Only around 50 % of the lithium capacity is used if the battery is in a charged state.

The thermodynamics of the cathode is mainly influenced by the phase transition of $LiFePO_4$ and $FePO_4$. Although good agreement was achieved in discharge curves at low C-rates and high temperatures, small distinctions remain in charge curves at these conditions. An exact reason cannot be given so far. An assumption is that the thermodynamics, extracted from literature, does not represent the real behavior. Additionally, the exact composition of the cathode, produced by A123 systems, is not known. We assume that the cathode consists of a blend of different active materials causing different electrochemical behavior.

The macro-model is able to predict the thermal behavior of the battery regarding the temperature rise during operation at different ambient temperatures and different C-rates. Good agreements with experiments could be achieved. Two main heating sources could be identified: thermodynamics and electron-transfer kinetics. The entropy contributions of both active materials mainly influence the temperature profile of the battery. Additionally, depending on current and ambient temperature, the electron-transfer processes lead to an off-set of the heat production. At low temperatures, the kinetic effects are dominant leading to a strong heat production. During operation, the characteristic shape of the heat production is caused by the thermodynamics. At high temperatures, the kinetic contribution is marginal, so that the heat production is mainly influenced by thermodynamics.

The macro-model predicts only small temperature gradients within the battery. The maximum temperature difference between center and surface is around 2 °C at an ambient temperature of −10 °C at 1C discharge. The fitted heat-transfer coefficient is very high for natural convection (55 W/m²K). We assume that the reason is the experimental setup. The cabin contains a fan to keep the temperature constant. The position of the battery-tester within this cabin was located such that a strong air flow cooled the battery.

Due to the fact that all thermodynamic data is extracted from available literature, a subtle distinction to the experiments can be found in discharge curves and temperature profiles. Nevertheless, it could be shown that the behavior of a battery can be generally reproduced over a wide range of temperatures and C-rates.

Outlook. The model does not include side or aging reactions, e.g. SEI formation or lithium plating. An implementation of these processes can predict the electrochemical and thermal aging of the battery. Also, the behavior under various conditions can be studied such as very high and low temperatures, high applied currents, aging while cycling and thermal run-away.

Further investigations are recommended regarding the measurements of the thermal battery behavior. To improve the experimental setup, the battery has to be enveloped to avoid air flow, e.g. using an aluminum foil. Additionally, to receive more information about the heat release of the battery, more temperature sensors should be installed at different locations of the battery including pole caps. It would be illustrative to contact both pole caps comparing the heat release depending on the electrode.

6 Micro-model: Results and discussion

6.1 Overview

The micro-model is an extension of the macro-model. Instead of using Butler-Volmer kinetics, elementary reactions are included. In chapter 5.2, discrepancies between experiment and simulation were reported concerning impedance spectra. The main advantage of the micro-model is the detailed expression of elementary reactions, instead of lumping all occurring processes into the Butler-Volmer equation. To recall, two reactions are assumed occurring on the anode side. Lithium ions adsorb on the particle surface and subsequently intercalate into the bulk material. On the cathode side, adsorption of lithium takes place, too. After an electron-transfer process, the lithium atoms diffuse along an interphase to the center of the particle. Here, a phase transition takes place in which FP is converted to LFP during discharge. Table 14 shows an overview of the micro-model versions. In the following sections, the results of the model "Micro 1" are shown and discussed concerning discharge and charge curves, impedance spectra, concentration gradients and sensitivity analysis. Further investigations were performed concerning the influence of interphase size and bulk diffusion of the cathode on charge and discharge curves ("Micro 2 − 4").

Table 14: Overview of micro-model versions

Model name	Interphase size	Bulk diffusion cathode
Micro 1	Constant	Constant
Micro 2	Constant	No bulk diffusion
Micro 3	Varying with SOC and current	Constant
Micro 4	Varying with SOC and current	No bulk diffusion

6.2 Results and discussion

Discharge and charge curves. Using the micro-model "Micro 1", different C-rates at 20 °C were simulated and compared with experiments. Results are shown in Figure 81. First, concentrating on discharge in a), a very good agreement is achieved for a 0.1C and 1C. The slope at the beginning of charge is well matched. The plateau has the same shape. At the end of discharge, the simulation predicts a stronger voltage decrease compared to the experiments. Therefore, less capacity is reached. Regarding higher C-rates, such as 2C, 5C and 10C, the simulated curves drop down nearly immediately after beginning. The reason is the interface

on cathode side between FP and LFP. The application of higher C-rates leads to a fast filling of the interface. The intercalation reaction is not fast enough to ensure free vacancies in the interface. This inhibits the electron-transfer reaction causing an increase of the resistance. This leads to a starvation of the curve.

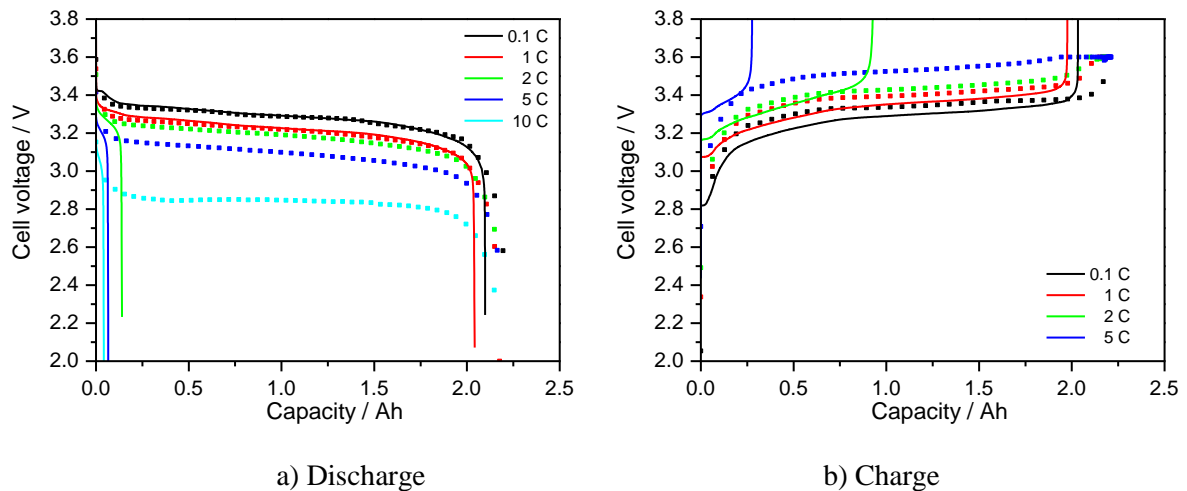a) Discharge   b) Charge

Figure 81: Discharge and charge curves at 20 °C applying different C-rates including bulk diffusion on cathode side.

To show that this effect is caused by the interface filling instead of a slow diffusion process, further simulations were performed wherein the diffusion on cathode side is disabled (cf. Table 14, "Micro 2"). Results are shown in Figure 82. Also there, a good agreement is achieved for 0.1C and 1C in contrast to the other C-rates, which show the characteristic behavior, too. This indicates two things. First, the diffusion is not the dominating process. Second, the filling of the interface in combination with the intercalation reaction is responsible for the voltage decrease.

Regarding the charge curves in Figure 81 b) and Figure 82 b), a similar behavior can be observed as in panel a). The rise at the beginning of charge is less pronounced compared to the experiments. The overpotential of the simulation is underestimated for all C-rates so that the plateau is below the experiments. The total capacity is not reached. The simulated voltage rises fast at around 2 Ah. But a difference can be observed between model "Micro 1" and "Micro 2". With bulk diffusion, the 2C-rate reaches 3.8 V at 0.3 Ah and the 5C-rate at 0.8 Ah (Figure 81). More capacity can be reached without bulk diffusion. Here, the 2C-rate achieves 1.6 Ah and the 5C-rate 0.4 Ah (Figure 82). This indicates that the main effect is caused by the interface and intercalation reaction. Nevertheless, the diffusion process is more dominant than at discharge. The explanation is that, while charging, the LFP is transformed to FP. This means that the interface is freed from lithium which diffuse from the center of the particle to

the surface where the electron transfer takes place. The intercalation reaction is too slow so that a starvation along the diffusion path occurs. This hinders the electron-transfer process leading to higher overpotentials with the result that the voltage raises too fast.

a) Discharge   b) Charge
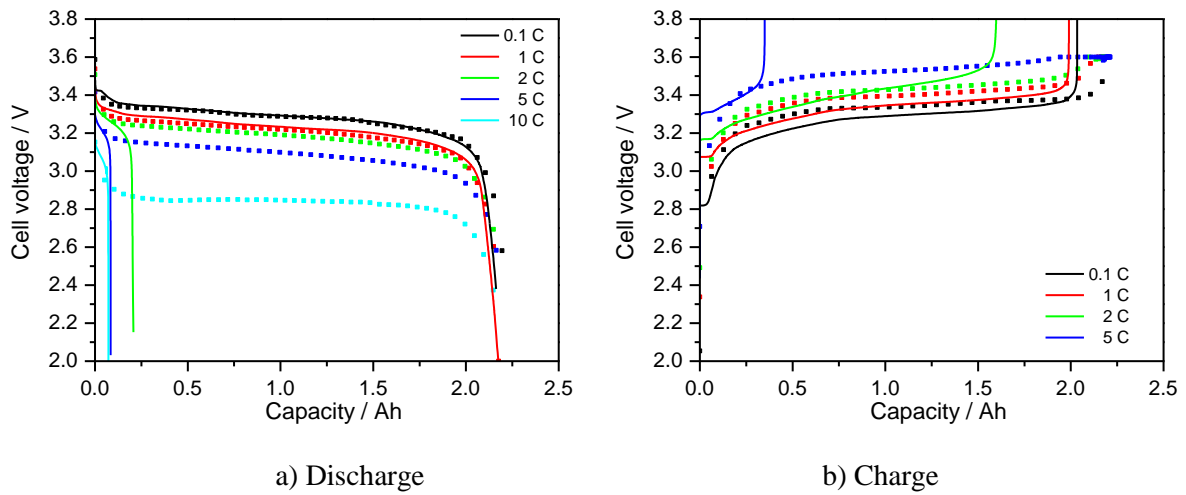
Figure 82: Discharge and charge curves at 20 °C applying different C-rates without bulk diffusion on cathode side.
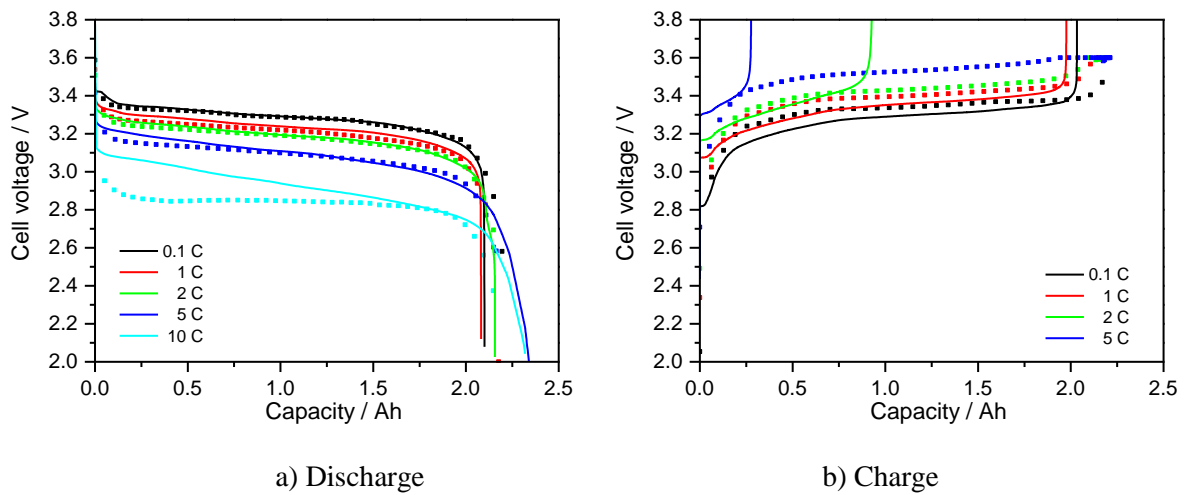

a) Discharge   b) Charge

Figure 83: Discharge and charge curves with a variable interface including bulk diffusion on cathode side.
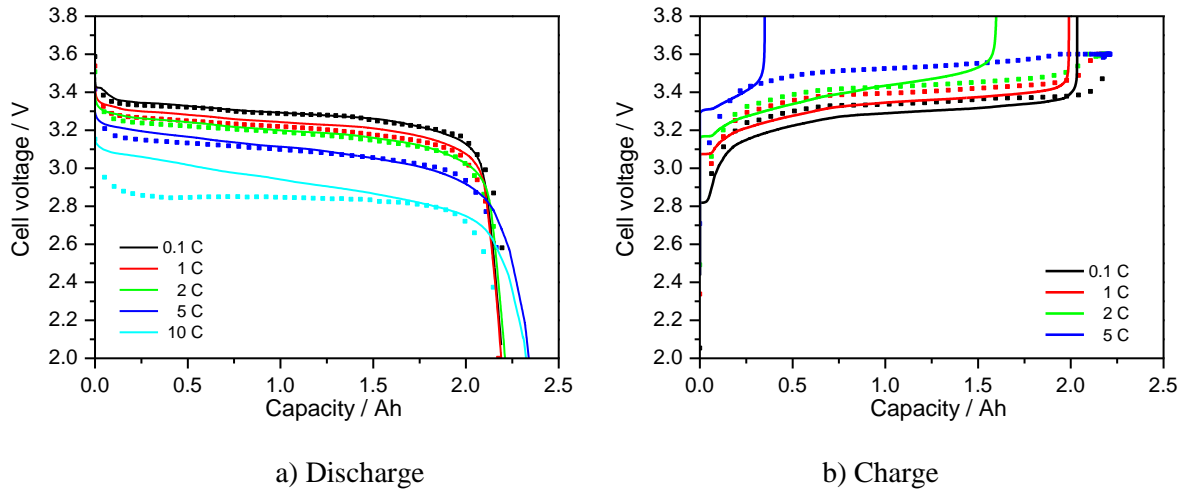
a) Discharge   b) Charge

Figure 84: Discharge and charge curves with variable interface without bulk diffusion on cathode side.

Current and SOC dependent interface area. Chiang et al. propose a mechanism change in transition of FP to LFP [108]. Using phase field modeling, they showed that under moderate overpotentials (e.g. 25 mV) misfit stress causes LFP to grow along the longitudinal direction [100] which is perpendicular to the fast-diffusion direction. Different behavior is seen at increasing overpotentials like 100 mV. They show that the particle will be filled in [010]-direction which has the highest Li-ion diffusion rate. This is indirectly supported by Islam et al., who calculated the energy for every migration direction [100]. This means that the diffusion direction depends on the overpotential. Again, the overpotential depends on applied current which leads to misfit stresses. Both reports lead to the conclusion that the misfit stress depends the interface area which we assume in our micro-model. Both models, "Micro 1" and "Micro 2", are able to reproduce the behavior at low C-rates, up to 1C. The observation that the diffusion is not the rate-limiting process indicates that the interface and the intercalation reaction dominate the battery performance at higher C-rates. Specifically, the interface acts as buffer for lithium ions.

As first step towards describing a mechanism change as a function of operating conditions, the present model was extended by assuming that the FP−LFP interfacial area depends on current and SOC (cf. Table 14, "Micro 3" and "Micro 4"). An assumed increase in interfacial area with increasing current can be interpreted as the occurrence of an additional reaction pathway. The correlation between current, SOC, and interface area is described in chapter 4.3.2 and shown in equations 52 and 53. This model leads to a better agreement in discharge curves which can be seen in Figure 83 a). Beside the low C-rates, higher C-rates show a good agreement with experiments, too. The 2C and 5C discharge curve reach the full capacity and

they show the same plateau as the experiment. The 5C-rate shows a higher reached capacity than the experiment. Also, the 10 C-rate shows an improvement. The discharge curve ends at around 2.3 Ah which is the nominal capacity. The plateau shows a characteristic shape. At the beginning the overpotential is too low, but it rises with operation time. In contrast, the experiment has a high overpotential from beginning, a nearly constant plateau over the total discharge. In between, a small voltage increase can be observed which is assumed to be caused by heat generation and, therefore, by a decrease of overpotentials. To be sure that the diffusion is not responsible for this effect, the diffusion was disabled (cf. Table 14, "Micro 4"). The results are shown in Figure 84. The discharge curves are shown in a). Here, no relevant changes are recognizable. This indicates that the diffusion process has no main influence on the battery performance.

Another behavior can be seen regarding charge curves of both cases. These are shown in Figure 83 b) and Figure 84 b). There is no improvement compared to the results without an interface variation. Furthermore, there are the same capacity shifts of various C-rates which are already attributed to diffusion.
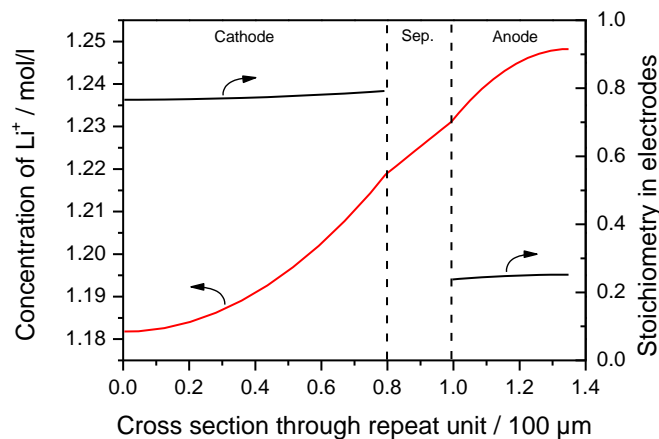
Figure 85: Concentration gradients along cross section within electrolyte and solid phase.

Concentration gradients. In Figure 85, concentration gradients within electrolyte and solid phase are shown along the cross section of a repeat unit. It represents a snap shot at a capacity of 1 Ah at 20 °C after a 1C discharge. The behavior is already known from the macro-model. The concentration of lithium ions is higher on the anode side and lower on the cathode side. Compared to the macro-model, which is shown in Figure 39, the gradient is less intense. The concentration that is reached on the cathode current collector is around 1.18 mol/l in contrast to the macro-model which is ca. 1.17 mol/l. This causes a shift of the gradient towards the cathode which means that the concentration of 1.2 mol/l is around 60 µm of the micro-model and ca. 0.75 µm of the macro-model. This indicates that the intercalation

process on the cathode side is faster than that of the macro-model. The concentrations within the solid phase show a gradient along the cross section, too. A large difference can be observed on cathode side. Here, the concentration is higher with a stoichiometry of 0.8 compared to the macro-model, wherein the stoichiometry is around 0.5. The reason is the interface of the micro-model. This acts as additional lithium storage leading to slower changes in the stoichiometry of the bulk species. This is the reason that the discharge curves reach the full capacity.

Bulk diffusion.   Due to bulk diffusion, a gradient along the particle radius occurs. Applying a 1C discharge using model "Micro 1", this is shown in Figure 86 for different operation times given as capacity for a better comparison with discharge curves. The radius of 0 μm represents the particle surface where the electron transfer and lithium intercalation take place. In panel a), a particle of the anode is depicted representing a particle from the center of the anode thickness. Due to discharge, the stoichiometry of the anode decreases. With increasing operation time, the concentration shows a growing gradient which vanishes after 2 Ah. At 0.5 Ah, a small gradient occurs showing a higher concentration at the center of the particle. The gradient increases to 1 Ah. At 1.5 Ah, the gradient is reduced showing a changing point at around 1 μm. At 2 Ah, the concentration is constant overall. This correlates to the change of the diffusion coefficient. With operation time the stoichiometry, or the concentration of lithium, changes and, depending on that, the diffusion coefficient, too. In Figure 33, the diffusion coefficient changes about one order of magnitude with stoichiometry which results in a gradient of concentration along the particle radius. On the cathode side (panel b), the stoichiometry rises with operation time. Starting from low stoichiometry values, a gradient occurs already from the beginning. The intercalation reaction is quite fast so that after only ¼ of operation time, the stoichiometry is already at around 0.8. The stoichiometry rises not linearly due to a slow phase-transition reaction. At all operation points, a gradient is observed induced by diffusion.

Next, a comparison is given to see the influence of an interface variation on the lithium concentration within the solid phase material using model "Micro 3". So in the following, the interface is current and SOC dependent. Results are shown in Figure 87. The behavior is the same concerning the anode side (panel a), because no changes were made here. On the cathode side, the behavior is similar compared to the results of model "Micro 1". Differences in concentrations along particle radius are recognizable with less steep gradients. In Figure 88, the rapid rise of stoichiometry directly after starting discharge is shown. Beginning from a de-

lithiated FP particle, it is filled rapidly reaching a stoichiometry of 0.4 after only 1.4 minutes (0.05 Ah). That indicates that the electron-transfer reaction is very fast. But, the value of the electron-transfer reaction is fitted to show good agreement in impedance spectra so that this value is in the correct order of magnitude (cf. impedance spectra). Therefore, the phase transition is the rate-determining step.

a) Anode   b) Cathode

Figure 86: Concentration gradient within electrode particle without interface variation.
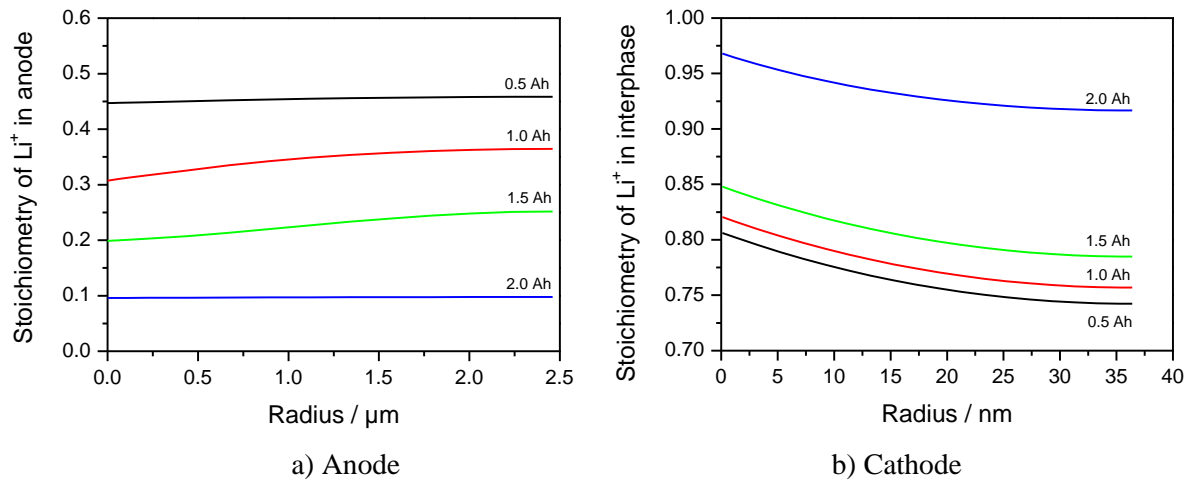

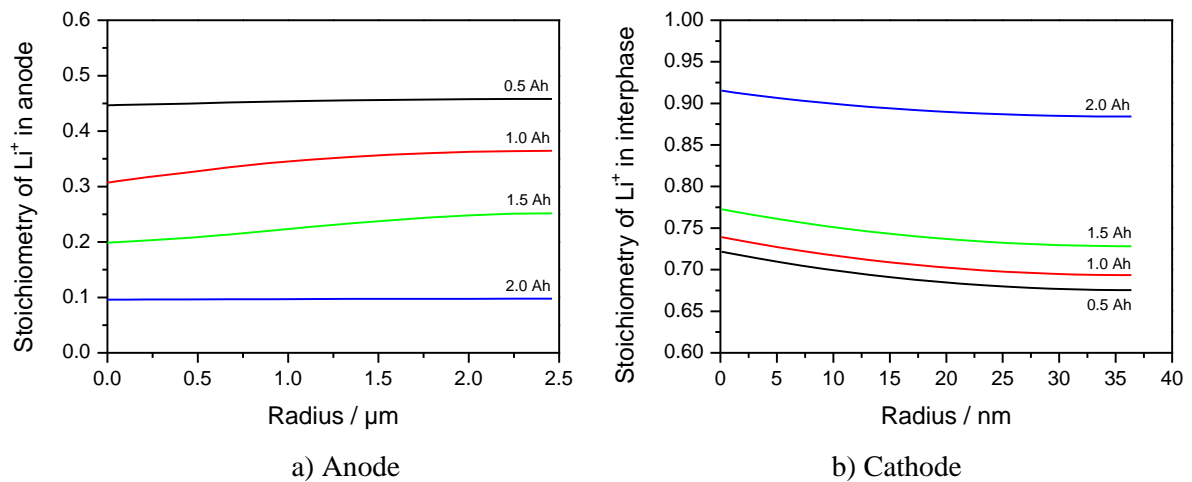a) Anode   b) Cathode

Figure 87: Concentration gradient within electrode particle with interface variation.
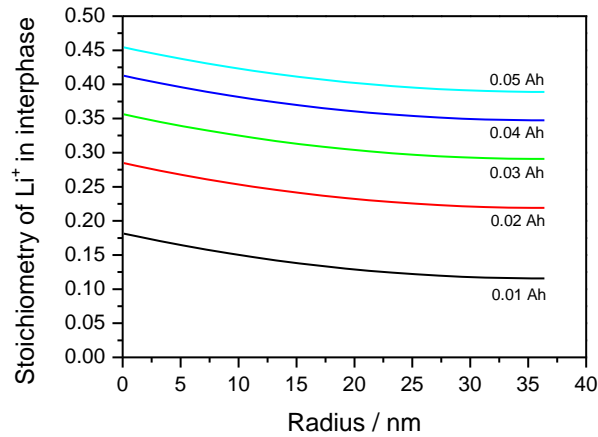
Figure 88: Concentration gradients at various operation times near starting discharge on cathode side.

Impedance spectra. In contrast to the macro-model, the micro-model considers electron transfer and bulk transport separately. This gives rise to a more complex impedance behavior. The results at different SOCs are shown in form of Bode plots in Figure 89. The real part of the impedance is shown in panel a). Depending on SOC, the simulation shows more or less good agreement with experiment. The SOCs of 90 %, 70 %, 50 % and 30 % match very well. In contrast, the SOC of 100 % shows a smaller impedance compared to the experiment in a frequency range between 1 mHz and 100 Hz. Also, the simulation at 10 % SOC shows a strong rise of the impedance at a frequency of 100 Hz which the experiment does not. At 0 % SOC, the simulation show a smaller impedance between 5 Hz and 1000 Hz. Also, the impedance rises at 5 Hz. In panel b, the imaginary part of the impedance is shown for different SOC. The same classification in categories can be given here concerning the SOC. The SOCs between 90 % and 30 % matches well with the experiments except at a frequency between 1 mHz and 5 mHz. The experiment shows a rise of the impedance, in contrast to the simulation, which predicts a decrease of the impedance. At a SOC of 100 %, the simulation shows a strong rise at 50 Hz and also at a SOC of 0 % at a frequency of 100 Hz. At SOC 10 %, the simulation shows an increase of the impedance between 1 Hz and 1000 Hz with a peak at 100 Hz. Using the same division into three domains, as already described in chapter 5.2.1., it shows the same tendency in increasing of the impedance in the LFR like the experiment.

a) Real part   b) Imaginary part
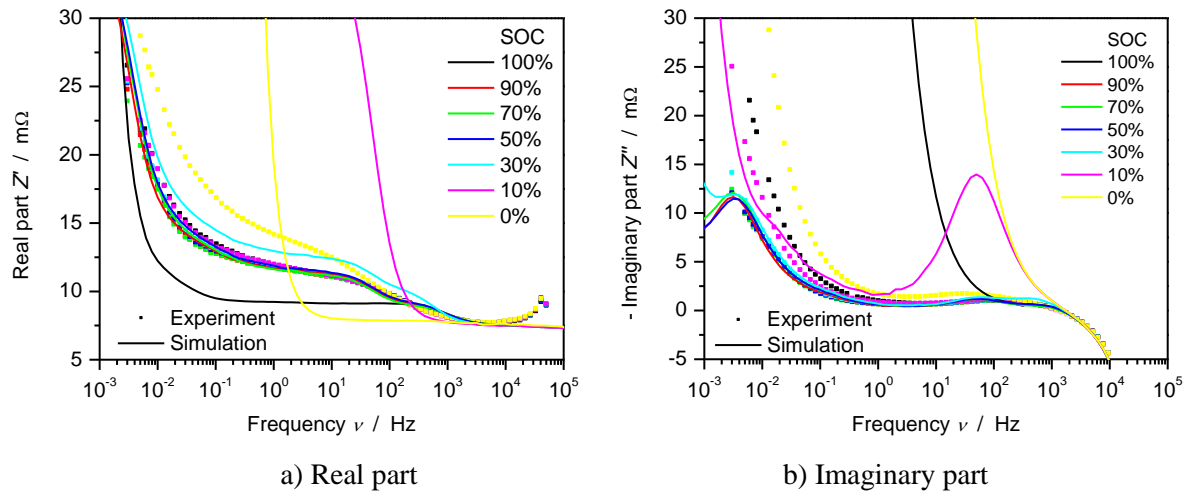
Figure 89: Impedance spectra showing the real and the imaginary part versus frequency.
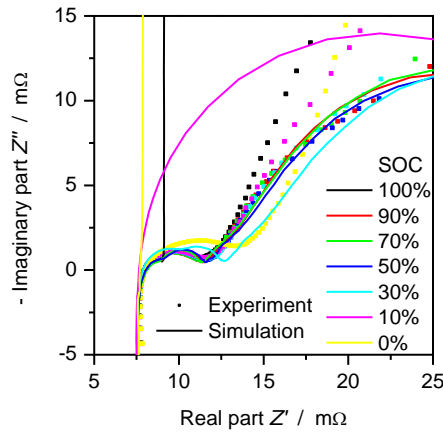
Figure 90: Bode-plot of impedance spectra.

Another representation is given as Nyquist plot in Figure 90. With rising real part of the impedance, a stretched semi-circle occurs followed by a strong increase of the imaginary part. The stretched semi-circle results from the electron-transfer contributions of anode and cathode. The behavior at higher impedance ($Z' \geq 12$ mΩ) corresponds to the LFR in the Bode plots. They show a dependence on the SOC. For SOCs between 90 % and 30 %, the increase of the imaginary part is less intense than for the other SOCs. Also here, the simulation shows the same tendency as the experiments for the SOC between 90 % and 30 %. The simulation at a SOC of 10 % predicts only one big circle while the simulations of SOC 100 % and 0 % show a strong rise of the imaginary part of the impedance.

The simulations show the same behavior like the experiments at SOC between 90 % and 30 % in the Bode plot and in the Nyquist plot. The LFR in the Bode plot is dominated by transport, such as diffusion and phase transition of LFP. The LFR correlates with the domain in the

Nyquist plot above $Z' = 10\ m\Omega$. The simulation shows good agreement here. The cathode is assumed to be slower concerning charge-transfer reaction and to have a lower double-layer capacity. This results in two characteristic increases of the real part of the impedance in the MFR (Figure 89a) coming from high frequencies going to lower frequencies. At around 1000 Hz, the increase can be attributed to the charge-transfer reaction of the anode while the increase of the charge-transfer reaction of the cathode is around 20 Hz. The MFR can be correlated to the stretched semi-circle in the Nyquist plot. Here, the corresponding circle of the anode overlaps with this of the cathode.
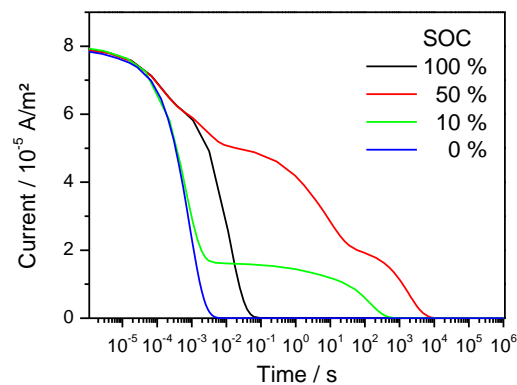
Figure 91: Current relaxation for different SOCs.

The impedance shows a strong dependence on the SOC towards at the limit of the operational range, i.e., SOC 100 % and SOC 0 %. At these conditions the particles are completely filled or emptied of lithium, respectively. Depending on the electrode, the extraction or intercalation of lithium is hindered leading to a rise of overpotentials. This decreases the current which is recorded in impedance measurements. To visualize the current distribution at different SOC, the relaxation of the current density versus time after a voltage step is shown in Figure 91. The SOC of 50 % is shown as reference. With increasing time, the current decreases stepwise until the current density reaches the value of 0. Strong relaxations occur at around 1 ms, 10 s and 200 s. The relaxation is less intense between these times. The current density at SOC 0 % decreases fast within 10 ms reaching 0 A/m². The deviation from the behavior of the relaxation at SOC 50 % starts at around 0.1 ms. The relaxation at 10 % shows a similar behavior concerning the fast relaxation. But a stagnation of the relaxations occurs at around 5 ms. The current density is nearly constant over a wide time range (5 ms – 10 s) until it decreases to 0 A/m². The relaxation of the current density at 100 % SOC shows the same behavior as the reference until 2 ms. Then, it decreases fast within around 50 ms reaching 0 A/m².

This diagram allows comparing the transferred charges at different SOC by integrating the area below the curves [A · s = C/s · s = C]. At SOC 100 % and SOC 0 %, the transferred

charge is less than at SOC 50 %. This confirms the assumption that the electron-transfer process is hindered. In general, it depends on the concentration of lithium in the active material. First, it depends on the initial concentration, because there is a dependence on SOC. Second, it depends on the concentration while operation, because the concentration is linearly correlated to the charge transfer. Kinetic processes, such as diffusion, influence the concentration. To proof this assumption, a parameter variation was performed concerning diffusion coefficient and diffusion length (particle radius). They show an influence on the impedance, but an improvement was not achieved concerning the agreement with experiments.

Sensitivity analysis. The model "Micro 1" was subject to a sensitivity analysis using the same procedure as described in chapter 5.2.1 to identify physicochemical processes which influence the voltage and represent rate-determining processes. Results are shown in Figure 92 − 94. It can be noticed that no process has a direct proportionality between model parameter and cell voltage. But a few parameters show an influence on the cell voltage. On the anode side (Figure 92), these are the stoichiometry range, the density, the electrode thickness and the volume fraction of the active material. An increase of all these parameters correlates with a change of the concentration of stored lithium ions in the active material leading to higher cell voltages. On the cathode side (Figure 93), there are similar parameters causing a change in lithium concentration, such as electrode thickness, density of FP, LFP and the surface, respectively, and the surface area. Furthermore, an increase of the surface-adsorption coefficient leads to higher coverage, and therefore, it influences the phase-transition reaction changing the lithium content in the active material. Another parameter is the total winding area showing an influence on the cell voltage. This parameter describes the measured total area after unfurling the sheets. It is not the microscopic active surface area which is unknown. It influences the cell voltage because current density and capacity are given as surface associated values in our model, such as A/m² or Ah/m². E.g. the capacity is given in our model in Ah/m² and is multiplied by the total winding area, given in m², to obtain the capacity in Ah. Due to this simple mathematical correlation, a shift occurs leading to different cell voltages compared to the reference. The same is valid for the current density given in our model. To apply a 1C-rate, the current density of 13.45 A/m² is given, which is the current 2.3 A divided by the total winding area of 0.171 m². A change of the area leads to a change of the current density which is applied to the whole battery model. This application causes a change in overpotentials resulting in different gradients compared to the reference simulation. So, the total winding area has an influence on the whole simulation and not only on one parameter process. In contrast,

processes, associated with electron transfer, show no important influence on the cell voltage by changing only one value. This means that these processes are not rate determining.
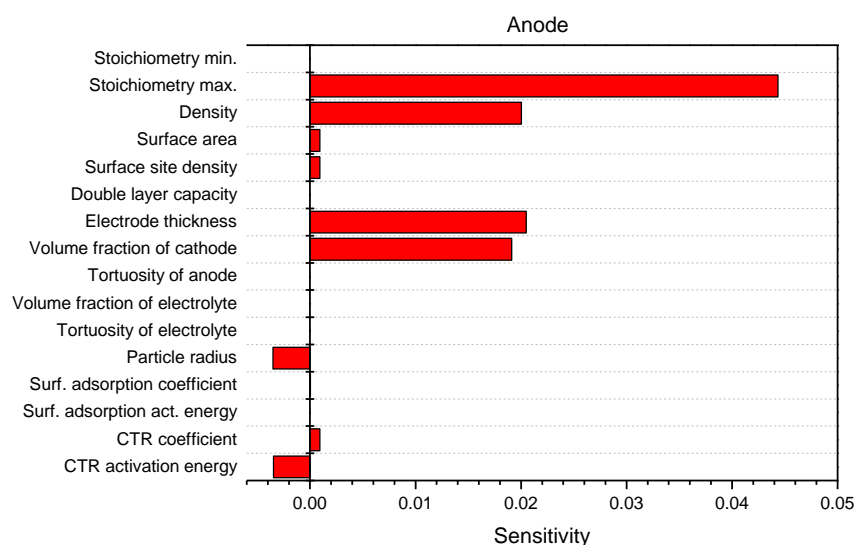
Figure 92: Sensitivity analysis of parameters related to anode. CTR means charge-transfer reaction.
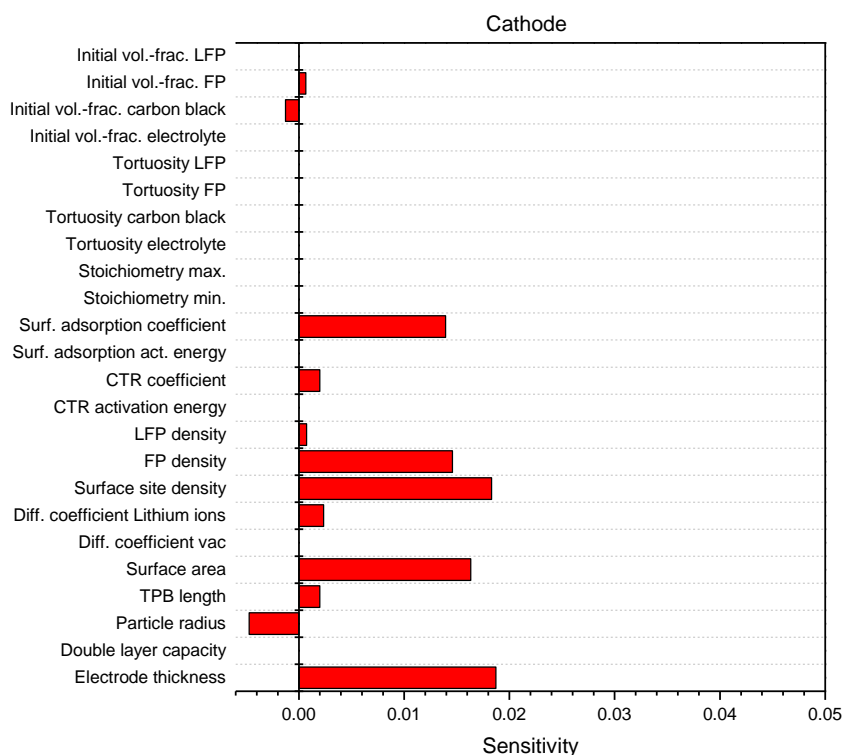
Figure 93: Sensitivity analysis of parameters related to cathode. CTR means charge-transfer reaction.
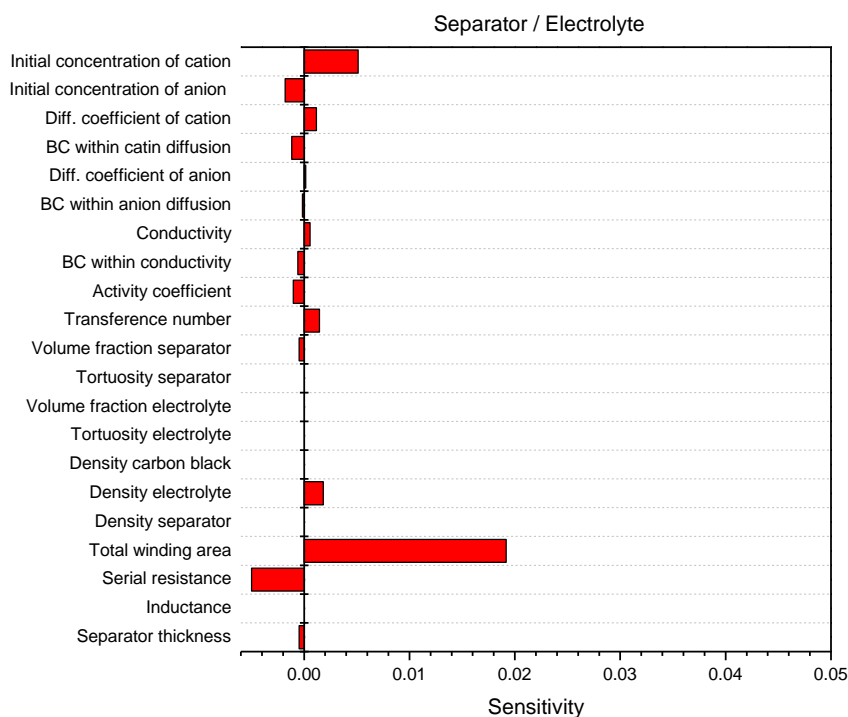
Figure 94: Sensitivity analysis of parameters related to separator or electrolyte, respectively. BC means Bruggeman-coefficient.

Compared to the macro-model "Macro 1", the results show similar behavior. Mainly, processes are responsible for cell-voltage variations which are correlated to the lithium content. But, a general difference can be observed between the macro-model "Macro 1" and the micro-model "Micro 1". In the latter, electron transfer and bulk transport are explicitly defined, so all processes can be varied separately. In contrast, concerning "Macro 1", nearly all information is lumped into the Butler-Volmer equation. Due to the fact that processes within the bulk are not represented here, the activation energy of the charge-transfer reaction of model "Macro 1" is very sensitive to changes.

6.3 Conclusions and outlook

Conclusions. Compared to the macro-model, the micro-model shows an improved agreement with experiments regarding impedance spectra at intermediate SOC. Due to use of elementary kinetics in form of different elementary reactions on anode and cathode side, it is possible to reproduce the processes time-resolved and in a correct weighting. The total frequency range can be distributed into three domains: the high frequency range (HFR), the medium frequency range (MFR) and the low frequency range (LFR). In the HFR, ohmic resistances can be recognized. In the MFR, electron-transfer processes can be observed from anode and cathode. In case of an LFP battery, the electron-transfer reaction of the cathode is

149

slower than that of the anode. In the LFR, the strong resistance increase is attributed to the phase-transition reaction.

Applying the model to charge and discharge curves, C-rates up to 1C can be reproduced. A better agreement with experiments at higher C-rates can be obtained only by applying a SOC- and current-dependent surface area. The results show, that, when discharging, the interface size is important, in contrast to the diffusion rate. In opposite, when charging, the diffusion process dominates the curves instead of the interface size. It was concluded that the intercalation reaction is too slow. While discharging, lithium ions must be buffered in the interface. Therefore, while charging, the interface is irrelevant, because diffusion dominates depending on lithium concentration in the interface. The latter is significantly dictated by the intercalation reaction. But, if this reaction is accelerated, the real part of the impedance decreases immensely in the low frequency region, so that no agreement with experiments can be achieved. Especially, the resistance in the LFR is responsible for a correct reproduction of all discharge curves, charge curves and impedance spectra. The current model predicts that the resistance in the LFR is due to the phase-transition reaction. For discharging a buffering species is necessary, because the intercalation reaction is too slow. On the other hand, for charging, no buffering species exist, because the diffusion is too fast and the intercalation reaction is too slow.

Outlook.   The micro-model forms the base for further improvements and extensions. One option is to couple this model with the macro-model. Further information was obtained regarding heat production and temperature variation depending on elementary kinetics.

Going into more detail, it was extended by adding an additional interface including diffusion which is orthogonal to the current diffusion direction. This idea is inspired by Chang et al (cf. chapter 2.5.3.3, [108]). This clarifies the spatial growing of the LFP phase, in order to specify the rate-limiting step.

Furthermore, the transition of FP to LFP, or LFP to FP respectively, was investigated in more detail. Tang et al. reports that LFP is more stable than FP or lithium metal using electron density calculations [110]. This is plausible because LFP has a lower potential than FP. This implies that the phase transition has different activation energies which, again, result in different overpotentials. This explains why the overpotentials are higher at charge than the micro-model predicts. The phase transition (lithium-ion transport and electron-transfer reaction) includes structural rearrangement of atoms while an energetically excited state is passed. The state corresponds to the interface applied in the micro-model, but the further conclusion is that the diffusion is not the bottle-neck or the rate-determining step. Unfortunately, it cannot be

reproduced by the micro-model that the phase transition has a direct influence on discharge curve or impedance spectra. This leads to a possible improvement of the current model in this way: an integration of an energetically excited state (ES) within the intercalation reaction. Here, the ES reacts as buffering species depending on current demand. The following reactions could be defined:

Discharge:

$$FP + e^- \rightleftarrows ES^- , \tag{72}$$

$$ES^- + Li_{EL}^+ \rightleftarrows LFP , \tag{73}$$

and charge:

$$LFP \rightleftarrows ES^+ + e^- , \tag{74}$$

$$ES^+ \rightleftarrows FP + Li_{EL}^+ . \tag{75}$$

The justification is simple: An additional charge leads to a change of electron-density distribution. This causes repulsion between atoms which is compensated by rearrangement of atoms. The change of crystal structure leads to an energetically excited state which is the entatic state. Having this situation, two possible ways are allowed: Again, a release of the electron reaching the original state, which is here FP, or, the incorporation of a lithium ion while keeping the positive charge. In total, the acceptance of a lithium ion and an electron sums to a lithium atom. The incorporation of lithium leads to LFP. The reverse reaction is carried out by release of an electron which again results in an ES. In the following, a lithium ion can be emitted. The result is that the electron transfer takes place before lithium incorporation or release, respectively. Following this concept, the interface area acts as a lithium-buffering phase which widens or shrinks depending on current requirement. Furthermore, it was concluded that a non-equilibrium state occurs during operation. After operation an internal relaxation may take place leading to an equilibrium state. It permits a rearrangement of the crystal structure to minimize misfit stresses.

It has to be mentioned that the assumptions which were made for the cathode here should be valid for the anode in principle, too. This means that the diffusion can be assumed as nearly constant. The change of the diffusion coefficient, shown in Figure 33, can be explained by the change of the structural order of graphite. This is a topic for further development of the model gaining further understanding of principle mechanisms occurring within the active material on the anode. Furthermore, the idea of an entatic state may be transferred to the anode, too. This opens the possibility to reproduce different states of charge and volume changes.

In our model the reactions on the anode side are split into two parts: the adsorption of lithium

ions on the surface and the intercalation reaction. This splitting allows further connection to side reactions, like lithium plating, or aging reactions, such as SEI formation. Both are important topics which should be further investigated.

7 Appendix

7.1 Derivation of electrolyte-model implementation

To describe the transport of solvated and fully dissociated ions with a continuum ansatz, the charge neutrality condition

$$\sum_i (\varepsilon \cdot c_i \cdot z_i) = 0, \tag{76}$$

where ε is the porosity, c_i the concentration of compound i and z_i is the charge of the species i, has to be fulfilled at each time step ∂t:

$$\frac{\partial \left(\sum_i (\varepsilon \cdot c_i \cdot z_i) \right)}{\partial t} = 0. \tag{77}$$

Replacing the concentration with the density of species $i\, \rho_i$ devided by the molar mass of the species $i\ M_i$, it leads to following expression:

$$\frac{\partial \left(\sum_i \frac{z_i \varepsilon \rho_i}{M_i} \right)}{\partial t} = 0. \tag{78}$$

After rearrangement of this equation to

$$\sum_i \frac{\partial \left(\frac{z_i \varepsilon \rho_i}{M_i} \right)}{\partial t} = 0 \tag{79}$$

and

$$\sum_i \frac{z_i}{M_i} \frac{\partial (\varepsilon \rho_i)}{\partial t} = 0 \tag{80}$$

the change of the density with time can be replaced with the partial differential equation

$$\frac{\partial (\varepsilon \rho_i)}{\partial t} = -\nabla J_i + M_i \dot{s}_i^{\mathrm{V}}, \tag{81}$$

where ∇j_i is the flux of species i and $\dot{s}_i^{\mathrm{V}}$ is the source term. This leads to:

$$\sum_i \frac{z_i}{M_i} \left(-\nabla J_i + M_i \dot{s}_i^{\mathrm{V}} \right) = 0 \tag{82}$$

and after rearrangement, we obtain:

$$\sum_i \left(-\frac{z_i}{M_i} \nabla J_i \right) + \sum_i z_i \dot{s}_i^{\mathrm{V}} = 0. \tag{83}$$

The Nernst-Planck equation relates the flux with the concentration change of the species

$$J_i = -D_i \nabla c_i - \frac{z_i F}{RT} D_i c_i \nabla \phi, \tag{84}$$

where the first term of the right hand side describes the diffusion, which depends on the diffusion coefficient D_i and the concentration c_i of species i, and the second term describes the migration of species i, where ϕ is the local potential, R the ideal gas constant and T the temperature. Substituting equation 84 into equation 83 yields:

$$\sum_i \left(\frac{z_i}{M_i} \nabla (D_i \nabla \rho_i) \right) + \sum_i \left(\frac{z_i}{M_i} \nabla \left(\frac{z_i F}{RT} D_i \rho_i \nabla \phi \right) \right) + \sum_i z_i \dot{s}_i^{\mathrm{v}} \quad = \quad 0. \tag{85}$$

Equation 85 is rearranged to

$$\sum_i \left(\frac{z_i}{M_i} \nabla \left(\frac{z_i F}{RT} D_i \rho_i \nabla \phi \right) \right) \quad = -\sum_i \left(\frac{z_i}{M_i} \nabla (D_i \nabla \rho_i) \right) \; - \sum_i z_i \dot{s}_i^{\mathrm{v}}, \tag{86}$$

where the terms which are independent of the potential are separated and put on the right hand side. After rearranging the left hand side via

$$\sum_i \left(\nabla \left(\frac{z_i^2 F}{RT} \frac{D_i \rho_i}{M_i} \nabla \phi \right) \right) \quad = -\sum_i \left(\nabla \left(\frac{z_i D_i}{M_i} \nabla \rho_i \right) \right) \; - \sum_i z_i \dot{s}_i^{\mathrm{v}}, \tag{87}$$

to

$$\nabla \sum_i \left(\frac{z_i^2 F}{RT} \frac{D_i \rho_i}{M_i} \nabla \phi \right) \quad = -\sum_i \left(\nabla \left(\frac{z_i D_i}{M_i} \nabla \rho_i \right) \right) \; - \sum_i z_i \dot{s}_i^{\mathrm{v}}, \tag{88}$$

and multiplying the whole equation with F, the following expression can be obtained:

$$\nabla \sum_i \left(\frac{z_i^2 F^2}{RT} \frac{D_i \rho_i}{M_i} \nabla \phi \right) \quad = -\sum_i \left(\nabla \left(\frac{z_i D_i F}{M_i} \nabla \rho_i \right) \right) \; - \sum_i \left(z_i F \dot{s}_i^{\mathrm{v}} \right). \tag{89}$$

Equation 89 has now the form of

$$\nabla (\sigma \nabla \phi) = b, \tag{90}$$

with

$$\sigma = \sum_i \left(\frac{z_i^2 F^2}{RT} \frac{D_i \rho_i}{M_i} \right), \tag{91}$$

and

$$b = -\sum_i \left(\nabla \left(\frac{z_i D_i F}{M_i} \nabla \rho_i \right) \right) \; - \sum_i z_i F \dot{s}_i^{\mathrm{v}}. \tag{92}$$

The units are $\left[\dfrac{1}{\Omega \cdot m} \right]$ for σ and $\left[\dfrac{A}{m^3} \right]$ for b.

7.2 Derivation of thermal model implementation

Thermal energy is the energy associated with atomic-scale rotational, vibrational and translational motion of atoms and molecules. The total internal energy of a material also includes the potential energy stored in the chemical bonds. To describe the energy conservation

$$\frac{d(\rho e)}{dt} = \frac{dQ}{dt} + \frac{dW}{dt} \quad , \tag{93}$$

where e is the specific energy, ρ is the density, dQ is the heat added to the system and dW is the work done on the system. Replacing the specific energy with the specific enthalpy at a constant pressure, using $h = e + p/\rho$, where p is the pressure, it follows that

$$\frac{d(\rho h)}{dt} = \frac{dp}{dt} + \frac{dQ}{dt} + \frac{dW}{dt} \quad . \tag{94}$$

In the following, only the enthalpy form will be discussed due to its higher relevance for chemical systems

A change in energy leads to a change in temperature depending on the heat capacity of the system. The heat capacity describes the amount of thermal energy that can be stored in a material. The specific heat capacity at constant pressure c_p correlates with the enthalpy dh as $dh = c_p\, dT$. Therefore the energy conservation can be written as function of T as

$$\frac{d(\rho c_p T)}{dt} = \frac{dp}{dt} + \frac{dQ}{dt} + \frac{dW}{dt} \quad . \tag{95}$$

The temperature of a multi-species system depends on occurring chemical reactions. For a chemical system the total enthalpy is given as sum of the species enthalpies:

$$h = \sum_k^K X_k M_k h_k(T) \quad , \tag{96}$$

where X_k is the mole fraction of species k, M_k is the molar mass of species k, h_k is the molar enthalpy of species k and K is the number of species. Then the energy conservation as function of T can be derived as (cf. Kee et al. [162]):

$$\frac{d(\rho c_p T)}{dt} = \frac{dp}{dt} + \frac{dQ}{dt} + \frac{dW}{dt} + \sum_k^K h_k \dot{s}_k \quad , \tag{97}$$

where $\dot{s}_k$ is the chemical production rate of species k.

In the case of an electrochemical reaction, a part of the chemical energy is used to perform external work, which is therefore not available to heating up the system:

$$\frac{dW}{dt} = -E \cdot i^V = -(E_0 - \eta) \cdot i^V = -\left(\frac{\Delta G}{zF} - \eta\right) \cdot i^V = -\left(\frac{\Delta H - T\Delta S}{zF} - \eta\right) \cdot i^V \quad , \tag{98}$$

where E is the cell voltage and i^V is the volumetric current density. The cell voltage can be described as relation between the overpotential η and the Nernst voltage E_0, which is the equi-

librium voltage. This voltage can be substituted using the free reaction enthalpy ΔG devided by the sum of the transferred electrons z and the Faraday's constant F. The right hand side of the equation can be obtained using the Gibbs-Helmholtz equation, where ΔH is the reaction enthalpy of the electrochemical reaction and ΔS is the reaction entropy. If we assume that only one single electrochemical reaction and no other thermochemical reactions take place, then the heat source term can be set equal to

$$\sum_{k}^{K} h_k \dot{s}_k = \Delta H \frac{i^{\mathrm{V}}}{zF} \quad . \tag{99}$$

Substituting eq. 98 and eq. 99 into eq. 97 yields

$$\frac{d(\rho c_p T)}{dt} = \frac{dp}{dt} + \frac{dQ}{dt} + \frac{T\Delta S}{zF} i^{\mathrm{V}} + \eta \cdot i^{\mathrm{V}} \quad . \tag{100}$$

This is the standard formulation for heat conservation in an electrochemical system. The entropy term is also referred to as reversible heat. The overpotentials cause irreversible heat due to several contributions, such as activation overpotential (charge transfer), concentration overpotential (transport effects) and ohmic overpotential, which leads to Joule heating. If the overpotential η is independent of i, it can also be represented as internal resistance: $r_{\mathrm{int}} = \eta \, / \, i$. In this case, the last term changes to

$$\left(\frac{dQ}{dt} \right)_{\mathrm{irreverible}} = \eta \cdot i^{\mathrm{V}} = r_{\mathrm{int}} \cdot \left(i^{\mathrm{V}} \right)^2 \quad . \tag{101}$$

For the formulation used in the present work, we neglect pressure and additional heat sources. Therefore eq. 97 results in

$$\frac{d(\rho c_p T_e)}{dt} = \frac{dW}{dt} + \sum_{k=1}^{K} h_k \dot{s}_k \quad . \tag{102}$$

Substituting again eq. 98 and eq. 99 into eq. 102, we obtain:

$$\frac{d(\rho c_p T)}{dt} = -E \cdot i^{\mathrm{V}} + \Delta H \frac{i^{\mathrm{V}}}{zF} \quad , \tag{103}$$

or

$$\frac{d(\rho c_p T)}{dt} = i^{\mathrm{V}} \cdot \left(\frac{\Delta H}{zF} - E \right) . \tag{104}$$

This general expression must be applied to both electrodes which results in

$$\frac{d(\rho c_p T)}{dt} = i_e^{\mathrm{V}} \cdot \left(\frac{\Delta H_e}{zF} - \Delta\phi_e \right) , \text{ with } e = [\text{an, ca}]. \tag{105}$$

This formulation is implemented in DENIS.

8 References

[1]   M. Piccolino, The bicentenial of the Voltaic battery (1800 - 2000): the artificial electric organ, Trends in Neuroscience, 23 (2000) 147–151.

[2]   J.-M. Tarascon, M. Armand, Issues and challenges facing rechargeable lithium batteries, Nature, 414 (2001) 359–367.

[3]   Y.F. Reynier, R. Yazami, B. Fultz, The entropy and enthalpy of lithium intercalation into graphite, Journal of Power Sources, 119-121 (2003) 850–855.

[4]   Y.F. Reynier, R. Yazami, B. Fultz, Thermodynamics of lithium intercalation into graphites and disordered carbons, Journal of the Electrochemical Society, 151 (2004) A422–A426.

[5]   M. Doyle, Y. Fuentes, Computer simulations of a lithium-ion polymer battery and implications for higher capacity next-generation battery designs, Journal of the Electrochemical Society, 150 (2003) A706–A713.

[6]   G. Sikha, R.E. White, B.N. Popov, A mathematical model for a lithium-ion battery/electrochemical capacitor hybrid system, Journal of the Electrochemical Society, 152 (2005) A1682–A1693.

[7]   H. Lee, C. Wan, Y. Wang, Identity and thermodynamics of lithium intercalated in graphite, Journal of Power Sources, 114 (2003) 285–291.

[8]   S. Lee, Y. Kim, H. Chun, Modeling on lithium insertion of porous carbon electrodes, Electrochimica Acta, 47 (2002) 1055–1067.

[9]   M. Wissler, Graphite and carbon powders for electrochemical applications, Journal of Power Sources, 156 (2006) 142–150.

[10]   Y. Reynier, J. Graetz, T. Swan-wood, P. Rez, R. Yazami, B. Fultz, Entropy of Li intercalation in Li_xCoO_2, Physical Review B, 174304 (2004) 1–7.

[11]   J.L. Dodd, PhD thesis, California Institute of Technology, (2007).

[12]   P. Strobel, C. Darie, F. Thie, M. Bacia, O. Proux, A. Ibarra-palos, J.B. Soupart, New nanocrystalline manganese oxides as cathode materials for lithium batteries : Electron microscopy , electrochemical and X-ray absorption studies, Solid State Ionics, 177 (2006) 523–533.

[13]   B. Dunn, H. Kamath, J. Tarascon, for the Grid : A Battery of Choices, Science, 334 (2011) 982.

[14]   C. Delmas, M. Maccario, L. Croguennec, F. Le Cras, F. Weill, Lithium deintercalation in $LiFePO_4$ nanoparticles via a domino-cascade model, Nature Materials, 7 (2008) 665–671.

References

[15] W. Zhang, Structure and performance of $LiFePO_4$ cathode materials: A review, Journal of Power Sources, 196 (2011) 2962–2970.

[16] Z. Li, D. Zhang, F. Yang, Developments of lithium-ion batteries and challenges of $LiFePO_4$ as one promising cathode material, Journal of Materials Science, 44 (2009) 2435–2443.

[17] J.L. Dodd, R. Yazami, B. Fultz, Phase diagram of Li_xFePO_4, Electrochemical and Solid-State Letters, 9 (2006) A151–A155.

[18] J.L. Dodd, R. Yazami, B. Fultz, Phase Diagram of Li_xFePO_4, Electrochemical and Solid State Letters, 9 (2006) A151–A155.

[19] J. Li, W. Yao, S. Martin, D. Vaknin, Lithium ion conductivity in single crystal $LiFePO4$, Solid State Ionics, 179 (2008) 2016–2019.

[20] V. Srinivasan, J. Newman, Discharge model for the lithium iron-phosphate electrode, Journal of the Electrochemical Society, 151 (2004) A1517–A1529.

[21] W. Dreyer, J. Jamnik, C. Guhlke, R. Huth, J. Moskon, M. Gaberscek, The thermodynamic origin of hysteresis in insertion batteries, Nature Materials, 9 (2010) 448–453.

[22] D. Morgan, A. Van der Ven, G. Ceder, Li Conductivity in Li_xMPO_4 (M = Mn, Fe, Co, Ni) Olivine Materials, Electrochemical and Solid State Letters, 7 (2004) A30–A32.

[23] Z. Li, D. Zhang, F. Yang, Developments of lithium-ion batteries and challenges of $LiFePO_4$ as one promising cathode material, Journal of Material Science, 44 (2009) 2435–2443.

[24] R. Dominko, M. Bele, M. Gaberscek, M. Remskar, D. Hanzel, S. Pejovnik, J. Jamnik, Impact of the carbon coating thickness on the electrochemical performance of $LiFePO_4$/C composites, Journal of the Electrochemical Society, 152 (2005) A607–A610.

[25] P. Arora, Z.J. Zhang, Battery Separators, Chemical Reviews, 104 (2004) 4419–4462.

[26] J. Vetter, P. Novák, M.R. Wagner, C. Veit, K.-C. Möller, J.O. Besenhard, M. Winter, M. Wohlfahrt-Mehrens, C. Vogler, A. Hammouche, Ageing mechanisms in lithium-ion batteries, Journal of Power Sources, 147 (2005) 269–281.

[27] A.K. Shukla, T.P. Kumar, Materials for next-generation lithium batteries, Current Science, 94 (2008) 314–331.

[28] S.S. Zhang, A review on electrolyte additives for lithium-ion batteries, Journal of Power Sources, 162 (2006) 1379–1394.

[29] Christoph Fehrenbacher, Personal communication, Director of Application Engineering Europe, A123, Personal communication (2011).

References

[30] V. Srinivasan, C.Y. Wang, Analysis of Electrochemical and Thermal Behavior of Li-Ion Cells, Journal of the Electrochemical Society, 150 (2003) 98–106.

[31] H. Ishikawa, O. Mendoza, Y. Sone, M. Umeda, Study of thermal deterioration of lithium-ion secondary cell using an accelerated rate calorimeter (ARC) and AC impedance method, Journal of Power Sources, 198 (2012) 236–242.

[32] G.G. Botte, V.R. Subramanian, R.E. White, Mathematical modeling of secondary lithium batteries, Electrochimica Acta, 45 (2000) 2595–2609.

[33] G.G. Botte, B.A. Johnson, R.E. White, Influence of Some Design Variables on the Thermal Behavior of a, Journal of the Electrochemical Society, 146 (1999) 914–923.

[34] T.D. Hatchard, D.D. Macneil, A. Basu, J.R. Dahn, Thermal Model of Cylindrical and Prismatic Lithium-Ion Cells, Journal of the Electrochemical Society, 148 (2001) 755–761.

[35] L.S. Kanevskii, V.S. Dubasova, Degradation of Lithium-Ion Batteries and How to Fight It : A Review, Russian Journal of Electrochemistry, 41 (2005) 1–16.

[36] C. Forgez, D.V. Do, G. Friedrich, M. Morcrette, C. Delacourt, Thermal modeling of a cylindrical $LiFePO_4$ / graphite lithium-ion battery, Journal of Power Sources, 195 (2010) 2961–2968.

[37] A.M. Colclasure, K.A. Smith, R.J. Kee, Electrochimica Acta Modeling detailed chemistry and transport for solid-electrolyte-interface (SEI) films in Li − ion batteries, Electrochimica Acta, 58 (2011) 33–43.

[38] D. Aurbach, B. Markovsky, I. Weissman, E. Levi, Y. Ein-eli, On the correlation between surface chemistry and performance of graphite negative electrodes for Li ion batteries, Electrochimica Acta, 45 (1999) 67–86.

[39] F.M. Wang, D.T. Shieh, J.H. Cheng, C.R. Yang, An investigation of the salt dissociation effects on solid electrolyte interface (SEI) formation using linear carbonate-based electrolytes in lithium ion batteries, Solid State Ionics, 180 (2010) 1660–1666.

[40] J. Newman, T.W. Chapman, Restricted Diffusion in Binary Solutions, American Institute of Chemical Engineers Journal, 19 (1973) 343–348.

[41] J. Newman, K.E. Thomas, H. Hafezi, D.R. Wheeler, Modeling of lithium-ion batteries, Journal of Power Sources, 119 (2003) 838–843.

[42] M. Doyle, T.F. Fuller, J. Newman, Modeling of Galvanostatic Charge and Discharge of the Lithium / Polymer / Insertion Cell, Journal of the Electrochemical Society, 140 (1993) 1526–1533.

[43] M. Doyle, J.P. Meyers, J. Newman, Computer Simulations of the Impedance Response of Lithium Rechargeable Batteries, Journal of the Electrochemical Society, 147 (2000) 99–110.

References

[44] M. Doyle, J. Newman, Design of lithium / polymer battery systems, Electrochimica Acta, 40 (1995) 2191–2196.

[45] C.R. Pals, J. Newman, Thermal Modeling of the Lithium/Polymer Battery: 1. Discharge Behavior of a Single-Cell, Journal of the Electrochemical Society, 142 (1995) 3274–3281.

[46] P.M. Gomadam, J.W. Weidner, R.A. Dougal, R.E. White, Mathematical modeling of lithium-ion and nickel battery systems, Journal of Power Sources, 110 (2002) 267–284.

[47] W. Lai, F. Ciucci, Electrochimica Acta Mathematical modeling of porous battery electrodes — Revisit of Newman ' s model, Electrochimica Acta, 56 (2011) 4369–4377.

[48] S. Santhanagopalan, Q.Z. Guo, P. Ramadass, R.E. White, Review of models for predicting the cycling performance of lithium ion batteries, Journal of Power Sources, 156 (2006) 620–628.

[49] T.F. Fuller, M. Doyle, J. Newman, Relaxation Phenomena in Lithium-Ion-Insertion Cells, Journal of the Electrochemical Society, 141 (1994) 982–990.

[50] T.F. Fuller, M. Doyle, J. Newman, Simulation and Optimization of the Dual Lithium Ion Insertion Cell, Journal of the Electrochemical Society, 141 (1994) 1–9.

[51] M. Park, X.C. Zhang, M.D. Chung, G.B. Less, A.M. Sastry, A review of conduction phenomena in Li-ion batteries, Journal of Power Sources, 195 (2010) 7904–7929.

[52] M.S. Whittingham, Lithium Batteries and Cathode Materials, Chemical Reviews, 104 (2004) 4271–4301.

[53] A.M. Colclasure, R.J. Kee, Electrochimica Acta Thermodynamically consistent modeling of elementary electrochemistry in lithium-ion batteries, Electrochimica Acta, 55 (2010) 8960–8973.

[54] C.R. Pals, J. Newman, Thermal Modeling of the Lithium/Polymer Battery: 1. Discharge Behavior of a Single-Cell, Journal of the Electrochemical Society, 142 (1995) 3274–3281.

[55] J. Newman, W. Tiedemann, Porous-Electrode Theory with Battery Applications, American Institute of Chemical Engineers Journal, 21 (1975).

[56] G.G. Botte, R.E. White, Modeling Lithium Intercalation in a Porous Carbon Electrode, Journal of the Electrochemical Society, 148 (2001) 54–66.

[57] M.W. Verbrugge, B.J. Koch, Electrochemical Analysis of Lithiated Graphite Anodes, Journal of the Electrochemical Society, (2003) 374–384.

[58] V.R. Subramanian, V.D. Diwakar, D. Tapriyal, Efficient macro-micro scale coupled modeling of batteries, Journal of the Electrochemical Society, 152 (2005) A2002–A2008.

[59] Q. Zhang, R.E. White, Moving Boundary Model for the Discharge of a LiCoO$_2$ Electrode, Journal of the Electrochemical Society, 154 (2007) 587–596.

[60] S. Golmon, K. Maute, M.L. Dunn, Numerical modeling of electrochemical-mechanical interactions in lithium polymer batteries, Computers & Structures, 87 (2009) 1567–1579.

[61] W.B. Gu, C.Y. Wang, Thermal-Electrochemical Modeling of Battery Systems, Journal of the Electrochemical Society, 147 (2000) 2910–2922.

[62] A. Nyman, Electrochimica Acta Electrochemical characterisation and modelling of the mass transport phenomena in LiPF$_6$ – EC – EMC electrolyte, Electrochimica Acta, 53 (2008) 6356–6365.

[63] G. Sikha, R.E. White, B.N. Popov, A Mathematical Model for a Lithium-Ion Battery/Electrochemical Capacitor Hybrid System, Journal of the Electrochemical Society, 152 (2005) A1682–A1693.

[64] S. Stewart, J. Newman, Measuring the Salt Activity Coefficient in Lithium-Battery, Journal of the Electrochemical Society, 155 (2008) 458–463.

[65] D. Danilov, P.H.L. Notten, Electrochimica Acta Mathematical modelling of ionic transport in the electrolyte of Li-ion batteries, Electrochimica Acta, 53 (2008) 5569–5578.

[66] D. Danilov, P.H.L. Notten, Li-ion electrolyte modeling : The impact of adding supportive salts, Journal of Power Sources, 189 (2009) 303–308.

[67] Y. Saito, H. Kataoka, A.M. Stephan, Investigation of the conduction mechanisms of lithium gel polymer electrolytes based on electrical conductivity and diffusion coefficient using NMR, Macromolecules, 34 (2001) 6955–6958.

[68] Q. Wang, H. Li, X.J. Huang, L.Q. Chen, Determination of chemical diffusion coefficient of lithium ion in graphitized mesocarbon microbeads with potential relaxation technique, Journal of the Electrochemical Society, 148 (2001) A737–A741.

[69] L.O. Valoen, J.N. Reimers, Transport Properties of LiPF$_6$ -Based Li-Ion Battery Electrolytes, Journal of the Electrochemical Society, 152 (2005) 882–891.

[70] V. Srinivasan, J. Newman, Discharge model for the lithium iron-phosphate electrode, Journal of the Electrochemical Society, 151 (2004) A1517–A1529.

[71] S. Harinipriya, V.D. Diwakar, V.R. Subramanian, Performance Characteristics of Cathode Materials for Lithium-Ion Batteries: A Monte Carlo Strategy, Journal of the Electrochemical Society, 155 (2008) A875–A878.

[72] C.W. Wang, A.M. Sastry, Mesoscale modeling of a Li-ion polymer cell, Journal of the Electrochemical Society, 154 (2007) A1035–A1047.

[73] E. Deiss, D. Haringer, P. Novak, O. Haas, Modeling of the charge-discharge dynamics of lithium manganese oxide electrodes for lithium-ion batteries, Electrochimica Acta, 46 (2001) 4185–4196.

[74] P. Arora, M. Doyle, A.S. Gozdz, R.E. White, J. Newman, Comparison between computer simulations and experimental data for high-rate discharges of plastic lithium-ion batteries, Journal of Power Sources, 88 (2000) 219–231.

[75] M. Doyle, J. Newman, A.S. Gozdz, C.N. Schmutz, J.M. Tarascon, Comparison of modeling predictions with experimental data from plastic lithium ion cells, Journal of the Electrochemical Society, 143 (1996) 1890–1903.

[76] G.G. Botte, B.A. Johnson, R.E. White, Influence of some design variables on the thermal behavior of a lithium-ion cell, Journal of the Electrochemical Society, 146 (1999) 914–923.

[77] K.A. Smith, C.D. Rahn, C.Y. Wang, Control oriented ID electrochemical model of lithium ion battery, Energy Conversion and Management, 48 (2007) 2565–2578.

[78] K. Hayamizu, Y. Aihara, S. Arai, W.S. Price, Self-diffusion coefficients of lithium, anion, polymer, and solvent in polymer gel electrolytes measured using Li-7,F-19, and H-1 pulsed-gradient spin-echo NMR, Electrochimica Acta, 45 (2000) 1313–1319.

[79] M. Doyle, Y. Fuentes, Computer simulations of a lithium-ion polymer battery and implications for higher capacity next-generation battery designs, Journal of the Electrochemical Society, 150 (2003) A706–A713.

[80] K. Persson, Y. Hinuma, Y.S. Meng, A. Van Der Ven, G. Ceder, Thermodynamic and kinetic properties of the Li-graphite system from first-principles calculations, Physical Review B, 82 (2010) 1–9.

[81] K. Persson, V.A. Sethuraman, L.J. Hardwick, Y. Hinuma, Y.S. Meng, A. Van Der Ven, V. Srinivasan, R. Kostecki, Lithium Diffusion in Graphitic Carbon, The Journal of Physical Chemistry Letters, 1 (2010) 1176–1180.

[82] E. Barsoukov, J.H. Kim, C.O. Yoon, H. Lee, Kinetics of lithium intercalation into carbon anodes: in situ impedance investigation of thickness and potential dependence, Solid State Ionics, 116 (1999) 249–261.

[83] P. Yu, B.N. Popov, J.A. Ritter, R.E. White, Determination of the lithium ion diffusion coefficient in graphite, Journal of the Electrochemical Society, 146 (1999) 8–14.

[84] S. Santhanagopalan, P. Ramadass, J. Zhang, Analysis of internal short-circuit in a lithium ion cell, Journal of Power Sources, 194 (2009) 550–557.

[85] R. Huang, F. Chung, E.M. Kelder, Impedance simulation of a Li-ion battery with porous electrodes and spherical Li^+ intercalation particles, Journal of the Electrochemical Society, 153 (2006) A1459–A1465.

References

[86] B.K. Purushothaman, U. Landau, Rapid charging of lithium-ion batteries using pulsed currents - A theoretical analysis, Journal of the Electrochemical Society, 153 (2006) A533–A542.

[87] P. Albertus, J. Couts, V. Srinivasan, J. Newman, II. A combined model for determining capacity usage and battery size for hybrid and plug-in hybrid electric vehicles, Journal of Power Sources, 183 (2008) 771–782.

[88] Q. Zhang, R.E. White, Capacity fade analysis of a lithium ion cell, Journal of Power Sources, 179 (2008) 793–798.

[89] S.J. Harris, A. Timmons, D.R. Baker, C. Monroe, Direct in situ measurements of Li transport in Li-ion battery negative electrodes, Chemical Physics Letters, 485 (2010) 265–274.

[90] V. Srinivasan, J. Newman, Discharge model for the lithium iron-phosphate electrode, Journal of the Electrochemical Society, 151 (2004) A1517–A1529.

[91] A.K. Padhi, K.S. Nanjundaswamy, J.B. Goodenough, Phospho-olivines as Positive-Electrode Materials for Rechargeable Lithium Batteries, Journal of the Electrochemical Society, (1997) 1188–1194.

[92] S. Motupally, C.C. Streinz, J.W. Weidner, Proton diffusion in nickel hydroxide - Prediction of active material utilization, Journal of the Electrochemical Society, 145 (1998) 29–34.

[93] B. Paxton, J. Newman, Variable diffusivity in intercalation materials - A theoretical approach, Journal of the Electrochemical Society, 143 (1996) 1287–1292.

[94] K. Striebel, J. Shim, V. Srinivasan, J. Newman, Comparison of LiFePO4 from different sources, Journal of the Electrochemical Society, 152 (2005) A664–A670.

[95] C.S. Wang, U.S. Kasavajjula, P.E. Arce, A discharge model for phase transformation electrodes: Formulation, experimental validation, and analysis, Journal of Physical Chemistry C, 111 (2007) 16656–16663.

[96] A. Yamada, H. Koizumi, N. Sonoyama, R. Kanno, Phase change in Li_xFePO_4, Electrochemical and Solid State Letters, 8 (2005) A409–A413.

[97] J.A. Allen, T.R. Jow, J. Wolfenstine, Kinetic study of the electrochemical $FePO_4$ to $LiFePO_4$ phase transition, Journal of Chemical Materials, 19 (2007) 2108–2111.

[98] C. Delmas, M. Maccario, L. Croguennec, F. Le Cras, F. Weill, Lithium deintercalation in $LiFePO_4$ nanoparticles via a domino-cascade model, Nature Materials, 7 (2008) 665–671.

[99] L. Laffont, C. Delacourt, P. Gibot, M.Y. Wu, P. Kooyman, C. Masquelier, J.M. Tarascon, Study of the $LiFePO_4/FePO_4$ two-phase system by high-resolution electron energy loss spectroscopy, Chemistry of Materials, 18 (2006) 5520–5529.

[100] M.S. Islam, D.J. Driscoll, C.A.J. Fisher, P.R. Slater, Atomic-scale investigation of defects, dopants, and lithium transport in the $LiFePO_4$ olivine-type battery material, Chemistry of Materials, 17 (2005) 5085–5092.

[101] C. V Ramana, A. Mauger, F. Gendron, C.M. Julien, K. Zaghib, Study of the Li-insertion/extraction process in $LiFePO_4/FePO_4$, Journal of Power Sources, 187 (2009) 555–564.

[102] M. Safari, C. Delacourt, Modeling of a Commercial Graphite/$LiFePO_4$ Cell, Journal of the Electrochemical Society, 158 (2011) A562–A571.

[103] M. Safari, C. Delacourt, Mathematical Modeling of Lithium Iron Phosphate Electrode: Galvanostatic Charge/Discharge and Path Dependence, Journal of the Electrochemical Society, 158 (2011) A63–A73.

[104] M. Safari, C. Delacourt, Aging of a Commercial Graphite/$LiFePO_4$ Cell, Journal of the Electrochemical Society, 158 (2011) A1123–A1135.

[105] M. Tang, W.C. Carter, J.F. Belak, Y.-M. Chiang, Modeling the competing phase transition pathways in nanoscale olivine electrodes, Electrochimica Acta, 56 (2010) 969–976.

[106] M. Tang, H.Y. Huang, N. Meethong, Y.H. Kao, W.C. Carter, Y.M. Chiang, Model for the Particle Size, Overpotential, and Strain Dependence of Phase Transition Pathways in Storage Electrodes: Application to Nanoscale Olivines, Chemistry of Materials, 21 (2009) 1557–1571.

[107] B.C. Han, A. van der Ven, D. Morgan, G. Ceder, Electrochemical modeling of intercalation processes with phase field models, Electrochimica Acta, (2004) 4691–4699.

[108] Y.-M. Chiang, Building a Better Battery, Science, 330 (2010) 1485–1486.

[109] D. Morgan, A. Van der Ven, G. Ceder, Li Conductivity in Li_xMPO_4 (M = Mn, Fe, Co, Ni) Olivine Materials, Electrochemical and Solid-State Letters, 7 (2004) A30–A32.

[110] P. Tang, N.A.W. Holzwarth, Electronic structure of $FePO_4$, $LiFePO_4$, and related materials, Physical Review B, 68 (2003) 165107.

[111] F. Zhou, C.A. Marianetti, M. Cococcioni, D. Morgan, G. Ceder, Phase separation in Li_xFePO_4 induced by correlation effects, Physical Review B, 69 (2004).

[112] S. Harinipriya, V.D. Diwakar, V.R. Subramanian, Performance Characteristics of Cathode Materials for Lithium-Ion Batteries: A Monte Carlo Strategy, Journal of the Electrochemical Society, 155 (2008) A875–A878.

[113] M.A. Roscher, J. Vetter, D.U. Sauer, Characterisation of charge and discharge behaviour of lithium ion batteries with olivine based cathode active material, J. Power Sources, 191 (2009) 582–590.

References

[114] J.P. Schmidt, T. Chrobak, M. Ender, J. Illig, D. Klotz, E. Ivers-Tiffee, Studies on LiFePO$_4$ as cathode material using impedance spectroscopy, Journal of Power Sources, 196 (2011) 5342–5348.

[115] J.P. Schmidt, D. Manka, D. Klotz, E. Ivers-Tiffee, Investigation of the thermal properties of a Li-ion pouch-cell by electrothermal impedance spectroscopy, Journal of Power Sources, 196 (2011) 8140–8146.

[116] M. Pasquali, A. Dell'Era, P.P. Prosini, Fitting of the voltage-Li$^+$ insertion curve of LiFePO$_4$, Journal of Solid State Electrochemistry, 13 (2009) 1859–1865.

[117] H. Joachin, T.D. Kaun, K. Zaghib, J. Prakash, Electrochemical and Thermal Studies of Carbon-Coated LiFePO$_4$ Cathode, Journal of the Electrochemical Society, 156 (2009) A401–A406.

[118] C. Ho, I.D. Raistrick, R.A. Huggins, Application of A-C Techniques to the Study of Lithium Diffusion in Tungsten Trioxide Thin Films, Journal of Electrochemical Society, 127 (1980) 343–350.

[119] P.P. Prosini, M. Lisi, D. Zane, M. Pasquali, Determination of the chemical diffusion coefficient of lithium in LiFePO$_4$, Solid State Ionics, 148 (2002) 45–51.

[120] W. Weppner, R.A. Huggins, Determination of the Kinetic Parameters of Mixed-Conducting Electrodes and Application to the System Li$_3$Sb, Journal of Electrochemical Society, 124 (1977) 1569–1578.

[121] P.P. Prosini, Modeling the voltage profile for LiFePO$_4$, Journal of the Electrochemical Society, 152 (2005) A1925–A1929.

[122] U.S. Kasavajjula, C.S. Wang, P.E. Arce, Discharge model for LiFePO$_4$ accounting for the solid solution range, Journal of the Electrochemical Society, 155 (2008) A866–A874.

[123] P.X. Zhang, Y.P. Wu, D.Y. Zhang, Q.M. Xu, J.H. Liu, X.Z. Ren, Z.K. Luo, M.L. Wang, W.L. Hong, Molecular dynamics study on ion diffusion in LiFePO$_4$ olivine materials, Journal of Physical Chemistry A, 112 (2008) 5406–5410.

[124] K. Striebel, J. Shim, V. Srinivasan, J. Newman, Comparison of LiFePO$_4$ from different sources, Journal of the Electrochemical Society, 152 (2005) A664–A670.

[125] S. Dargaville, T.W. Farrell, Predicting Active Material Utilization in LiFePO$_4$ Electrodes Using a Multiscale Mathematical Model, Journal of the Electrochemical Society, 157 (2010) A830–A840.

[126] Y. Chen, J.W. Evans, Three-Dimensional Thermal Modeling of Lithium-Polymer Batteries under Galvanostatic Discharge and Dynamic Power Profile, Journal of the Electrochemical Society, 141 (1994) 2947–2955.

[127] C.R. Pals, J. Newman, Thermal Modeling of the Lithium / Polymer Battery, Journal of the Electrochemical Society, 142 (1995) 3247–3281.

References

[128] S. Al Hallaj, H. Maleki, J.S. Hong, J.R. Selman, Thermal modeling and design considerations of lithium-ion batteries, Journal of Power Sources, 83 (1999) 1–8.

[129] S.C. Chen, C.C. Wan, Y.Y. Wang, Thermal analysis of lithium-ion batteries, Journal of Power Sources, 140 (2005) 111–124.

[130] M. Guo, R.E. White, Thermal Model for Lithium Ion Battery Pack with Mixed Parallel and Series Configuration, Journal of the Electrochemical Society, 158 (2011) 1166–1176.

[131] K. Kumaresan, G. Sikha, R.E. White, Thermal Model for a Li-Ion Cell, Journal of the Electrochemical Society, 155 (2008) 164–171.

[132] G. Kim, A. Pesaran, R. Spotnitz, A three-dimensional thermal abuse model for lithium-ion cells, Journal of Power Sources, 170 (2007) 476–489.

[133] Q. Huang, M. Yan, Z. Jiang, Thermal study on single electrodes in lithium-ion battery, Journal of Power Sources, 156 (2006) 541–546.

[134] R.E. Williford, V. V Viswanathan, J. Zhang, Effects of entropy changes in anodes and cathodes on the thermal behavior of lithium ion batteries, Journal of Power Sources, 189 (2009) 101–107.

[135] V. V Viswanathan, D. Choi, D. Wang, W. Xu, S. Towne, R.E. Williford, J. Zhang, J. Liu, Z. Yang, Effect of entropy change of lithium intercalation in cathodes and anodes on Li-ion battery thermal management, Journal of Power Sources, 195 (2010) 3720–3729.

[136] K. Somasundaram, E. Birgersson, A. Sadashiv, Thermal – electrochemical model for passive thermal management of a spiral-wound lithium-ion battery, Journal of Power Sources, 203 (2012) 84–96.

[137] Y. Ye, Y. Shi, N. Cai, J. Lee, X. He, Electro-thermal modeling and experimental validation for lithium ion battery, Journal of Power Sources, 199 (2012) 227–238.

[138] G. Guo, B. Long, B. Cheng, S. Zhou, P. Xu, B. Cao, Three-dimensional thermal finite element modeling of lithium-ion battery in thermal abuse application, Journal of Power Sources, 195 (2010) 2393–2398.

[139] G.C.S. Freitas, F.C. Peixoto, A.S. Vianna, Simulation of a thermal battery using Phoenics ®, Journal of Power Sources, 179 (2008) 424–429.

[140] H. Gaul, Elektrochemische Charakterisierung von einer LiFePO$_4$-basierten Lithium-Ionen-Batterie, Student research project, 2010 (Collaboration supervised by Christian Hellwig).

[141] S. Sörgel, DLR-internal experimental results, 2009.

[142] M. Tahir, DLR-internal experimental results, 2011.

[143] R. Jemmali, DLR-internal experimental results, 2009.

References

[144] R. Ruckdäschel, I. Plock, DLR-internal experimental results, 2010.

[145] N. Otsu, A Threshold Selection Method from Gray-Level Histograms, IEEE Transactions on Systems, 9 (1979) 62–66.

[146] A. Wiebelt, T. Isermeyer, T. Siebrecht, T. Heckenberger, Thermomanagement von Lithium-Ionen-Batterien, Automobiltechnische Zeitschrift, (2009) 500–504.

[147] C. Hellwig, S. Sörgel, W. Bessler, A Multi-Scale Electrochemical and Thermal Model of a LiFePO$_4$ Battery, ECS Transactions, (2011).

[148] W. Mielke, Modellierung von Kennlinien, Impedanzen und thermischen Verhalten einer Lithium-Eisenphosphat Batterie, University of Stuttgart, 2011 (Collaboration supervised by Christian Hellwig).

[149] W.G. Bessler, S. Gewies, M. Vogler, A new framework for physically based modeling of solid oxide fuel cells, Electrochimica Acta, 53 (2007) 1782–1800.

[150] A. V Randall, R.D. Perkins, X. Zhang, G.L. Plett, Controls oriented reduced order modeling of solid-electrolyte interphase layer growth, Journal of Power Sources, 209 (2012) 282–288.

[151] M. Hedwig, Skalen übergreifende Modellierung und Simulation des thermischen Verhaltens einer Lithium-Ionen Batterie, University of Stuttgart, 2012 (Collaboration supervised by Christian Hellwig).

[152] D.G. Goodwin, Cantera, Http://code.google.com/p/cantera, (2001).

[153] J. Newman, K.E. Thomas-Alyea, Electrochemical Systems, 3rd ed., John Wiley & Sons, Hoboken, New Jersey, 2004.

[154] J.P. Neidhardt, D.N. Fronczek, T. Jahnke, T. Danner, A flexible framework for modeling multiple solid , liquid and gaseous phases in batteries and fuel cells, Journal of the Electrochemical Society, 159 (2012) 1528–1542.

[155] M.D. Levi, D. Aurbach, Diffusion Coefficients of Lithium Ions during Intercalation into Graphite Derived from the Simultaneous Measurements and Modeling of Electrochemical Impedance and Potentiostatic Intermittent Titration Characteristics of Thin Graphite Electrodes, Journal of Physical Chemistry B, 101 (1997) 4641–4647.

[156] Verein-Deutscher-Ingenieure, VDI-Wärmeatlas, Springer, 1997.

[157] P. Deuflhard, E. Hairer, J. Zugck, One-step and Extrapolation Methods for Differential-Algebraic Systems, Numerische Mathematik, 51 (1987) 501–516.

[158] I. Berg, muParser, (2005).

[159] R.C. Weast, ed., Handbook of Chemistry and Physics, 51st ed., The Chemical Rubber Company.

References

[160] M. Vogler, A. Bieberle-Hütter, L.J. Gauckler, J. Warnatz, W.G. Bessler, Modelling study of surface reactions, diffusion, and spillover at a Ni/YSZ patterned anode, Journal of the Electrochemical Society, 156 (2009) B663–B672.

[161] J. Daubenschmidt, Thermische Modellierung einer Lithium-Ionen-Batterie, Student research project, 2010 (Collaboration supervised by Christian Hellwig).

[162] R.J. Kee, M.E. Coltrin, P. Glaborg, Chemically reaction flow. Theory and practice, John Wiley & Sons, 2003.

Curriculum Vitae

Persönliches

Name:	Christian Hellwig
Geburtsdatum:	3. Juni 1980
Geburtsort:	Köln
Nationalität:	Deutsch

Ausbildung

Seit 10/2008	**Promotion, Deutsches Zentrum für Luft- und Raumfahrt e.V.**
	Institut für Technische Thermodynamik
	Abteilung Elektrochemische Energietechnik (10/2008 bis 01/2013)
	Abteilung Computergestütze Elektrochemie (seit 01/2013)
	Angestrebter Abschluss: Dr. rer.-nat.
03/2003 – 09/2008	**Chemie, Universität Heidelberg**
	Diplom
10/2000 – 03/2003	**Chemie, Universität Heidelberg**
	Vordiplom
08/1990 – 06/1999	**Bunsen-Gymnasium, Heidelberg**
	Abitur

Declaration of authorship

I hereby certify that the dissertation entitled

"Modeling, simulation and experimental investigation of the thermal and electrochemical behavior of a $LiFePO_4$-based lithium-ion battery"

is entirely my own work except where otherwise indicated. Passages and ideas from other sources have been clearly indicated.

Erklärung über die Eigenständigkeit der Dissertation

Ich versichere, dass ich die vorliegende Arbeit mit dem Titel

"Modeling, simulation and experimental investigation of the thermal and electrochemical behavior of a $LiFePO_4$-based lithium-ion battery"

selbständig verfasst und keine anderen als die angegebenen Quellen und Hilfsmittel benutzt habe; aus fremden Quellen entnommene Passagen und Gedanken sind als solche kenntlich gemacht.

Name/Name: Christian Hellwig

Unterschrift/Signed:

Datum/Date: 20.06.2013

Acknowledgements

In the recent years I received help and support from numerous directions, which significantly contributed to the success of this work.

First of all, I thank Prof. Dr. Wolfgang G. Besser. He gave me the opportunity to start my thesis in the field of batteries and to broaden my knowledge in electrochemistry. His goal-oriented guidance and the professional discussions inspired my investigations

Also, I thank Prof. Dr. Emil Roduner for co-supervising my work. Due to regular presentations I got a lot of positive response and further hints for continuing my work.

Furthermore, big thanks to my students which were Julian Daubenschmidt, Henrik Gaul, Wolfgang Mielke, Michael Hedwig. It was an excellent collaboration.

In this work, a lot of experimental investigations were performed. Big thanks to Seniz Sörgel (Charge-, Discharge curves, Impedance spectra, temperature measurements, battery opening), Muhammad Tahir (Charge-, Discharge curves, temperature measurements), Robert Ruck-däschel (SEM), Ina Plock (SEM) and Raoulf Jemmali (CT). Their measurements and experience helped a lot for model development and validation. Thanks to the Initiative and Networking fund of the Helmholtz Association for funding of this work.

I thank all members of the modeling group and all other colleagues. They offered me fruitful discussions and scientific exchange in a friendly atmosphere.

Finally, I thank my family, my mother in particular, my girl-friend Christiane Walter, her family and all my friends who accompanied me the whole years. Their trust in me and my work reloaded my energy over and over.